

UNIVERSITÀ DELLA CALABRIA



UNIVERSITA' DELLA CALABRIA

Dipartimento di Fisica

Dottorato di Ricerca in

Scienze e Tecnologie Fisiche, Chimiche e dei Materiali in convenzione con il Consiglio Nazionale delle Ricerche (STFCM)

CICLO

XXXI

TITOLO TESI

Design of nanostructured composite membranes for water desalination

Settore Scientifico Disciplinare CHIM/05

Coordinatore: Ch.mo Prof. Vincenzo Carbone

Firma oscurata in base alle linee guida del Garante della privacy

Supervisore/Tutor: D.ssa Annarosa Gugliuzza

Firma oscurata in base alle linee guida del Garante della privacy

Co-Tutor: D.ssa Lidia Giorno

Firma oscurata in base alle linee guida del Garante della privacy

Dottoranda: Maria Luisa Perrotta

Firma oscurata in base alle linee guida del Garante della privacy

ITALIAN ABSTRACT

L'accesso alle risorse di acqua pulita al giorno d'oggi, continua ad essere uno dei più urgenti bisogni a livello globale, in cui esigenze economiche ed ecologiche richiedono tecnologie sempre più efficienti. L'acqua di mare potrebbe essere una preziosa fonte naturale per il recupero di acqua dolce e di minerali, da riutilizzare nelle catene produttive industriali e agricole e nelle attività comunali. In quest'ottica, le separazioni basate sulla tecnologia a membrana per ottenere dissalazione stanno giocando un ruolo sempre più importante, al fine di fornire adeguate risorse idriche di qualità, per un ampio spettro di applicazioni designate. Oggi, nella strategia di utilizzo di processi integrati a membrana per la dissalazione dell'acqua, uno degli obiettivi più importanti è lo sviluppo di membrane altamente performanti e selettive e, la ricerca si sta sempre più focalizzando su tecniche che potrebbero essere sia rispettose dell'ambiente che altamente efficienti.

Il progetto di ricerca realizzato durante i tre anni del corso di dottorato, ha visto la combinazione di diversi materiali e tecniche, al fine di impiegare le membrane progettate in processi differenti ma entrambi connessi fortemente con i diversi step della dissalazione.

Il lavoro, possiamo riassumere, ha perseguito i seguenti principali obiettivi:

- Progettazione e sviluppo di membrane innovative attraverso la combinazione di differenti materiali al fine di ottimizzare le caratteristiche chimiche e morfologiche delle membrane per le applicazioni desiderate. Nello specifico sono state percorse due strade, al fine di raggiungere due diversi target: l'ottenimento di pori ordinati e regolari con un elevato carattere idrofobo per membrane con strutture a nido d'ape da utilizzare nella *distillazione a membrana (MD)* e, l'esplorazione delle capacità di nanomateriali 2D quando miscelati in matrici polimeriche di fluoruro di poli-vinilidene (PVDF), al fine di creare particolari interazioni per meccanismi assistiti nella *crystallizzazione a membrana (MCr)*.
- Applicazione delle membrane progettate e preparate per la dissalazione, nei due processi distinti: MD ed MCr, utilizzando soluzioni saline di cloruro di sodio (NaCl) a diversa concentrazione.
- Comprensione degli effetti ottenuti attraverso la combinazione dei materiali utilizzati, a livello molecolare, con l'utilizzo di un approccio integrato computazionale-sperimentale.

L'idea di base del lavoro è stata quella di progettare una differente gamma di membrane nanostrutturate, caratterizzate da una morfologia controllata e con specifica funzionalità chimica. Sono stati utilizzati diversi metodi per sviluppare le membrane, con lo scopo di ottenere proprietà superficiali ed intrinseche tali da determinare prestazioni migliori nei contattori a membrana, in particolare nelle tecnologie MD e MCr, citate in precedenza.

Descrivendo brevemente le due tecniche, per quanto riguarda la distillazione a membrana, qui usata con configurazione a contatto diretto, è caratterizzata dalla presenza di correnti acquose mantenute a differenti temperature che sono separate da una membrana porosa idrofobica. In questo caso la temperatura di una delle due correnti (quella della corrente da trattare) è maggiore rispetto all'altra (che rappresenta il distillato) in modo da creare una differenza di temperatura ai due lati della membrana e quindi, una differenza nella tensione di vapore. Le molecole di vapore che si formano, attraversano i pori della membrana dal lato in cui la tensione di vapore è più alta, condensando dal lato in cui essa è più bassa.

La cristallizzazione a membrana, può essere considerata come un'estensione della distillazione a membrana, e, viene usata anche in questo caso una membrana idrofobica microporosa per creare e sostenere un ambiente supersaturo e controllato in cui i cristalli possono nucleare e crescere. I vantaggi che possono verificarsi se si utilizza MCr, rispetto ai processi tradizionali, sono: elevato livello di purezza; controllo nella formazione dei diversi polimorfi; maggiore omogeneità nella dimensione e forma dei cristalli ottenuti e tempi di nucleazione più rapidi. MD ed MCr sono due processi distinti che però possono operare in un ciclo unico, in cui è necessario trattare corsi d'acqua con composizione diversa e diverso grado di salinità.

Nell'ottica del lavoro svolto, l'attenzione si è concentrata sullo sviluppo di due tipi di membrane polimeriche a partire da diversi concetti e metodologie. Nel primo caso è stato utilizzato il metodo del **"Breath Figures"** per preparare membrane a nido d'ape multistrato con una struttura ben ordinata, al fine di migliorare la produttività e l'efficienza termica senza indurre resistenza al trasporto di massa, per l'applicazione nella distillazione a membrana. Nel secondo caso, la **"Dry/Wet Phase Inversion"** è stata preferita al fine di confinare i cristalli di materiali 2D nelle reti polimeriche del PVDF, con l'intento di promuovere meccanismi di chemiassorbimento tali, da determinare una riduzione dei tempi di supersaturazione e quindi nucleazione, con allo stesso tempo un maggior controllo nei parametri cinetici dei cristalli ottenuti. Tale lavoro sperimentale ha visto la validazione dei risultati ottenuti attraverso l'utilizzo della dinamica molecolare, e quindi di un lavoro computazionale volto alla comprensione molecolare dei diversi meccanismi coinvolti.

I due differenti target, oggetto di studio in questa tesi di dottorato, sono stati proposti al fine di dimostrare come la manipolazione delle membrane utilizzando materiali e tecniche di entità diversa, consenta di migliorare la produttività e l'efficienza per i due processi descritti (MD e MCr), rispetto a quanto presente attualmente in letteratura. In entrambi i casi è stata comunque utilizzata la configurazione a contatto diretto della tecnologia di distillazione a membrana (DCMD), come descritto in precedenza.

Nella prima fase del lavoro sono state preparate, caratterizzate ed applicate in MD, membrane **“Honeycomb”**, con cui il principale risultato raggiunto è stata l’ottenimento in contemporanea di un’alta produttività e di un’alta selettività. L’esplorazione di diversi tipi di tensioattivi, ha permesso di identificare nel sale viologeno dell’1,1’ -Ditetradecil-4,4’-dipiridinio [bis (trifluorometansolfonil)] ammido ($14\text{bp}14(\text{Tf}_2\text{N})_2$), appartenente alla classe dei cristalli liquidi ionici (ILC), l’elemento chiave di base per migliorare l’equilibrio idrofilico/idrofobico, nella realizzazione di membrane con pori perfettamente ordinati.

Infatti il suo utilizzo ha permesso di creare geometrie significativamente più ordinate, migliorando notevolmente il carattere idrofobo delle membrane realizzate. Successivamente è stato creato un coating nanoporoso sulla superficie della membrana honeycomb, realizzata con il polietersolfone (PES), utilizzando come materiale l’HYFLON AD, materiale perfluorurato e a bassa conducibilità termica, che ha quindi costituito il nanofilm attivo delle membrane a nido d’ape multistrato, permettendo l’ottenimento di prestazioni molto efficienti. Infatti sono stati raggiunti flussi elevati ($> 50 \text{ L} / \text{m}^2\text{h}$), ottima reiezione al sale NaCl ($> 99\%$) ed alta efficienza termica ($> 70\%$).

Nella seconda fase del lavoro invece è stato esplorato il potenziale del Grafene e di un altro materiale 2D, il seleniuro di bismuto, confinati come nanofillers nelle matrici di PVDF. Per quanto concerne la realizzazione di tali membrane **nanocomposite PVDF-grafene**, sono state esplorate tre diverse concentrazioni percentuali di grafene, rispetto al PVDF tal quale: 0,5%, 5 % e 10 % p/p. Il principale target raggiunto è stato la riduzione dei tempi di induzione nella formazione di cristalli di NaCl, rispetto al PVDF tal quale. Con il grafene all’interno della matrice polimerica, i tempi di formazione dei cristalli sono compresi in tempi che variano tra i 230 e i 260 minuti (per una concentrazione di grafene che va dallo 0,5 al 10% p/p,) rispetto ai 286 minuti ottenuti con il PVDF tal quale. Inoltre sono stati anche ottenuti parametri cinetici migliori, come quelli del coefficiente di variazione [CV%], che indica il livello di omogeneità nella forma e nella dimensione dei cristalli. Infatti l’intervallo ottenuto per il CV è stato dal 26,67% al 35,8% per le membrane di PVDF-Grafene rispetto al PVDF tal quale, dove il CV registrato è stato dell’48,1%. Per il seleniuro di bismuto, miscelato nella matrice di PVDF, è stata utilizzata solo la concentrazione del 5% p/p, ed è stato raggiunto un CV del 46,40%. In termini di crescita dei cristalli, abbiamo ottenuto valori da 1 a $1,6 \times 10^{-4} \text{ mm/min}$ per le membrane di PVDF-grafene e $2,75 \times 10^{-4} \text{ mm/min}$ per la membrana di PVDF-seleniuro di bismuto, rispetto al PVDF tal quale dove il valore della velocità di crescita ottenuto è stato pari a $0,8 \times 10^{-4} \text{ mm/min}$. Inoltre, l’approccio integrato sperimentale-computazionale, ci ha dato la possibilità di esplorare a livello microscopico ogni singolo fenomeno che si è verificato nel processo di MCr (nucleazione, formazione e crescita di cristalli) in particolare comprendendo l’interazioni esistenti ione-ione e quindi i fenomeni di aggregazione che si verificano nei meccanismi di formazione dei cristalli. Dal

punto di vista computazionale, sono state esplorate solo due concentrazioni di grafene rispetto il PVDF tal quale: 5% e 10 % p/p, e i tempi di nucleazione sono risultati essere anche in questo caso ridotti rispetto al semplice PVDF, raggiungendo valori compresi tra 0,45 e 0,70 ns rispettivamente per PVDF-grafene al 5 % p/p e PVDF-grafene al 10%p/p. Invece con il PVDF tal quale è stato ottenuto un tempo di induzione pari a 0,9 ns. Sia sperimentalmente che attraverso gli studi teorici, è stata quindi validata la capacità del grafene di consentire la sovrasaturazione in meno tempo, e quindi meccanismi di nucleazione ridotti.

Per concludere possiamo dire che il lavoro di tesi condotto nei tre anni di dottorato, ha esplorato una vasta gamma di materiali (PES, HYFLON, PVDF, materiali 2D, ecc.) al fine di calibrare finemente le caratteristiche chimico-fisiche e morfologiche delle membrane. nella prospettiva della desalinizzazione, utilizzando approcci sia sperimentali che computazionali, e applicando anche diverse metodologie di preparazione (Breath Figures e Dry/Wet Phase Inversion). Il leitmotiv del lavoro è stato quindi in linea con l'obiettivo principale della ricerca proposta all'inizio dell'attività di dottorato: manipolare materiali innovativi al fine di rendere funzionali le membrane polimeriche nanostrutturate per applicazioni nella desalinizzazione delle acque.

Index

| | |
|--|-----------|
| Acknowledgments | 6 |
| Preface | 7 |
| Framework, objectives, strategies and achievements | 8 |
| <i>References</i> | <i>17</i> |
| Chapter 1 | 19 |
| Nanostructured materials: an increasingly development field in membrane technology | 19 |
| 1.1 Introduction | 19 |
| 1.2 Nanostructured materials: a brief classification | 19 |
| 1.3 Nanostructured materials in membrane technology: possible applications in water treatment | 23 |
| 1.4 Micro and nanoporous membranes: strategies for new ordered structures | 26 |
| 1.4.1 Lithographic techniques | 26 |
| 1.4.2 Techniques based on colloidal templates | 28 |
| 1.4.3 Self-assembly copolymers | 28 |
| 1.4.4 Breath figure for bio-inspired high-defined membranes | 29 |
| 1.4.5 Honeycomb membranes: from 2D to 3D polymeric films | 30 |
| 1.5 Nanocomposite membranes | 31 |
| 1.5.1 Multi-layer membranes | 31 |
| 1.5.2 Mixed matrix nanocomposite membranes (MMNMs) | 32 |
| 1.6 Two-dimensional materials: application in membrane separation | 34 |
| 1.6.1 Graphene: a 2D material as nanofiller in water treatment | 34 |
| 1.6.2 Beyond graphene: new materials and new perspectives | 36 |
| 1.6.3 Effects of Nanoparticles (NPs) on human health and environment | 37 |
| <i>References</i> | <i>39</i> |
| Chapter 2 | 47 |

| | |
|---|-----------|
| Membrane Distillation and Membrane Assisted Crystallization: membrane operations in water desalination and reuse | 47 |
| 2.1 Introduction | 47 |
| 2.2 Membrane Distillation modes and membrane's features | 48 |
| 2.2.1 Direct Contact Membrane Distillation (DCMD) and its using in water desalination | 52 |
| 2.3 Membrane Assisted Crystallization (MCR) technology: an experimental point of view | 56 |
| 2.3.1 Membrane Crystallization via Membrane Distillation | 57 |
| 2.4 Membrane Assisted Crystallization technology from computational point of view | 61 |
| References | 66 |
| Chapter 3 | 73 |
| Materials and Strategies implemented to manufacture nanostructured membranes and related applications | 73 |
| 3.1 Introduction | 73 |
| 3.2. Materials | 73 |
| 3.2.1 Honeycomb membranes | 73 |
| 3.2.2 Double honeycomb membranes: structure in the structure | 74 |
| 3.2.3 Nanocomposite 2D materials-PVDF membranes | 74 |
| 3.3 Several approaches for preparation of different kind of membranes | 77 |
| 3.3.1 Honeycomb PES membrane preparation | 77 |
| 3.3.2 Structure in the structure: a new porous nanofilm of HYFLON AD | 78 |
| 3.3.3 2D nanomaterials-PVDF composite membranes preparation: dry/wet phase inversion | 79 |
| 3.4 Characterization of solutions for preparing Honeycomb membranes | 81 |
| 3.4.1 Surface Tension | 81 |
| 3.4.2 Dynamics Light Scattering (DLS) for aggregation state | 82 |
| 3.4.3 Kinematic Viscosity | 83 |

| | |
|---|-----------|
| 3.5 Characterization of 2D materials used for preparing PVDF nanocomposite membranes, by X-ray photoelectron spectroscopy (XPS) | 84 |
| 3.6 Membrane morphology characterization | 85 |
| 3.6.1 Molecular structure by H- Nuclear Magnetic Resonance Spectroscopy (H-NMR) | 85 |
| 3.6.2 Wettability by contact angle measurements | 86 |
| 3.6.3 Morphology by Scanning Electron Microscopy (SEM) | 87 |
| 3.6.4 Roughness and topography by Atomic Force Microscopy (AFM) | 89 |
| 3.6.5 Thickness | 90 |
| 3.6.6 Pore size and pore size distribution | 90 |
| 3.6.7 Overall porosity | 92 |
| 3.6.8 Water vapor transmission rate (WVTR) | 93 |
| 3.6.9 Mechanical strength | 93 |
| 3.6.10 Optical microscopy for NaCl crystals analysis in Membrane Crystallization Technology | 93 |
| 3.6.11 Surface Tension analysis for 2D-PVDF based membranes, through Van Oss-Chaudhury approach | 94 |
| 3.7 Water desalination: Membrane Distillation (MD) and Membrane Crystallization (MCr) technology how final applications of membranes produced | 95 |
| 3.7.1 Membrane distillation application for new tailored honeycomb membranes | 95 |
| 3.7.2 2D-PVDF nanocomposite membranes for Membrane Crystallization technology | 97 |
| 3.8 Molecular Dynamics (MD) simulations: a new combined theoretical and experimental approach to evaluate membranes behavior in MCr technology | 99 |
| 3.8.1 Materials | 100 |
| 3.8.2 Force Field Based Simulation | 101 |
| 3.8.3 The Force Field | 101 |
| 3.8.4 Molecular Dynamics (MD) | 103 |
| 3.8.5 Condensed Phase Simulation | 104 |

| | |
|---|------------|
| 3.8.6 Periodic Boundary Conditions | 104 |
| 3.8.7 Amorphous Cell Construction | 105 |
| 3.8.8 The Concept of Ensembles | 105 |
| 3.8.9 Gromacs: new highlighted tools for MD simulation. Its implementation on Membrane Assisted Crystallization | 107 |
| 3.8.10 Radial distribution function (RDF) and Coordination number (CN): analysis systems to evaluate ion-ion interactions in crystallization phenomena | 108 |
| References | 110 |
| Chapter 4 | 117 |
| Layered hydrophobic honeycomb membranes designed for highly productive and efficient membrane distillation | 117 |
| 4.1 Introduction | 117 |
| 4.2 From self-assembly to direct assisted self-assembly: a phenomenological study on bulk properties for preparation of honeycomb Polysulfone membranes | 119 |
| 4.2.1 Influence of the Surfactant on the Surface Structural Order | 121 |
| 4.2.2 Influence of the Alcohol Chain Length on the Pore Size | 125 |
| 4.3 Organization of ordered honeycomb PES membranes via hydrophobic ionic liquid crystals surfactant | 128 |
| 4.4 Layered honeycomb membranes: HYFLON AD porous nanofilm suspended onto PES honeycomb top surface | 134 |
| 4.4.1 HYFLON AD nanocoating preparation | 138 |
| 4.4.2 Structure–properties relationships | 139 |
| 4.4.3 Membrane productivity-efficiency trade-off | 141 |
| 4.4.4 A synthetic summary of properties-performances relationship for honeycomb membranes produced | 146 |
| 4.5 Conclusions | 147 |
| References | 148 |
| Chapter 5 | 151 |
| 2D materials assisted Membrane Crystallization Technology: | 151 |

| | |
|--|-------------------|
| A new combined experimental-computational approach | 151 |
| <i>5.1 Introduction</i> | <i>151</i> |
| <i>5.2 Graphene-PVDF based membranes characteristics</i> | <i>152</i> |
| <i>5.3 MCr process: experimental and computational data</i> | <i>157</i> |
| <i>5.4 Beyond graphene: bismuth selenide</i> | <i>169</i> |
| <i>5.5 Conclusions</i> | <i>176</i> |
| <i>References</i> | <i>177</i> |
| Conclusions | 180 |
| <i>References</i> | <i>185</i> |

Acknowledgments

*A part of this research work has been carried out within the frame of **2DMEMPUR** project funded by 'a grant from the Italian Ministry of Foreign Affairs and International Cooperation' within the frame of the **Great Relevance International Project Italy (MAECI)-China (NSFC) 2018–2020 - New Materials**, with particular reference to Two-dimensional systems and Graphene.*

Preface

In the thesis at first an introduction has been done, reporting framework, objectives, strategies and achievements. Then, first two chapter aimed at analysing knowledge achieved in the literature about:

- i) Nanomaterials, their role in the field of membrane technology and nanostructured membranes (Chapter 1).
- ii) Membrane Distillation (MD) and Membrane Crystallization (MCr) (Chapter 2). These are the processes for which membranes were designed and developed in the present research work.

In Chapter 2 Molecular Dynamics (MD) approach is also discussed and it has been introduced to study MCr and better understanding mechanisms occurring at the membrane surface during heterogeneous crystallization.

In the subsequent three chapters the research activities carried out in this work were discussed. In particular, in Chapter 3, materials and methods were reported. In Chapter 4, results about the preparation and characterization of honeycomb membranes and their performances in MD process were discussed. In Chapter 5, experimental and computational results related to the development and performance of 2D “nanomaterials”/PVDF based membranes for MCr were argued. General conclusions highlighted the major results and achievement of the work.

Framework, objectives, strategies and achievements

Access to clean water resource, continues to be the most urgent at global level where economic and ecological needs have urged for more efficient technologies.

Seawater could be a precious natural source for the recovery of fresh water (Figure 1) and minerals to reuse in industrial and agricultural productive chains and in municipal activities.



Figure 1. Schematic representation and illustration on how membrane technology enter in the strategy of water treatment.

Water reuse is the use of treated wastewater for beneficial purposes, which increases a community's available water supply and makes it more reliable, especially in times of drought [1]. It is playing an increasingly important role in the management of sustainable water resources.

There are two main types of water reuse field:

- Non potable reuse strategies, that treat wastewater for specific purposes other than drinking, such as industrial uses, agriculture, or landscape irrigation. Non potable reuse could also include the use of reclaimed water to create recreational lakes or to build or replenish wetlands that support wildlife.
- Potable reuse strategies, which use highly treated reclaimed wastewater to augment a water supply that is used for drinking and all other purposes.

Potable reuse systems, that are the most important fields of interest in membrane technology, use advanced treatment processes to remove contaminants from wastewater, so it needs to

meet drinking water standards and other appropriate water quality objectives. Typically, the highly treated reclaimed water is then released into a surface water body or aquifer (also called an environmental buffer) before being withdrawn, further treated, blended with other conventional water supply sources, and piped to homes and buildings.

In 2008, United States reused a greater volume of water than any other country (data shown in Figure 2), and it was ranked thirteenth among countries by per capita water reuse. Qatar and Israel used to have the highest water reuse per capita [2].

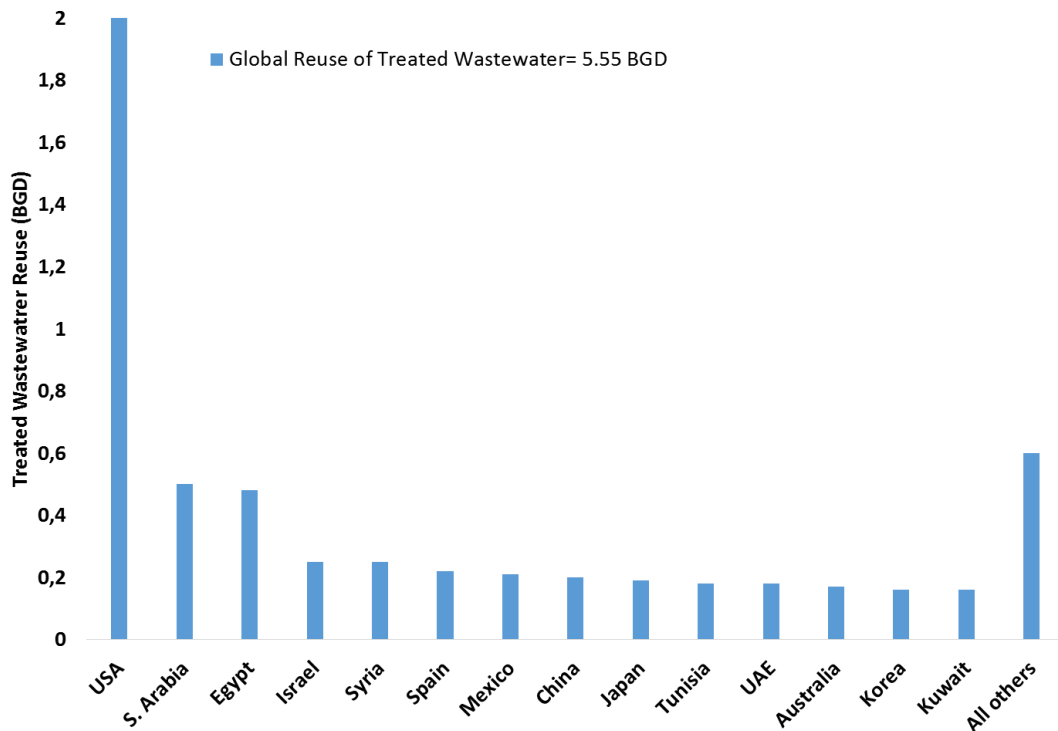


Figure 2. Global Reuse of Treated Wastewater (billions of gallons per day BGD). Adapted from [2].

Over the years the reuse of treated wastewater is rapid increasing in other countries, where desalination is envisaged a practical route to supply fresh reusable water. In 2016, 150 Countries used desalination practices and more than 300 million of people used fresh desalinated water (Figure 3) [3]. Most of the modern interest in desalination is focused on cost-effective provision of fresh water for human use. Along with recycled wastewater, it is one of the few rainfall-independent water sources [4].

Due to its energy consumption, desalinating sea water is generally more costly than fresh water from rivers or groundwater, water recycling and water conservation. However, these alternatives are not always available and depletion of reserves is a critical problem worldwide [5]. Desalination processes are usually driven by either thermal (e.g. distillation) or electrical (e.g., photovoltaic or wind power) as the primary energy types.

Currently, approximately 1% of the world's population is dependent on desalinated water to meet daily needs, but the UN expects that 14% of the world's population will encounter water scarcity by 2025 [6]. Desalination is particularly relevant in dry countries such as Australia, which traditionally have relied on collecting rainfall behind dams for water.

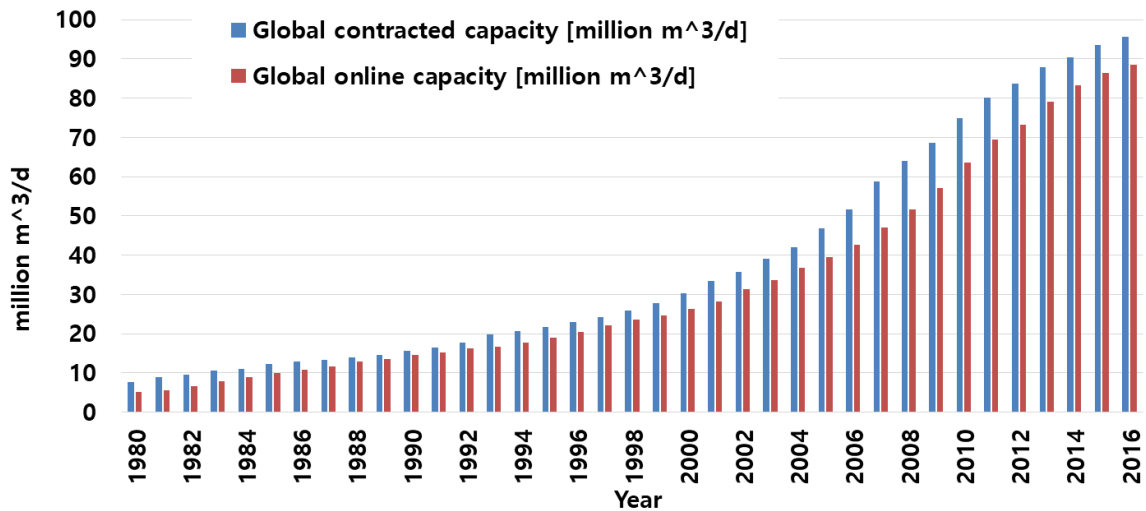


Figure 3. Forecast desalination capacities by technology (at 2016 [3]).

Membrane-based separations for desalination are playing an increasingly important role to provide adequate water resources of desirable quality for a wide spectrum of designated applications.

Nowadays, in the strategy of using integrated membrane processes for water desalination, one of the most important targets is to develop membranes high performing and selective. Research is now focused on techniques that might be both environmentally friendly and highly efficient.

Energy cost in desalination processes varies considerably depending on water salinity, plant size and process type. At present the cost of seawater desalination, for example, is higher than traditional water sources, but it is expected that costs will continue to decrease. It can be possible with technology improvements that include, but are not limited to, improved efficiency [7], reduction in plants footprint, improvements to plant operation and optimization, more effective feed pre-treatment, and lower cost energy sources [8].

The leading process for desalination in terms of installed capacity and yearly growth is Reverse Osmosis (RO) [9], which is a pressure driven process and uses semipermeable membranes. Also, high energy consumption and brine disposal problem are faced in RO process due to the limited recovery of water. These problems may be overcome by

integration of other membrane processes such as a Membrane Distillation (MD) and Membrane Crystallization (MCr). They are two distinct processes that can operate in a cycle where it's necessary to treat water streams with different composition and different salinity degree. In fact, the implementation of an integrated system where a reverse osmosis step is followed by a membrane distillation one, allow to improve quality of fresh water and also the percentage (%) of the recovery factor, as can be seen in Figure 4. Herein, it's possible to see how water coming from RO plant can be further treated increasing the recovery of fresh water from seawater, how is reported in literature [10]. Furthermore, the integration of a membrane crystallizer can allow the recovery and the reuse of salts and other kind of compounds. In terms of

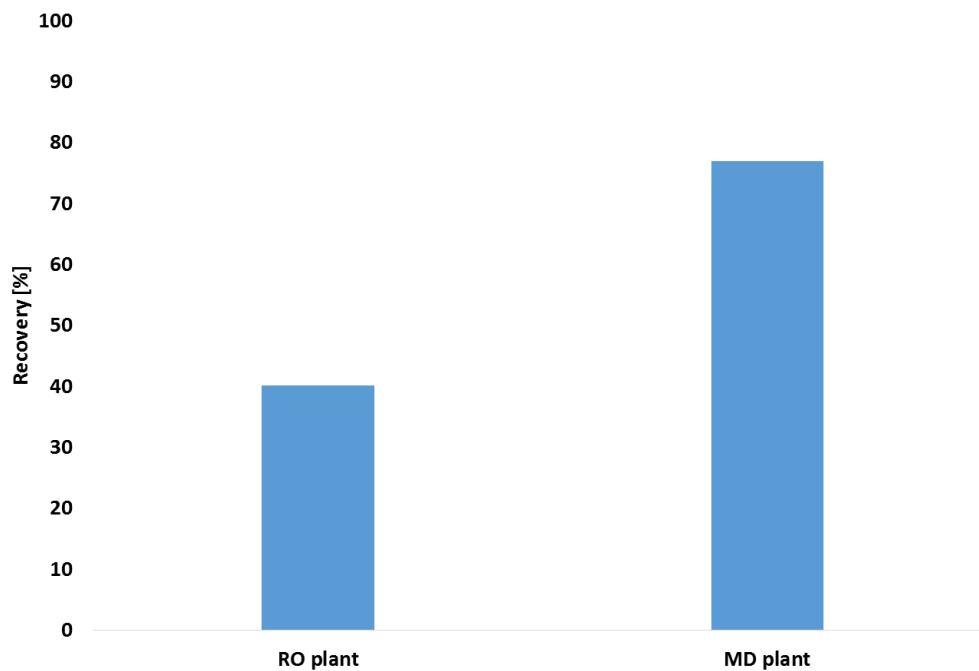


Figure 4. Recovery factor [%] of potable water from seawater coming from Reverse Osmosis (RO) and then treated with Membrane Distillation (MD). Adapted from [10].

Membrane Distillation is a thermally driven separation process in which separation happens for a phase change. Hydrophobic porous membranes that act as barrier for the liquid phase, allow the vapour phase (e.g. water vapour) to pass through the membrane's pores [11, 12]. The driving force of the process is given by a partial vapour pressure gradient commonly triggered by a temperature difference.

MD desalination operations are in conjunction with a power plant or any other source of waste heat, so the cost of energy for heating the feed water is affordable, hence thermally polluted water can be treated economically. Other sources of energy such as renewable solar or geothermal energy could be utilized to heat the feed water.

On the other hand, Membrane Crystallization (MCr) is a process that is gradually replacing the traditional Crystallization in many field. Most of the current crystallization processes are performed under batch or continuous mode based on a stirred tank process. Anyway, the need for breakthrough technologies has been highlighted by numerous authors and reports. Membranes are one of the potentially attracting strategies in order to achieve this target. Nevertheless, a relatively limited number of publications have been reported on membranes related to crystallization processes, with respect to other unit operations [13].

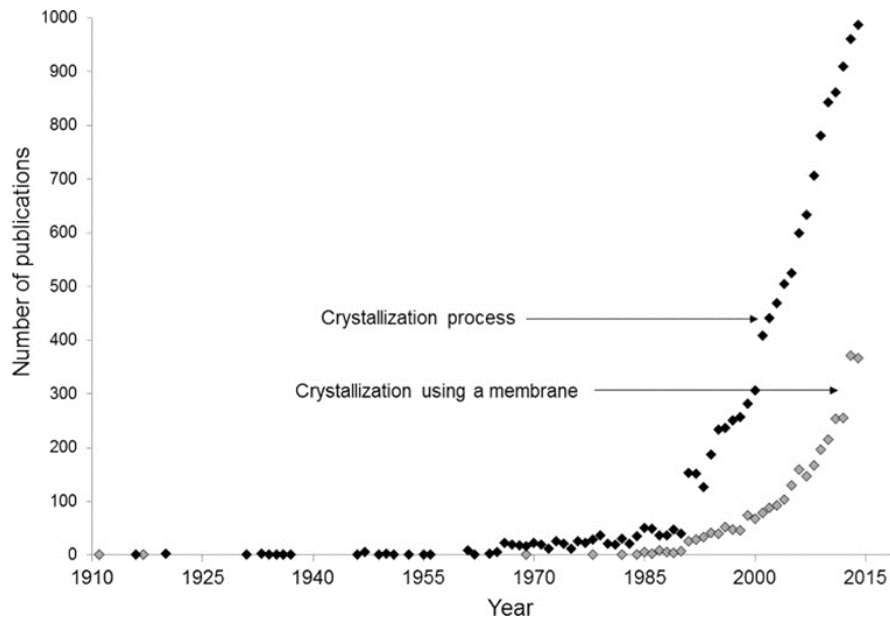


Figure 5. Evolution of the number of publications per year in scientific journals which include the key words “Crystallization” (black diamond) and “membrane crystallization or membrane distillation” (gray diamond). ISI Web of Science, April 2015. Reprinted from [13] Copyright© 2016, with permission from Elsevier B.V. All rights reserved.

Membrane processes have recently been proposed in order to improve performance of crystallization operations, and they are considered as one of the most promising strategies. The number of publications dedicated to crystallization/precipitation processes using a membrane have effectively increased these last years (Figure 5).

In Membrane Crystallization a microporous hydrophobic membrane can be used to create and sustain a controlled supersaturated environment in which crystals can nucleate and grow. The advantages that can be derived if MCr is used, with respect to traditional processes, are:

- High purity level.
- Control of polymorphic form, narrow crystal shape and crystal size distribution.
- Faster nucleation times.

The critical issue remains however the lack of high performing membranes with suitable structural and chemical features for equipping MCr plants. The overcoming

productivity-selectivity trade-off is in high demand, but the exploration of new classes of materials is necessary to go beyond the state of the art and make MD and MCr two competitive eco-friendly tools for supplying fresh water and high-quality minerals.

The purpose of this PhD research work was to explore different classes of materials and procedures of confinement in well-defined volumetric spaces such as membranes, assessing related effects on productivity and selectivity of MD and MCr.

Scientific objectives

The present project carried out during the three years of PhD course has pursued the following main objectives:

- Design and development of innovative membranes through the combination of different materials in order to tune membranes chemical and morphological features for the desired applications. The main purposes were: the achievement of ordered and regular pores with a high hydrophobic character for high performing honeycomb membranes to be used in Membrane Distillation; the exploring of 2D nanomaterials capabilities when blended in PVDF matrix, in order to evaluate the establishing of fruitful interactions for assisting Membrane Crystallization.
- Application of designed and prepared membranes for desalination technology with a focus on two distinct processes: Membrane Distillation and Membrane Crystallization, as mentioned before.
- Understanding of the effects that the selected materials can have on the performance of the process through integrated computational-experimental approaches.

Strategies

The basic idea of the work was to design a range of nanostructured membranes characterized from a controlled morphology and chemical functionality. Different methods were used to develop membranes with the aim to obtain surface properties with improved performance in membrane contactors, in particular in MD and MCr technologies. The attention was focused on the development of two types of polymeric membranes starting from different concepts and methodologies. In the first case the breath figures method was used to prepare multi-layered honeycomb membranes with well-ordered structure, in order to improve productivity and thermal efficiency without inducing resistance to mass transport for application in Membrane Distillation. In the second case, dry-wet phase inversion was

preferred to confine 2D materials crystals in PVDF polymeric networks with the intent to promote controllable chemisorption mechanisms at the vacancies of the nanofiller. Water sequestration mechanisms allowed to manage nucleation and growth of salt crystals during MCr operations. This second approach, allowed to accelerate the mass transfer of water vapor through membranes, via assisted mechanisms by combining different chemical functions. The two different and practical routes were proposed to prepare nanostructured functional membranes with the intent to demonstrate how the manipulation of membranes enable one to improve productivity and efficiency of purification for the two described processes (MD and MCr), by the using of DCMD configuration.

Target achieved

The major target achieved with honeycomb membranes prepared by Breath Figures, was the producing of high productivity and high selectivity, by combination of different materials, The exploring of several kind of materials to use as surfactants, allowed to identify in the viologen salt 1,1'-ditetradecyl-4,4'-dipyridinium [bis(trifluoromethanesulfonyl)] amide (14bp14(Tf₂N)₂), belonging to class of Ionic Liquid Crystals (ILCs), the basic key element in order to improve the hydrophilic/hydrophobic balance. Its using allowed to create significantly more ordered geometries and to enhance the hydrophobic character.

Then, for the first time, a nanoporous coating onto Honeycomb PES top surface was created. It was used HYFLON AD, perfluorinated and low thermal conductivity material to produce the active nanofilm of the multi-layered honeycombmembranes, able to exhibits interesting performances (in MD): high fluxes (> 50 L/m²h), very good salt rejection (> 99 %) and high thermal efficiency (> 70 %).

On the other hand, when graphene and another 2D material, the bismuth selenide, were confined as nanofiller in matrix membranes based on PVDF, they exhibit improved performances in Membrane assisted Crystallization. In this case the major target achieved was the reducing of induction times in NaCl crystals formation, with respect to traditional pristine PVDF.

With graphene inside polymer matrix, times of crystals formation were in a range from 230 to 260 min (for a concentration of graphene from 0.5 to 10 wt %, respectively) compared to 286 min for pristine PVDF.

Better values of Coefficient of Variation [CV %], which indicates how crystals products are uniform in shape and size, were obtained introducing these 2D materials in a confined space as polymeric membrane, and also higher growth rate. The range for CV was from 26.67 %

to 35.8 % for graphene-PVDF membranes (depends on graphene concentration) with respect to pristine PVDF, where CV was 48.1 %. Instead for bismuth selenide, blended in PVDF matrix only at 5 wt %, it was achieved a CV of 46.40 %. In terms of crystal growth, we obtained values from 1 to 1.6×10^{-4} mm/min for graphene-PVDF membranes, and 2.75×10^{-4} mm/min for bismuth selenide-PVDF membrane, with respect to pristine PVDF where the value of growth rate was 0.8×10^{-4} mm/min.

Furthermore, a combined experimental-computational approach gave us the possibility to explore at microscopic level each single phenomenon occurring in MCr process (nucleation, crystals growth) in particular understanding the ion-ion interaction and so aggregation that occur in crystals formation. Reduced induction time were reached with graphene (G) systems: 0.45 and 0.70 ns respectively for PVDF-G 5 and PVDF-G 10 wt %, with respect to 0.9 ns for pristine PVDF. Furthermore, the ability of graphene to allow supersaturation in less time, is in full agreement with theoretical studies, where the water uptake was validated by the detection of radial distribution function (rdf) between graphene layer and water.

The work explored a wide range of materials (PES, HYFLON, PVDF, 2D materials, etc.) in order to tune membranes in the perspective of desalination, using both experimental and computational approaches, and applying also different preparation methodologies (Breath Figures and Dry/Wet Phase Inversion). All details are described in the experimental session. Herein a list of publications produced:

Papers:

- A. Gugliuzza, **M.L. Perrotta**, E. Drioli, Controlled Bulk Properties of Composite Polymeric Solutions for Extensive Structural Order of Honeycomb Polysulfone Membranes, **Membranes** 2016, 6, 27.
- **M.L. Perrotta**, G. Saielli, G. Casella, F. Macedonio, L.Giorno, E. Drioli, A. Gugliuzza, HYFLON – AD nano- membrane suspended on PES honeycomb pattern for a highly productive and thermally efficient membrane distillation process, 2017, **Appl. Mater. Today** 2017, 9, 1-9.
- J.H. Tsai, **M.L. Perrotta**, A. Gugliuzza, F. Macedonio, L. Giorno, E. Drioli, K.L. Tung, E. Tocci, Membrane -Assisted Crystallization: A molecular view of NaCl Nucleation and Growth, **Appl. Sci.**, 2018, 8,2145

Chapter in book:

Maria Luisa Perrotta e Annarosa Gugliuzza, 'Fabrication of ordered micro and nanoporous membranes' in: Functional Nanostructured Membranes (Eds. Enrico Drioli, Lidietta Giorno, Annarosa Gugliuzza), 2019 Pan Stanford Publishing Pte. Ltd. ISBN 978-981-4774-79-6

References

1. Understanding Water Reuse: Potential for Expanding the Nation's Water Supply Through Reuse of Municipal Wastewater, The National Academics of Science, Engineering and Medicine, (2012).
2. B. Jiménez, T. Asano, Water reuse : an international survey of current practice, issues and needs, London : IWA Publishing, (2008).
3. Desalination industry enjoys growth spurts as scary starts to bite, globalwaterintel.com.
4. M. Fischetti, Fresh from the Sea, *Sci. American*, 297 (2007) 118–119, <https://doi.org/10.1038/scientificamerican0907-118>.
5. A. Ebrahimi, G. D. Najafpour, D. Yousefi Kebria, Performance of microbial desalination cell for salt removal and energy generation using different catholyte solutions, *Desalination*, 432 (2019) 1-9, <https://doi.org/10.1016/j.desal.2018.01.002>.
6. L. Henthorne, The Current State of Desalination, International Desalination Association, Retrieved September 5, 2016.
7. G. P. Thiel, Salty solutions, *Phys. Tod.*, 68 (2015) 66–67, <https://doi.org/10.1063/PT.3.2828>.
8. C. Fritzmann, J. Lowenberg, T. Wintgens, T. Melin, State-of-the-art of reverse osmosis desalination, *Desalination*, 216 (2007) 1–76, <https://doi.org/10.1016/j.desal.2006.12.009>.
9. D. M. Warsinger, E. W. Tow, K. G. Nayar, G. Kishor, L. A. Maswadeh, J. H. Lienhard V, Energy efficiency of batch and semi-batch (CCRO) reverse osmosis desalination, *Wat. Res.*, 106 (2016) 272–282, <http://doi.org/10.1016/j.watres.2016.09.029>.
10. F. Macedonio, E. Drioli, Pressure-driven membrane operations and membrane distillation technology integration for water purification, *Desalination*, 223(1–3) (2008) 396–409, <https://doi.org/10.1016/j.desal.2007.01.200>.
11. L. Eykens, K. De Sitter, C. Dotremont, L. Pinoy, B. Van der Bruggen, How To Optimize the Membrane Properties for Membrane Distillation: A Review, *Ind. Eng. Chem. Res.*, 55 (2016) 9333–9343, <http://doi.org/10.1021/acs.iecr.6b02226>.
12. E. Drioli, A. Ali, F. Macedonio, Membrane distillation: Recent developments and perspectives, *Desalination* , 356 (2015) 56-84, <https://doi.org/10.1016/j.desal.2014.10.028>

13. E. Chabanon, D. Mangin, C. Charcosset, Membranes and crystallization processes: State of the art and Prospects, *J. of Membr. Sci.*, 509 (2016) 57–67, <https://doi.org/10.1016/j.memsci.2016.02.051>.

Chapter 1

Nanostructured materials: an increasingly development field in membrane technology

1.1 Introduction

Nowadays, nanomaterials research is in increasingly evolution in several scientific areas, thanks to the possibility to manage these materials for the desired application. Nanomaterials exhibit a single sized unit in at least one dimension between 1 to 1000 nanometres, even if the usual size is 1 to 100 nm [1].

Materials with structure on nanoscale have unique optical, electronic, or mechanical properties [2]. Nanotechnology covers a broad spectrum of research field and requires real interdisciplinary and multidisciplinary efforts. In general, it is regarded as a technology of design, fabrication and applications of nanostructures and nanomaterials. Nanotechnology also includes fundamental understanding of physical properties and phenomena of nanomaterials and nanostructures. The study on fundamental relationships between physical properties and phenomena with material dimensions in the nanometer scale, is also referred to as nanoscience. In the United States, nanotechnology has been defined as being “concerned with materials and systems, whose structures and components exhibit novel and significantly improved physical, chemical and biological properties, phenomena and processes due to their nanoscale size” [3].

In recent years the concept of nanotechnology has been also directed towards membrane technology. The purpose was to develop nanostructured and nanocomposite membranes based on particular polymers and on appropriate combination of 'nanofillers' with well-defined size and porosity and polymers. This approach is dictated by the need to achieve a considerable improvement of the permeable-selective properties compared to currently available membranes, to be able to successfully replace some of the traditional separation processes using membrane processes.

1.2 Nanostructured materials: a brief classification

Applications of nanotechnology are currently touching every aspect of modern life. The increased use of nanomaterials in consumer products, chemical and medical equipments,

information technology, and energy, among others, has increased the interest of research in this field. Nanomaterials are usually man-made synthetic materials, but exist many nanomaterials and nanostructures in nature that promote peculiar properties. It include self-cleaning such as for some plant leaves, which can remain clean even if present in dirt environment. Over the years, it was understood that such a feature involves hydrophobic materials on the rough surface and the outermost lower waxy surface arranged by nano-order (100-200 nm) rules. The nanorough surface is the primary factor in the mechanism that protects the leaves from dirt. Even when the leaves are covered by pollutants, their surface can be easily washed and clean with water. This is called self-cleaning effect or lotus effect. It was found that pigeons, dolphins, butterflies, bees, water magnetotactic bacteria, and other organisms have magnetic ultrafine particles within their bodies that enable this type of organism to navigate under a geomagnetic field. Magnetic ultrafine particles in the bodies of bees are essentially a biological magnetic compass that can accurately position the geomagnetic field and determine the magnetic declination and magnetic inclination; it is the flight navigation system of bees. These are just some of the many examples existing in nature, where nanotechnology is the protagonist and it is from here that the man took, and take inspiration every day, in order to bring innovation in many fields of science but also in everyday life.

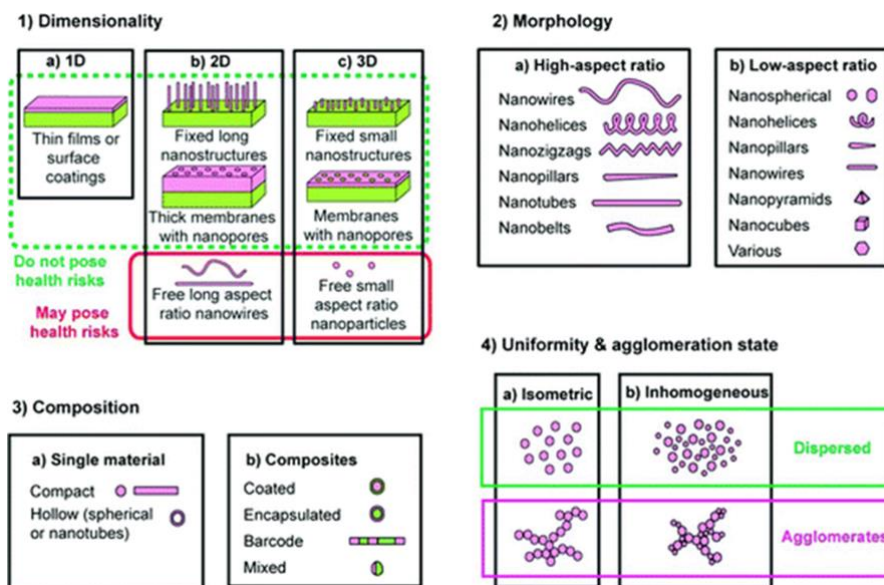


Figure 1.1. Classification of nanostructured materials according to their dimensionality, morphology, composition, uniformity, and agglomeration state. Reprinted from [14] Copyright© 2017, with permission from Elsevier B.V. All rights reserved.

Classification of nanomaterials can be done on different levels: according to origin, dimensionality and their chemical composition (Figure 1.1).

First, nanomaterials can be differentiated according to their origin: natural or anthropogenic. For example, inorganic material resources that give rise to formation of nanomaterials may be erupting volcanoes, the breaking of sea waves, forest fires, storms, etc [5].

Nowadays nanomaterials receive attention in research and industry. Therefore, there is a wide variety of chemical components (organic and inorganic), which they are made of, as a result of human activity and abilities, in science and technology [6]. They are tailored in order to have specific functionalities, thus engineered materials take on important peculiarities when compared to natural and incidental nanomaterials, because characterized by their controlled dimension, shape, and composition.

A second classification of nanomaterials can be made according to their dimensionality: 0D, 1D, 2D, 3D. Nanomaterials with all external dimensions at the nanoscale, between 1 and 100 nm, may be classified as zero-dimensional (0D). The 0D nanomaterials include also various types of nanoparticles, as for example, full spheres like titanium dioxide; dendrimers highly symmetrical, branched macromolecules; hollow spheres made, for example, of carbon (fullerenes), etc. The 0D nanomaterials can be used individually, for example, as a cell marker [7], in solution as an emulsifier [8] or within a solid matrix as a reinforcement filler [9].

In One-dimensional (1D) nanomaterials the electrons are free to travel in one direction and confined in the other two directions. They include nanofibers, nanotubes, nanowires, and nanorods. With only one external dimension at the nanoscale. 2D nanomaterials comprise thin films, nanocoatings, and nanoplates. Thin films mostly used in physics and electronics, for example, to manufacture electronic components with insulating or conductive surface properties or to change the optical reflectivity of surfaces [10]. They can be amorphous or crystalline, made up of various chemical compositions, used as a single layer or as multilayer structures, deposited on a substrate, integrated in a surrounding matrix material, metallic, ceramic, or polymeric.

The last dimensional category of nanomaterials, 3D nanomaterials, show internal nanoscale features but no external dimension at the nanoscale. Bulk nanomaterials are materials that are not confined to the nanoscale in any dimension; these materials are thus characterized by having three arbitrarily dimensions above 100 nm. They possess a nanocrystalline structure or involve the presence of features at the nanoscale. In terms of nanocrystalline structure, bulk nanomaterials can be composed of a multiple arrangement of nanosize crystals, most typically in different orientations. With respect to the presence of features at the nanoscale, 3-D nanomaterials can contain dispersions of nanoparticles, bundles of nanowires, and nanotubes as well as multi nanolayers. [11].

For examples carbon nanotubes can be seen, like the fullerene, as one of the allotropic forms of carbon. Carbon-based materials are those that more than any other, show how the macroscopic properties of a material are strongly influenced by properties at the micro and nanometric level. In elemental form, carbon occurs in three different allotropic forms: diamond, graphite and fullerene. The first two are solids that give rise to extended architectures. The third is by definition a nanostructure. Different properties correspond to the different structures and therefore uses. In Figure 1.2 is showed a brief classification of nanostructured materials about their different morphologies, where fall allotropic carbon forms (nanotubes (1D), graphene (2D), etc) widely applied in nanotechnologies, and also in membrane technology.

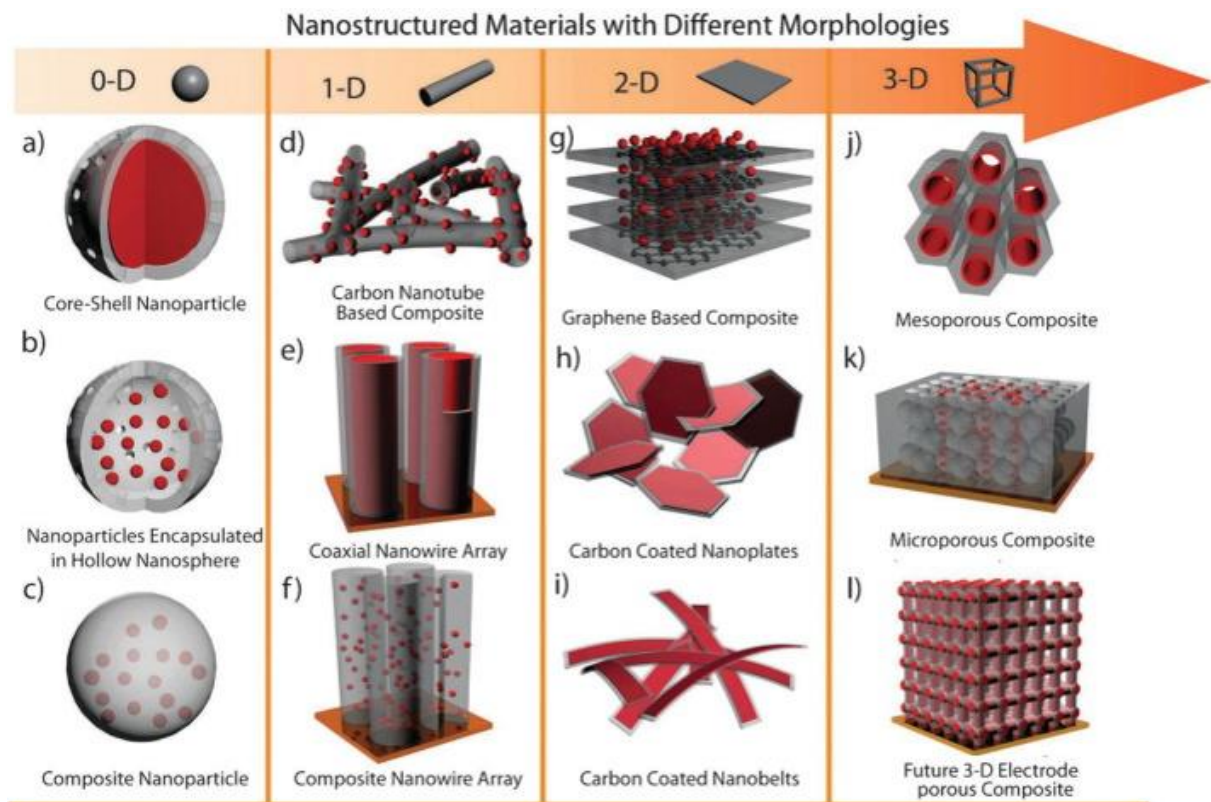


Figure 1.2. Different nanostructured materials based on their complex morphologies. Reprinted from [12] Copyright© 2017, with permission from Elsevier B.V. All rights reserved.

The term nanocomposite is generally used to describe nanofillers dispersed in a bulk matrix. Finally, nanostructured materials include nanoporous structures, for example, aerogels with an extremely low thermal conductivity [13], coatings with nanoprotusions displaying super hydrophobic properties [14], block copolymers [15], and nanostructured metals and alloys used, for instance, as shape-memory materials.

Another possible categorization of nanomaterials is based on the chemical nature of the constituents [16].

They can be subdivided in this way:

- Metal and metal alloy nanomaterials that include silver, gold, copper, iron, aluminum, magnesium, etc.
- Metal oxides (titanium dioxides, zinc oxides, etc)
- Carbon nano-objects, representing one of the best known categories of nanomaterials. They include graphene, carbon nanotubes, carbon nanofibers, fullerenes, and carbon black.
- Semiconductors
- Silicates, Carbonates, and Nitrides. One of the most used nanosilicate is clay, a magnesium aluminum silicate [17]
- Polymers are the last category of nanomaterials. Three types of polymers, that are thermoplastics, thermosets, and elastomers, can be used to make nano-objects including nanospheres, nanofibers, and nanoporous membranes.

Accordingly, nanoparticles can be classified as isometric and inhomogeneous. From the point of view of their agglomeration status, nanoparticles can be dispersed or agglomerate. Their agglomeration state depends on their electromagnetic properties, such as surface charge and magnetism [18].

In general, the most important physicochemical aspects of nanoparticles that make possible their usage in several research field are: composition and surface composition, crystalline phase, particle size distribution, agglomeration/aggregation, shape, specific surface area, roughness/porosity, water solubility/dispersion or hydrophobicity/hydrophilicity, and so on. The unique properties of these various types of intentionally produced nanomaterials give them novel electrical, catalytic, magnetic, mechanical, thermal, or imaging features that are highly desirable for several applications sectors. These materials may also find their way into more complex nanostructures and systems. It can be seen therefore that there are a wide variety of chemical constituents used for the realization of engineered nanomaterials so, as we have discussed previously, nanomaterials arouse interest starting with the little things of everyday life up to more complex scientific applications.

1.3 Nanostructured materials in membrane technology: possible applications in water treatment

Developments in nanoscale research have made it possible to invent economically feasible and environmentally stable treatment technologies. This made possible to effectively treat the polluted waters meeting the increasing water quality standards [19]. Advances in nanotechnology have provided the opportunities to meet the fresh water demands of the future generations. It is suggested that nanotechnology can adequately address many of the water quality issues by using different types of nanomaterials and nanostructures [20]. Nanomaterials possess novel and significantly changed physical, chemical and biological properties mainly due to their structure, so to make real the possibility to combine nanotechnology in membrane technology in order to have significant and better processes performance.

Recent advances in membrane technology have led to an increased use of synthetic membranes for water treatment including desalination, wastewater treatment, surface water purification [21]. In the concept of nanostructured materials, it's possible to subdivide membranes in:

- Nanostructured membranes with controlled morphology, different from that commercially available, that are arousing interest in water treatment when the objective is to turn the selectivity-productivity trade-off towards a unique direction.
- Nanocomposite membranes, functionalized with innovative nanomaterials with different properties, in order to modulate the use according to the type of application and the desired process.

When we say the word “nanostructured membranes”, it's important to underline the multitude of products and related application that can be inserted in this field. We can distinguish them in those already employed at an industrial level, such as Microfiltration (MF), Ultrafiltration (UF), Nanofiltration (NF), Osmosis Reverse (RO) and processes in development (studied and tested on a pilot scale, but not yet installed in industrial plants, such as membrane distillation).

Herein the focus will be mainly on Membrane Distillation and Membrane Crystallization processes.

Nanostructured membranes can be made from ceramic materials or, most commonly, from polymers. Ceramic membranes have the advantage of being more resistant to mechanical forces, chemicals and temperature (they can be sterilized), but are significantly more expensive to manufacture. Furthermore, mechanical, thermal and chemical properties are crucial to ensuring the stability of the membrane under pressure and to allow cleaning and regeneration [22].

Water purification with polymeric membranes is a promising method because high-grade of drinking water can be obtained with low energy consumption at low costs [23]. Current commercial membrane materials are cross-linked polyamides and cellulose derivatives for their using in osmosis reverse. However, it is difficult to obtain ordered sub-nanopores with uniform diameters in these conventional membranes. New materials such as carbon-based materials, synthetic or recombinant channel peptides, polymerized liquid crystals, and block copolymers, have been developed as components for water treatment membranes. These materials can be used to prepare membranes with ordered nanopores and sub-nanopores, with different kind of methodologies (see paragraph 1.4).

On the other hand, as previously mentioned, nanocomposites are solid multi-phase materials where one of the phases has one, two or three dimensions less than 100 nanometers (nm). Another case is that their structures have distances that repeat the nanoscale in the different phases that make up the material. In the broadest sense this definition may include porous media, colloids, gels, copolymers and polymeric mixtures (mixtures between different polymers), but usually means the solid combination of a coarse matrix (part of continuous composite that gives shape to the material) and the nanodimensional phase (or phases). Sure they differ in properties due to differences in structure and chemistry.

Several methodologies can be used to impart new properties to membranes structures, in order to modulate behavior for application desired. Their functionalization with different kind of nanomaterials, can control modulation of the stimulus (light, pH, ionic strength, etc.) [24]. In nanocomposite membranes, the incorporation of nanomaterials into polymers structure can tune morphological and physicochemical properties such as hydrophilicity, charge. density, porosity, chemical, thermal and mechanical stability. With the intent of imitating the multiple functionalities of naturally occurring membranes, various polymers, biological compounds, nanostructures, and functional groups have been incorporated onto the surfaces of synthetic membranes, or blended in polymer matrix extending their applicability to more advanced separation processes [25-31]. A more detailed explanation, regarding in particular different systems used in this work will be given in paragraph 1.5.

Two topics were carried out during PhD:

- The manufacturing of high-ordered honeycomb membranes to apply in MD process, acting on their morphology in order to improve permeability, maintaining at the same time an appreciable selectivity.
- The possibility to give new functionalities to traditional Polyvinylidene fluoride (PVDF) membranes with blending of 2D nanomaterials, carrying on combined experimental and computational approaches.

The main objective has been water treatment for desalination of sea and brackish water with recovery of minerals and salts.

1.4 Micro and nanoporous membranes: strategies for new ordered structures

The availability of nanostructured membranes with a high-defined pore shape, size and distribution is considered as a goal for the improvement in the correlations between morphology and transport properties. As well as controlled thickness and high degree of porosity are considered important factors. A large number of regular pores per surface area together with a high porosity is associated with ideal structures that possess an ordered structural pattern wherein every event can be reproduced point by point without additional resistance to transport. The major output is an optimization of the productivity-selectivity trade-off, thus resulting in highly performing membrane processes. The scientific research is always directed at the improvement of existing techniques, but today there is a great demand for the implementation of new greener, timesaving and economically competitive technologies that can bring new advanced solutions and benefits in the membrane-manufacturing field. High-defined and ordered nanostructures can give a way to new horizons on front of the membrane preparation.

Several kinds of manufacturing techniques are proposed for the development of nanostructured membranes with a high degree of geometric order through two-dimensional (2D) and tridimensional (3D) space.

These are:

- Lithographic techniques [32,33]
- Phase separation and micro-molding combined technique [34,35]
- Techniques based on colloidal templates [36]
- Self-assembly copolymers [37,38]
- Breath figures [39,40]

Each approach takes advantages and limitations, even if over the years a lot of research has been done to improve the features of each of them and to go beyond the state-of-the-art. The major targets are not only under the costs profile, but also in terms of eco-sustainability and rapidity in realizing and producing nanostructures. The techniques used for obtaining regular and uniform structures will be described below, so as then, to focus the attention on advantages that can be derived from Breath Figures which is that studied in thesis work.

1.4.1 Lithographic techniques

The lithographic technique is frequently proposed to achieve polymeric surfaces characterized by a regular structure and having a precise geometric order. Lithography is precisely a mechanical reproduction technique of images. Mainly, the nanolithography is used in the manufacture of semiconductors integrated advanced circuits or nano electromechanical systems (NEMS). It refers to the manufacture of structures on the nanometer scale - at least one lateral dimension between the size of a single atom and that of about 100 nm. Generally, the nano-imprinting lithographic techniques allow imprinting patterns on micro and nano-scale, thus achieving surfaces with extensive structural periodicity. Using a substrate [41] on which the polymer or monomer solution is laid, a force is applied with a mold, causing the formation of a surface with a specific structure. Patterns are created by mechanical deformation of the imprint resist and subsequent processes [42]. When using lithography approach the percentage of success to get extensive structural order is very high, but on the other hand, molds sized in the order of nano are quite expensive and difficult to make a great resolution on scale, thus resulting certainly not advantageous from the economical point of view.

1.4.1 Phase separation and micro-molding combined techniques

Micro-molding combined with phase separation is another attractive manufacturing approach for patterning nanostructures with hierarchical ordered morphology. It can be envisaged as an evolution of traditional phase inversion. It is a process in which, a polymer is precipitated from a solution assuming a desired configuration, including flat, cylindrical or spherical shape [43]. The solidification process begins with a transition from a liquid into two liquid phases: one rich in polymer, the other one rich in solvent. The first one solidifies forming a solid network; the second one generates the pores or voids in the matrix [44].

The fabrication procedure consists of some steps [45]:

- The building up of a mold having a corresponding predetermined micro to nanosized structure at the surface.
- The contact between a casting fluid containing a casting material and the molded surface.
- The coagulation of the casting solution into a non-solvent for the polymer
- The solidification and shrinkage of the polymeric film contacting the molded surface.
- The removal of the patterned film from the molded surface

This approach is considered as a microfabrication technique very innovative to achieve micro and nanostructures from a very broad range of polymers [46].

1.4.2 Techniques based on colloidal templates

Membranes with morphological features of high structural order at nanometric scale may be achieved according to colloidal template method [47].

Colloid crystalline particles are three-dimensional close-packed crystals of submicrometer spheres working as imprinting agents, whose long-ranged ordered structure is replicated in a solid matrix, thus yielding materials with ordered pores. The method to replicate the colloidal crystal in a durable matrix has the purpose of use as templates not only the spheres, but also the voids between the colloidal particles. In this way, the material solidifies without disrupting the order of the crystal lattice and, subsequently, the spheres are removed leaving imprinted in the material the long-ranged periodic structure of the crystal.

Colloidal crystal structures with this ordered architecture, are of great interest for the tissue engineering wherein the availability of arrays for cellular proliferation is requested to promote the optimum environment for a good adhesion and consequent cells proliferation.

1.4.3 Self-assembly copolymers

Self-assembly means the capability of some materials to assemble spontaneously in complex nanostructures bringing to advanced nanostructures. Single or connected components spontaneously form ordered aggregates [48] depending on intrinsic structure and chemistry of molecules involved: lipids, proteins, carbohydrates and nucleic acids [49]; molecular crystals [50]; liquid crystals [51]; semi crystalline and phase-separated polymers [52]. The techniques by which one can get ordered nanostructured membranes using self-assembled block copolymers, are of manifold nature. And, the success of a nanoporous membrane, both in structure and in correlation to its functional properties, depends on the capability of these polymers to self-assemble on the nanoscale, when processed into a membrane.

The two main strategies that have been used by researchers were [37]:

- To use block polymers, which give rise to a cylindrical morphology with measures, such as to make sure that the cylindrical domains are oriented perpendicularly to the thin dimension of the film.
- To use a block polymer with a bi-continuous morphology (e.g., a gyroid-like phase) that obviates the need for alignment [53].

1.4.4 Breath figure for bio-inspired high-defined membranes

One of the most innovative and bio-inspired methods to achieve micro porous membranes with an ordered pore geometry is well-known as a 'Breath Figures' (BF) [38].

This approach is a commonly observed phenomenon in daily life, because it refers to the fog that forms when water vapor contacts a cold surface (Figure 1.3). During this event, condensing water droplets tend to rearrange in ordered geometry resembling honeycomb patterns. John Aitken [54, 55] was the first to investigate BF phenomena in 1985; later, Lord Rayleigh [56] revealed the morphology of water droplets on a cold surface.

BF allows the formation of droplets rearrangement in well-defined geometries. This capability can be exploited to shape holes (pores) in polymeric films under well-established thermodynamics, phenomena of capillarity and Marangoni effects.

The approach is somewhat simple and cheap, because it is based on the condensation of water droplets on the surface of dilute polymer solutions, containing immiscible or partially miscible solvents. This means an easier recovery of the solvent at the end of the process. Also, the water is a non toxic templating agent largely available, so that the overall approach can be regarded as a green manufacturing technology.

In spite of handle manufacturing approach, the mechanism controlling for BF geometry formation can be very complex and not perfectly unique. This can depend on polymeric materials and solvents used, but also changes in the surrounding experimental conditions, which make the water droplets dynamics somewhat difficult to manage [57]. One of the most important advantages for this kind of membrane manufacturing technique is that water is largely available and the using of non toxic agent. So the formation of nanostructure results to be more competitive from economics point of view.

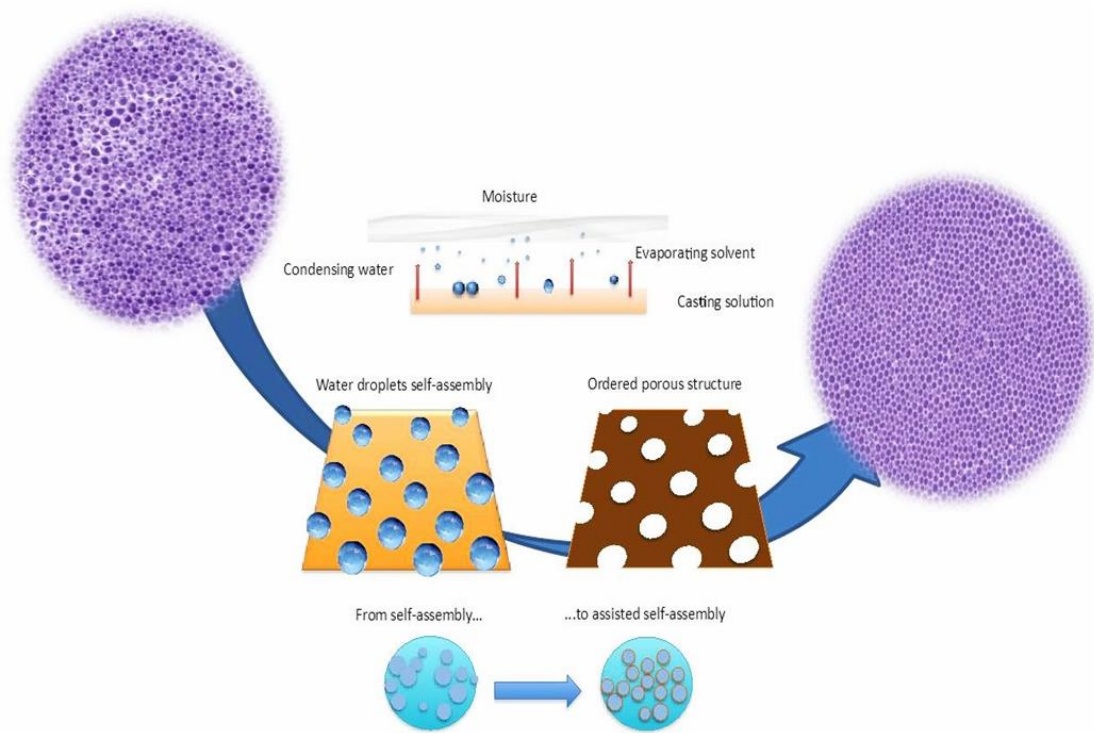


Figure 1.3. Schematic representation of Breath Figures methodology, used for preparation of new ordered nanostructured membranes. Readapted from [45].

1.4.5 Honeycomb membranes: from 2D to 3D polymeric films

Honeycomb membranes arouse interest in membrane processes for their morphological and physicochemical features (Figure 1.4). The transition from two-dimensional to three-dimensional nanomaterials involve nanotechnology in many areas, also including membrane technology. The main objective is to identify materials and in particular morphological structures, ever more promising from the application point of view.

The concept is the same: preparation of membranes with lithographic precision according to a bioinspired BF process. The condensing water droplets act like imprinting agents on the polymeric surface and with the balance between evaporation of the solvent and condensation of humid air in a 3D constructions, honeycomb membranes can be achieved in one single step. After condensation, submerging water droplets grow and self-assemble in ordered arrays, yielding a highly defined hexagonally packed geometry as a result of their imprinting action, different from what was observed for conventional phase separation techniques [58]. The major limitation to commercially producing large scale films, is the lack of control on the structural order at long range through the surface area of the films realized: For this reason, a study of the behavior of water droplets dynamics during self-assembly [59] was did, changing the hydrophilic/hydrophobic balance in solution, with the use of different kind

of surfactants. The ambition was to achieve a very high degree of order through honeycomb film textures with well-shaped and well-sized pores when fruitful interactions are established at the water-casting solution interface, and also to suppress the disordered and confused regions, moving from a self-assembly to assisted self-assembly.

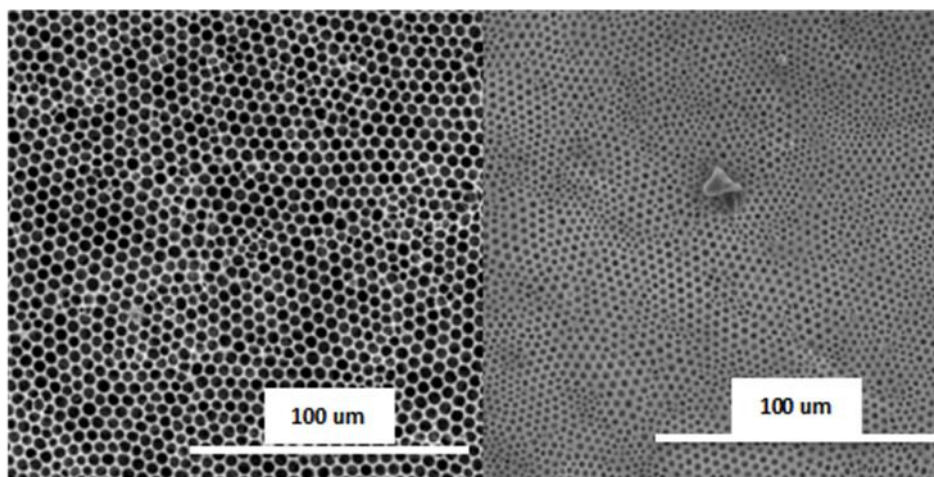


Figure 1.4. SEM pictures of Honeycomb polymeric membrane [45].

1.5 Nanocomposite membranes

1.5.1 Multi-layer membranes

In physical sciences, a multilayer or stratified medium is a stack of different thin films. Typically, a multilayer is man made for a specific purpose. Since layers are thin with respect to some relevant length scale, interface effects are much more important than in bulk materials, giving rise to novel physical properties.

The term "multilayer" is not an extension of "monolayer" and "bilayer", which describes a single layer that is one or two molecules thick. A multilayer medium rather consists of several thin films. This kind of terminology can be applied also in membrane technology, where multilayers composite membranes are considered as new target for different application, because of their advantages, including the possibility to optimize membrane materials independently by layers according to their different functions and to reduce the overall transport resistance by using ultrathin selective layers, and less limitations on the material mechanical properties and processability [60].

In detail a multi-layer composite membrane, particularly used in gas separation, but object of interest in other kind of membrane separation processes, is fabricated by depositing

different materials on a porous support. It generally contains (Figure 1.5) at least a porous support and a selective layer, and for many cases, a gutter layer between the porous support and selective layer, and a protective layer above the selective layer.

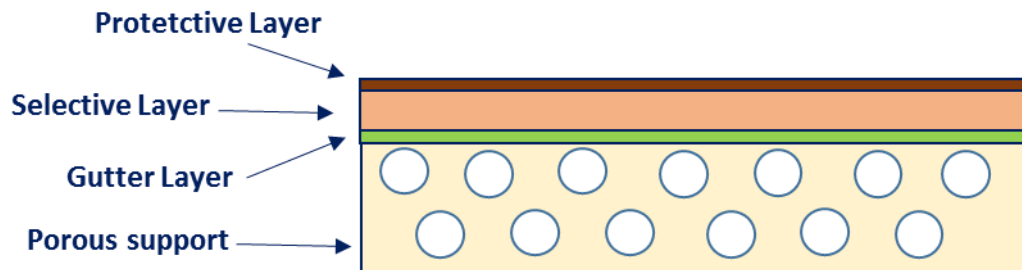


Figure 1.5. Schematic representation of a typical multilayer membrane structure. Readapted from [60].

In composite membranes, different layers contribute various functions to the composite membrane, thus their requirements on the properties are also different. The porous support mainly offers mechanical strength, therefore the support should have high porosity and low mass transfer resistance. In addition, the material should be cheap and easy to process into a porous structure. The main purpose of employing a gutter layer between the selective layer and porous support is to reduce the possible penetration of the coating solution into the membrane pores. It can also help to reduce the surface roughness of the support. The selective layer is the core part of a composite membrane, which offers the main separation properties of the membrane. Ideally, high gas permeance and high selectivity are the first two selection criteria for a selective layer membrane material, while other properties such as life-time, cost, aging and stability should also be considered. With the purpose of protecting the membrane during handling and fabrication into membrane modules, a protective layer can be employed if needed.

This kind of structures find their major application in gas separation. When compared with integral asymmetric membranes prepared by the Loeb-Sourirajan technique, the principal advantages of composite membranes include fewer limitations on the material mechanical properties and processability. Furthermore, a much smaller quantity needed to deposit the selective layer of a composite membrane ($0.1\text{--}2\text{ g/m}^2$), thus some high performance but expensive materials can be used. Nowadays this methodology is increasing also in other advanced membranes application, like desalination of sea and brackish water.

1.5.2 Mixed matrix nanocomposite membranes (MMNMs)

Mixed matrix nanocomposite membranes (MMNMs) have been studied intensively in the recent years. (Figure 1.6) They are generally considered to be the next-generation of advanced membranes, where nanomaterials are dispersed in a polymer matrix [61]. The use of MMNMs has received much attention during recent years, particularly as a new technique to combine the potential advantages of both nanomaterials and polymer membranes. These structurally engineered membranes are indeed expected to combine the unique properties of nanomaterials with the processability of polymeric membranes to achieve synergistic separation performance for gas-gas, liquid-liquid, and liquid- solid separations.

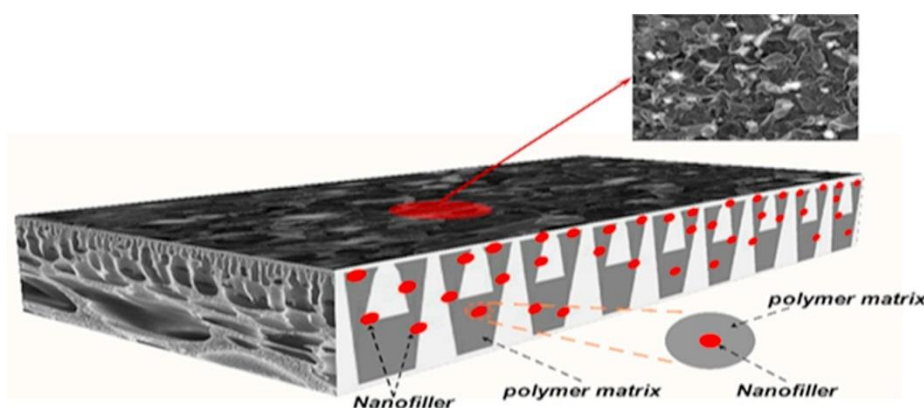


Figure 1.6. Schematic representation of MMNMs structure. Reprinted from [61] Copyright© 2019, with permission from Elsevier B.V. All rights reserved.

In addition, physical characteristics such as strength and modulus can be improved as a result of strong interfacial interactions between the nanoparticles and the surrounding polymer matrix [62]. To derive positive benefits without compromising the integrity of these membranes, the interplay and potential trade-off between enhanced properties provided by the incorporated nanomaterial and the potential for defect formation in the polymer matrix must be balanced in materials development.

In general, three are the several approaches used for preparing mixed matrix membranes:

- A predetermined mass of nanofiller is dispersed into the solvent and stirred for a certain period of time leading to a homogeneous suspension, and then the polymer is added.
- The polymer is dissolved in the solvent and stirred for a period leading to a homogeneous polymeric solution, and then a predetermined mass of nanoparticles is added.
- A predetermined mass of nanofiller is dispersed into the solvent and stirred for a certain period, and the polymer is dissolved in a solvent separately. The nanofiller suspension is then added to the homogeneous polymeric solution.

A number of MMNMs preparation techniques such as phase inversion, stretching, track-etching, and electrospinning are used to fabricate a membrane from a given material. The selection of polymer and desired structure limits the choice of the technique for membrane fabrication.

1.6 Two-dimensional materials: application in membrane separation

Two dimensional materials are arousing interest in membrane technology for their using in various separation process. Control in monolayers distance is one of the ways practiced to control the passage of molecules. Another way is to practice regular and uniform nanopores on monolayers with strong precision. This kind of approach allowed to use 2D nanomaterial in separation processes, but big difficulties are related for high costs in manufacturing processes for a scalable procedure. So two-dimensional materials (2DMs) – e.g., graphene, dichalcogenides, MXene, metal–organic frameworks, and covalent organic framework nanosheets – are rapidly emerging in the development of membranes with improved selectivity and permeability. The rational tunability and precise control of interlayer distances and/or nanoporous apertures of 2DMs enable 2DM-based membranes, allow to achieve highly specific separations. Furthermore, the ultrathin structure of 2DMs offers minimal transport resistance and thus leads to extraordinary flux rates. However, the integration of nonporous nanosheets can possibly block molecular transport pathways, increasing mass transfer resistance, but it depends on the combination of structure-properties relationship. Nowadays a possible and less expensive alternative is to confine 2D materials in polymeric networks using more traditional approaches, generally used for typical membranes preparations. The objective is to combine the excellent properties of 2D materials in nanocomposite membrane systems directed towards selective molecular transports.

1.6.1 Graphene: a 2D material as nanofiller in water treatment

Graphene is a monolayer of carbon atoms orderly packed in a 2D honeycomb lattice (Figure 1.7). Apart from the ultrathin structure, the unique properties of high stiffness, thermal conductivity and surface area potentially allow graphene to be a promising candidate for membrane-based separations [63]. Yet a pristine one-atom-thick graphene is even impermeable to small gas molecules like helium, making it difficult to be directly utilized for molecule- or ion-based separation. In this case, the analyses of molecular dynamics (MD)

simulations [64-67] provide a bright prospect of nanoporous graphene (NPG) with both high permeability and selectivity for water purification [68] and gas separation [69].

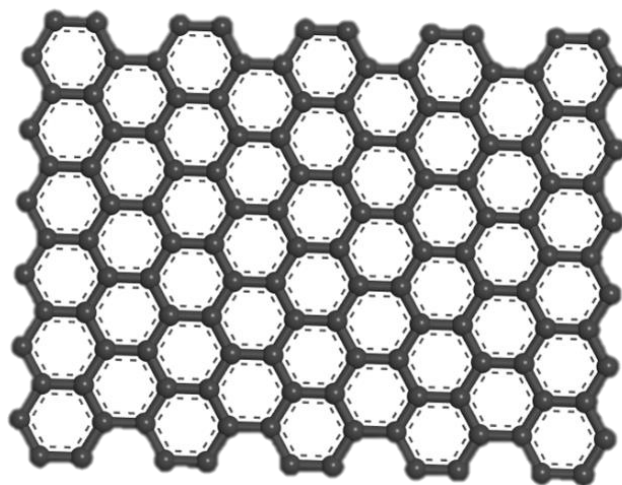


Figure 1.7. Typical honeycomb structure of graphene material. Built through Material Studio.

Membrane desalination represents an important contribution to face water problems, for recovery of fresh water from saline and brackish water. In this direction Graphene-based materials may promote advantages in the desalination process due to their features, including single atomic layer structure, large specific surface area, hydrophobic property, rich modification approaches, etc. [70].

Graphene is the lightest, strongest, thinnest, best heat-and-electricity conducting material ever discovered. Graphene, as hydrophobic monolayer, has a good capacity to repel water when used for water treatment via membrane distillation. Resistance to wetting is one of the most important criteria for a membrane to be used in desalination, furthermore when narrow pores are made in it, a rapid water permeation is allowed. This sparked ideas regarding the use of graphene derived for water filtration and desalination, especially once the technology for making these micro-pores has been achieved. Graphene sheets (perforated with miniature holes) are studied as a method of water filtration, because they are able to let water molecules pass but block the passage of contaminants and substances.

Challenge nowadays is not to generate graphene membranes from their auto- assembling, but to include it, used as nanofiller, in a specific space like a polymeric membrane to assist different kind of membrane processes. It has already showed that graphene blended in a polymer membrane matrix can improve performance from rejection to salts and fluxes when used in Membrane Distillation (MD) process. Gontarek et al [71] studied recently effects of multilayer graphene-derived platelets when confined in hydrophobic microporous polymeric membranes. They demonstrated how intermolecular interactions between water vapour

molecules and nanocomposite membranes allow to assist transport of water vapour in membrane distillation processes when a suitable filler-polymer ratio is reached. In this studies, hydrophobic graphene nano-platelets have been blended in polymer matrix but with the purpose of Membrane Crystallization technology.

1.6.2 Beyond graphene: new materials and new perspectives

Despite interesting properties and capabilities of graphene, it consists of an absence of band gap that make not it suitable for different kind of applications. On a molecular level, the band gap is the minimum amount of energy required for an electron to break free. Once it does, the electron can participate in conduction. Because of the absence of a band gap, the electrons in graphene flow continuously, causing graphene to act more like a metal than a semiconductor. The energetic gap between the highest occupied and the lowest unoccupied electronic level is an important factor in determining the optical and electronic properties of a material [72].

In the past few years, transition metal dichalcogenides (TMDs) have also attracted considerable attention because of the intrinsically opened bandgap, resulting much more interesting than graphene for specific applications [73]. One of these new interesting materials, bismuth selenide (Bi_2Se_3) was recently studied like nano-filler in Membrane Crystallization Technology in order to assist nucleation and crystallization of NaCl salts. Bismuth selenide (Bi_2Se_3) is a gray compound of bismuth and selenium also known as bismuth (III) selenide. It is a semiconductor and a thermoelectric material.[74] While perfect stoichiometric bismuth selenide should be a semiconductor (with a gap of 0.3 eV) naturally occurring selenium vacancies act as electron donors and it often acts as a semimetal.[75] Topologically protected surface states have been observed in bismuth selenide,[76] which is the subject of ongoing scientific research [77].

Macedonio et al [78] explored the potential of bismuth chalcogenides in water desalination and recovery of minerals, through MCr technology. The confinement of Bi_2Se_3 in polymeric hydrophobic matrices has produced an unexpected increase in the growth rate and uniform dispersion of NaCl crystals, providing assistance to the MCr process. The presence of defect sites at the surface of the material chalcogenide promotes water adsorption at the vacancies, causing water exclusion mechanisms to take place under low saturation conditions.

Studies regarding Bi_2Se_3 -PVDF based membranes were carried out in this work for the purpose of Membrane assisted Crystallization technology, comparing results with those

achieved with graphene-PVDF based membranes. Results and discussion will be implemented in Chapter 5.

1.6.3 Effects of Nanoparticles (NPs) on human health and environment

Nowadays interest in nanoscience is particularly focused on the using of nanoparticles (NPs) of graphene, derivatives and 2D materials beyond graphene such as transition metal dichalcogenides and xene, for different purpose. As described in the previous paragraphs they have unique properties that make them ideal to be used in several scientific areas, as photonic, optoelectronics, biomedicine and also in membrane science. They can be managed for desired applications, how for example with their inclusion as nanofillers in polymer network as was did in this work. On the other hand, it's necessary to study the toxicity level, both for human health and also for the environment. It's necessary to consider that for the human body their toxicity depends on their biocompatibility and mobility and reactivity that have with specific cells components [78]. In fact, NPs can pass through different cell membranes of mammals and be absorbed in them. Size of the nanoparticles, their distribution, aggregation, and sedimentation in cells, are the most important parameters in determining their absorption rates [79]. Furthermore, their toxicity is related not only to their small size, but also to large surface area and their ability to produce reactive oxygen species, causing inflammation and fibrosis in multicellular organisms. It implies the valuation and validation of a safety profile and the study of the impact on human health [80]. Possible risks were investigated by several in vitro and in vivo studies that evaluated on one side toxicity implications of NPs and on the other no relevant risks. So exist two face of medal, and graphene, derivatives and previous cited 2D beyond cannot be excluded from this type of investigation. However, in order to give rights information, it's important to explore the level of toxicity of graphene and more, and to what degree they are safe. From the environmental point of view, nanomaterials can interact with organic or inorganic compounds, and even though they can have harmful environmental effects, they also can be helpful for the environment, when NPs are used for example in the removal of contaminants. In our case the purpose was to use nanomaterials as elements (fillers) for improving assisted mechanism in MCr operations. Their environmental impact depend on how they are used in the workplace, how they are separated into different media (e.g., water and air), their mobility in each of these media, and their stability, with an important reference to the quantity with which they are used. Graphene and Bismuth selenide are the two 2D materials, used in this PhD thesis for the improving of NaCl crystals quality when inserted in PVDF

matrix, a biocompatible polymer [80, 81], for Membrane assisted Crystallization. With their vacancies and defects, they allowed to nanocomposite membranes to enhance water sequestration for faster supersaturation and to achieve major uniformity in crystals shape and size distribution. In order to insert NPs into polymeric membranes with activity in water treatment, a long-term study is required, for the evaluating of their stability in order to assess 2D nanomaterials safety. In this work, Raman investigation were performed in order to confirm that no release of 2D nanomaterials in feed and permeate streams occurred. These can be considered as preliminary information about the possibility to use these novel materials in desalination processes.

References

1. C. Buzea, I. Pacheco, K. Robbie, Nanomaterials and Nanoparticles: Sources and Toxicity, *Biointerphases*, 2 (2007) 17-71, <https://doi.org/10.1116/1.2815690>.
2. A.W. Hubler, O. Osuagwu, Digital quantum batteries: Energy and information storage in nano vacuum tube arrays, *Complexity*, 15 (2010) 48-55, <https://doi.org/10.1002/cplx.20306>.
3. National Nanotechnology Initiative 2000 Leading to the Next Industrial Revolution, A Report by the Interagency Working Group on Nanoscience, Engineering and Technology (Washington, DC: Committee on Technology, National Science and Technology Council), <http://www.nano.gov>.
4. C. Buzea, I. Pacheco, Nanomaterials and their Classification. In: A. Shukla (eds) EMR/ESR/EPR Spectroscopy for Characterization of Nanomaterials, Springer, New Delhi, 2017.
5. C.S.S.R. Kumar, Nanomaterials for the life sciences, Nanostructured oxides, In: Biosensor nanomaterials, Weinheim: WILEY-VCH Verlag GmbH & Co. KGaA, 2009.
6. G. Oberdorster, E. Oberdorster, J. Oberdorster, Nanotoxicology: an emerging discipline evolving from studies of ultrafine particles, *Environ. Health Perspect.*, 113 (2005) 823-839, <https://doi.org/10.1289/ehp.7339>.
7. O.V. Salata, Applications of nanoparticles in biology and medicine, *J. Nanobiotech.*, 2 (2004) 1-6, <https://doi.org/10.1186/1477-3155-2-3>.
8. J. Luo, Q. Zhou, J. Sun, R. Liu, X. Liu, Micelle-assisted synthesis of PANI nanoparticles and application as particulate emulsifier, *Colloid Pol. Sci.*, 292 (2014) 653-660, <https://doi.org/10.1007/s00396-013-3108-5>.
9. F. Gao, Advances in polymer nanocomposites types and applications, Oxford, Cambridge, Philadelphia, New Delhi: Woodhead Publishing Limited; 2012.
10. M. Ohring, Materials science of thin films. Boston (MA): Academic Press; 2001.
11. P.H.C. Camargo, K.G. Satyanarayana, F. Wypych, Nanocomposites: synthesis, structure, properties and new application opportunities, *J. Mat. Res.*, 12 (2009) 1-39.
12. P. Kumar, K.H. Kim, V. Bansal, P. Kumar, Nanostructured materials: A progressive assessment and future direction for energy device applications, *Coord. Chem. Rev.*, 353 (2017) 113-141, <https://doi.org/10.1016/j.ccr.2017.10.005>

13. J. Fricke, A. Emmerling, Aerogels preparation, properties, applications. In: R. Reisfeld, C.K Jørgensen, editors, Chemistry, spectroscopy and applications of sol-gel glasses, Springer Berlin Heidelberg, 77, 1992, pp 37-87.
14. N. Zhao, J. Xu, Q. Xie, L. Weng, X. Guo, X. Zhang, L. Shi, Fabrication of biomimetic superhydrophobic coating with a micro-nano-binary structure, *Macromol. Rapid Comm.*, 26 (2005) 1075-1080, <https://doi.org/10.1002/marc.200500188>.
15. R.K. O'Reilly, C.J. Hawker, K.L. Wooley, Cross-linked block copolymer micelles: functional nanostructures of great potential and versatility, *Chem. Soc. Rev.*, 35 (2006) 1068-1083, <https://doi.org/10.1039/b514858h>.
16. M.F. Ashby, P.J. Ferreira, D.L. Schodek, Nanomaterials, nanotechnologies and design: an introduction for engineers and architects. Burlington (USA): Elsevier; 2009.
17. F. Uddin, Clays, Nanoclays, and montmorillonite minerals, *Metall. Mater. Trans. A*, 39A (2008) 2804-2814, <https://doi.org/10.1007/s11661-008-9603-5>.
18. Read SAK, Jimenez AS, Ross BL, Aitken RJ, von Tongeren M. Nanotechnology and exposure scenarios. In: Vogel U, Savolainen K, Wu Q, van Tongeren M, Brouwer D, Berges M, (Eds.), Handbook of nano safety measurement, exposure and toxicology. Elsevier; 2013.
19. N. Savage, M.S. Diallo, Nanomaterials and water purification: Opportunities and challenges, *J. Nanoparticle Res.*, 7(4-5) (2005) 331-342, <https://doi.org/10.1007/s11051-005-7523-5>.
20. M.A. Shannon, P.W. Bohn, M. Elimelech, J.G. Georgiadis, B.J. Mariñas, A.M. Mayes, Science and technology for water purification in the coming decades, *Nature* 452 (2008) 301–310, https://doi.org/10.1142/9789814287005_0035.
21. A. Kumar, A. Srivastava, I.Y. Galaev, B. Mattiasson, Smart polymers: Physical forms and bioengineering applications. *Prog. Polym. Sci.*, 32 (2007) 1205–1237, <https://doi.org/10.1016/j.progpolymsci.2007.05.003>.
22. Samhaber, Wolfgang M., Erfahrungen und Anwendungspotential der Nanofiltration, 2004, available at: 6 Publikationen/pdf/Membrantechnik%20in%20der%20Prozessindustrie.pdf
23. T. Sakamoto, T. Ogawa, H. Nada, K. Nakatsuji, M. Mitani, B. Soberats, K. Kawata, M. Yoshio, H. Tomioka, T. Sasaki, M. Kimura, M. Henmi, T. Kato, Development of Nanostructured Water Treatment Membranes Based on Thermotropic Liquid Crystals: Molecular Design of Sub-Nanoporous Materials, *Adv. Sci.*, 5 (2018) 1700405, <https://doi.org/10.1002/advs.201700405>.

24. D. Wandera, S.R. Wickramasinghe, S.M. Husson, Stimuli-responsive membranes, *J. Membr. Sci.*, 357 (2010) 6–35, <https://doi.org/10.1016/j.memsci.2010.03.046>.
25. M.A. Stuart, W.T. Huck, J. Genzer, M. Müller, C. Ober, M. Stamm, G.B. Sukhorukov, I. Szleifer, V.V. Tsukruk, M. Urban, F. Winnik, S. Zauscher, I. Luzinov, S. Minko, Emerging applications of stimuli-responsive polymer materials, *Nat. Mater.*, 9 (2010) 101–113, <https://doi.org/10.1038/nmat2614>.
26. K.B. Jirage, J.C. Hulteen, C.R. Martin, Nanotubule-based molecular-filtration membranes, *Science*, 278 (1997) 655–658, <https://doi.org/10.1126/science.278.5338.655>.
27. S.B. Lee, D.T. Mitchell, L. Trofin, T.K. Nevanen, H. Söderlund, C.R. Martin, Antibody-based bio-nanotube membranes for enantiomeric drug separations. *Science*, 296 (2002) 2198–2200, <https://doi.org/10.1126/science.1071396>.
28. S.E. Letant, B.R. Hart, A.W. Van Buuren, L.J. Terminello, Functionalized silicon membranes for selective bio-organism capture, *Nat. Mater.*, 2 (2003) 391–396, <https://doi.org/10.1038/nmat888>.
29. T.C. Merkel, B.D. Freeman, R.J. Spontak, Z. He, I. Pinnau, P. Meakin, A.J. Hill, Ultraporous, reverse-selective nanocomposite membranes, *Science*, 296 (2002) 519–522, <https://doi.org/10.1126/science.1069580>.
30. H.B. Park, C.H. Jung, Y.M. Lee, A.J. Hill, S.J. Pas, S.T. Mudie, E. Van Wagner, B.D. Freeman, D.J. Cookson, Polymers with cavities tuned for fast selective transport of small molecules and ions, *Science*, 318 (2007) 254–258, <https://doi.org/10.1126/science.1146744>.
31. Y. Lu, Y. Mei, M. Drechsler, M. Ballauff, Thermosensitive core-shell particles as carriers for Ag nanoparticles: Modulating the catalytic activity by a phase transition in networks. *Angew Chem. Int. Ed. Engl.*, 45 (2006) 813–816, <https://doi.org/10.1002/anie.200502731>.
32. H.J. Lee, T.H. Yoon, J.H. Park, J. Perumal, D.P. Kim, Characterization and fabrication of polyvinylsilazane glass microfluidic channels via soft lithographic technique, *J. Ind. Eng. Chem.*, 14 (2008) 45–51, <https://doi.org/10.1016/j.jiec.2007.06.002>.
33. Y. Zou, L. Moreel, H. Lin, J. Zhou, L. Li, S. Danto, J.D. Musgraves, E. Koontz, K. Richardson, K.D. Dobson, R. Birkmire, J. Hu, Solution Processing and Resist-Free Nanoimprint Fabrication of Thin Film Chalcogenide Glass Devices: Inorganic-Organic Hybrid Photonic Integration, *Adv. Opt. Mater.*, 2 (2014) 759–764, <https://doi.org/10.1002/adom.201400068>.

34. U.M. Attia, J.R. Alcock, Fabrication of hollow, 3D, micro-scale metallic structures by micro-powder injection moulding, *J. Mater. Proc. Tech.*, 212 (2012) 2148– 2153, <https://doi.org/10.1016/j.jmatprotec.2012.05.022>.
35. Johannes, C., Van Rijn, M., Vogelaar, L., Nijdam, W., Barsema, J.N., Wessling, M., (2009) Patent N° US7531120 B2.
36. O.D. Velev, E.W. Kaler, Structured Porous Materials via Colloidal Crystal Templating: From Inorganic Oxides to Metals, *Adv. Mater.*, 12 (2000) 531-534, [https://doi.org/10.1002/\(SICI\)1521-4095\(200004\)12:7<531::AID-ADMA531>3.0.CO;2-S](https://doi.org/10.1002/(SICI)1521-4095(200004)12:7<531::AID-ADMA531>3.0.CO;2-S).
37. Y. Zhang, J.L. Sargent, B.W. Boudouris, W.A. Phillip, Nanoporous membranes generated from self-assembled block polymer precursors: Quo Vadis?, *J. Appl. Pol. Sci.*, 132 (2015) 41683, <https://doi.org/10.1002/app.41683>.
38. A. Zhang, H. Bai, L. Li, Breath Figure: A Nature-Inspired Preparation Method for Ordered Porous Films, *Chem. Rev.*, 115 (2015b) 9801–9868, <https://doi.org/10.1021/acs.chemrev.5b00069>.
39. A. Gugliuzza, E. Drioli, PVDF and HYFLON AD membranes: Ideal interfaces for contactor applications, *J. Membrane Sci.*, 300, (2007) 51-62, <https://doi.org/10.1016/j.memsci.2007.05.004>.
40. M. Srinivasarao, D. Collings, A. Philips, S. Patel, Three-Dimensionally Ordered Array of Air Bubbles in a Polymer Film, *Science*, 292 (2001) 79-83, <https://doi.org/10.1126/science.1057887>.
41. H.J. Lee, T.H. Yoon, J.H. Park, J. Perumal, D.P. Kim, Characterization and fabrication of polyvinylsilazane glass microfluidic channels via soft lithographic technique, *J. Ind. Eng. Chem.*, 14 (2008) 45–51, <https://doi.org/10.1016/j.jiec.2007.06.002>.
42. H. Schiff, A. Kristensen, Springer Handbook of Nanotechnology, Springer Berlin Heidelberg, 2007, pp. 239-278.
43. R.W. Baker, Membrane Technology and Applications, McGraw-Hill, 2000.
44. M. Mulder, Basic Principles of Membrane Technology, Second edition, Kluwer Academic Publishers, 1996.
45. M.L. Perrotta, A. Gugliuzza, Fabrication of ordered micro and nanoporous membranes in: E. Drioli, L. Giorno, A. Gugliuzza (Eds.), Functional Nanostructured Membranes, Pan Stanford Publishing Pte. Ltd, 2018.
46. M. Girones, I.J. Akbarsyah, W. Nijdam, C.J.M. Van Rijn, V. Jansen, R.G.H. Lammertink, M. Wessling, Polymeric microsieves produced by phase separation

- micromolding, *J. Membrane Sci.*, 283 (2006) 411–424, <https://doi.org/10.1016/j.memsci.2006.07.016>.
47. O.D. Velev, E.W. Kaler, Structured Porous Materials via Colloidal Crystal Templating: From Inorganic Oxides to Metals, *Adv. Mater.*, 12 (2000) 531–534, [https://doi.org/10.1002/\(SICI\)1521-4095\(200004\)12:7<531::AID-ADMA531>3.0.CO;2-S](https://doi.org/10.1002/(SICI)1521-4095(200004)12:7<531::AID-ADMA531>3.0.CO;2-S).
48. G.M. Whitesides, M. Boncheva, Beyond molecules: self-assembly of mesoscopic and macroscopic components, *Proc. Natl Acad. Sci. USA*, 99 (2002) 4769–4774, <https://doi.org/10.1073/pnas.082065899>.
49. B. Alberts, D. Bray, J. Lewis, M. Raff, K. Roberts, J.D. Watson, *Mol. Biol. Cell*, 3^d Ed, Garland, New York, 1994.
50. K.E. Schwiebert, D.N. Chin, J.C. MacDonald, G.M. Whitesides, Engineering the Solid State with 2-Benzimidazolones, *J. Am. Chem. Soc.*, 118 (1996) 4018–4029, <https://doi.org/10.1021/ja952836l>.
51. L. Schmidt-Mende, A. Fechtenkötter, K. Mullen, E. Moons, R.H. Friend, J.D. MacKenzie, Self-Organized Discotic Liquid Crystals for High-Efficiency Organic Photovoltaics, *Science*, 293 (2001) 1119–1122, <https://doi.org/10.1126/science.293.5532.1119>.
52. C. De Rosa, C. Park, E.L. Thomas, B. Lotz, Microdomain patterns from directional eutectic solidification and epitaxy, *Nature*, 405 (2000) 433–437, <https://doi.org/10.1038/35013018>.
53. D.A. Olson, L. Chen, M.A. Hillmyer, Templating Nanoporous Polymers with Ordered Block Copolymers, *Chem. Mater.*, 20 (2008) 869–890, <https://doi.org/10.1021/cm702239k>.
54. J. Aitken, Breath Figures, *Nature*, 86 (1911) 516–517.
55. J. Aitken, Breath figure, *Proc. R. Soc. Edinburgh*, 20 (1895) 94–97.
56. Rayleigh. Breath figures, *Nature*, 86 (1911) 416–417.
57. A. Gugliuzza, M.L. Perrotta, E. Drioli, Controlled Bulk Properties of Composite Polymeric Solutions for Extensive Structural Order of Honeycomb Polysulfone Membranes, *Membranes*, 6 (2016) 27, <https://doi.org/10.3390/membranes6020027>.
58. I.M. Wienk, R.M. Boom, M.A.M. Beerlage, A.M.W. Bulte, C.A. Smolders, H. Strathmann, Recent advances in the formation of phase inversion membranes made from amorphous or semi-crystalline polymers, *J. Membr. Sci.*, 113(2) (1996) 361–371, [https://doi.org/10.1016/0376-7388\(95\)00256-1](https://doi.org/10.1016/0376-7388(95)00256-1).

59. F. Trotta, E. Drioli, A. Gordano, Nitro derivatives of PEEK-WC, *J. Appl. Polym. Sci.*, 80 (2001) 1037–1045, <https://doi.org/10.1002/app.1187>.
60. Z. Dai, L. Ansaloni, L. Deng, Recent advances in multi-layer composite polymeric membranes for CO₂ separation: A review, *Green En. Env.*, 1 (2) (2016) 102-128, <https://doi.org/10.1016/j.gee.2016.08.001>.
61. M.R. Esfahani, S.A. Aktij, Z. Dabaghian, M.D. Firouzjaei, A. Rahimpour, J. Eke, I.C. Escobarc, M. Abolhassani, L.F. Greenlee, A.R. Esfahani, A. Sadmani, N. Koutahzadeh, Nanocomposite membranes for water separation and purification: Fabrication, modification, and applications, *Sep. Purif. Tech.*, 213 (2019) 465-499, <https://doi.org/10.1016/j.seppur.2018.12.050>.
62. M.Z. Rong, M.Q. Zhang, Y.X. Zheng, H.M. Zeng, R. Walter, K. Friedrich, Structure–property relationships of irradiation grafted nano-inorganic particle filled polypropylene composites, *Polymer* 42 (2001) 167–183, [https://doi.org/10.1016/S0032-3861\(00\)00325-6](https://doi.org/10.1016/S0032-3861(00)00325-6). J. Zhu, J. Hou, A. Uliana, Y. Zhang, M. Tiana, B. Van der Bruggen, The rapid emergence of two-dimensional nanomaterials for high-performance separation membranes, *J. Mater. Chem. A*, 6 (2018) 3773, <https://doi.org/10.1039/C7TA10814A>.
63. G. Wei, X. Quan, S. Chen, H. Yu, Superpermeable atomic-thin graphene membranes with high selectivity, *ACS Nano*, 11 (2017) 1920–1926, <https://doi.org/10.1021/acsnano.6b08000>.
64. R. R. Nair, H. A. Wu, P. N. Jayaram, I. V. Grigorieva, A. K. Geim, Unimpeded Permeation of Water Through Helium-Leak–Tight Graphene-Based Membranes, *Science*, 335 (2012) 442–444, <https://doi.org/10.1126/science.1211694>.
65. K. Sint, B. Wang, P. Kral, Selective Ion Passage through Functionalized Graphene Nanopores, *J. Am. Chem. Soc.*, 130 (2008) 16448–16449, <https://doi.org/10.1021/ja804409f>.
66. W. Hauser, P. Schwerdtfeger, Methane-selective nanoporous graphene membranes for gas purification, *Phys. Chem. Chem. Phys.*, 14 (2012) 13292–13298, <https://doi.org/10.1039/C2CP41889D>.
67. Sun, M.S. Boutilier, H. Au, P. Poesio, B. Bai, R. Karnik, N.G. Hadjiconstantinou, *Langmuir*, 30 (2014) 675–682, <https://doi.org/10.1021/la403969g>.
68. M. Shan, Q. Xue, N. Jing, C. Ling, T. Zhang, Z. Yan, J. Zheng, Influence of chemical functionalization on the CO₂/N₂ separation performance of porous graphene membranes, *Nanoscale*, 4 (2012) 5477, <https://doi.org/10.1039/c2nr31402a>.

69. N. Song, X. Gao, Z. Ma, X. Wang, Y. Wei, C. Gao, A review of graphene-based separation membrane: Materials, characteristics, preparation and applications, *Desalination*, 437 (2018) 59-72, <https://doi.org/10.1016/j.desal.2018.02.024>.
70. E. Gontarek, F. Macedonio, F. Militano, L. Giorno, M. Lieder, A. Politano, E. Drioli, A. Gugliuzza, Adsorption-assisted transport of water vapour in superhydrophobic membranes filled with multilayer graphene platelets, *Nanoscale*, (2019), 1-22 [epub ahead of print].
71. K. Geim, K. S. Novoselov, The rise of graphene, *Nat. Mat.*, 6 (2007) 183–191, https://doi.org/10.1142/9789814287005_0002.
72. D. Geng, H.Y. Yang, Recent Advances in Growth of Novel 2D Materials: Beyond Graphene and Transition Metal Dichalcogenides, *Adv. Mater.*, 30 (2018) 1800865, <https://doi.org/10.1002/adma.201800865>.
73. S.K. Mishra, S. Satpathy, O. Jepsen, Electronic structure and thermoelectric properties of bismuth telluride and bismuth selenide. *Journal of Physics: Condensed Matter*, 9(2) (1997) 461–470, <https://doi.org/10.1088/0953-8984/9/2/014>.
74. Y.S. Hor, A. Richardella, P. Roushan, Y. Xia, J.G. Checkelsky, A. Yazdani, M.Z. Hasan, N.P. Ong, R.J. Cava, p-type Bi₂Se₃ for topological insulator and low-temperature thermoelectric applications, *Physical Review B.*, 79 (2009) 195208, <https://doi.org/10.1103/PhysRevB.79.195208>.
75. D. Hsieh, Y. Xia, D. Qian, L. Wray, J.H. Dil, F. Meier, J. Osterwalder, L. Patthey, J.G. Checkelsky, N.P. Ong, A.V. Fedorov, H. Lin, A. Bansil, D. Grauer, Y.S. Hor, R.J. Cava, M.Z. Hasan, A tunable topological insulator in the spin helical Dirac transport regime, *Nature*, 460 (2009) 1101–1105, <https://doi.org/10.1038/nature08234>.
76. G. Brumfield, Topological insulators: Star material: Nature News, *Nature*, 466 (2010) 310–311. <https://doi.org/10.1038/466310a>.
77. F. Macedonio, A. Politano, E. Drioli, A. Gugliuzza, Bi₂Se₃-assisted membrane crystallization, *Mater. Horiz.*, 5 (2018) 912-919, <https://doi.org/10.1039/C8MH00612A>.
78. S. M. Taghavi, M. Momenpour, M. Azarian, M. Ahmadian, F. Souri, S. A. Taghavi, M. Sadeghain, M. Karchani, Effects of Nanoparticles on the Environment and Outdoor Workplaces, *Elec. Phys.* 5 (2013), 706-712, <https://doi.org/10.14661/2013.706-712>.
79. G. Oberdörster, E. Oberdörster, J. Oberdörster, Nanotoxicology: an emerging discipline evolving from studies of ultrafine particles, *Env. Health Persp.* 113 (2005), 823-39, <https://doi.org/10.1289/ehp.7339>.
80. A. Bianco, Graphene: Safe or Toxic? The Two Faces of the Medal, *Angew. Chem. Int.* 52 (2013), 4986 – 499, <https://doi.org/10.1002/anie.201209099>.

81. G. Laroche, Y. Marois, R. Guidoin, M.W. King, L. Martin, T. How, Y. Douville, Polyvinylidene fluoride (PVDF) as a biomaterial: from polymeric raw material to monofilament vascular suture, *J Biomed Mater Res.* 29 (1995), 1525-1536. [https://doi.org/ 10.1002/jbm.820291209](https://doi.org/10.1002/jbm.820291209).
82. Y. Yu, H. Sun, H. Orbay, F. Chen, C. G. England, W. Cai and X. Wang, Biocompatibility and In Vivo Operation of Implantable Mesoporous PVDF-Based Nanogenerators, *Nano Energy*, <http://dx.doi.org/10.1016/j.nanoen.2016.07.015>.

Chapter 2

Membrane Distillation and Membrane Assisted Crystallization: membrane operations in water desalination and reuse

2.1 Introduction

Process intensification is a strategy that aims to bring concrete benefits in the production cycles by several steps. They are: the reducing of the bulk of the equipment, the increasing of efficiency, the saving of energy, the reducing of the costs, the mitigating of environmental impact, the improving of safety and the automation and control of devices. Membrane processes have the potential to integrate or replace conventional energetically expensive techniques, allow selective and efficient transport, improve the performance of reactive processes according to the sustainable industrial growth. The realization of compact membrane systems capable to carry out separations much better compared to traditional process units, represents today a real perspective. Interesting are the developments linked to their integration due to the synergistic effects deriving from them. Research is now focused on techniques that may be environmentally friendly and which at the same time are able to allow faster processes and higher productivity.

In this work we prepared membranes for their using in Membrane Distillation (MD) and Membrane Crystallization (MCr) technologies, for desalination of sea and brackish water and for recovery of NaCl crystals. These kind of methodologies are integrating traditional techniques leading to interesting results. In particular MD is carried out at lower pressure values (a few hundred kPa) compared to the reverse osmosis (RO) process, bringing benefits from the energy and economical point of view and at the same time fouling phenomena are also less accentuated than in RO, so leading to better performance in selectivity and productivity.

MC technology, in particular via MD as was carried out in this work, it's particularly used for achieve faster induction times and more control in shape and size of crystals distribution. Both processes find application in membrane contactors and become part of integrated membrane processes for desalination. Smart integration of membrane operations in desalination can contribute to the conventional mining industry by recovering minerals from the brine. At the same time, it solves some of the drawbacks of the mining and the desalination industry [1] (Figure 2.1).

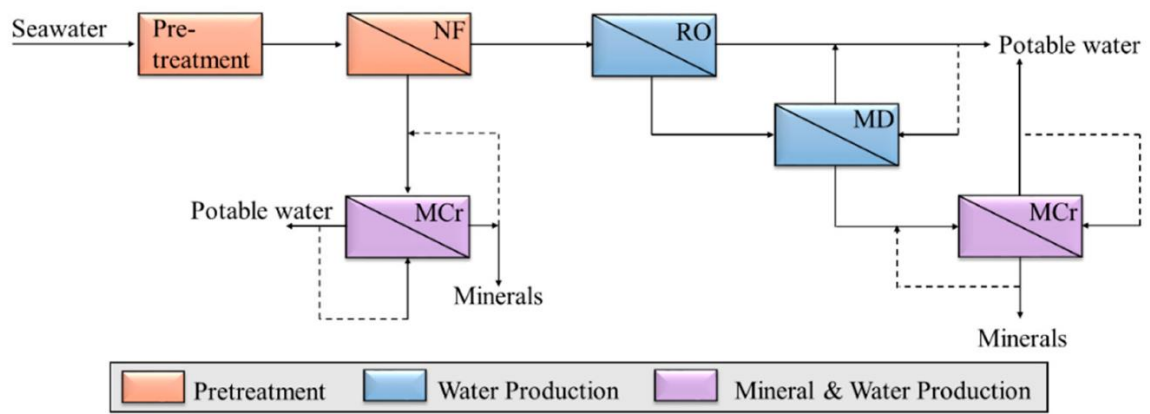


Figure 2.1. Schematic representation and illustration of an integrated membrane desalination plant. Integrated membrane desalination system for water and mineral production. NF: Nanofiltration; RO: Reverse Osmosis; MD: Membrane Distillation; MCr: Membrane Crystallization. Reprinted from [1], 2016.

2.2 Membrane Distillation modes and membrane's features

Membrane Distillation is a promising technology for desalting highly saline waters [2]. MD is a separation process, in which only vapor molecules are able to pass through a porous hydrophobic membrane. This separation process is driven by the vapor pressure difference between the porous hydrophobic membrane surfaces. Using MD has many attractive features, such as low operating temperatures and solution (mainly water) not necessarily heated up to the boiling point. Despite of osmosis revers is the leader technology for desalination, high energy consumption and brine disposal are in RO process connected to the limited recovery of water. These problems can be overcome by the integration of other processes like MD, and a system where a reverse osmosis step is followed by a membrane distillation one. In this way it's possible to improve (%) the recovery factor, as can be seen in Table 2.1. [3].

Table 2.1. [%] Recovery of potable water from seawater with RO followed by MD [3].

| Recovery [%] | | | |
|--------------|----------|----------|-----------|
| Feed source | RO plant | MD plant | Reference |
| Seawater | 40.08 | 77 | [3] |

The MD system has the feasibility to be combined with other separation processes to create an integrated separation system, such as ultrafiltration (UF) [4] or with a RO unit [5]. Furthermore, MD has the ability to utilize alternative energy sources, such as solar energy

[6, 7], geothermal and wind energy [8]. The MD process is competitive for desalination of brackish water and sea water [10] and it is also an effective process for removing organic and heavy metals from aqueous solution [11] and from waste water [12]. MD has also been used to treat radioactive waste, where the product could be safely discharged to the environment [13].

Mass transfer in MD is controlled by three basic mechanisms, which are Knudsen diffusion, Poiseuille flow (viscous flow) and molecular diffusion. This gives rise to several types of resistance to mass transfer resulting from transfer of momentum to the supported membrane (viscous), collision of molecules with other molecules (molecular resistance) or with the membrane itself (Knudsen resistance). In this context, the dusty gas model is used to describe the mass transfer resistances in the MD system, as given in equation 2.1

$$J_i^v = - \frac{\varepsilon r^2 p_i}{8 RT \tau \mu} \nabla P \quad (2.1)$$

Where J_i^v is the viscous flux, ε porosity, r pore radius, p_i partial pressure, P total pressure, R gas constant, T temperature, τ tortuosity, μ gas viscosity.

Exist different kinds of configurations for MD (Figure 2.2), including:

- Air Gap Membrane Distillation (AGMD) wherein the feed solution is in direct contact with the hot side of the membrane surface only. Stagnant air is introduced between the membrane and the condensation surface. The vapor crosses the air gap to condense over the cold surface inside the membrane cell. The benefit of this design is the reduced heat loss by conduction. However, additional resistance to mass transfer is created, which is considered a disadvantage. This configuration is suitable for desalination and removing volatile compounds from aqueous solutions [14].
- Sweeping Gas Membrane Distillation (SGMD) wherein inert gas is used to sweep the vapor at the permeate membrane side to condense outside the membrane module. There is a gas barrier, like in AGMD, to reduce the heat loss, but this is not stationary, which enhances the mass transfer coefficient. This configuration is useful for removing volatile compounds from aqueous solution. The main disadvantage of this configuration is that a small volume of permeate diffuses in a large sweep gas volume, requiring a large condenser [15].
- Vacuum Membrane Distillation (VMD) wherein vacuum is applied to the permeate membrane side. Condensation takes place outside the membrane module. The heat

lost by conduction is negligible, which is considered a great advantage [16]. This type of MD is used to separate aqueous volatile solutions and is the suitable choice for hollow fiber membrane and it requires often high pressure values to work well.

- Direct Contact Membrane Distillation (DCMD) wherein, the hot solution (feed) is in direct contact with the hot membrane side surface. Therefore, evaporation takes place at the feed-membrane surface. The vapor is moved by the feed side to the permeate side (through pressure difference across the membrane) and condenses inside the membrane module. Because of the hydrophobic characteristics of the membrane, the feed cannot penetrate the membrane, but only the gas phase exists inside the membrane pores [17,18]. It is usually the most common choice for those application in which the feed solution mainly consisted of water, and it has also the simplest design, suitable for its using on lab scale.

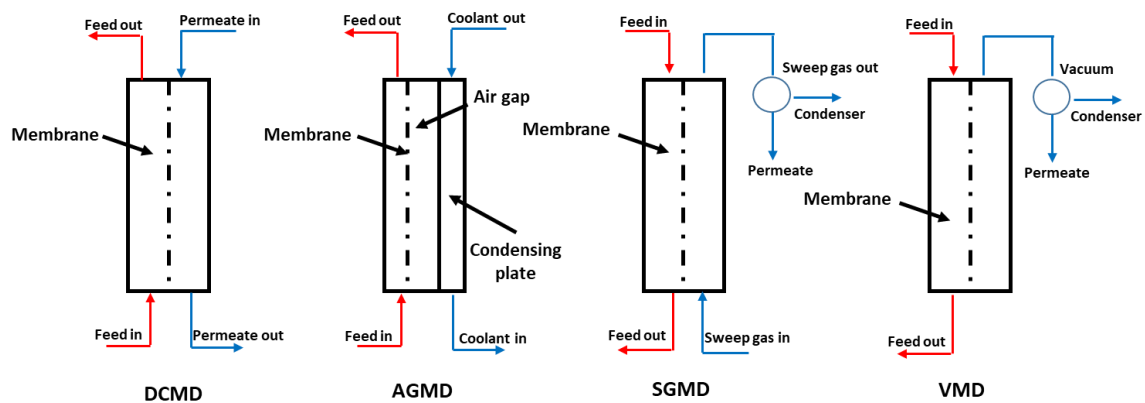


Figure 2.2. Schematic representation of possible configuration for Membrane Distillation (MD).
Readapted from [19].

Concerning membrane's features, some requirements need to be accomplished for making MD operation high performing [2]:

- Well-shaped pore size and narrow pore distribution (preferably within the range of 0.1 to 0.2 μm)
- Controlled thickness and tortuosity factor
- Stable hydrophobic characteristics
- High (60-80%) porosity and exhibit good mechanical strength
- Minimized thermal conductivity
- Scaling resistance

Each of these parameters can influence MD process in several ways, but it is important also a good combination between them, in order to have good productivity, resistance to wetting, rejection to salts and endurance in time.

Methodological studies have to be targeted for preparing membranes with suitable features, because the membrane available on the market do not meet fully all desired characteristics. Various kinds of membrane configuration (summary in Figure 2.3) can be used for MD processes [20]:

- Plate and frame where membranes and spacers are layered together between two plates.
- Hollow fiber where thousands of hollow fibers are bundled and sealed inside a shell tube.
- Tubular membrane where the membrane is tube-shaped and inserted between two cylindrical chambers (hot and cold fluid chambers).
- Spiral wound membrane where flat sheet membrane and spacers are enveloped and rolled around a perforated central collection tube, particularly employed in DCMD and AGMD.

Among others, flat sheet membrane configuration is widely used on laboratory scale due to ease to clean and replace it. However, the packing density, referred as the ratio of membrane area to the packing volume, is low and a membrane support is required. Hollow fiber modules have very high packing density and low energy consumption, but on the other hand, it has high tendency to clogging and is difficult to clean and maintain. It is worth mentioning that, if feed solution penetrates the membrane pores in shell and tube modules, the whole module should be changed.



Figure 2.3. Schematic representation of typical membranes configuration. Readapted from [20].

2.2.1 Direct Contact Membrane Distillation (DCMD) and its using in water desalination

Among MD configurations, direct contact membrane distillation (DCMD) has the simplest design and operation, but it needs interfaces with well-tailored structure, which is difficult to achieve in current available membranes. In this kind of configuration, aqueous streams are separated by a hydrophobic porous membrane. The temperature of one of the two currents (at feed side) is greater than the other one (at permeate side) so as to create a temperature difference across the membrane and, hence, a difference in partial pressure, which is the real driving force of the process. High hydrophobic surface character is essential to preserve membrane from wetting while water vapor diffuses through the pores under soft processing conditions. Reduced resistance to mass transfer is also highly desirable, which implies short free paths at low tortuosity factor. Also, heat loss must be prevented when thermally driven operations are applied, in order to prevent reduction of the difference of temperature across the membrane, and consequently the abatement of the flux. DCMD is generally the most used configuration on lab scale for its simple design and operations, particularly used when stream composition is mainly made up of water. Despite of it is generally characterized from low water productivity, with respect to Osmosis Reverse (RO), greater water fluxes can be achieved tuning membrane properties by a morphological and a chemical point of view. In fact, one of the topics of the PhD thesis was the preparation, characterization and application of honeycomb membranes, with high-defined ordered structure. This element, in combination with reduced pore size, a more thin active layer and the using of a material with low thermal conductivity (HYFLON AD), allowed to direct productivity (water flux > 50 L/m²h) selectivity (rejection of 99.1 %) and thermal efficiency (> 70.2 %) of DCMD towards a unique direction. It's necessary also to underline that Membrane Distillation in general is not a substitute process of RO for water desalination, but its major future goal can be its using as a consequent step in integrated membrane processes. All experimental details will be described in Chapter 3 and Chapter 4.

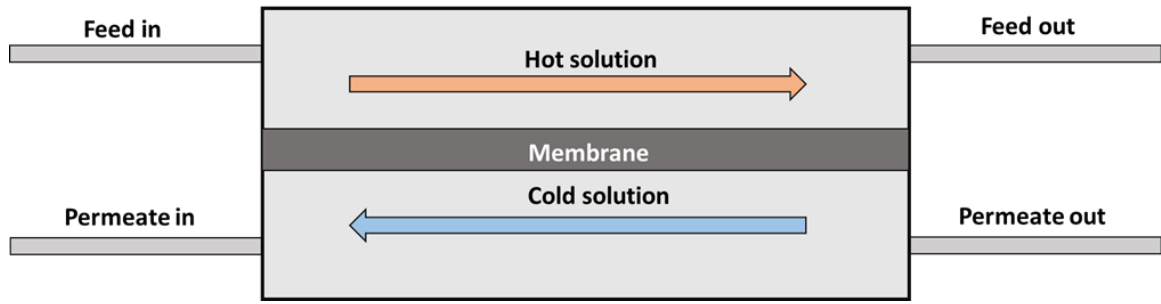


Figure 2.4. Schematic representation of thermally driven Direct Contact Membrane Distillation configuration (DCMD).

Membrane thickness δ (μm) and membrane porosity ε (%) are indeed two significant structural features to be considered for MD systems [22], because there is an inversely proportional relationship between the membrane thickness δ and the permeate flux J , while a direct dependence on the porosity exists:

$$J \propto \frac{\langle r^\alpha \rangle \cdot \varepsilon}{\tau \cdot \delta} \quad (2.2)$$

where $\langle r^\alpha \rangle$ is the average pore size for Knudsen diffusion ($\alpha = 1$) or the average squared pore size for viscous flux ($\alpha = 2$), τ the membrane tortuosity. From Eq. (2.2) it is clear how membrane porosity and pore size can be managed to maximize the flux, while minimized path length through the membrane section should be preferred. Regarding the latter, asymmetric membranes with a really thin top-layer on porous substructures restrict the mass transfer resistance in the top-layer mainly, because the sub-layer has a supporting function only.

Membrane porosity and thickness are two critical parameters for the heat transfer as well [23]. This is because the thermal conduction is considered as a heat loss mechanism through the membrane material and the vapor that fills the pores. It can be expressed as:

$$Q_m = h_m \cdot \Delta T_m \quad (2.3)$$

Where

$$h_m = \varepsilon \cdot h_{mg} + (1 - \varepsilon)h_{ms} = \frac{K_g \cdot \varepsilon + (1 - \varepsilon)K_s}{\delta} \quad (2.4)$$

Here, h_{ms} and h_{mg} represent the heat transfer coefficients of the vapor within the membrane pores and the solid membrane material, respectively; k_g and k_m the thermal conductivity of vapor and polymer.

Total heat transfer across the membrane is given by

$$Q_m = Q_v + Q_m \quad (2.5)$$

Where

$$Q_v = h_v \cdot \Delta T_m = J \cdot \Delta H_v \quad (2.6)$$

is the heat of vaporization. On the other hand, the heat transfer by convection in the feed f and permeate p boundary layers can be expressed as:

$$Q = h_f \cdot \Delta T_f = h_f \cdot (T_f - T_{fm}) \quad (2.7)$$

$$Q = h_p \cdot \Delta T_p = h_p \cdot (T_p - T_{pm}) \quad (2.8)$$

Therefore, the overall heat transfer coefficient of the MD process is given by

$$\begin{aligned} \frac{1}{U} &= \frac{1}{h_f} + \frac{1}{h_m + h_v} + \frac{1}{h_p} \\ &= \frac{1}{h_f} + \frac{1}{((k_g \cdot \varepsilon + k_m(1-\varepsilon))/\delta) + (J \cdot \Delta H_v)/(T_{fm} - T_{pm})} + \frac{1}{h_p} \end{aligned} \quad (2.9)$$

where each h and each T represent the corresponding heat transfer coefficients and temperatures either at feed (f) side or permeate (p) side or at membrane surface (m).

Finally, the total heat transferred across the membrane is expressed as:

$$Q = U \cdot \Delta T \quad (2.10)$$

while the thermal efficiency in MD can be specified as the ratio of latent heat of vaporization to the total (latent and conduction) heat.

In DCMD, a sensible heat loss results in a difference in the bulk and membrane interface temperatures [24]. Figure 2.5 shows the temperatures of the different parts of a typical

DCMD configuration. Due to the lowering of temperature, the feed moves from the feed channel through the membrane, to the permeate channel, as a result of temperature polarization, and the driving force of heat transfer becomes negatively affected. In DCMD, there is simultaneous transfer of both heat and mass, determined by the heat flux and transfer coefficients in both feed and permeate sides [25].

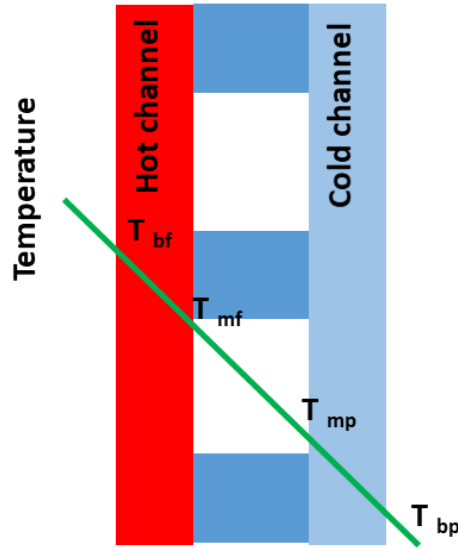


Figure 2.5. The bulk and membrane interface temperatures where T_{bf} is the bulk feed temperature, T_{mf} is the membrane interface temperature at the feed side, T_{mp} is the membrane interface temperature at the permeate side, and T_{bp} is the bulk permeate temperature [25]. Readapted from [23].

Thermal efficiency is one of the most important parameters to consider and to improve in Membrane Distillation processes.

For DCMD, the thermal efficiency is, hence, expressed as:

$$\text{Thermal efficiency} = \frac{J \cdot \Delta H}{U \cdot \Delta T} \cdot 100 \quad (2.11)$$

On this basis, tiny active layers based on materials with very low thermal conductivity would be desirable for MD membrane processes. Traditionally, polymers such as polytetrafluoroethylene (PTFE), polypropylene (PP) and polyvinylidene fluoride (PVDF) are used to fabricate porous membranes due to their intrinsic hydrophobic character and relatively low thermal conductivity ($0.21\text{--}0.37 \text{ Wm}^{-1} \text{ K}^{-1}$ for PVDF, $0.25\text{--}0.27 \text{ Wm}^{-1} \text{ K}^{-1}$ for PTFE and $0.11\text{--}0.16 \text{ Wm}^{-1} \text{ K}^{-1}$ for PP respectively). However, high thermal efficiency continues to be an ambitious target for MD processes.

Another parameter to consider is Reynolds number. The Reynolds number (Re) is a dimensionless parameter used in fluid dynamics, proportional to the ratio between inertial forces and viscous forces [26]. It is used to predict the transition from laminar to turbulent flow, and at low Reynolds numbers, flows tend to be dominated by laminar (sheet-like) flow, while at high Reynolds numbers turbulence results from differences in the fluid's speed and direction, which may sometimes intersect or even move counter to the overall direction of the flow (eddy currents).

In the most general cases, the Reynolds number is written as:

$$Re = \frac{\rho \langle v \rangle d}{\mu} = \frac{\langle v \rangle d}{D_V} \quad (2.12)$$

Where:

- ρ is the density or density (kg / m^3);
- $\langle v \rangle$ is the macroscopic speed (average) (m / s);
- d is a characteristic length of the phenomenon considered. For example in the case of the motion of a fluid in a pipe it corresponds to the diameter of the pipe, while in the case of a wing profile it corresponds to the length of the rope (m);
- μ is the dynamic viscosity ($\text{Pa} \cdot \text{s}$ or $\text{N} \cdot \text{s} / \text{m}^2$ or $\text{kg} / (\text{m} \cdot \text{s})$);
- D_V is the kinematic diffusivity (m^2 / s)

2.3 Membrane Assisted Crystallization (MCr) technology: an experimental point of view

Crystallization is a solid-liquid separation technique in which solid crystals are formed from a liquid solution under supersaturation conditions. It has been usually employed in separation and purification of industrial streams using traditional devices as crystallizers or evaporators. Nowadays, membrane technology appears as the alternative technology that could replace the conventional crystallizers because of its advantages related to its adaptability and the low energy consumption in comparison with the conventional technology [27]. In this context, MCr appears as an innovative idea to incorporate membrane technology in crystallization processes, to take advantage of its intrinsic benefits, including well controlled nucleation induction time and growth kinetics. Furthermore, the possibility to have control in crystals shape and size and also on the polymorphism of molecular crystals is one of the most appealing and fascinating phenomena of solid state chemistry, where membrane technology

falls. In fact, the possibility to have polymorphism, represents an open challenge for being able to rationally design and construct crystalline solids with defined architectures [28].

2.3.1 Membrane Crystallization via Membrane Distillation

Membrane Crystallization (MCr) technology works applying a temperature and/or concentration gradient as a driving force and using solutions close to the supersaturation.

MCr has to be conducted under specific operative conditions and with membranes that possesses specific requirements, in order to be suitable for crystallization and so for recovery of several kind of molecules.

Crystallization is characterized by laminar flow conditions that minimize the shear stress, promoting the formation of good structured crystalline forms. Besides, the membrane provides an excellent support for heterogeneous nucleation (nuclei grow at a surface), easier than the homogeneous nucleation (nuclei grow in the bulk solution) [29]. This happens because the energy barrier (Gibbs free energy) for heterogeneous nucleation is lower than the one for homogenous nucleation [23]. In this regard, the membrane selection plays an important role. High surface area, porosity and roughness favor the nucleation because particles can deposit easily and “be trapped” [30-32], reducing the induction time, i.e. period between the moment in which supersaturation conditions are reached and the first crystal appears. Furthermore the action on transmembrane flow rate, by changing the driving force of the process, enables one to modulate the final properties of the crystals produced both in terms of structure (polymorphism) and morphology (habit, shape, size, and size distribution). (Figure 2.6)

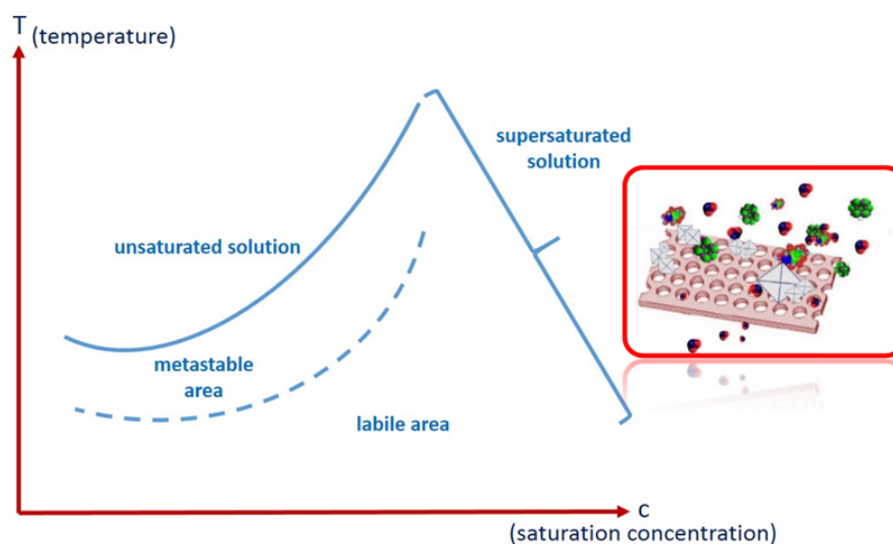


Figure 2.6. Schematic illustration of supersaturation phenomena.

Crystallization is one of the most widely applied separation processes in the chemical industry [33], because a large number of daily-used products like additives, pharmaceuticals, fine chemicals, pigments, etc., are marketed in crystalline form. In order to obtain a high-quality product, it is crucial to control product properties such as crystal morphology (shape, habit, average size, size distribution), structure (polymorphism), and purity (regular arrangement of the building blocks into the lattice) (Figure 2.5). All these properties have a considerable impact on the final use of a crystalline product.

This technology can be implemented for a wide range of applications, including desalination of seawater and brines [34-37], wastewater treatment for the recovery of high-purity silver [38] or sodium sulphate [39], CO₂ capture [40, 41], nanotechnology such as the synthesis of BaSO₄ and CaCO₃ particles [42], the recovery of antibiotics [43] or polystyrene microparticles [44]. Membrane Crystallization technique is also widely used for the recovery of biomolecules [45] (Figure 2.7).

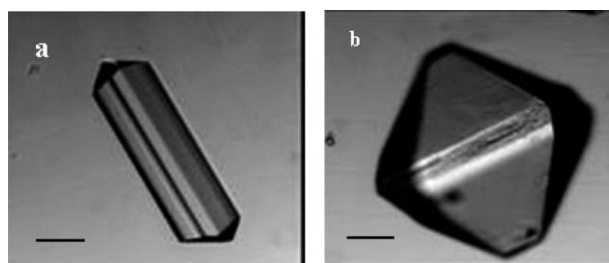
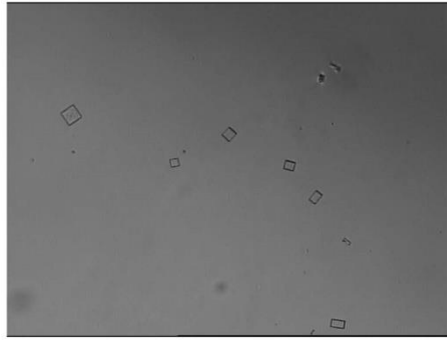


Figure 2.7. Optical images of the two crystal morphologies obtained during the membrane crystallization tests of glycine: (a) Form I; (b) Form II (the unit bar inside the figure corresponds to 50 μm). Reprinted from [45] Copyright (2007), with permission from American Chemical Society.

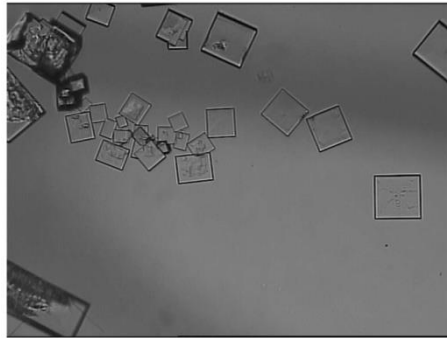
2.3.2 Membrane Crystallization in seawater desalination

MCr technology is expected to give a fundamental contribution in seawater desalination, which is becoming the most economically competitive way to resolve the potable water demand in regions with high deficiencies [28]. Reverse Osmosis (RO) is considered in water desalination as the most cost-effective solution to potable water demand, but day by day it is starting to be integrated with other competitive techniques like Membrane Distillation (MD), widely described in previous section for improvements in cost reduction, enhancement of water recovery factor, water quality, and new brine disposal strategies. In fact, a fundamental problem in desalination is the environmental aspects of brine discharge from RO plants. The most frequent disposal practice is the direct discharge in the environment. However, the more and more stringent environmental regulations preclude in many cases this low-cost practice, aiming to protect the aquatic environment.

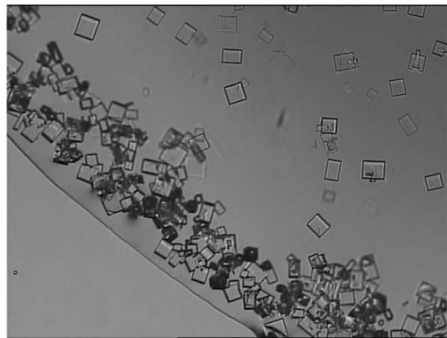
Various process engineering strategies have been investigated in order to perform environmentally friendly strategy for brine disposal. A suitable solution is the possibility to completely redesign a desalination system by introducing and integrating with MCr operations [46]. Again, hydrophobic porous membranes are in direct contact with a hot feed and a cold distillate. Water evaporates at the feed/membrane interface, diffuse through the membrane pores and condense in the cold distillate stream, while the stream is concentrated until ion aggregation preceding crystallization. Therefore, membrane structural properties will strongly affect membrane crystallization performance both in terms of solvent evaporation rate and in terms of crystals nucleation and growth. As a matter of fact, a crystallizing solution can be imagined as a certain number of solute molecules moving among the molecules of solvent and colliding with each other, so that a number of them converge forming clusters (Figure 2.8).



AD40H_010 membrane



AD40H_022 membrane



AD40H_045 membrane

Figure 2.8. NaCl crystalline habit. Magnification: $\times 10$, achieved with different kind of PVDF-HYFLON nanocomposite membranes: AD40H_010; AD 40H_022; AD40H_045. Reprinted from [47] Copyright© 2018, with permission from Elsevier B.V. All rights reserved.

In general, several are the advantages derived from using MCr technology, such as:

- High purity level,
- Control of polymorphic form, narrow crystal shape and crystal size distribution.
- Faster nucleation times

Continuous removal of pure water as permeate from the feed solution induced saturation and thus crystallization. To characterize the obtained crystals, the feed containing NaCl crystals are removed from the feed solution after regular intervals from onset of crystallization and

were examined visually by optical microscope for determining various crystals mean diameter, coefficient of variation (CV), nucleation and growth rate [47]. Coefficient of variation (CV) is a parameter indicating the dispersion of a distribution around the mean crystal size. CV was calculated using the following equation:

$$CV = \frac{F_{80\%} - F_{20\%}}{2 \cdot F_{50\%}} \cdot 100 \quad (2.13)$$

where CV is expressed as percentage and F is the crystal length at the indicated percentage. Growth (G) and nucleation rate (B^0) have been estimated on the basis of the Randolph-Larson model [48] as follows:

$$\ln(n) = \frac{-L}{Gt} + \ln(n^0) \quad (2.14)$$

$$B^0 = n^0 G \quad (2.15)$$

where n is the crystal population density, L is crystal size, t is retention time and n^0 is population density at L equal to zero.

The quantification of these parameters enables one to build kinetics growth of crystals, providing information about crystals size and shape distribution as well as velocity of nucleation.

2.4 Membrane Assisted Crystallization technology from computational point of view

Computational studies may predict and support the understanding of mechanisms and phenomena at molecular level, including assisted membrane crystallization [29].

The molecular details of the process appear in very small length scale of the order of nanometers, and they are, by definition, unstable and therefore form only transiently, so quite challenging to probe in real time even. However, today, with state-of-the-art measurements, nucleation has also been observed at the molecular scale [49, 51-53]. The rapid advance of experimental techniques such as in situ atomic force microscopy [54], liquid-cell transmission electron microscopy [55], cryo-TEM [52], are expected to deliver novel results in order to refine the understanding of crystal nucleation and growth [56]. Computational modelling including fully atomistic simulations, where the temporal evolution of the liquid

into the crystal is studied, complementing experiments, support in providing insight on the mechanisms of such phenomena and enables kinetic and thermodynamic quantities to be estimated. Surely, the rapid progresses in computational methodology have unraveled crucial aspects of crystal nucleation in liquids. Several studies have been performed to depict the mechanism of heterogeneous crystal nucleation by simulation [50, 57-58] such as atomic simulation [59-61] and phase field theory [62], while there are limited publications for heterogeneous salt crystal nucleation from aqueous solution [63-65]. Moreover, the mechanics of the earliest stages of the crystallization assisted by membranes still remain an important fundamental issue. However, there are several papers discussing crystal nucleation in aqueous solution [66-70], which focus on available force fields and models. Chakraborty et al [67] investigated how crystals nucleate and growth in aqueous NaCl solution. Large-scale molecular dynamics simulations have been performed to examine the microscopic mechanism of crystal nucleation and growth in a slightly supersaturated solution of NaCl in water at 300 K and 1 atm. Early-stage nucleation has been observed, and the growth of a single crystal has been followed for ~ 140 ns. It has been demonstrated that the nucleation and growth process is better described by Ostwald's rule of stages than by classical nucleation theory. A disordered region of high local salt concentration forms prior to crystal nucleation; the early stage nucleus is not a mini crystal of anhydrous NaCl but rather a less ordered arrangement of ions that retains a significant amount of water. From Ostwald's perspective, this is not surprising because is expected the ion-water composition of the early nucleus to be closer in free energy to the metastable solution than would be the case for an anhydrous NaCl cluster. The residual water appears to be very slowly (on simulation time scales) excluded as the crystal evolves toward its stable anhydrous state.

Tsai et al [29] for the first time have carried out molecular dynamics simulations studies of the crystal nucleation and growth of sodium chloride solution in contact with hydrophobic polymer surfaces of PVDF and PP at a supersaturated concentration of salt. At the same time they choose crystallization of NaCl from aqueous solutions, because it is a typical example of most inorganic crystallizing systems.

At first, crystals nucleation and grow have been simulated in a slightly supersaturated aqueous bulk solution as performed by Chakraborty [67]. Then, PVDF and PP membrane surfaces interfacing NaCl solution have been studied by Tsai et al [68] and the results have been compared with that on bulk solution and with experimental data. In parallel, membrane crystallization experiments have been performed utilizing the same kind of polymeric membranes in order to compare the experimental findings with the computational data.

Figure 2.9, following Chakraborty procedure, shows the two different steps that happen in nucleation phenomena when at first (Figure 2.9a and c) disordered regions are particularly present in NaCl solution and then when they leave space to aggregation of Na^+ Cl^- ions, giving shape to ordered structures (Figure 2.9b and d). This is the first computational work where molecular dynamics simulation tools have been used to confirm how the use of hydrophobic polymer matrices can assist crystallization of salts reducing nucleation times (Figure 2.9c and d).

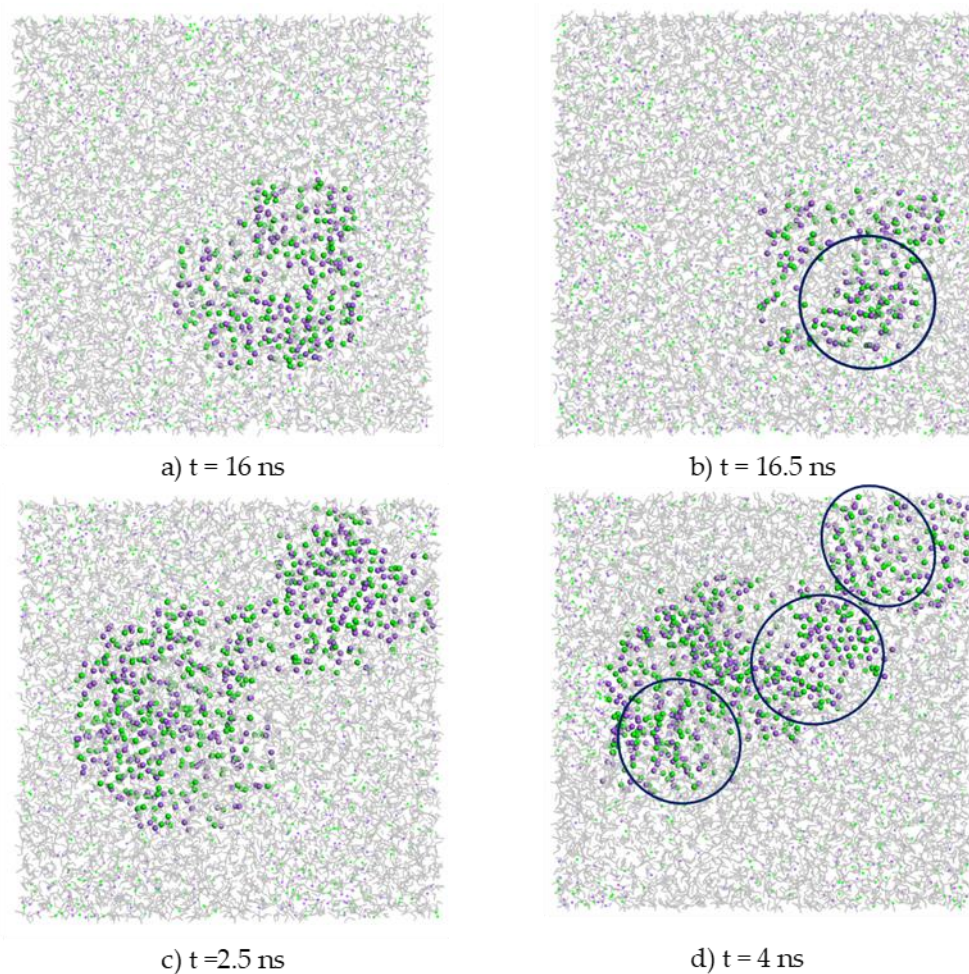


Figure 2.9. Snapshots showing the amorphous and crystal phases of Na^+ and Cl^- in supersaturated solutions at different time of simulations. a) and b) in NaCl bulk solution; c) and d) on PP surface. Blue circles indicate the region with higher density and partial order of NaCl ions. Na^+ in purple, Cl^- in green, water molecules in grey. Readapted from [29].

In this work, NaCl crystals growth during simulation time has been identified in a quantitative overview by radial distribution function $r^2h^+ - (r)$ for times ranging from 5 to 100 ns. Here, $h^+ - (r) = g(r) - 1$, where $g(r)$ is the radial distribution function and multiplied by r^2 to magnify the structural details [69]. The function $h^+ - (r)$ is averaged over all ions in the system. However, ions in the growing crystal contributed to the long-range structure. At

first nanosecond very short ranged rdf refer to the metastable solution with one discernable peak indicating few ordered ions. At the end of simulation, the structural peaks, related to the ion-ion correlation, are visible indicating the growth of NaCl crystals. Difference are estimated for bulk NaCl solution, where a larger order is visible up to 2 nm whereas for NaCl in contact with the hydrophobic membranes it is up to 1.5 nm. The presence of PP and PVDF membranes modified the shape of $r^2h(r)$ function. Only positive regions are present in both Figure 2.10b and 2.10c indicating the augmented ion density in the crystal.

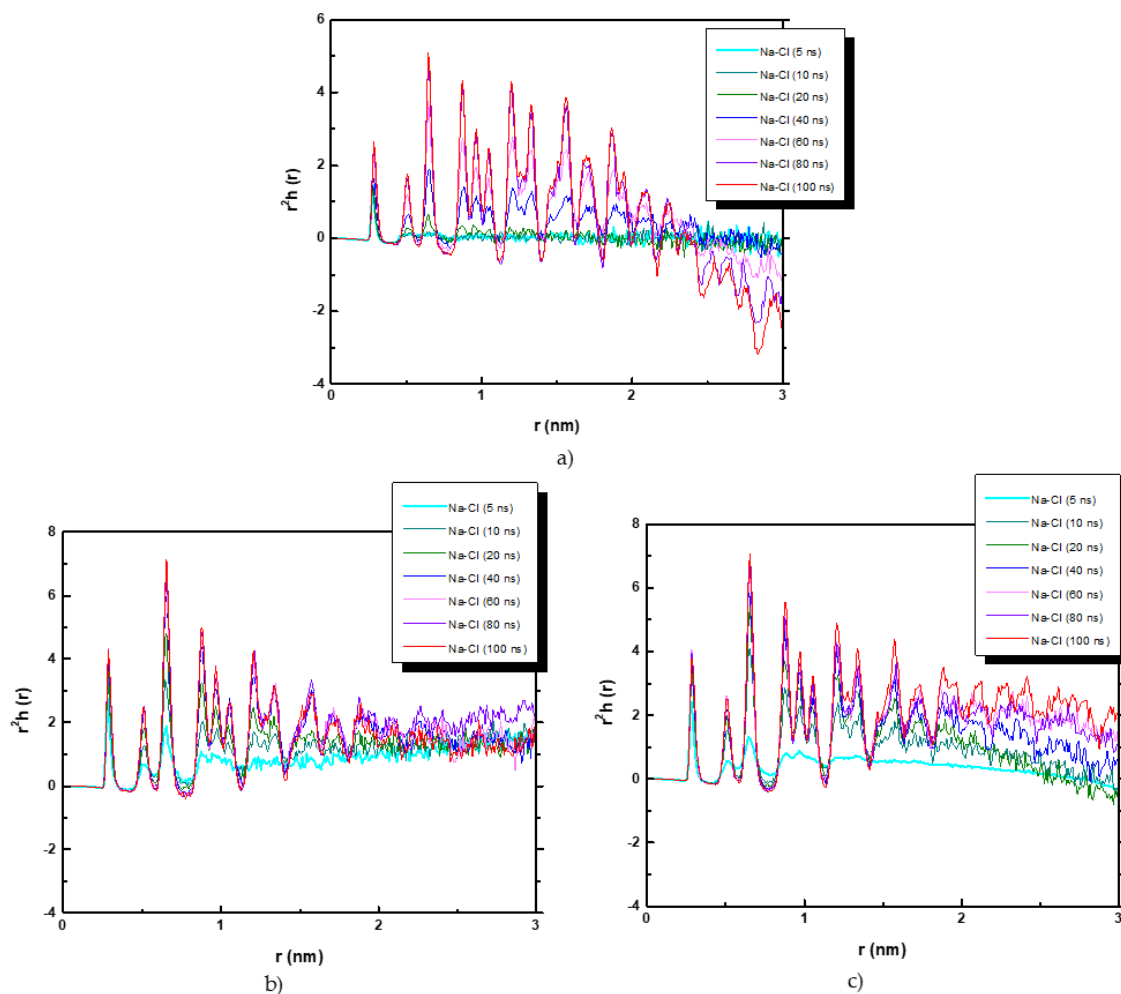


Figure 2.10 $r^2h(r)$ function of NaCl a) in bulk solution; b) in PVDF system; c) in PP system. Readapted from [29].

With respect to traditional crystallization technology the presence of an hydrophobic membrane with $90^\circ < \theta < 180^\circ$ promotes nucleation. The special effect of the heterogeneous contribution allows crystals to nucleate faster and/or by using lower initial amount of substance with respect to usual comparable techniques. By considering the interactions between solute and solid substrate in terms of contact angle (θ), which the crystallizing

solution droplets form with the solid substrate, the reduction of ΔG due to heterogeneous nucleation is equal to [70-71]:

$$\frac{\Delta G_{heter}}{\Delta G_{homog}} = \frac{1}{4}(2 + \cos\theta)(1 - \cos\theta)^2 \left[1 - \varepsilon \frac{(1 + \cos\theta)^2}{(1 - \cos\theta)^2}\right]^3 \quad (2.16)$$

where ε is the overall surface porosity defined as the ratio between the area of the pores to the total membrane surface area. In the case of a non-porous system ($\varepsilon = 0$), when contact angle is equal to 180° then $\Delta G_{heter} = \Delta G_{homog}$, whereas if contact angle is equal to 90° , then $\Delta G_{heter} = \frac{1}{2}\Delta G_{homog}$.

Hydrophobic porous membranes assist crystallization phenomena. Their performances, widely studied from experimental point of view, are now object of interest in computational studies. This study gives attention to each aspect of the process with theoretical models, going beyond what already exists in literature, where crystallization is described only in aqueous solution.

References

1. C.A. Quist-Jensen, F. Macedonio, E. Drioli, Integrated Membrane Desalination Systems with Membrane Crystallization Units for Resource Recovery: A New Approach for Mining from the Sea, *Crystals*, 6 (2016) 1-13, <https://doi.org/10.3390/cryst6040036>.
2. A. Alkhudhiri, N. Darwish, N. Hilal, Membrane distillation: A comprehensive review, *Desalination*, 287 (2012) 2–18, <https://doi.org/10.1016/j.desal.2011.08.027>.
3. B.L. Pangarkar, M.G. Sane, M. Guddad, Reverse Osmosis and Membrane Distillation for Desalination of Groundwater: A Review, *ISRN Mat. Sci.*, 2011 (2011) Article ID 523124, 9, <https://doi.org/10.5402/2011/523124>.
4. M. Gryta, K. Karakulski, A.W. Morawski, Purification of oily wastewater by hybrid UF/MD, *Water Res.*, 35 (15) (2001) 3665–3669, [https://doi.org/10.1016/S0043-1354\(01\)00083-5](https://doi.org/10.1016/S0043-1354(01)00083-5).
5. H. Kurokawa, T. Sawa, Heat recovery characteristics of membrane distillation, *Heat transfer-Japanese Research.*, 25 (1996) 135–150, [https://doi.org/10.1002/\(SICI\)1520-6556\(1996\)25:3<135::AID-HTJ1>3.0.CO;2-Y](https://doi.org/10.1002/(SICI)1520-6556(1996)25:3<135::AID-HTJ1>3.0.CO;2-Y).
6. J. Blanco Gálvez, L. García-Rodríguez, I. Martín-Mateos, Seawater desalination by an innovative solar-powered membrane distillation system: the MEDESOL project, *Desalination*, 246 (1–3) (2009) 567–576, <https://doi.org/10.1016/j.desal.2008.12.005>.
7. N. Ghaffour, S. Lattemann, T. Missimer, K.C. Ng, S. Sinha, G. Amy, Renewable energy-driven innovative energy-efficient desalination technologies, *Applied Energy*, 136, (2014), 1155-1165, <https://doi.org/10.1016/j.apenergy.2014.03.033>.
8. F.A. Banat, J. Simandl, Desalination by membrane distillation: a parametric study, *Sep. Sci. Technol.*, 33 (2) (1998) 201–226, <https://doi.org/10.1080/01496399808544764>.
9. M.C. García-Payo, M.A. Izquierdo-Gil, C. Fernández-Pineda, Air gap membrane distillation of aqueous alcohol solutions, *J. Membr. Sci.*, 169 (1) (2000) 61–80, [https://doi.org/10.1016/S0376-7388\(99\)00326-9](https://doi.org/10.1016/S0376-7388(99)00326-9).
10. P.P. Zolotarev, V.V. Ugrozov, I.B. Volkina, V.M. Nikulin, Treatment of waste water for removing heavy metals by membrane distillation, *J. Hazard. Mater.*, 37 (1) (1994) 77–82, [https://doi.org/10.1016/0304-3894\(94\)85035-6](https://doi.org/10.1016/0304-3894(94)85035-6).
11. G. Zakrzewska-Trznadel, M. Harasimowicz, A.G. Chmielewski, Concentration of radioactive components in liquid low-level radioactive waste by membrane distillation, *J. Membr. Sci.*, 163 (2) (1999) 257–264, [https://doi.org/10.1016/S0376-7388\(99\)00171-4](https://doi.org/10.1016/S0376-7388(99)00171-4).

12. M.P. Godino, L. Peña, C. Rincón, J.I. Mengual, Water production from brines by membrane distillation, *Desalination*, 108 (1–3) (1997) 91–97, [https://doi.org/10.1016/S0011-9164\(97\)00013-1](https://doi.org/10.1016/S0011-9164(97)00013-1).
13. S.T. Hsu, K.T. Cheng, J.S. Chiou, Seawater desalination by direct contact membrane distillation, *Desalination*, 143 (3) (2002) 279–287, [https://doi.org/10.1016/S0011-9164\(02\)00266-7](https://doi.org/10.1016/S0011-9164(02)00266-7).
14. S. Bandini, G.C. Sarti, Heat and mass transport resistances in vacuum membrane distillation per drop, *AIChE Journal*, 45 (1999) 1422–1433, <https://doi.org/10.1002/aic.690450707>.
15. N.N. Li, A.G. Fane, W.S.W. Ho, T. Matsuura, *Advanced Membranes Technology and Applications*, John Wiley & Sons, Inc., 2008, Chapter 12, pp. 297-301.
16. V. Karanikola, A.F. Corral, P. Mette, H. Jiang, R.G. Arnoldand, W.P. Ela, Solar membrane distillation: desalination for the Navajo Nation, *Rev. Env. Health*, 29 (2014) 67–70, <https://doi.org/10.1515/reveh-2014-0019>.
17. J. Walton, H. Lu, C. Turner, S. Solis, H. Hein, Solar and waste heat desalination by membrane distillation, Final Report, College of Engineering University of Texas, El Paso, 2004.
18. M.C. García-Payo, C.A. Rivier, I.W. Marison, U. Stockar, Separation of binary mixtures by thermostatic sweeping gas membrane distillation: II. Experimental results with aqueous formic acid solutions, *J. Membr. Sci.*, 198 (2) (2002) 197–210, [https://doi.org/10.1016/S0376-7388\(01\)00649-4](https://doi.org/10.1016/S0376-7388(01)00649-4).
19. M. Asghari, A. Harandizadeh, M. Dehghani, H.R. Harami, Persian Gulf desalination using air gap membrane distillation: Numerical simulation and theoretical study, *Desalination*, 374 (2015) 92-100, <https://doi.org/10.1016/j.desal.2015.07.019>.
20. M. Mulder, *Basic Principles of Membrane Technology*, second edition, Kluwer Academic Publishers, 1996, Chapter 8, pp. 465-471.
21. M. Gryta, Effectiveness of Water Desalination by Membrane Distillation Process, *Membranes*, 2 (2012) 415-429, <https://doi.org/10.3390/membranes2030415>.
22. F.A. Banat, J. Simandl, Theoretical and experimental study in membrane distillation, *Desalination*, 95 (1) (1994) 39–52, [https://doi.org/10.1016/0011-9164\(94\)00005-0](https://doi.org/10.1016/0011-9164(94)00005-0).
23. B.B. Ashoor, S. Mansour, A. Giwa, V. Dufour, S. W. Hasan, Principles and applications of direct contact membrane distillation (DCMD): A comprehensive review, *Desalination*, 398 (2016) 222-246, <https://doi.org/10.1016/j.desal.2016.07.043>.

24. M. Qtaishat, T. Matsuura, B. Kruczek, A. Khayet, Heat and mass transfer analysis in direct contact membrane distillation, *Desalination*, 219 (2008) 272-292, <https://doi.org/10.1016/j.desal.2007.05.019>.
25. D.U. Lawal, A.E. Khalifa, Flux prediction in direct contact membrane distillation, *Int. J. Mater. Mech. Manuf.*, 2 (2014) 302-308, <https://doi.org/10.7763/IJMMM.2014.V2.147>.
26. R.B. Bird, W.E. Stewart, E.N. Lightfoot, Transport Phenomena, 2^a ed., New York, Wiley, 2005.
27. I. Ruiz Salmón, P. Luis, Membrane crystallization via membrane distillation, *Che. Eng. Proc. Proc. Int.*, 123 (2018) 125-135, <https://doi.org/10.1016/j.cep.2017.11.017>.
28. E. Drioli, G. Di Profio, E. Curcio, Progress in membrane crystallization, *Curr. Op. Chem. Eng.*, 1 (2012) 178-182, <https://doi.org/10.1016/j.coche.2012.03.005>.
29. J.H. Tsai, M.L. Perrotta, A. Gugliuzza, F. Macedonio, L. Giorno, E. Drioli, K.L. Tung, E. Tocci, Membrane-Assisted Crystallization: A Molecular View of NaCl Nucleation and Growth, *Appl. Sci.*, 8(11) (2018) 2145, <https://doi.org/10.3390/app8112145>.
30. E. Drioli, A. Criscuoli, E. Curcio, Membrane Contactors: Fundamentals Applications and Potentialities, Membrane Sciences and Technology Series 11, Elsevier, 2011.
31. E. Chabanon, D. Mangin, C. Charcosset, Membranes and crystallization processes: state of the art and prospects, *J. Membr. Sci.*, 509 (2016) 57-67, <https://doi.org/10.1016/j.memsci.2016.02.051>.
32. A. Gugliuzza, M.C. Aceto, E. Drioli, Interactive functional poly (vinylidene fluoride) membranes with modulated lysozyme affinity: a promising class of new interfaces for contactor crystallizers, *Polymer Int.*, 58 (12) (2009) 1452-1464, <https://doi.org/10.1002/pi.2681>.
33. J.T.M. Sluys, D. Verdoes, J.H. Hanemaaijer, Water treatment in a Membrane-Assisted Crystallizer (MAC), *Desalination*, 104 (1996) 135-139, [https://doi.org/10.1016/0011-9164\(96\)00036-7](https://doi.org/10.1016/0011-9164(96)00036-7).
34. X. Ji, E. Curcio, S. Al Obaidani, G. Di Profio, E. Fontananova, E. Drioli, Membrane distillation-crystallization of seawater reverse osmosis brines, *Sep. Purif. Technol.*, 71 (2010) 76-82, <https://doi.org/10.1016/j.seppur.2009.11.004>.
35. E. Drioli, E. Curcio, G. Di Profio, F. Macedonio, A. Criscuoli, Integrating membrane contactors technology and pressure-driven membrane operations for seawater desalination: energy, exergy and costs analysis, *Chem. Eng. Res. Des.*, 84 (2006) 209-220, <https://doi.org/10.1205/cherd.05171>.

36. D.H. Kim, A review of desalting process techniques and economic analysis of the recovery of salts from retentates, *Desalination*, 270 (2011) 1–8, <https://doi.org/10.1016/j.desal.2010.12.041>.
37. L. Mariah, C.A. Buckley, C.J. Brouckaert, E. Curcio, E. Drioli, D. Jaganyi, D. Ramjugernath, Membrane distillation of concentrated brines—role of water activities in the evaluation of driving force, *J. Memb. Sci.*, 280 (2006) 937–947, <https://doi.org/10.1016/j.memsci.2006.03.014>.
38. B. Tang, G. Yu, J. Fang, T. Shi, Recovery of high-purity silver directly from dilute effluents by an emulsion liquid membrane-crystallization process, *J. Hazard. Mater.*, 177 (2010) 377–383, <https://doi.org/10.1016/j.jhazmat.2009.12.042>.
39. W. Li, B. Van der Bruggen, P. Luis, Integration of reverse osmosis and membrane crystallization for sodium sulphate recovery, *Chem. Eng. Process. Process Intensif.*, 85 (2014) 57–68, <https://doi.org/10.1016/j.cep.2014.08.003>.
40. I. Ruiz Salmon, R. Janssens, P. Luis Alconero, Membrane crystallization of sodium carbonate in CO₂ capture scenario: mass and heat transfer study, *Sep. Purif Technol.*, 176 (2017) 173–183, available at: <http://hdl.handle.net/2078.1/182707>. ORAL COMMUNICATION
41. P. Luis, D. Van Aubel, B. Van der Bruggen, Technical viability and exergy analysis of membrane crystallization: closing the loop of CO₂ sequestration, *Int. J. Greenhouse Gas Control*, 12 (2013) 450–459, <https://doi.org/10.1016/j.ijggc.2012.11.027>.
42. Z. Jia, Z. Liu, F. He, Synthesis of nanosized BaSO₄ and CaCO₃ particles with a membrane reactor: effects of additives on particles, *J. Colloid Interface Sci.*, 266 (2003) 322–327, [https://doi.org/10.1016/S0021-9797\(03\)00187-5](https://doi.org/10.1016/S0021-9797(03)00187-5).
43. S.Z. Li, X.Y. Li, D.Z. Wang, Membrane (RO-UF) filtration for antibiotic wastewater treatment and recovery of antibiotics, *Sep. Purif. Technol.*, 34 (2004) 109–114, [https://doi.org/10.1016/S1383-5866\(03\)00184-9](https://doi.org/10.1016/S1383-5866(03)00184-9).
44. E. Drioli, M.C. Carnevale, A. Figoli, A. Criscuoli, Vacuum Membrane Dryer (VMDr) for the recovery of solid microparticles from aqueous solutions, *J. Memb. Sci.*, 472 (2014) 67–76, <https://doi.org/10.1016/j.memsci.2014.08.047>.
45. G. Di Profio, S. Tucci, E. Curcio, E. Drioli, Selective Glycine Polymorph Crystallization by Using Microporous Membranes, *Cryst. Growth Des.*, 7 (2007) 526–530, <https://doi.org/10.1021/cg0605990>.
46. E. Drioli, E. Curcio, A. Criscuoli, G. Di Profio, Integrated system for recovery of CaCO₃, NaCl and MgSO₄ 7H₂O from nanofiltration retentate. *J. Membr. Sci.*, 239 (2004) 27–38, <https://doi.org/10.1016/j.memsci.2003.09.028>.

47. Z. Cui, X. Li, Y. Zhang, A. Gagliuzza, F. Militano, E. Drioli, F. Macedonio, Testing of three different PVDF membranes in membrane assisted-crystallization process: Influence of membrane structural-properties on process performance, *Desalination*, 440 (2018) 68–77, <https://doi.org/10.1016/j.desal.2017.12.038>.
48. C.C. Koa, A. Ali, E. Drioli, K.L. Tunga, C.H. Chena, Y.R. Chena, F. Macedonio, Performance of ceramic membrane in vacuum membrane distillation and in vacuum membrane crystallization, *Desalination*, 44 (2018) 48-58, <https://doi.org/10.1016/j.desal.2018.03.011>.
49. P.G. Vekilov, The two-step mechanism of nucleation of crystals in solution, *Nanoscale*, 2 (2010) 2346–2357, <https://doi.org/10.1039/c0nr00628a>.
50. J. Anwar, D. Zahn, Uncovering Molecular Processes in Crystal Nucleation and Growth by Using Molecular Simulation. *Angew. Chem. Int. Ed.*, 50 (2011) 1996–2013, <https://doi.org/10.1002/anie.201000463>.
51. M. Sleutel, J. Lutsko, A.E.S. Van Driessche, M.A. Duraín-Olivencia, D. Maes, Observing classical nucleation theory at work by monitoring phase transitions with molecular precision, *Nat. Commun.*, 5 (2014) 5598, <https://doi.org/10.1038/ncomms6598>.
52. T. Yamazaki, Y. Kimura, P.G. Vekilov, E. Furukawa, M. Shirai, H. Matsumoto, A.E.S. Van Driessche, K. Tsukamoto, Two types of amorphous protein particles facilitate crystal nucleation. *Proc. Nat. Ac. Sci. USA*, 114 (2017) 2154-2159, <https://doi.org/10.1073/pnas.1606948114>.
53. A.E.S. Van Driessche, N. Van Gerven, P.H.H. Bomans, R.R.M. Joosten, H. Friedrich, D. Gil-Carton, N.A.J.M. Sommerdijk, M. Sleutel, Molecular nucleation mechanisms and control strategies for crystal polymorph selection, *Nature*, 556 (2018) 89-94, <https://doi.org/10.1038/nature25971>.
54. S. Chung, S.H. Shin, C.R. Bertozzi, J.J. De Yoreo, Self-catalyzed growth of S layers via an amorphous-to-crystalline transition limited by folding kinetics, *Proc. Nat. Ac. Sci. USA*, 107 (2010) 16536–16541, <https://doi.org/10.1073/pnas.1008280107>.
55. L.R. Parent, E. Bakalis, A. Ramírez-Hernández, J.K. Kammeyer, C. Park, J. de Pablo, F. Zerbetto, J.P. Patterson, N.C. Gianneschi, Directly Observing Micelle Fusion and Growth in Solution by Liquid-Cell Transmission Electron Microscopy, *J. Am. Chem. Soc.*, 139 (47) (2017) 17140–17151, <https://doi.org/10.1021/jacs.7b09060>.
56. R.G. Alberstein, F.A. Tezcan, Observations of the birth of crystals, *Nature*, 556 (2018) 41-42, <https://doi.org/10.1038/d41586-018-03801-5>.

57. R. Demichelis, A. Schuitemaker, N.A. Garcia, K.B. Koziara, M. De La Pierre, P. Raiteri, J.D. Gale, Simulation of Crystallization of Biominerals, *Annu. Rev. Mater. Res.*, 48 (2018) 327–352, <https://doi.org/10.1146/annurev-matsci-070317-124327>.
58. S. Whitelam, Control of pathways and yields of protein crystallization through the interplay of nonspecific and specific attractions, *Phys. Rev. Lett.*, 105 (2010) 088102, <https://doi.org/10.1103/PhysRevLett.105.088102>.
59. G.C. Sosso, J. Chen, S.J. Cox, M. Fitzner, P. Pedevilla, A. Zen, A. Michaelides, Crystal Nucleation in Liquids: Open Questions and Future Challenges in Molecular Dynamics Simulations, *Chem. Rev.*, 116 (2016) 7078–7116, <https://doi.org/10.1021/acs.chemrev.5b00744>.
60. S. Toxvaerd, Molecular dynamics simulation of heterogeneous nucleation at a structureless solid surface, *J. Chem. Phys.*, 117 (2002) 10303-10310, <https://doi.org/10.1063/1.1519255>.
61. A. Cacciuto, S. Auer, D. Frenkel, Onset of heterogeneous crystal nucleation in colloidal suspensions, *Nature*, 428 (2004) 404-406, <https://doi.org/10.1038/nature02397>.
62. Y. Yang, S. Meng, Atomistic nature of NaCl nucleation at the solid-liquid interface, *J. Chem. Phys.*, 126 (2007) 044708, <https://doi.org/10.1063/1.2431363>.
63. E.B. Webb, G.S. Grest, D.R. Heine, Precursor Film Controlled Wetting of Pb on Cu, *Phys. Rev. Lett.*, 91 (2003) 236102, <https://doi.org/10.1103/PhysRevLett.91.236102>.
64. L. Gránásy, T. Pusztai, D. Saylor, J.A. Warren, Phase Field Theory of Heterogeneous Crystal Nucleation, *Phys. Rev. Lett.*, 98 (2007) 035703, <https://doi.org/10.1103/PhysRevLett.98.035703>.
65. S. Yamanaka, A. Shimosaka, Y. Shirakawa, J. Hidaka, Molecular dynamics simulations of the formation for NaCl cluster at the interface between the supersaturated solution and the substrate, *J. Nanopart. Res.*, 12 (2010) 831-839, <https://doi.org/10.1007/s11051-009-9713-z>.
66. H. Dashtian, H. Wang, M. Sahimi, Nucleation of Salt Crystals in Clay Minerals: Molecular Dynamics Simulation, *J. Phys. Chem. Lett.*, 8(14) (2017) 3166-3172, <https://doi.org/10.1021/acs.jpcllett.7b01306>.
67. D. Chakraborty, G.N. Patey, How Crystals Nucleate and Grow in Aqueous NaCl Solution, *J. Phys. Chem. Lett.*, 4(4) (2013) 573-578, <https://doi.org/10.1021/jz302065w>.
68. J.H. Tsai, M.L. Perrotta, A. Gugliuzza, F. Macedonio, L. Giorno, E. Drioli, K.-L. Tung, E. Tocci, Membrane-Assisted Crystallization: A Molecular View of NaCl Nucleation and Growth, *Appl. Sci.*, 8 (2018) 2145, <http://doi.org/doi:10.3390/app8112145>.

69. G. Lanaro, G.N. Patey, Molecular Dynamics Simulation of NaCl Dissolution, *J. Phys. Chem. B.*, 119(11) (2015) 4275-4283, <https://doi.org/10.1021/jp512358s>.
70. K. Kobayashi, Y. Liang, T. Sakka, T. Matsuoka, Molecular dynamics study of salt–solution interface: Solubility and surface charge of salt in water, *J. Chem. Phys.*, 140 (2014) 144705, <https://doi.org/10.1063/1.4870417>.
71. D. Chakraborty, G.N. Patey, Evidence that crystal nucleation in aqueous NaCl solution Occurs by the two-step mechanism, *Chem. Phys. Lett.*, 587 (2013) 25-29, <https://doi.org/10.1016/j.cplett.2013.09.054>.

Chapter 3

Materials and Strategies implemented to manufacture nanostructured membranes and related applications

3.1 Introduction

In the present research work were developed different methodologies for the design and preparation of nanostructured polymeric membranes. The application target were Membrane Distillation (MD) and Membrane Crystallization (MCr) technologies.

In this chapter, materials and strategies used for preparation, characterization and application of nanostructured functional membranes were described. Membranes were designed to enhance the performance of MD and MCr during the production of fresh water and recovery of minerals from high concentration saline solution.

3.2. Materials

In this work different kind of materials have been used to manufacture tailored membranes and we can subdivide them on the basis of the type of membrane produced.

3.2.1 Honeycomb membranes

To produce tailored honeycomb patterned membranes, materials used were:

- Polyethersulfone (PES, Radel A100NT, Solevey Solexis, Alpharetta, GA, USA), 0.5 wt % - 2 wt %.
- Dicloromethane (DCM, 99.5 %, Carlo Erba Reagents, Milan, Italy) at 99.5-98 wt %.
- Polyoxyethylene (20) sorbitan monolaurate (Tween 20, Mw = 1227.54, Sigma-Aldrich SRL, Milan, Italy); in a concentration from 10^{-5} to 10^{-3} M.
- Various alcohols with different chain length ($(\text{CH}_2)_n = 2-4\text{OH}$, Ethanol, n-Propanol, n-Butanol, 2-Propanol water content < 0.02 %, degree of purity of 99.5 %, Carlo Erba Reagents) in a concentration of 12 wt %.
- Viologen salt, in the class of Ionic Liquid Crystals (ILC): 1,1'-ditetradecyl-4,4'-dipyridinium [bis(trifluoromethanesulfonyl)amide (14bp14(Tf₂N)₂) synthesized and used

as surfactant for preparation of honeycomb membranes with an increasing ordered geometry (15 wt % with respect to amount of polymer).

3.2.2 Double honeycomb membranes: structure in the structure

Herein honeycomb made by PES was used like a sublayer, because was created a nanoporous coating onto the top surface using:

- Tetra-fluoroethylene (TFE) and 2,2,4-trifluoro-5-tri-fluoromethoxy-1,3-dioxol (TTF) with 60 mol % in TTF content (HYFLON AD 60, Solvay Specialty Polymers Italy) at 1.3 wt %.
- Methoxy-nonafluorobutane (HFE7100® 3M™ Novec) solvent.
- A polyamide textile (G. Crespi Srl, Italy) to achieve further inert mechanical support for honeycomb membranes.

At the same time commercial PVDF membrane (GVS SpA) was used for comparative desalination tests.

3.2.3 Nanocomposite 2D materials-PVDF membranes

Nanocomposite membranes were produced with traditional phase inversion technique using:

- Polyvinylidene fluoride (SOLEF ® 60/20 Solvay speciality polymers Italy) as polymer (11.7 wt %).
- Graphene powder, as nanofiller (Graphene nanoplatelets, powder hydrophobic, Merk, Italy) at different concentration percentage (0.5, 5, 10 wt %).
- Bismuth selenide (Bi_2Se_3 , Merk, Italy) gray compound of bismuth and selenium also known as bismuth (III) selenide. It was synthesized and then grinded reaching a powder diameter $< 60 \mu\text{m}$. It was used as nanofiller at a concentration percentage of 5 wt %.
- 1-Methyl-2-pyrrolidinone (NMP $\geq 99\%$, TECHNICAL, VWR chemicals, Italy) as solvent.
- 2-Propanolo $\geq 99.7\%$, AnalaR NORMAPUR® ACS, Reag. Ph. Eur. for analysis (VWR chemicals, Italy), used as solvent in coagulation bath after casting the solution.

In table 3.1 all materials used were reported with chemical structure, their most important features, operative conditions used to manipulate them and their usage for methodology of preparation and application desired.

Table 3.1. Synthetic representation of all materials used with related properties.

| Material | Chemical Structure | Concentration used in preparation | Properties | Role in membrane preparation | Membrane preparation methodology |
|---|---------------------|-----------------------------------|--|-----------------------------------|----------------------------------|
| <i>PES, Radel</i> ® | | 0.5 wt % 2 wt % | High thermal stability; High mechanical resistance.[1] | Polymer in Honeycomb membranes | Breath Figures |
| <i>DCM 99.5 %</i> | | 99.5 wt % 98 wt % | Low viscosity; Ability to dissolve many organic compounds. [2] | Solvent in Honeycomb membranes | Breath Figures |
| <i>Tween 20</i> | | $10^{-3} - 10^{-5}$ M | Non-ionic; Water-soluble; Resistant to PH variations. [3] | Surfactant in Honeycomb membranes | Breath Figures |
| <i>Ethanol</i> <i>n-Propanol</i> <i>n- Butanol</i> <i>2-Propanol</i> | $(CH_2)_n - 2-4 OH$ | 12 wt % | Miscibility in water; High boiling point. [2] | Surfactant in Honeycomb membranes | Breath Figures |
| <i>(14bp14(Tf₂N)₂)</i> | | 15 wt % | Cationic head able to interact with droplet in water uptake (Breath Figures). [4] | Surfactant in Honeycomb membranes | Breath Figures |
| <i>HYFLON AD 60</i> ® | | 1.3 wt % | High temperature stability; Low thermal conductivity; High hydrophobicity. [4] | Polymer in nanocoating | Breath Figures |

| | | | | | |
|--|---------------|-------------------------------|--|--|-------------------------|
| HFE7100 ® 3M™ Novec | $C_4F_9OCH_3$ | 99.7 wt % | Thermal stability; Low toxicity. [5] | Solvent in nanocoating | Breath Figures |
| Polyamide textile | | - | High mechanical resistance; High resistance to organic solvents. [6] | Support in Honeycomb membranes | Breath Figures |
| PVDF SOLEF® 60/20 | | 11.7 wt % | High chemical resistance; High solubility in polar solvents; Thermal applicability range: -40 °C / 150 °C. [7] | Polymer in 2D nanocomposite membranes | Dry/Wet Phase Inversion |
| Graphene nanoplatelets, powder hydrophobic | | 0.5 wt % 5 wt % 10 wt % | Thin; Light; Flexible; High resistance to temperature and pH. [8] | Nanofiller in 2D nanocomposite membranes | Dry/Wet Phase Inversion |
| Bismuth Selenide | Bi_2Se_3 | 5 wt % | Thermoelectric material; Topological protected surface states. [9] | Nanofiller in 2D nanocomposite membranes | Dry/Wet Phase Inversion |
| NMP ≥99% | | 88.3 wt % | High solvent power; High purity level. [10] | Solvent in 2D nanocomposite membranes | Dry/Wet Phase Inversion |
| 2-Propanolo ≥99.7%, AnalaR NORMAPUR® ACS | | - | High purity level; Optimum for its using as coagulation bath. [11] | Solvent for coagulation bath | Dry/Wet Phase Inversion |

3.3 Several approaches for preparation of different kind of membranes

In these studies, different are the approaches used to prepare polymeric functionalized membranes. In particular Breath Figures as innovative manufacturing procedure for ordered nanostructure was used in the first part of the work, then the attention was focused on traditional phase inversion (dry/wet) method, in order to achieve nanocomposite membranes with 2D nanomaterials blended in polymer matrix. They will be described in detail in the next paragraphs.

3.3.1 Honeycomb PES membrane preparation

To prepare honeycomb patterned membranes, at first, the polymer PES was dissolved in the solvent DCM, where Tween 20, and alcohols at different ratios were added, in order to identify difference in structural order, and in order to improve the hydrophobic/hydrophilic balance through the establishment of fruitful interactions.

Then, the choice of the surfactant has fallen on another typology of materials: viologen salts of ionic liquid crystals (ICL): with a cationic head and chains of different length [12]. It was synthesized and characterized according to the protocol described in literature [13] by G. Casella et al. group from ITM-CNR of Padova, Italy [14]. Briefly, 5.00 g (32 mmol) of bipyridine were refluxed at 82 °C in 50 mL of acetonitrile with a 2.5:1 excess (25 mL) of 1-bromotetradecane for 24 h. A yellow precipitate, [14bp14][Br₂], was formed. The precipitate was filtered, washed with cold acetone, and then recrystallized from water/acetone 15:85 v/v with a yield of 85%. Successively, 20 g (28 mmol) of [14bp14][Br₂] were dissolved in 40 mL of methanol; then 40 mL of a methanol solution containing 24 g (84 mmol) of LiTf₂N were slowly added and left to react under stirring for 4 h. The solvent was removed under vacuum and a white precipitate was formed after adding water to the flask. The white precipitate was then filtered and washed with water until the complete removal of the halide ions (essay with acidic solution of silver nitrate) and dried under vacuum in presence of CaCl₂ with a yield of 85%. This made it possible to improve the hydrophilic/hydrophobic balance and to create significantly more ordered geometries, which are described in the experimental session (Chapter 4). The final choice was 14bp14(Tf₂N)₂.

The specific technique that was used for preparing Honeycomb membranes was Breath Figures, already described in the previous chapter. It mimics what happen in nature when water vapor droplets approach cold surfaces. Specifically, condensing water droplets work

as pore builders through the polymeric solution leading to the formation of well-defined 3D polymeric architectures where pores are packed each other in honeycomb geometries. In the first part of the work, this kind of membranes were prepared from mixtures of polymer PES and surfactant Tween20 and alcohol at different chain length (mentioned before) in several concentration percentage.

Exactly the clear dopes were placed in clean and dried stainless steel supports, having an area of around 4 cm² located inside a pre-equilibrated box at 20 °C and under a partial pressure of water vapor of 17.54 mmHg until the films were formed. The viscosity of the various polymer dopes was measured at 20 °C by a capillary rheometer ($\eta = 0.00243$ cst/s). In the second and innovative part of the work, PES was used in addition with the viologen salt 14bp14(Tf₂N)₂ under flux of humid air. The viologen salt was dissolved in DCM. Then, the polymer (PES at 0.5 wt%) was added into the homogenous dope and the mixture was alternatively stirred and sonicated at 20 °C for 24 h. The solution was poured in a stainless steel with an area of around 65 cm² and exposed to humid air inside a chamber with controlled atmosphere (T, 25 °C; RH, 70%) until complete formation of the honeycomb polymeric film (Figure 3.1). Self-standing and polyamide-supported membranes were prepared according to the same procedure.

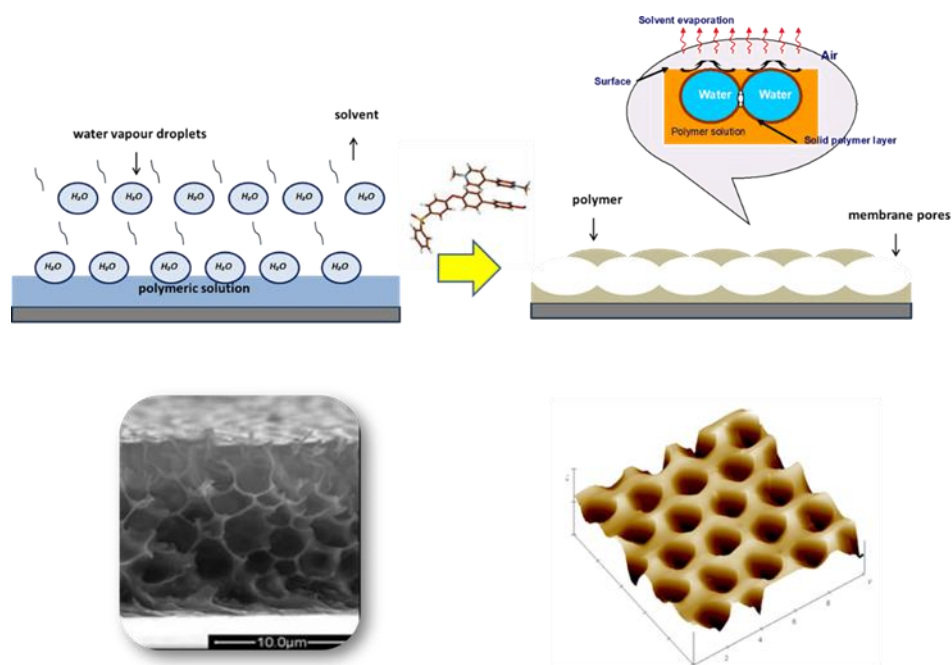


Figure 3.1. Schematic representation of Breath Figures methodology and final result of honeycomb geometries in membranes structure.

3.3.2 Structure in the structure: a new porous nanofilm of HYFLON AD

The basic idea in this research was to realize nanostructured membranes by combining morphology and chemistry in a unique volumetric space. The per-fluorinated polymer HYFLON AD, was used to generate a suspended honeycomb nanofilm onto the top surface of the PES honeycomb membrane. Hyflon AD was dissolved at 1.3 wt % in HFE7100 under magnetic stirring (20 °C for 24 h). The honeycomb PES membrane was prepared as previously discussed, therefore, it was immersed sequentially for 5 min in ethanol, water and HYFLON AD solutions cooled at 4 °C, respectively. Then, the membrane was again exposed to humid air inside the chamber at 25 °C and 70% of relative humidity for 10 min. A porous nanofilm with a thickness of 80 ± 5 nm was uniformly generated and suspended onto the PES honeycomb pattern (Figure 3.2).

To produce the active nanofilm, the material HYFLON AD, was used in combination with Ethanol (99.5%, Carlo Erba Reagents,) ultra-pure water (filtered by USF ELGA plant) to control wetting properties during formation of the tiny hydrophobic membrane with an estimated thickness of 80 ± 5 nm.

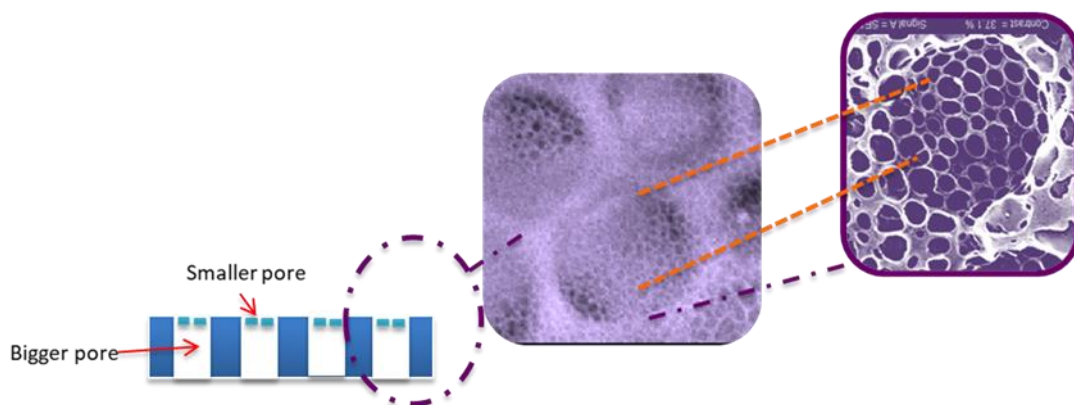


Figure 3.2. HYFLON AD nanofilm formation to create a superstructure onto PES top surface with smaller pores.

3.3.3 2D nanomaterials-PVDF composite membranes preparation: dry/wet phase inversion

A number of methods can be used to achieve phase inversion. Among these, the dry–wet phase inversion technique and thermally induced phase separation (TIPS) are the most commonly used in membrane manufacturing. The dry–wet phase inversion technique (Figure 3.3), also called the Loeb-Sourirajan technique, was used by Loeb and Sourirajan in their development of the first cellulose acetate membrane for seawater desalination [15]. In this method, a polymer solution is prepared by mixing polymer and solvent (sometimes even

non solvent). The solution is then cast on a suitable surface by a doctor blade to a precalculated thickness. After a partial evaporation of the solvent, the cast film is immersed in a non solvent medium called a gelation bath. Due to a sequence of two desolvation steps, i.e., evaporation of the solvent and solvent–non solvent exchange in the gelation bath, solidification of the polymer film takes place. It is desirable to choose a solvent of strong dissolving power with a high volatility. During the first step of desolvation by solvent evaporation, a thin skin layer of solid polymer is formed instantly at the top of the cast film due to the loss of solvent. In the solvent– non solvent exchange process that follows, the non solvent diffuses into the polymer solution film through the thin solid layer while the solvent diffuses out.

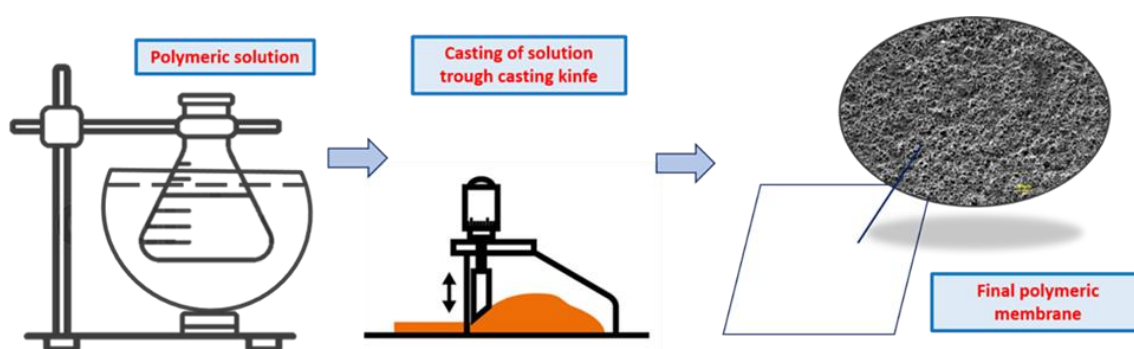


Figure 3.3. Schematic illustration and representation of dry/wet phase inversion method.

Herein so, at first 2D nanofiller were introduced in a partial amount of solvent under magnetic stirring at room temperature, left for 10-15 minutes. Then, it was transferred in a sonication bath at a temperature of 80°C for 4 hours, to allow perfect dispersion of powder inside solvent. When a homogenous solution was obtained, it was left to cool, measuring temperature through a thermometer, in order to have a T°C of 25°-30° C. In this way it was possible to add at the solution, the polymer (PVDF) under mechanical stirring, and with the immersion of solution in an oil bath at a temperature of 30°C. The remaining amount of solvent was added in order to leave the solution stirring for 24 hours at this temperature. The day before casting the polymeric films, the mechanical stirrer was switched off in order to remove bubbles air in the solution. When it was clear that they were gone away (mainly causes of structural defects), the polymeric solution was casted with a casting knife, a specific Doctor Blade (Doctor Blade Applicator S/S Res 180 mm, Elcometer®, Italy) with a gap precision of 250 µm. The solution was casted onto glass substrates and then transferred in an IPA 100 wt % coagulation bath for 15-20 minutes until the complete formation of

polymeric membrane. Then membranes were cleaned two times in distilled pure water baths, in order to achieve complete removing of the solvent, and later dried.

The drying of membranes was very precise: at first, they were dried under paper sheets for few minutes to remove the water excess, then, we attached membranes on glass substrates using paper scotch membranes on edges. The complete drying of membranes happened in a hoven at 30°C for 1 hour and half. This is the procedure followed for achieving the complete polymeric PVDF-composite membrane by dry/wet phase inversion.

The nanofillers used to prepare nanocomposite membranes with 2D materials were: graphene hydrophobic nanoplatelets at different concentration percentage: 0.5, 5 and 10 wt % (compared with pristine PVDF). Furthermore, as we said before, we performed also MCr experiments with the using of bismuth selenite (Bi_2Se_3), a gray compound of bismuth and selenium also known as bismuth (III) selenide, and it is a semiconductor and a thermoelectric material [9]. Acting as topological insulator, it has been explored in research their potential in photonics, but, in the last year it was used for the first time to assist MCr technology reaching interesting results [16, 17].

Then after grinding Bi_2Se_3 crystals, the powder form was blended in matrix PVDF membrane at a concentration percentage of 5 wt %, exactly the same of graphene with which we achieved most interesting results.

3.4 Characterization of solutions for preparing Honeycomb membranes

3.4.1 Surface Tension

Surface tension is a physical force in the surface of the liquid that arises as a result of the atoms of the liquid pulling their neighbors in all directions. In the first part of the work, we explored surfactant concentration effect (Tween 20) on honeycomb packed geometries and the surface free tensions of the solutions were estimated according to the pendant drop method (Figure 3.4) by using a micro-syringe with an automatic dispenser and a digital camera to capture images (CAM 200-KSV Instrument Ltd., Helsinki, Finland). The parameters of solubility were calculated according to the following equations [18]:

$$e_{coh} = \left(\frac{\gamma_s}{0.75} \right), \delta = (e_{coh})^{1/2} \quad (3.1)$$

where e_{coh} (106 J/m^3) is the energy cohesion density and δ ($103 \text{ J}^{1/2}/\text{m}^{3/2}$) the solubility parameters. Interfacial tensions between water and dichloromethane solutions containing polymer at 2.0 wt % and Tween20, within a range of concentration from 0 to 10^{-3} M , were also measured by pendant drop method at $20 \text{ }^\circ\text{C}$. Each solution was poured in the quartz glass cuvette, and then a water drop was injected into the solution by using a syringe connected to an automatically liquid volume dispenser. The interfacial tensions were measured at 0 and 60 s after water injection. The average interfacial tension values were calculated from five measurement results with a standard deviation that decreases from ± 0.23 to ± 0.13 with rising surfactant content into the mixture [19]. The same methodology of pendant drop measurements were implemented to evaluate then, effects of the viologen salt on water droplets rearrangement.

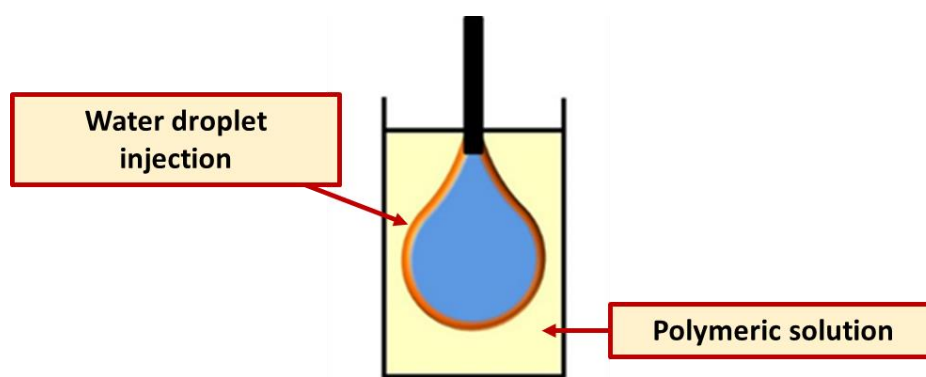


Figure 3.4. Illustrative representation of Pendant Drop method, used for evaluating surface free tension of polymeric solution.

Experiments in CD_2Cl_2 solutions were carried out to investigate the interaction between 14bp14(Tf_2N)₂ and polysulfone by using ^1H NMR (Bruker AVANCE III 500, 500.13 MHz ^1H) equipped with a 5 mm z-gradient BBI probe.

3.4.2 Dynamics Light Scattering (DLS) for aggregation state

In the first part of the work (where honeycomb patterned membranes have been produced with surfactant Tween 20 in different concentrations and with alcohol at different chain length) changes in the aggregation state were evaluated by Dynamic Light Scattering (DLS). These measurements were carried out by using a 90 plus Particle Size Analyzer (Malvern Instruments Ltd., Worcestershire, UK).

Dynamic light scattering (DLS) is a technique in physics that can be used to determine the size distribution profile of small particles in suspension or of polymers in solution [20]. In the scope of DLS, temporal fluctuations are usually analyzed by means of the intensity or

photon auto-correlation function (also known as photon correlation spectroscopy or quasi-elastic light scattering). In the time domain analysis, the autocorrelation function (ACF) usually decays starting from zero delay time, and faster dynamics due to smaller particles lead to faster decorrelation of scattered intensity trace. It has been shown that the intensity ACF is the Fourier transformation of the power spectrum, and therefore the DLS measurements can be equally well performed in the spectral domain. DLS can also be used to probe the behavior of complex fluids such as concentrated polymer solutions. The DLS principle uses the thermal energy of suspended particles (Brownian Motion) to determine their size. The suspended sample is irradiated by a laser and the light is dispersed in a direction detected with very small time resolutions. From the fluctuation of the intensity of the dispersed light, the mobility of the particles can be calculated. Therefore, thanks to the Stokes-Einstein formula (for diffusion of spherical particles through a liquid with low Reynolds number), its dimensions can be calculated as follow:

$$D = \frac{K_b T}{6\pi\eta r} \quad (3.2)$$

Where D is diffusion constant, k_B is Boltzmann's constant, T is the absolute temperature, η is the dynamic viscosity, and r is the radius of the spherical particle.

3.4.3 Kinematic Viscosity

The viscosity of a fluid is a measure of its resistance to deformation at a given rate. In reality, there are several different terms that come under the heading of viscosity [21]. These terms are derived from how the viscosity is measured. When people talk about viscosity, they are talking about one of two things: kinematic viscosity or dynamic viscosity. One way is to measure a fluid's resistance to flow when an external force is applied: this is dynamic viscosity, while kinematic viscosity is the measure of the inherent resistance of a fluid to flow when no external force is exerted, except gravity. It is the ratio of the dynamic viscosity to its density, a force independent quantity. It is given by following equation:

$$\nu = \frac{\eta}{\rho} \quad (3.3)$$

Where ν is the kinematic viscosity, η is the dynamic viscosity, and ρ is the fluid density.

In this work the behavior of the solutions with increasing content of surfactant has been examined when coming in contact with humid air, while kinetics and thermodynamic aspects have been analyzed as well. As the concentration of the surfactant increases, a local increase in gelation comes through the solution, resulting in an increased kinematic viscosity. Results are reported in Chapter 4.

3.5 Characterization of 2D materials used for preparing PVDF nanocomposite membranes, by X-ray photoelectron spectroscopy (XPS)

The possibility to enhance water sequestration during MCr with the using of 2D materials as nanofiller blended in PVDF membranes, was evaluated by XPS (X-ray photoelectron spectroscopy) measurements. They were carried out on surfaces of graphene, epitaxially grown on Ni (111) and Bi₂Se₃ single crystal (exfoliated in situ by micromechanical cleavage) exposed to water at room temperature.

X-ray photoelectron spectroscopy (XPS) is a surface-sensitive quantitative spectroscopic technique that measures the elemental composition at the parts per thousand range, empirical formula, chemical state and electronic state of the elements that exist within a material. Put more simply, XPS is a useful measurement technique because it not only shows what elements are within a film but also what other elements they are bonded to. The operating principle is the following: the sample is irradiated with a monochromatic X-ray source. Photons enter the material and undergo various interactions, including the photoelectric effect and the Auger emission. In both cases an electron is ejected from the material with a kinetic energy linked to its binding energy. Measuring the kinetic energy of the ejected electron, one goes back to its binding energy, indicative of the chemical element of interest. For the study of graphene nanosheets and other kinds of 2D materials, the procedure was developed by Politano et al. [22] where by means of a combination of surface-science spectroscopies and theory, they investigated the mechanisms ruling the catalytic role of epitaxial graphene (Gr) grown on transition-metal substrates for the production of hydrogen from water. Water decomposition at the Gr/metal interface at room temperature provided a hydrogenated Gr sheet, which was buckled and decoupled from the metal substrate. They evaluated the performance of Gr/metal interface as a hydrogen storage medium, with a storage density in the Gr sheet comparable with state-of-the-art materials.

3.6 Membrane morphology characterization

After preparing the samples, the subsequent step was to characterize them in order to validate structure properties relationship, for application in water desalination (MD and MCr).

The characterization tests performed were:

- Molecular structure by H- Nuclear Magnetic Resonance spectroscopy (H-NMR)
- Wettability by Contact angle measurement
- Morphology by Scanning electron microscopy (SEM)
- Roughness and topography by Atomic force microscopy (AFM)
- Thickness by micrometer
- Pore size and pore size distribution (by porometer instrument for PVDF-2D composite membranes and Image J software for Honeycomb membranes)
- Overall porosity, ϵ (-)
- Water Vapor Transmission Rate, WVTR ($\text{gm}^{-2}\text{day}^{-1}$)
- Mechanical strength, R_m (Nmm^{-2})
- NaCl crystals analysis by Optical microscopy
- Surface tension γ - (mjm^{-2}), for 2D-PVDF based membranes

In the next session each characterization will be described in detail.

3.6.1 Molecular structure by H- Nuclear Magnetic Resonance Spectroscopy (H-NMR)

Nuclear Magnetic Resonance (NMR) spectroscopy is an instrumental analytical technique which allows to obtain detailed information on the structure of the molecules observing the behavior of atomic nuclei in a magnetic field. After immersing the in a strong field magnetic, the absorption of a radio frequency radiation (from 100 to 1000 MHz) is measured causing nuclear spin transitions in particular atoms such as ^1H or ^{13}C . Proton nuclear magnetic resonance (H-NMR) is the application of nuclear magnetic resonance in NMR spectroscopy with respect to hydrogen-1 nuclei within the molecules of a substance, in order to determine the structure of its molecules [23]. In samples where natural hydrogen (H) is used, practically all the hydrogen consists of the isotope ^1H (hydrogen-1; i.e. having a proton for a nucleus). Simple NMR spectra are recorded in solution, and solvent protons must not be allowed to interfere. In fact deuterated (deuterium = ^2H , often symbolized as D) solvents especially for use in NMR are preferred. In this work deuterated dichloromethane (CD_2Cl_2) was used. Proton NMR spectra of most organic compounds are characterized by chemical shifts in the

range +14 to -4 ppm and by spin-spin coupling between protons. The integration curve for each proton reflects the abundance of the individual protons.

Chemical shift values, symbolized by δ , are not precise, but typical they are to be therefore regarded mainly as a reference and deviations are in ± 0.2 ppm range, sometimes more. The exact value of chemical shift depends on molecular structure and the solvent, temperature, magnetic field in which the spectrum is being recorded and other neighboring functional groups. Hydrogen nuclei are sensitive to the hybridization of the atom to which the hydrogen atom is attached and to electronic effects. Nuclei tend to be deshielded by groups which withdraw electron density. Deshielded nuclei resonate at higher δ values, whereas shielded nuclei resonate at lower δ values. In this work H-NMR was used to evaluate interaction among the viologen salt $(14\text{bp}14(\text{Tf}_2\text{N})_2$ and PES polymer, evaluating probable shifts in spectra achieved.

3.6.2 Wettability by contact angle measurements

The contact angle is generally used to measure hydrophilicity / hydrophobicity degree of membranes. The contact angle measurement allows to evaluate the interaction of a liquid with a surface, and it is a function of both surface tension and free energy of substrate surface. Membranes are generally considered hydrophilic if the values of contact angle between surface and water are less than 90° , while it is considered hydrophobic for values above 90° [24].

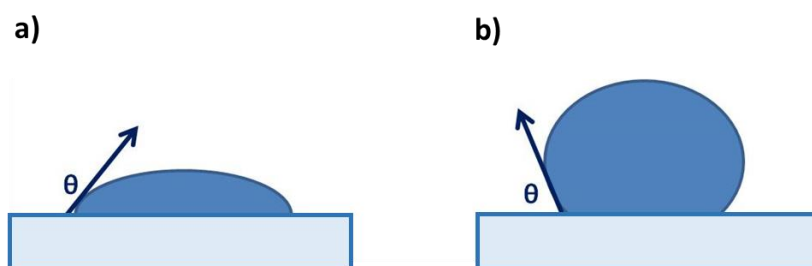


Figure 3.5. Illustration of a water droplet deposition on a solid surface for a) hydrophilic and b) hydrophobic membranes.

Contact angle is an index of wettability of solid surfaces and so of the polymeric membranes. In fact, if the wettability is high, the contact angle is low, while, if the wettability is low, the contact angle will be high. Since by definition the contact angle is the angle formed between two of the interfaces of a three-phase system, of which the membrane is the solid phase, the

water is the liquid phase, and the atmosphere is that of vapor, we can say that the model is described quantitatively by Young's equation:

$$\theta = \gamma_{sv} - \gamma_{sl} - \cos\theta \quad (3.4)$$

where γ_{sv} is the solid / vapor interfacial tension, γ_{sl} is the solid / liquid interfacial tension, while θ is the angle value at the solid / liquid / vapor interface [25].

Investigation of resistance to wetting from pure water and salt solutions was done by measuring the contact angle value with time, according to sessile drop method (Cam 200 KSV instruments, LTD). The mechanism is based on the automatic measurement by software, of the contact angle formed by a drop of water with the surface of membrane. The measurement of the contact angle value is allowed through an automatic detection system (by camera) which allows to capture an image of the drop of water (and of its evolution over time) when the instrument carries out the measurement. We used pure distillate water and NaCl solutions to detect contact angle. In particular solutions of NaCl of 5 mM for honeycomb membranes and NaCl of 5.3 M for 2D-PVDF based membranes, were used. They were the molar concentration respectively used for MD (honeycomb) and MCr (2D nanocomposite-PVDF) tests.

3.6.3 Morphology by Scanning Electron Microscopy (SEM)

In order to analyze the morphology of prepared membranes it is very important to use electron microscopy techniques. In this PhD thesis work, a scanning electron microscope (SEM) was used, model EVO MA10 (Zeiss). The objective was to analyze surfaces and also cross sections of the prepared membranes, in order to identify morphological structures and their changes when the different materials and different approaches were used in the two methods. To briefly describe how a SEM works, according to quantum theory, an electron moving at high speed behaves like an electromagnetic wave with a wavelength inversely proportional to the speed of the electron. By accelerating the electrons with a suitable potential difference, they can assume a wavelength that is within that of De Broglie, in the order of nanometers, and therefore able to detect morphological aspects of dimensions comparable to their wavelength:

$$\lambda = \frac{h}{mv} \quad (3.5)$$

where h is the Plank constant, m the electron mass, and v its speed.

SEM belongs to this category of microscopes and is usually based on the analysis of backscattered electrons from the sample. Electrons are emitted by a filament (usually tungsten or lantad hexaboride) due to the thermionic effect. Photoemess electrons are low energy and in order to have a shorter wavelength are accelerated by a potential difference of about 0.3-30 KeV; in this way their speed increases, decreasing their wavelength.

$$\lambda = \frac{12,4}{\sqrt{V}} \quad (3.6)$$

Where V is the applied potential, and λ the wavelength produced.

Samples before being analyzed by SEM, were metallized with gold foil in order to make them conductive and, in the case of section, samples were prepared by fracturing them in liquid nitrogen in order to obtain a precise cut.

The SEM works through a lens system that, placed between the source and the sample, focuses the electron beam; some bobbins deflect it so as to scan the surface of the sample. The image is reconstructed by analyzing the secondary electrons emitted by the surface, which are collected and transformed into a video signal.

From the moment the electron beam hits the surface of the sample, the electrons of the beam begin to interact with the nuclei and the electronic clouds of the atoms of which the sample is made, through two main mechanisms:

- Elastic diffusion
- Anaelastic diffusion

The result of these two processes is the production of a remarkable variety of signals: seconded electrons, backscattered electrons, absorbed electrons, transmitted electrons, Auger electrons, electron hole pairs, electromagnetic radiation (in the UV-IR spectrum) and X radiation.

Instant by instant, the secondary electrons emitted in a specific direction are analyzed by some photomultipliers and, the photomultiplied electron beam is sent following the scanning of the surface on a fluorescence monitor. Secondary electrons, are low energy electrons (up to few tens of eV), coming from the most superficial portion of the sample (a few nm). The main property of this type of signal is that of being strongly controlled by the morphology of the sample, therefore the resulting image will be the black and white image of the area affected by the scanning of the beam, in which the contrast of the shades of gray will set

highlighting the three-dimensional aspect of the sample under examination. Clearly the entire system is in Ultra-High-Vacuum, to prevent the electron beam from interfering with the atmosphere inside the microscope [26]. In this research work scanning electronic microscopy was one of the most important characterization technique used to observe very fast when structural properties changed for the several kind of membranes studied. A lot of pictures were captured at different magnification, from 500X to 20000X, in order to have a clear and precise idea both in totality and in particular way.

3.6.4 Roughness and topography by Atomic Force Microscopy (AFM)

Atomic force microscopy (AFM) or scanning force microscopy (SFM) is a very-high-resolution type of scanning probe microscopy (SPM), with demonstrated resolution on the order of fractions of a nanometer, more than 1000 times better than the optical diffraction limit [27].

In this work it was in particular employed to detect roughness and particular membrane honeycomb topography using AFM, Nanoscope III, in tapping mode.

The atomic force microscope consists of a cantilever at the end of which is mounted a sharp tip (tip), typically composed of silicon or silicon nitride, which has a radius of curvature of the order of nanometers.

The investigating tip is placed close to the surface of the sample to be scanned. The van der Waals force that acts between the tip and the sample, causes a deflection of the cantilever (whose elastic constant is known), according to Hooke's law. The deflection of the lever is measured using a laser point reflected from the top of the cantilever to a matrix of photodiodes. However, a laser detection system can be expensive and cumbersome; an alternative method to determine cantilever deflection is to use piezoresistive AFM probes. These probes are manufactured with piezoresistive elements that act as resistance strain gauges. Deformations of the probe of the atomic force microscope due to deflection can be measured using a Wheatstone bridge, but this method is not as accurate as the laser deflection method.

If the tip were explored at a constant height, there would be a risk that it could collide with the surface, damaging it. Consequently, in most cases a feedback mechanism is used to adjust the distance between the tip and the sample in order to keep the force acting between them, constant. Generally, the sample is placed on a piezoelectric tube, which can move it in a perpendicular direction (z direction) to maintain a constant force and in the plane (x and y

directions) to analyze its surface. The resulting map $s(x, y)$ represents the topography of the sample surface.

The atomic force microscope has several advantages compared to the electron microscope: unlike the latter, which provides a two-dimensional projection or a two-dimensional image of a sample, the AFM produces a real three-dimensional profile of the surface; furthermore, the samples analyzed by an atomic interaction microscope (AFM) do not require any special treatment (metallization and graphitization) which could modify or destroy the sample irretrievably.

While an electron microscope for a correct operation requires an expensive vacuum environment, most of the operating modes of the atomic interaction microscope (AFM) work perfectly in the normal environment or even in a liquid environment. This makes it an excellent tool for the study of biological macromolecules and living organisms, but also for detecting structure of materials on nanometric scale.

3.6.5 Thickness

Membrane thickness, a crucial parameter that can affect performances membranes in terms of fluxes, was measured using a digital micrometer (Mahr 0-25). This tool allows to measure the thickness with an accuracy up to the millionth of a meter. The operation of the micrometer is based on the advancement of a screw that pushes a movable cylinder against a fixed one, between which the object to be measured is placed. The membrane is then placed between the spindle and the anvil, taking care to handle it with extreme accuracy. Before starting the measurements, it is necessary to reset the instrument. The rotating drum is set to "0" and the instrument is reset to zero by pressing the "9" button; so the drum is rotated to "N" and the measurement can start. A manual adapter slides and the spindle moves towards the anvil. The measured thickness value is read on the digital display with which the micrometer is equipped. With this technique, the entire thickness of the membrane is measured, not only that of the surface selective layer. We have done different measurements, taking care to capture several values, in order to have not only a medium value but a representative and general morphological parameter of all area of manufactured membranes.

3.6.6 Pore size and pore size distribution

In membrane technology values of pore dimension and also the pore size distribution are very distinctive parameters to classify membranes for their application. Several can be the

methods to evaluate this morphological element but the most used is that which works by a capillary flow porometry. We used this methodology to evaluate pore size of 2D-PVDF composite membranes, while for honeycomb pore size, surface porosity and pores distribution were characterized from SEM images by using Image J, version 1.73 software.

- **Capillary flow porometry:** Capillary flow porometry, also known as the liquid ejection technique, uses the simple principle of gas pressure to force a wetting liquid out of the interconnected pores present in a sample. The pressure at which the pores are emptied is inversely proportional to their size, therefore large pores need a lower pressure than the smaller ones. The largest pore to be emptied (at the lowest pressure at which the flow can be detected) defines the so-called "bubble point". After all the pores have been emptied (up to the maximum pressure obtainable) during the "wetting" measurement (ie when the membrane is still impregnated with the wetting liquid), a second "dry" analysis is performed (ie when the membrane is dry in following removal of the wetting liquid) on the same sample. From the complete set of data, different parameters can be calculated, including pore size related to the flow and pore size distributions [28, 29]. In this work the instrument used was a capillary flow porometer, model CFP-1500-AEXL, series No. 03072001- 377 (Porous Material Inc.). Membrane samples were first cut, then immersed in a wetting liquid with a low surface tension (Fluorinet FC-40 (Santa Cruz Biotechnology)) for at about 30 minutes and then put in a cell with an area of 2,355 cm² to carry out the measurements.
- **DFT (Density functional theory)** [30]: a method like the Density Functional Theory (DFT) provide not only a microscopic model of adsorption but also a more realistic description of the thermodynamic properties of the pore fluid. These theory, which is based on statistical mechanics, connect macroscopic properties to the molecular behavior. Therefore, in order to achieve a more realistic description of adsorption phenomena and an accurate and comprehensive pore size analysis, DFT of inhomogeneous fluids bridge the gap between the molecular level and macroscopic approaches are needed. This method allows to calculate equilibrium density profiles of a fluid adsorbed on surfaces and in pores from which properties such as the adsorption/desorption isotherm, heats of adsorption, neutron scattering patterns and transport properties for model systems can be derived. DFT calculations of the interaction energy of simple model structures were run as well. The ωB97xd functional was used to account for dispersion interactions and the triple-ζ Gaussian basis set 6-311G**. Also, the PCM model was used for dichloromethane in order to

include long-range solvent effects for the estimation of interaction energies [31]. Calculations were run with the Gaussian09 software package.

- **Image J software:** ImageJ is a digital image processing computer program, released in the public domain, based on Sun-Java; developed by the National Institutes of Health of the United States [32]. ImageJ can display, edit, analyze, process, save, and print images at gray (8 bit, 16 bit and 32 bit) and color (8 bit and 24 bit) levels. It can read several image formats, and can calculate the area and statistics of pixel values in user-defined selections and segmented objects based on intensity thresholds. It can also measure distances and angles. It can create density histograms and draw profile lines (between defined points). It allows a series of function that make it suitable for analysis in several research field as biology, for cell count, mathematics to perform calculation functions and, in our case, to evaluate features of porosity and pore size of honeycomb membranes produced.

3.6.7 Overall porosity

Membranes of PVDF containing graphene and other 2D materials, were characterized by measurement of overall porosity (ε_m). It can be defined as the ratio between the volume occupied by the voids v divided by the total volume of membranes. Porosity degree of tailored membranes produced was measured using the wet / dry gravimetric method (wet / dry) [33].

Three samples for each kind of membranes, of same area (1,57 cm²) were prepared, weighed with an analytical balance noting their dry weight, and once weighed, samples were placed in falcon tubes containing kerosene, whose density is 0.78 g/cm³. After 30 minutes, samples were quickly buffered from excess liquid and weighed again, obtaining their wet weight. Based on the difference between weight of the dry and wet membrane, the porosity expressed as a percentage, was calculated according to the following equation:

$$\varepsilon = \left(1 - \frac{(V_m - V_l)}{V_m} \right) \cdot 100 \quad (3.7)$$

Where

- V_m is the membrane volume (sample area (cm²) per thickness (cm))
- V_l in the liquid volume (weight membrane wet minus weight membrane dry (g)).

3.6.8 Water vapor transmission rate (WVTR)

For honeycomb membranes, the water vapor transmission rate (WVTR) was tested at 25 °C according to the cup-right method (ASTM E96B) [34, 35]. Water Vapor Transmission Rate (WVTR), is a measure of the passage of water vapor through a substance. it is also called and known as “breathability”. With the cup method, a cup is filled with distilled water leaving a small gap (0.75" to 0.25") of air space between the specimen and the water. The cup is then sealed to prevent vapor loss except through the test sample. An initial weight is taken of the apparatus and then periodically weighed over time until results become linear. Caution must be used to assure that all weight loss is due to water vapor transmission through the specimen. 24 hours was the time employed to evaluate WVTR to humid air of tailor-made honeycomb membranes.

3.6.9 Mechanical strength

Resistance of membranes to breakage was evaluated by carrying out mechanical tests using the Zwick / Roell Z 2.5 dynamometer. This instrument calculates the Young's modulus of the membranes and measures the breaking load. The Young's modulus (or modulus of elasticity) can be defined by Hooke's law [36]:

$$E = \frac{\sigma}{\epsilon} \quad (3.8)$$

Where (σ), is the stress applied to a material along the X axis, while (ϵ) is the lengthening that the material undergoes along the same axis. For each membrane, three samples were cut with a length of at least 5 cm and locked between the two terminals of the instrument. Membrane under examination is progressively lengthened until it breaks. The resulting graph shows the Young's modulus indicating the stiffness of the material and its elongation capacity. The higher the Young's modulus, the greater the mechanical strength of the material.

3.6.10 Optical microscopy for NaCl crystals analysis in Membrane Crystallization Technology

As previously mentioned, the final part of the work was focused on the study of the behavior of 2D-PVDF based membranes in Membrane- assisted Crystallization. In order to observe nuclei and crystals formation, optical microscopy (Nikon Eclipse LV100ND) is the technique used to detect them.

The optical microscope is a type of microscope that uses light with wavelengths from the near infrared to ultraviolet, covering the entire visible spectrum.

The optical microscope is the most widely used diagnostic tool in medical and biological sciences; independently of the specific technical characteristics, all optical microscopes are composed by a mechanical, an optical and a lighting apparatus. In optical microscopy the simplest scheme that can be drawn up is the following:

- Object to be observed
- Objective lens
- Real picture
- Ocular lens
- Virtual image

The two situations are essentially combined: the objective lens creates an image real that becomes "object" for the ocular lens. From this, it is created a virtual and enlarged image, captured as a photo.

In our case, we took several photos of NaCl crystals from the moment they form, for three consecutive times, in order to measure crystals size and evaluate kinetics growth parameter. This characterization will be discussed in detail in next session.

3.6.11 Surface Tension analysis for 2D-PVDF based membranes, through Van Oss-Chaudhury approach

The Van Oss-Chaudhury-Good (VCG) theory of wettability is used to understand the role of hydrophilic and hydrophobic interfacial forces in promoting heterogeneous nucleation from solution-phase precipitation processes. The interfacial free energy of nucleation for heterogeneous processes is simply related to the relative nucleus-solvent and nucleus surface areas and their individual interfacial free energies. VCG theory is used to extend this relationship to the individual surface free energies of the isolated phases. Surface free energies obtained from, for example, surface tension measurements and surface probe contact-angle measurements provide independent measure of the needed quantities.

The Lifshitz-van der Waals γ^{LW} (mJm⁻²), polar γ^{AB} (mJm⁻²), acid (electron acceptor) γ^+ (mJm⁻²), base (electron donor) γ^- (mJm⁻²) components of the surface free energy γ_s (mJm⁻²) were calculated from averaged values of the contact angles estimated for three different liquid probes (Water, Glycerol and Diiodomethane) according to Good, van Oss and Chaudhury approach [37] through the using of the following equations:

$$\gamma_s^{LW} = \frac{\gamma_l^{LW} \cdot (1 + \cos\theta)^2}{4} \quad (3.9)$$

$$\gamma_l \cdot (1 + \cos\theta) = 2 \cdot \left(\sqrt{\gamma_s^{LW} \cdot \gamma_l^{LW}} + \sqrt{\gamma_s^+ \cdot \gamma_l^-} + \sqrt{\gamma_s^- \cdot \gamma_l^+} \right) \quad (3.10)$$

$$\gamma_s^{AB} = 2 \cdot \sqrt{\gamma_s^+ \gamma_s^-} \quad (3.11)$$

These measurements allowed us to understand in a better way, mechanisms of water sequestration happening during nuclei and crystals formation.

3.7 Water desalination: Membrane Distillation (MD) and Membrane Crystallization (MCr) technology how final applications of membranes produced

This research explored the potential of innovative nanostructured membranes in water desalination, in particular in some of integrated membranes operations used to achieve pure water from saline and brackish water and to recovery organic and inorganic compounds (MD and MCr). Initially, innovative polymeric honeycomb patterned membranes were prepared, so that to have structures very close to that considered ideals. Then, 2D-PVDF composite membranes were prepared and tested in a MCr system, in order to evaluate how this 2D materials (different concentration percentage of graphene and spot like test of Bi₂Se₃) can affect and assist crystallization phenomena of sodium chloride salt solution. The configuration used and the procedure followed are described below.

3.7.1 Membrane distillation application for new tailored honeycomb membranes

Direct contact membrane distillation (DCMD) was chosen as a suitable configuration with the intent to develop a new nanostructured membrane enabling one to shift the productivity-efficiency trade-off, making this kind of configuration much more competitive than other configurations-types. DCMD is the simplest MD configuration, and is widely investigated in desalination processes and for concentration of aqueous solutions in food industries, or acids manufacturing. The main drawback of this design is the heat lost by conduction. In this kind of configuration, schematically reported in Figure 3.6, aqueous streams are maintained at different temperatures and are separated by a hydrophobic porous membrane. In our case a module for flat sheet membranes was used. The temperature of one of the two currents (that to treat, the feed) is greater than the other one (which represents the distillate) so as to create a temperature difference on the two sides of the membrane. Therefore, a difference in the voltage of vapor is also created. The forming vapor molecules will cross membranes pores from the side where the vapor pressure is highest to that where it is lowest. The two streams circulate in opposite way through the operation of two circulating pump. Furthermore two sensors (one at the feed and the other one at the permeate side), are used to control the effective temperature at the two sides. A conductivity meter is used for the controlling of feed and permeate ionic conductivity (μm) during and at the end of the experiments, in order to evaluate if membrane works well or not, so if it is wet during the process, allowing not only vapor water molecules transport, but also that of $\text{Na}^+ \text{Cl}^-$ ions.

The mechanism consists essentially of three stages [38]:

- Higher temperature water evaporation of the current
- Transport of vapor molecules through the pores of the hydrophobic membrane
- Steam condensation in the part of the membrane where the temperature is lower

In order to evaluate the flux during the entire experiments, permeate mass (g) was detected every twenty minutes until the end of the process.

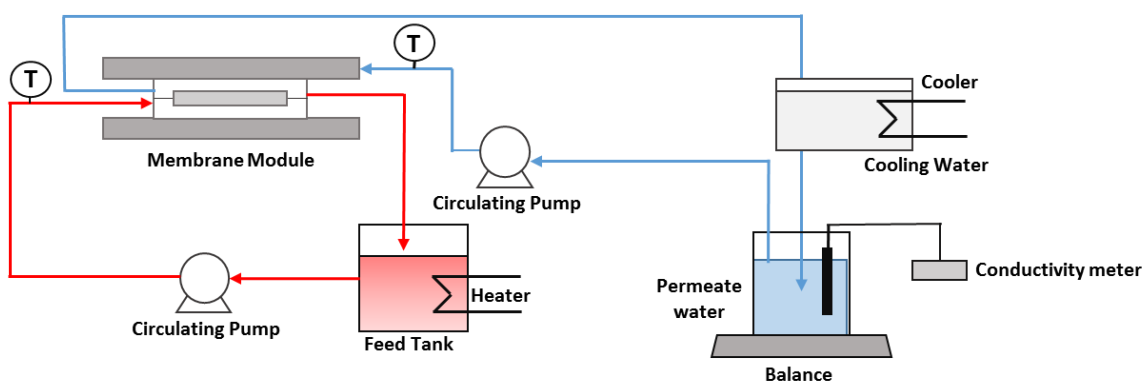


Figure 3.6. Schematic representation of Direct Contact Membrane Distillation configuration.

In this kind of configuration, the mass flux (J) is assumed to be proportional to the vapour pressure difference across the membrane, and is given by:

$$J = C_m [P_2 - P_3] \quad (3.12)$$

where C_m is the membrane coefficient, P_f and P_p are the vapour pressure at the membrane feed and permeate surfaces, which can be found from the Antoine equation [39-41].

Herein Thermally-driven DCMD experiments were executed using NaCl solutions 5 mM – flow rate_{feed} = 100 mL min⁻¹ and flow rate_{perm} = 80 ml⁻¹; $T_{feed} = 38$ °C and $T_{perm.} = 15$ °C. The trans-membrane fluxes were estimated by evaluating the weight variations in the distillate tanks. The thermal efficiency was calculated considering each single layer forming the tailor-made membrane. The salt conductivity of the feed and permeate streams were measured by using a conductive meter (Eutech Instruments PC 2700).

Mass transfer was calculated by the following equation:

$$J \propto \frac{\langle r^\alpha \rangle \cdot \varepsilon}{\tau \cdot \delta} \quad (3.13)$$

where $\langle r^\alpha \rangle$ is the average pore size for Knudsen diffusion ($\alpha = 1$) or the average squared pore size for viscous flux ($\alpha = 2$), τ the membrane tortuosity. The total heat transferred across the membrane is expressed as:

$$Q = U \cdot \Delta T \quad (3.14)$$

while the thermal efficiency in MD can be specified as the ratio of latent heat of vaporization to the total – latent and conduction – heat.

So the thermal efficiency was calculated in this way:

$$\text{Thermal efficiency} = \frac{J \cdot \Delta H}{U \cdot \Delta T} \cdot 100 \quad (3.15)$$

All details regarding equations for membrane distillation process are reported in Chapter 2.

3.7.2 2D-PVDF nanocomposite membranes for Membrane Crystallization technology

As it was already described in Chapter 2, MCr is a membrane process used to recovery different crystalline compounds. MCr is progressively replacing crystallization traditional technique [42-44]. In this work the attention was directed on studying the crystallization of NaCl salt highly concentrated with the use of direct contact configuration (DCMD). In particular, we used NaCl solutions 5.3 M; $T_{\text{feed}}= 35^{\circ}\text{C}$, $T_{\text{perm}}= 11^{\circ}\text{C}$; Flow rate $_{\text{feed}}=250$ ml/min; Flow rate $_{\text{perm}}= 100$ ml/min. As it was already said, hydrophobic porous membranes are in direct contact with a hot feed and a cold distillate. Volatile components of the feed evaporate at the feed/membrane interface, diffuse through the air inside the membrane pores and condense in the cold distillate stream. In the case of nonvolatile solutes, e.g. NaCl, only water vapour flows through the membrane. Continuous removal of pure water as permeate from the feed solution induced saturation and thus crystallization. To observe crystals, a sample of feed solution (NaCl 5.3 M) of almost 15 ml was taken and put in a plastic Eppendorf. A little amount of solution was then distributed homogeneously on a glass slide on the rotator table of optical microscope. The time where we have seen the first nuclei, was the first time to collect NaCl crystals pictures in order to start to build kinetics growth parameter. In order to have accurate kinetics, samples were taken every 30 min, and at each time three samples of salt solutions were analyzed. Through highlighted software of electronic optical microscope, it has been possible to evaluate crystal size, measuring two sides of each single NaCl crystals. So we were able to evaluate crystals mean diameter, coefficient of variation (CV), nucleation and growth rate B^0 [45].

Herein we report again: Coefficient of variation (CV), that is a parameter indicating the dispersion of a distribution around the mean crystal size. CV was calculated using the following equation:

$$CV = \frac{F_{80\%} - F_{20\%}}{2 \cdot F_{50\%}} \cdot 100 \quad (3.16)$$

where CV is expressed as percentage and F is the crystal length at the indicated percentage. Growth (G) and nucleation rate (B^0) have been estimated on the basis of the Randolph-Larson model [46] as follows:

$$\ln(n) = \frac{-L}{Gt} + \ln(n^0) \quad (3.17)$$

$$B^0 = n^0 G \quad (3.18)$$

where n is the crystal population density, L is crystal size, t is retention time and n^0 is population density at L equal to zero.

3.8 Molecular Dynamics (MD) simulations: a new combined theoretical and experimental approach to evaluate membranes behavior in MCr technology

As discussed in the previous paragraphs this research work developed new nano-composite PVDF membranes containing 2D nano-materials in polymer matrix. They were applied in MCr technology in order to evaluate their performance in nuclei formation and crystals growth. One of the objectives of this work was to carry out both computational and experimental studies to understand every crucial aspect of crystallization phenomena. Progresses in this direction have been done in recent years thanks to new highlighted software. In the past, computational methodologies have in particular revealed crucial aspects of crystal nucleation in liquids. Several studies have been performed to depict the mechanism of heterogeneous crystal nucleation by simulation [47-50] such as atomic simulation [51-54] and phase field theory [55], while there are limited publications for heterogeneous salt crystal nucleation from aqueous solution [56, 57]. First, crystals nucleation and growth were simulated in a slightly supersaturated aqueous bulk solution as performed by Chakraborty et al [58].

One of the most common and also used software in Molecular Dynamics applied to polymeric materials is Material Studio. It is nowadays a complete modeling and simulation environment designed to allow researchers in materials science and chemistry to predict and understand the relationships of a material's atomic and molecular structure with its properties and behavior. Using Materials Studio, researchers in many industries are engineering better performing materials of all types, including pharmaceuticals, catalysts, polymers and composites, metals and alloys, batteries and fuel cells, and more.

Moreover, it is interesting to investigate morphological parameter of membranes or their behavior in membrane operations. In this PhD work software GROMACS [59] was used. It is one of the most widely used open-source and free software codes in chemistry, used primarily for dynamical simulations of biomolecules, but nowadays in a lot of different fields (including membrane technology). It provides a rich set of calculation types, preparation and analysis tools. Several advanced techniques for free-energy calculations are supported. In version 5 [60, 61], it reaches new performance heights, through several new and enhanced parallelization algorithms.

3.8.1 Materials

The computational systems, were built with Amorphous Cell module using Material Studio version 7.0. They were:

- PVDF pristine
- PVDF and graphene (G) 5 wt %
- PVDF and graphene (G) 10 wt %

The models were completed with Gromacs 5.1.3 reaching an X, Y and Z axes size of (5.63x5.63x11,38) nm³ for pristine PVDF; of (5.55x5.55x10.90) nm³ for PVDF-G 5 wt % and (5.71x5.71x10.91) nm³ for PVDF-G 10 wt %. Theoretical parameters of models achieved were reported in table 3.1. While an example of a box built with Materials Studio is shown in Figure 3.7.

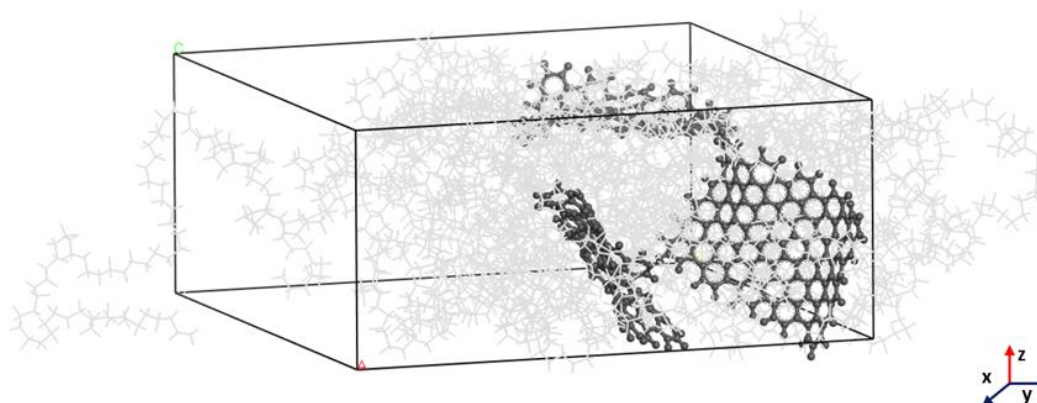


Figure 3.7. Graphene 5% wt- PVDF membrane model built with Materials Studio Software. Grey light lines are PVDF chains, while ball and stick aromatic graphene structures are in black.

Tabella 3.2 Theoretical parameters of membrane systems produced by computational studies.

| System | V box (nm ³) | N° of NaCl molecules | N° of H ₂ O molecules | NaCl initial concentration (mol/L) |
|--------------------------|--------------------------|----------------------|----------------------------------|------------------------------------|
| PVDF | 350.23 ± 4.23 % | 793.5 ± 4.4 % | 7405.5 ± 4.4 % | 6.016 ± 0.100 % |
| PVDF G 5 % wt | 337.08 ± 0.56 % | 765.5 ± 1.2 % | 7052.5 ± 1.3 % | 6.012 ± 0.017 % |

| | | | | |
|---------------------------|-----------------|---------------|----------------|-----------------|
| PVDF G 10 % wt | 357.16 ± 0.57 % | 772.0 ± 0.0 % | 7197.5 ± 0.1 % | 6.013 ± 0.216 % |
|---------------------------|-----------------|---------------|----------------|-----------------|

Methodology was the same used from Tsai et al [62] where it was investigated behavior of commonly used polymeric membranes (PVDF and PP) in membrane crystallization technology with respect to traditional process. This research was partially involved in this further computational and experimental study, so some of results achieved will be discussed in Chapter 5.

3.8.2 Force Field Based Simulation

The interaction of particles, bonded or nonbonded, is subject to a quantum mechanical description. In principle, for the physically most accurate description available, the Schrödinger-equation for each particle (electrons and nuclei) must be devised, leading to a complex set of equations. Its solution is, though possible, beyond reasonable effort for the size of the systems and the CPU-power available. However, the properties which are under investigation in this work, i.e., static, thermodynamic and dynamic (transport and relaxational) properties of non-reactive organic polymers, are well described using forcefield based molecular mechanics (MM), molecular dynamics (MD) and classical Monte Carlo (MC) simulations [63,64] methods based on classical mechanics of multi-particle systems. Needless to say, some quantum mechanical information and experimental data are needed to establish the forcefield in the first place. The information is obtained for relatively small units and is, by extrapolation, assumed to be valid for larger systems of equal classes.

3.8.3 The Force Field

Forcefields allow the calculation of the potential energy U of an ensemble of N atoms, as a function of their coordinates ($r_1 \dots r_N$). It is composed of individual contributions which describe the interactions of bonded atoms (bond-lengths, -angles, conformation angles) and nonbonded interactions (van der Waals, electrostatic):

$$\begin{aligned}
U(\mathbf{r}_1, \mathbf{r}_2, \dots, \mathbf{r}_N) = & \sum_{\text{bonds}} \text{bond-length-deformations} & \text{(bond length)} \\
& + \sum_{\text{angles}} \text{bond-angle-deformations} & \text{(bond angle)} \\
& + \sum_{\text{conf. angles}} \text{torsional-deformation} & \text{(torsion)} \\
& + \sum_{\text{atom-pairs}} \text{nonbonded-interactions}
\end{aligned}
\tag{3.19}$$

The contributions of bonded interactions are represented by anharmonic oscillators of the form [65]:

$$U_{ij}(r_{ij}) = k_1(r_{ij} - r_{ij}^0)^2 + k_2(r_{ij} - r_{ij}^0)^3 + k_3(r_{ij} - r_{ij}^0)^4 \quad \text{(stretch)}$$

$$U_{ijk}(\theta_{ijk}) = k_1(\theta_{ijk} - \theta_{ijk}^0)^2 + k_2(\theta_{ijk} - \theta_{ijk}^0)^3 + k_3(\theta_{ijk} - \theta_{ijk}^0)^4 \quad \text{(angle)}$$

$$\begin{aligned}
U_{ijkl}(\Phi_{i-l}) = & k_1[1 - \cos(\Phi_{i-l} - \Phi_1^0)]^2 + k_2[1 - \cos(\Phi_{i-l} - \Phi_2^0)]^3 + k_3[1 - \cos(\Phi_{i-l} - \Phi_3^0)]^4 \\
& \text{(torsion)}
\end{aligned}
\tag{3.20}$$

The force constants k_i and the equilibrium positions r_{ij} , θ_{ijk} and Φ_{i-l} are based on results of quantum mechanics and constitute the integral part of the forcefield. The nonbonded interactions are expressed by a van der Waals term with a 9,6- or 12-6 potential and a coulomb-term:

$$\begin{aligned}
U_{ij}(r_{ij}, q_i, q_j) = & \left(\frac{A_{ij}}{r_{ij}^9} - \frac{B_{ij}}{r_{ij}^6} \right) + \frac{q_i q_j}{\epsilon_0 r_{ij}} & \text{(nonbonded)} \\
& \tag{3.21}
\end{aligned}$$

where A_{ij} and B_{ij} are parameters describing the strength of the repulsive and attractive force, q_i and q_j are the partial charges of the interacting atoms and ϵ_0 is the vacuum permittivity. The forcefield is defined by the functional form (eqns. 3.19, 3.20) and a set of parameters k_i , r_{ij}^0 , . . . which are specific to types of atoms, i.e., account for different bonded states of the atoms.

For a given molecular structure, the force- field results in a potential energy surface, which can be evaluated with respect to local energy minima. These methods are known as molecular mechanics (MM). In the course of optimization, geometrically reasonable (static) structures can be obtained from the initially guessed geometry by varying the atom positions and minimizing the potential energy of the system.

It should be noticed that the evaluation of the nonbonded energy terms is the numerically most extensive part in molecular modeling calculations because these terms include contributions from each pair of atoms in a model. This leads to restrictions on the maximum possible size of a simulated membrane system (e. g. an amorphous polymer packing). The number of atoms N cannot be much higher than 2000–10000 for typical transport simulations on modern workstations, while N may be up to about a factor of ten higher for selected simulations on currently available supercomputers.

3.8.4 Molecular Dynamics (MD)

To perform molecular dynamics (MD) simulations, the forces that result from the forcefield and which act on each atom are applied to the system of finite temperature, i.e., finite kinetic energy E_{kin} .

Each of the N particles is assigned a random (Boltzmann) velocity vector v_i so that the total kinetic energy of the system corresponds to the desired temperature T :

$$E_{kin} = \sum_{i=1}^n \frac{1}{2} m_i v_i^2 = \frac{(3N - 6)}{2} k_B T \quad (3.22)$$

Here $(3N - 6)$ is the number of degrees of freedom and k_B is the Boltzmann constant. In the course of a simulation, integration of the Newtonian equations of motion:

$$F_i = -\nabla_{r_i} U_i(r_1, \dots, r_N) = m_i \ddot{r}_i \quad (3.23)$$

leads to a new velocity of each particle which can be extrapolated over the time step $\Delta t = 1$ fs of the simulation to determine the new coordinates r_i . The force F_i , acting on a particle i of mass m_i , results from the gradient of the potential energy U_i (see eq. 3.20) determined by the forcefield.

Using Eq. (3.19-20) it is then possible to follow the motions of the atoms of a polymer matrix and the diffusive movement of imbedded small penetrant molecules at a given temperature over a certain interval of time. Eq. (3.20) represents a system of usually several thousand coupled differential equations of second order. It can be solved only numerically in small timesteps Δt [66-68]. The choice of the time step Δt results from the consideration that the fastest vibration of the system should be sufficiently resolved. In a typical IR-spectrum, the C-H-bond shows a characteristic peak at $\nu(\text{C-H}) \approx 3000 \text{ cm}^{-1}$, which corresponds to an oscillation period of $\tau(\text{C-H}) \approx 10 \text{ fs}$.

3.8.5 Condensed Phase Simulation

When simulating condensed-phase systems, it is necessary to build systems that can present the bulk of the simulated materials correctly. Therefore, the size of the simulation cell must be large enough to be able to sample the configurational space of the properties of interested. On the other hand, the system size is also limited by computing power.

3.8.6 Periodic Boundary Conditions

When taking a small system out of the bulk of simulated object, the same bulky environment has to be preserved to avoid unrealistic surface effect. The common approach is to use the periodic boundary conditions, in which the primary cell (parent cell) is surrounded on all sides by replica of itself (image cells) to form a three-dimensional infinite lattice. The atoms initially in the parent cell are parent atoms, while those initially in the image cells are image atoms. There is an image centering technique to control the constant atom number, i.e. whenever an atom migrates to the edge of the primary cell, it will appear in the adjacent image cell.

However, its image will enter the primary cell on the opposite side. Thus, atoms may diffuse as far as they can during the course of the simulation instead of being confined in the small parent cell, and at the same time the number of atoms in the box is always constant. In an

explicit image model, a parent atom will interact with any image atoms (besides parent atoms) within the user-defined cut-off while implicit image model only counts the closest image atoms [69].

3.8.7 Amorphous Cell Construction

Polymer chain can adopt numerous conformations due to the existence of many rotatable bonds, whereas for small molecules, only limited number of conformations are accessible. Even a short polymer chain may have a few hundred rotatable bonds that give rise to millions of different conformers. This makes it difficult to sample all the conformations of a real polymer chain with a small simulation cell. It is almost impossible to find the “global” minimum energy conformation within such a large configuration space using energy minimization scheme. Also, it is very time consuming if not impossible to equilibrate polymers with unrealistic initial structure by molecular dynamics. The interdependent RIS (Rotational Isomeric State) model has been proved to be an efficient and effective way to build a polymer chain of reasonable initial structure since condensed-phase polymer chain is known to be at unperturbed state. However, the conventional pair wise RIS model does not explicitly prohibit overlapping of atoms separated by a few backbone atoms away or atoms belonging to different molecules.

A method developed by Theodorou and Suter [70] takes advantage of the conventional RIS model while overcomes such limitations. In their method, a Monte Carlo type bond-by-bond construction scheme is employed to build a polymer backbone.

Usually amorphous cells are built at a relatively low initial density with ease and are compressed to the experimental density gradually using high-pressure NPT dynamics.

These cells generally need to be further refined to “equilibrate” the structure. The refinement adopted in present studies is an annealing procedure, which will heat up polymer cell step by step using high temperature NPT molecular dynamics, then cool it back to the original conditions. High temperature dynamics may provide sufficient amount of energy for the polymer chains to overcome local energy barriers and reach “global” minimum energy conformation.

3.8.8 The Concept of Ensembles

In statistical thermodynamics, details of individual particles are usually not of great importance. On the contrary, for a realistic representation of thermodynamic behaviour, the

expectancy of observable properties are regarded. This may be achieved by taking the mean value with respect to time or as the average of a number of configurations.

In molecular dynamics, the evolution of a system with respect to time is observed. Depending on the property under investigation, different ensembles are evaluated, i.e., different state-variables are held constant to observe the behaviour of others.

In the microcanonical ensemble the number of particles N , the total energy E and the volume of the simulation cell V are held constant. While keeping N and E constant is quite straightforward and needs no further explanation, the volume V of a system may be kept constant by periodic boundary conditions, forcing a particle that leaves the virtual simulation cell to enter on the opposite side by assigning the appropriate coordinates.

A canonical ensemble is characterized by constant N , V and temperature T . The easiest way to control the temperature is to directly scale the particle velocities \dot{r}_i , whenever the system temperature T_{sys} leaves a predefined temperature window $T_0 \pm \Delta T$:

$$\dot{r}_{i,now} = \dot{r}_{i,old} \left(\frac{T_0}{T_{sys}} \right)^{\frac{1}{2}} \quad (3.24)$$

More refined methods like the Berendsen thermostat [71] are more commonly used because a temperature change per simulation time step leads to a more smooth progression of the temperature. In this work, molecular dynamics are applied to using canonical ensembles in the equilibration steps of packing procedure.

If, at constant N and T , the pressure p is held constant instead of the volume V the ensemble is called isothermal-isobaric. The pressure is evaluated using the virial Ξ and kinetic energy $E_{kin} \propto Nk_B T$ based on centers of mass [72]:

$$\Xi(t) = \frac{1}{2} \sum_{i<j} r_{ij}(t) F_{ij}(t) \quad (3.25)$$

It is controlled by changing the volume V of the simulation cell according to the relation:

$$pV = Nk_B T + \frac{2}{3} \langle \Xi \rangle \quad (3.26)$$

Molecular dynamics simulations of isothermal-isobaric ensembles (NPT -MD) are performed as final equilibration procedure of the packing models.

An ensemble of constant pressure, volume, temperature and chemical potential μ is called grand canonical. Here, the number of particles N is allowed to fluctuate. This is achieved by randomly inserting or deleting molecules. The chemical potential of the molecules within the matrix is balanced with a reference chemical potential.

3.8.9 Gromacs: new highlighted tools for MD simulation. Its implementation on Membrane Assisted Crystallization

GROMACS software version 5.1.4 [73], was used for all simulations performed. It is at the moment one of the most used in biophysical computational studies, but is in increasing development in the field of polymeric materials and membrane technology, including Membrane- assisted Crystallization (MCr), that is one of the most important topic discussed in this thesis. In these studies simulations were carried out at 308 K and at pressure of 1 atm, with a Cut-off distance of 1.25 nm. The SPC/E model [74] was used for water, and the ion parameters were those used in the OPLS force field [75, 76]. The force field parameters of the PVDF polymer developed by Bytner and Smith [77] were used with pair interactions consisted of Lennard-Jones (LJ). The LJ cross interactions were obtained using the usual Lorentz–Berthelot combining rules [78]. The equations of motion were integrated using the leapfrog algorithm with a time step of 1 fs. The Coulombic interactions were treated employing the particle mesh Ewald (PME) summation method [79] The simulations were carried out in the NPT ensemble, using a velocity rescaling algorithm [80] ($\tau = 0.1$ ps) to control the temperature and the Berendsen barostat [81] ($\tau_p = 0.1$ ps) for the pressure. The water molecules were kept rigid by constraining the interatomic distances using the LINCS algorithm [82].

At first the system was equilibrated for 2 ns (NVT and NPT), followed by a production run of 200 ns. It is important to note that the system was also equilibrated, so the solution properties (energy, radial distribution functions, etc.) were converged and unchanging before crystal nucleation occurred.

In this thesis MCr studies were performed with nanostructures inside polymer matrix in particular with graphene- PVDF based membranes at different concentration percentage (Chapter 5). All detailed results will be discussed in Chapter 5.

3.8.10 Radial distribution function (RDF) and Coordination number (CN): analysis systems to evaluate ion-ion interactions in crystallization phenomena

One of the targets of this work was to evaluate ion-ion interaction from computational chemistry point of view in order to evaluate when happened nuclei formation and relative crystals growth, comparing different systems studied. Two method were in particular validated to individuate this aggregation that allow to see in which system there were faster induction times:

- Radial Distribution Function (RDF)
- Coordination Number (CN)

In statistical mechanics, the *Radial Distribution Function (RDF)* (or pair correlation function) $g(r)$ in a system of particles (atoms, molecules, colloids, etc.), describes how density varies as a function of distance from a reference particle [83, 84]. If a given particle is taken to be at the origin O, and if:

$$\rho = \frac{N}{V} \quad (3.27)$$

is the average number density of particles, then the local time-averaged density at a distance r from O is $\rho g(r)$.

In simplest terms it is a measure of the probability of finding a particle at a distance of r away from a given reference particle, relative to that for an ideal gas. The general algorithm involves determining how many particles are within a distance of r and $r + dr$ away from a particle. This general theme is depicted to the right, where the red particle is our reference particle, and blue particles are those whose centers are within the circular shell, dotted in orange.

The radial distribution function is usually determined by calculating the distance between all particle pairs and binning them into a histogram. The histogram is then normalized with respect to an ideal gas, where particle histograms are completely uncorrelated. For three dimensions, this normalization is the number density of the system ρ multiplied by the volume of the spherical shell, which symbolically can be expressed as:

$$\rho 4\pi r^2 dr \quad (3.28)$$

Given a potential energy function, the radial distribution function can be computed either via computer simulation methods like the Monte Carlo method, or via the Ornstein-Zernike equation, using approximative closure relations like the Percus-Yevick approximation or the Hypernetted Chain Theory. It can also be determined experimentally, by radiation scattering techniques or by direct visualization for large enough (micrometer-sized) particles via traditional or confocal microscopy. The radial distribution function is of fundamental importance since it can be used, using the Kirkwood–Buff solution theory, to link the microscopic details to macroscopic properties. Moreover, by the reversion of the Kirkwood-Buff theory, it is possible to attain the microscopic details of the radial distribution function from the macroscopic properties. In chemistry, crystallography, and materials science, the *coordination number (CN)*, also called ligancy, of a central atom in a molecule or crystal is the number of atoms, molecules or ions bonded to it [85]. The ion/molecule/atom surrounding the central ion/molecule/atom is called a ligand. This number is determined somewhat differently for molecules than for crystal. The usual value of the coordination number for a given structure refers to an atom in the interior of a crystal lattice with neighbors in all directions. In contexts where crystal surfaces are important, such as materials science and heterogeneous catalysis, the number of neighbors of an interior atom is the bulk coordination number, while the number of surface neighbors of an atom at the surface of the crystal is the surface coordination number. From a theoretical point of view, the coordination numbers have been computed by using standard radial distribution functions (rdf) and then counting the average number of ions or water within the first hydration shell of the counterions (or integrating the *rdf* up to the location of the first minimum). In computational MCr studies, through the using of the two methods, it was possible to evaluate ion-ion interaction. In rdf standard curve, when peak became more distinct it was a clear sign of ion-ion encounters due to their greater closeness. Furthermore through evaluation of CN we were able to estimate the time scale on which crystallization took place, estimating time of nucleation and what system were more rapid in crystal formation. Every detail, will be discussed in Chapter 5.

References

1. T. Marino, E. Blasi, S. Tornaghi, E. Di Nicolò, A. Figoli, Polyethersulfone membranes prepared with Rhodiasolv® Polarclean as watersoluble green solvent, *J. Membr. Sci.*, 549 (2018) 192-204, <https://doi.org/10.1016/j.memsci.2017.12.007>.
2. A. Gugliuzza, M.L. Perrotta, E. Drioli, Controlled Bulk Properties of Composite Polymeric Solutions for Extensive Structural Order of Honeycomb Polysulfone Membranes, *Membranes*, 6 (2016) 27, <https://doi.org/10.3390/membranes6020027>.
3. C. Kim, Y.L. Hsieh, Wetting and absorbency of nonionic surfactant solutions on cotton fabrics. *Coll. Surf. A Phys. Eng. Asp.*, 187 (2001) 385–397, [https://doi.org/10.1016/S0927-7757\(01\)00653-7](https://doi.org/10.1016/S0927-7757(01)00653-7).
4. M.L. Perrotta, G. Saielli, G. Casella, F. Macedonio, L. Giorno, E. Drioli, A. Gugliuzza, An ultrathin suspended hydrophobic porous membrane for high-efficiency water desalination, *Appl. Mat. Today*, 9 (2017) 1-9, <https://doi.org/10.1016/j.apmt.2017.04.009>.
5. <http://multimedia.3m.com/mws/media/199818O/3mtm-novectm-7100-engineered-fluid.pdf>
6. B. Herzog, M.I. Kohan, S.A. Mestemacher, R.U. Pagilagan, K. Redmond, Polyamides, *Ullmann's Encyclopedia of Industrial Chemistry*, 2003, https://doi.org/10.1002/14356007.a21_179.pub.

7. L.K. Massey, *Permeability Properties of Plastics and Elastomers: a guide to packaging and Barrier Materials*, second edition, Plastic Design Library, 2003.
8. R.R. Nair, P. Blake, A.N. Grigorenko, K.S. Novoselov, T.J. Booth, T. Stauber, N.M.R. Peres, A.K. Geim, Fine Structure Constant Defines Visual Transparency of Graphene, *Science*, 320 (2008) 1308, <https://doi.org/10.1126/science.1156965>.
9. S.K. Mishra, S. Satpathy, O. Jepsen, Electronic structure and thermoelectric properties of bismuth telluride and bismuth selenide, *J. Phys. Cond. Mat.*, 9 (1997) 461–470, <https://doi.org/10.1088/0953-8984/9/2/014>.
10. <http://it.chinapyrrolidone.com/info/nmp-n-methyl-2-pyrrolidone-china26080357.html>
11. C.Y. Kuo, H.N. Lin, H.A. Tsai, D.M. Wang, J.Y. Lai, Fabrication of a high hydrophobic PVDF membrane, via nonsolvent induced phase separation, *Desalination*, 233 (2008) 40–47, <https://doi.org/10.1016/j.desal.2007.09.025>.
12. K. Binnemans, Ionic Liquid Crystals, *Chem. Rev.*, 105 (2005) 4148–4204, <https://doi.org/10.1021/cr0400919>.
13. P.K. Bhowmik, H.S. Han, J.J. Cebe, R.A. Burchett, B. Acharya, S. Kumar, Ambient temperature thermotropic liquid crystalline viologen bis(triflimide) salts, *Liquid Cryst.*, 30 (2003) 1433–1440, <https://doi.org/10.1080/02678290310001621895>.
14. G. Casella, V. Causin, F. Rastrelli, G. Saielli, Viologen-based ionic liquid crystals: induction of a smectic A phase by dimerisation, *Phys. Chem. Chem. Phys.*, 16 (2014) 5048–5051, <https://doi.org/10.1039/C3CP54628D>.
15. T. Matura, *Synthetic Membranes and Membrane Separation Process*, CRC Press, Inc, 1994, Chapter 3, pp. 48–58.
16. F. Macedonio, A. Politano, E. Drioli, A. Gugliuzza, Bi₂Se₃-assisted membrane crystallization, *Mater. Horiz.*, 5 (2018) 912–919, <https://doi.org/10.1039/C8MH00612A>.
17. D. Hsieh, Y. Xia, D. Qian, L. Wray, J. H. Dil, F. Meier, J. Osterwalder; L. Patthey, J. G. Checkelsky, N. P. Ong, A. V. Fedorov, H. Lin, A. Bansil, D. Grauer, Y. S. Hor, R. J. Cava, M. Z. Hasan, A tunable topological insulator in the spin helical Dirac transport regime, *Nature*, 460 (2009) 1101–1105, <https://doi.org/10.1038/nature08234>.
18. A. Gugliuzza, E. Drioli, PVDF and HYFLON AD membranes: Ideal interfaces for contactor applications, *J. Membr. Sci.*, 300 (2007) 51–62, <https://doi.org/10.1016/j.memsci.2007.05.004>.
19. M. Kojima, Y. Hirai, Y. Hiroshi, M. Shimomura, The effects of interfacial tensions of amphiphilic copolymers on honeycomb-patterned films, *Polym. J.*, 41 (2009) 667–671, <https://doi.org/10.1295/polymj.PJ2009027>.

20. B.J. Berne, R. Pecora, *Dynamic Light Scattering*, Courier Dover Publications (2000).
21. K. Symon, *Mechanics*, 3rd ed, Addison-Wesley, (1971).
22. A. Politano, M. Cattelan, D. W. Boukhvalov, D. Campi, A. Cupolillo, S. Agnoli, N. G. Apostol, P. Lacovig, S. Lizzit, D. Farias, G. Chiarello, G. Granozzi, R. Larciprete, Unveiling the Mechanisms Leading to H₂ Production Promoted by Water Decomposition on Epitaxial Graphene at Room Temperature, *ACS Nano*, 10 (2016) 4543-4549, <https://doi.org/10.1021/acsnano.6b00554>.
23. R. M. Silverstein, G. C. Bassler, T. C. Morrill, *Spectrometric Identification of Organic Compounds*, 5th Ed., Wiley, (1991).
24. www.alfatest.net.
25. <http://chemwiki.ucdavis.edu/PhysicalChemistry/PhysicalPropertiesofMatter/BulkProperties/CohesiveAndAdhesiveForces/ContactAngles>
26. L. Peruzzo, *Introduzione all'uso del SEM Camscan MX 2500*, Dipartimento di mineralogia e petrologia- Università di Padova, Dispensa tecnica, 2003.
27. G. Binnig, C.F. Quate, Ch. Gerber, Atomic Force Microscope, *Phys. Rev. Lett.*, 56 (1986) 930–933, <https://doi.org/10.1103/PhysRevLett.56.930>.
28. D. Li, M. W. Frey, Y. L.Joo, Characterization of nanofibrous membranes with capillary flow porometry, *J. Membr. Sci.*, 286 (2006) 104-114, <https://doi.org/10.1016/j.memsci.2006.09.020>.
29. M.J. Frisch, G.W. Trucks, H.B. Schlegel, G.E. Scuseria, M.A. Robb, J.R.G. Cheeseman, et al., *Gaussian 09*, Revision B.01Gaussian, Inc., Wallingford, CT (2010), available at: <http://gaussian.com/g09citation/>.
30. J.D. Chai, M. Head-Gordon, Long-range corrected hybrid density functionals with damped atom–atom dispersion corrections, *Phys. Chem. Chem. Phys.*, 10 (2008) 6615-6620, <https://doi.org/10.1039/B810189B>.
31. J. Tomasi, B. Mennucci, R. Cammi, Quantum mechanical continuum solvation models, *Chem. Rev.*, 105 (2005) 2999-3094, <https://doi.org/10.1021/cr9904009>.
32. T.J. Collins, Image J for microscopy, *BioTechniques*, 43 (2007) 25–30, <https://doi.org/10.2144/000112517>.
33. N.D. Koromilas, C. Anastasopoulos, E.K. Oikonomou, J.K. Kallitsis, Preparation of Porous Polymeric Membranes Based on a Pyridine Containing Aromatic Polyether Sulfone, *Polymers*, 11 (2019) 59, <https://doi.org/10.3390/polym11010059>.
34. A. Gugliuzza, E. Drioli, PVDF and HYFLON AD membranes: Ideal interfaces for contactor applications, *J. Membr. Sci.*, 300 (2007) 51-62, <https://doi.org/10.1016/j.memsci.2007.05.004>.

35. A Gugliuzza, E. Drioli, A review on membrane engineering for innovation in wearable fabrics and protective textiles, *J. Membr. Sci.*, 446 (2013) 350-375, <https://doi.org/10.1016/j.memsci.2013.07.014>.
36. J. Rychlewski, On Hooke's law, *J. Appl. Math. Mech.*, 48 (1984) 303-314, [https://doi.org/10.1016/0021-8928\(84\)90137-0](https://doi.org/10.1016/0021-8928(84)90137-0).
37. P.C. Rieke, Application of Van Oss-Chaudhury-Good theory of wettability to interpretation of interracial free energies of heterogeneous nucleation¹, *J. of Cryst. Growth*; 182 (1997) 472-484, [https://doi.org/10.1016/S0022-0248\(97\)00357-6](https://doi.org/10.1016/S0022-0248(97)00357-6).
38. N. Li, A.G. Fane, W.S.W. Ho, T. Matsuura, *Advanced Membranes Technology and Applications*, John Wiley & Sons, Inc., 2008, Chapter 12, pp. 297-301.
39. F.A. Banat, J. Simandl, Theoretical and experimental study in membrane distillation, *Desalination*, 95 (1994) 39–52, [https://doi.org/10.1016/0011-9164\(94\)00005-0](https://doi.org/10.1016/0011-9164(94)00005-0).
40. H. Kurokawa, O. Kuroda, S. Takahashi, K. Ebara, Vapor permeate characteristics of membrane distillation, *Sep. Sci. Technol.*, 25 (1990) 1349–1359, <https://doi.org/10.1080/01496399008050396>.
41. E. Drioli, V. Calabro, Y. Wu, Microporous membranes in membrane distillation, *Pure Appl. Chem.*, 58 (1986) 1657–1662, <https://doi.org/10.1351/pac198658121657>.
42. E. Drioli, Y. Wu, V. Calabro, Membrane distillation in the treatment of aqueous solutions, *J. Membr. Sci.*, 33 (1987) 277–284, [https://doi.org/10.1016/S0376-7388\(00\)80285-9](https://doi.org/10.1016/S0376-7388(00)80285-9).
43. E. Drioli, G. Di Profio, E. Curcio, Progress in membrane crystallization, *Curr. Op. Chem. Eng.*, 1 (2012) 178-182, <https://doi.org/10.1016/j.coche.2012.03.005>.
44. A.S. Myerson, *Handbook of Industrial Crystallization*, second edition, London: Butterworth-Heinemann, 2002.
45. J.T.M. Sluys, D. Verdoes, J.H. Hanemaaijer, Water treatment in a Membrane-Assisted Crystallizer (MAC), *Desalination*, 104 (1996) 135-139, [https://doi.org/10.1016/0011-9164\(96\)00036-7](https://doi.org/10.1016/0011-9164(96)00036-7).
46. Z. Cui, X. Li, Y. Zhang, Z. Wang, A. Gugliuzza, F. Militano, E. Drioli, F. Macedonio, Testing of three different PVDF membranes in membrane assisted-crystallization process: Influence of membrane structural-properties on process performance, *Desalination*, 440 (2018) 68–77, <https://doi.org/10.1016/j.desal.2017.12.038>.
47. C.C. Koa, A. Ali, E. Drioli, K.L. Tunga, C.H. Chena, Y.R. Chena, F. Macedonio, Performance of ceramic membrane in vacuum membrane distillation and in vacuum membrane crystallization, *Desalination*, 44 (2018) 48-58, <https://doi.org/10.1016/j.desal.2018.03.011>.

48. J. Anwar, D. Zahn, Uncovering Molecular Processes in Crystal Nucleation and Growth by Using Molecular Simulation, *Angew. Chem. Int. Ed.*, 50 (2011) 1996–2013. <https://doi.org/10.1002/anie.201000463>.
49. S. Whitelam, Control of pathways and yields of protein crystallization through the interplay of nonspecific and specific attractions, *Phys. Rev. Lett.*, 105 (2010) 088102, <https://doi.org/10.1103/PhysRevLett.105.088102>.
50. R. Demichelis, A. Schuitemaker, N.A. Garcia, K.B. Koziara, M. De La Pierre, P. Raiteri, J.D. Gale, Simulation of crystallization of biominerals, *Annu. Rev. Mater. Res.*, 48 (2018) 327–352, <https://doi.org/10.1146/annurev-matsci-070317-124327>.
51. G.C. Sosso, J. Chen, S.J. Cox, M. Fitzner, P. Pedevilla, A. Zen, A. Michaelides, Crystal Nucleation in Liquids: Open Questions and Future Challenges in Molecular Dynamics Simulations, *Chem. Rev.*, 116 (2016) 7078–7116, <https://doi.org/10.1021/acs.chemrev.5b00744>.
52. S. Toxvaerd, Molecular dynamics simulation of heterogeneous nucleation at a structureless solid surface. *J. Chem. Phys.*, 117 (2002) 10303-10310, <https://doi.org/10.1063/1.1519255>.
53. A. Cacciuto, S. Auer, D. Frenkel, Onset of heterogeneous crystal nucleation in colloidal suspensions, *Nature*, 428 (2004) 404-406, <https://doi.org/10.1038/nature02397>.
54. E.B. Webb, G.S. Grest, D.R. Heine, Precursor Film Controlled Wetting of Pb on Cu, *Phys. Rev. Lett.*, 91 (2003) 236102, <https://doi.org/10.1103/PhysRevLett.91.236102>.
55. L. Gránásy, T. Pusztai, D. Saylor, J.A. Warren, Phase Field Theory of Heterogeneous Crystal Nucleation, *Phys. Rev. Lett.*, 98 (2007) 035703, <https://doi.org/10.1103/PhysRevLett.98.035703>.
56. S. Yamanaka, A. Shimosaka, Y. Shirakawa, J. Hidaka, Molecular dynamics simulations of the formation for NaCl cluster at the interface between the supersaturated solution and the substrate, *J. Nanopart. Res.*, 12 (2010) 831-839, <https://doi.org/10.1007/s11051-009-9713-z>.
57. Y. Yang, S. Meng, Atomistic nature of NaCl nucleation at the solid-liquid interface, *J. Chem. Phys.*, 126 (2007) 044708, <https://doi.org/10.1063/1.2431363>.
58. D. Chakraborty, G.N. Patey, How Crystals Nucleate and Grow in Aqueous NaCl Solution, *J. Phys. Chem. Lett.*, 4 (2013) 573-578, <https://doi.org/10.1021/jz302065w>.
59. M.J. Abraham, T. Murtola, R. Schulz, S. Páll, J.C. Smith, B. Hessa, E. Lindahl, GROMACS: High performance molecular simulations through multi-level parallelism from laptops to supercomputers, *SoftwareX*, 1-2 (2015) 19-25, <https://doi.org/10.1016/j.softx.2015.06.001>.

60. H.J.C. Berendsen, D. van der Spoel, R. van Drunen, GROMACS: A Message-Passing Parallel Molecular Dynamics Implementation, *Comput. Phys. Commun.*, 91 (1995) 43–56, [https://doi.org/10.1016/0010-4655\(95\)00042-E](https://doi.org/10.1016/0010-4655(95)00042-E).
61. B. Hess, C. Kutzner, D. van der Spoel, E. Lindahl, GROMACS 4: Algorithms for Highly Efficient, Load-Balanced, and Scalable Molecular Simulation, *J. Chem. Theory Comput.*, 4 (2008) 435–447, <https://doi.org/10.1021/ct700301q>.
62. J.H. Tsai, M.L. Perrotta, A. Gugliuzza, F. Macedonio, L. Giorno, E. Drioli, K. Tung, E. Tocci, Membrane-Assisted Crystallization: A Molecular View of NaCl Nucleation and Growth, *App. Sci.*, 8 (2018) 2145, <https://doi.org/10.3390/app8112145>.
63. W. Paul, G.D. Smith, Structure and dynamics of amorphous polymers: computer simulations compared to experiment and theory, *Rep. Prog. Phys.*, 67 (2004) 1117, <https://doi.org/10.1088/0034-4885/67/7/R03>.
64. D.N. Theodorou, Principles of Molecular Simulation of Gas Transport in Polymers, in: Y. Yampolskii, I. Pinnau, B.D. Freeman (Eds.), *Materials Science of Membranes for Gas and Vapor Separation*, Wiley, 2006, chapter 2.
65. A. Hinchliffe, *Molecular Modelling for Beginners*, Wiley, 2003.
66. D.T. Punsalan, A Sorption and Dilation Investigation of Amorphous Glassy Polymers and Physical Aging. Dissertation, University of Texas at Austin, 2001.
67. Y. Kamiya, T. Hirose, Y. Naito, K. Mizoguchi, Sorptive dilation of polysulfone and poly(ethylene terephthalate) films by high-pressure carbon dioxide, *J. Polymer Sci. Part B: Polym. Phys.*, 26 (1988) 159-177, <https://doi.org/10.1002/polb.1988.090260109>.
68. G.C. Sarti, F. Doghieri, Predictions of the solubility of gases in glassy polymers based on the NELF model, *Chem. Eng. Sci.*, 53 (1998) 3435, [https://doi.org/10.1016/S0009-2509\(98\)00143-2](https://doi.org/10.1016/S0009-2509(98)00143-2).
69. Forcefield-based Simulation, General Theory & Methodology, Copyright (1997), available at: http://www.chem.cmu.edu/courses/09-560/docs/msi/ffbsim/FF_SimulTOC.doc.html.
70. D.N. Theodorou, U.W. Suter, Detailed molecular structure of a vinyl polymer glass, *Macromolecules*, 18 (1985) 1467-1478, <https://doi.org/10.1021/ma00149a018>.
71. H.J.C. Berendsen, J.P.M. Postma, W.F. Vangunsteren, A. DiNola, J.R. Haak, Molecular dynamics with coupling to an external bath, *J. Chem. Phys.*, 81 (1984) 3684, <https://doi.org/10.1063/1.448118>.
72. H.J.C. Berendsen, D. Van der Spoel, R. Van Drunen, GROMACS: A message-passing parallel molecular dynamics implementation, *Comput. Phys. Commun.*, 91 (1995) 43–56, [https://doi.org/10.1016/0010-4655\(95\)00042-E](https://doi.org/10.1016/0010-4655(95)00042-E).

73. B. Hess, C. Kutzner, D. Van der Spoel, E. Lindahl, GROMACS 4: Algorithms for Highly Efficient, Load-Balanced, and Scalable Molecular Simulation, *J. Chem. Theory Comput.*, 4 (2008) 435– 447, <https://doi.org/10.1021/ct700301q>.
74. H.J. Berendsen, J.R. Grigera, T.P. Straatsma, The missing term in effective pair potentials, *J. Phys. Chem.*, 191 (1987) 6269– 6271, <https://doi.org/10.1021/j100308a038>.
75. J. Chandrasekhar, D.C. Spellmeyer, W.L. Jorgensen, Energy component analysis for dilute aqueous solutions of lithium (1+), sodium (1+), fluoride (1-), and chloride (1-) ions, *J. Am. Chem. Soc.*, 106 (1984) 903– 910, <https://doi.org/10.1021/ja00316a012>.
76. J. Åqvist, Ion-water interaction potentials derived from free energy perturbation simulations, *J. Phys. Chem.*, 94 (1990) 8021– 8024, <https://doi.org/10.1021/j100384a009>.
77. O.G. Bytner, G.D. Smith, Quantum Chemistry Based Force Field for Simulations of Poly(vinylidene fluoride), *Macromolecules*, 33 (2000) 4264-4270, <https://doi.org/10.1021/ma9918295>.
78. M.P. Allen, D.J. Tildesley, Computer Simulation of Liquids, second edition, Clarendon: Oxford, U.K., 1989.
79. T. Darden, D. York, L. Pedersen, Particle mesh Ewald: An $N \cdot \log(N)$ method for Ewald sums in large systems, *J. Chem. Phys.*, 98 (1993) 10089–10092, <https://doi.org/10.1063/1.464397>.
80. U. Essmann, L. Perera, M.L. Berkowitz, T. Darden, H. Lee, L.G. Pedersen, A smooth particle mesh Ewald method, *J. Chem. Phys.*, 103 (1995) 8577– 8592, <https://doi.org/10.1063/1.470117>.
81. G. Bussi, D. Donadio, M. Parrinello, Canonical sampling through velocity rescaling, *J. Chem. Phys.*, 126 (2007) 014101, <https://doi.org/10.1063/1.2408420>.
82. B. Hess, H. Bekker, H.J.C. Berendsen, J.G.E.M Fraaije, LINCS: A linear constraint solver for molecular simulations, *J. Comput. Chem.*, 18 (1997) 1463–1472, [https://doi.org/10.1002/\(SICI\)1096-987X\(199709\)18:12<1463::AID-JCC4>3.0.CO;2-H](https://doi.org/10.1002/(SICI)1096-987X(199709)18:12<1463::AID-JCC4>3.0.CO;2-H).
83. J.L. Yarnell, M.J. Katz, R.G. Wenzel, S.H. Koenig, Structure Factor and Radial Distribution Function for Liquid Argon at 85 °K, *Phys. Rev. A*, 7 (1973) 2130, <https://doi.org/10.1103/PhysRevA.7.2130>.
84. D. Chandler, Introduction to Modern Statistical Mechanics, Oxford University Press, 1987.
85. M. De Graef, M.E. McHenry, Structure of Materials: An Introduction to Crystallography, Diffraction and Symmetry (PDF), Cambridge University Press, 2007 p. 515.

Chapter 4

Layered hydrophobic honeycomb membranes designed for highly productive and efficient membrane distillation

4.1 Introduction

The design of new types of structured membranes is one of the most important targets for developing advanced membrane distillation operations, which are part of integrated membrane systems dedicated to the production of fresh water. A lot of research is addressed at the fabrication of new membranes with structural and chemical features able to overcome some of the current shortcomings, including productivity and thermal efficiency. The assembly of well-structured materials in membranes, with capability to work as physical interfaces for membrane distillation operations, is the ambition in this field, because high performing membranes are not available on the market yet. Within the frame of this thesis, the building up of extensively regular membranes was done keeping in mind structural and chemical features, which are in full accordance with the basic criteria of the membrane distillation (MD) process. The methodology used for preparing breakthrough membranes was Breath Figures, which is regarded as a bio-inspired manufacturing procedure. Briefly, it is a self-assembly process, which leads to the formation of honeycomb micro-scaled polymer patterns by the condensation of water droplets on liquid films. "Breath-figure" refers to the fog that forms when water vapor contacts a cold surface [1, 2]. Specifically, water droplets (Figure 4.1) work as pore builders through the polymeric solution leading to the formation of well-defined 3D polymeric architectures wherein pores are packed each other in honeycomb geometries (Figure 4.2). In this work the attention was directed to achieve controlled ordered structures in a honeycomb geometry. Firstly, the study developed controlled methodology for long-range ordered packed pores in polyethersulphone (PES) membranes then, the attention was focused on the preparation of an innovative bilayered HYFLON-AD PES honeycomb membrane. The idea was to use Breath Figures as preparation technique, with a point of view beyond progresses already achieved. The combination of several type of materials, modelled in order to control intrinsic and

superficial characteristics of membranes, was the leitmotiv of the work, for final application in Membrane Distillation (MD).

The necessity to have more control in membrane morphological structure, induced us to find those materials that thanks to their intrinsic and peculiar properties could interact among them in order to assist Breath Figure procedure leading to more ordered structure (Figure 4.1 and Figure 4.2). Then, when the procedure was validated, the objective was the research of those materials to combine with PES which thanks to their high hydrophobicity and low thermal conductivity could create the same identical structure with a honeycomb pattern but with reduced pore size and increased porosity. Approaches followed, procedures and mechanism, will be discussed in the next paragraphs.

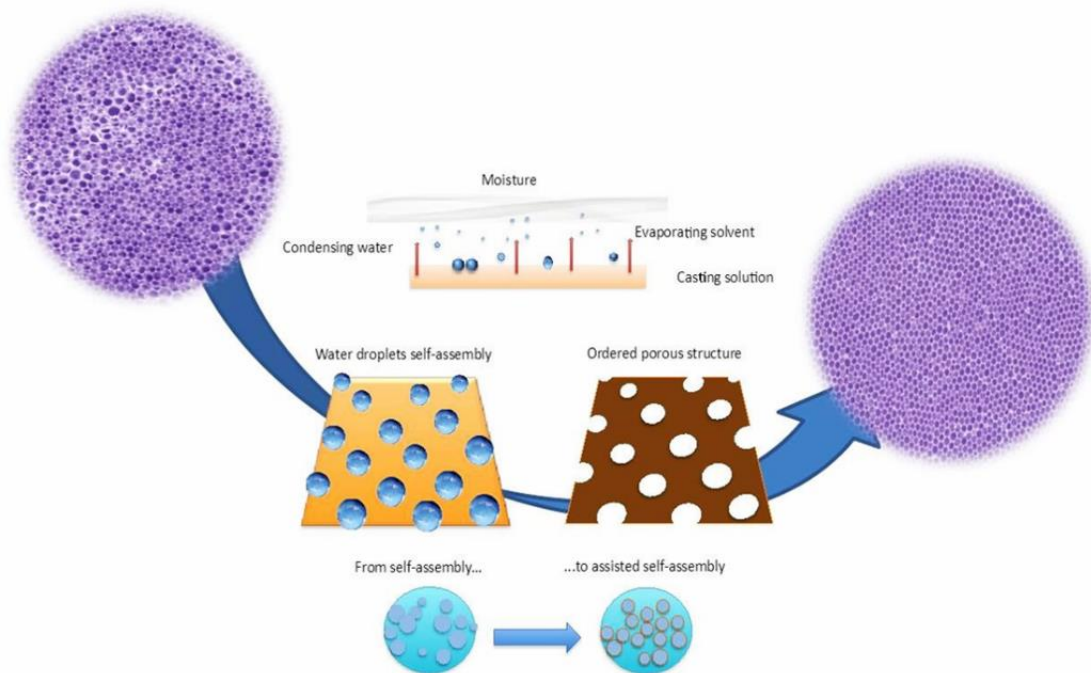


Figure 4.1. Schematic representation of Breath Figures self-assembly for achievement of honeycomb patterned porous structures.

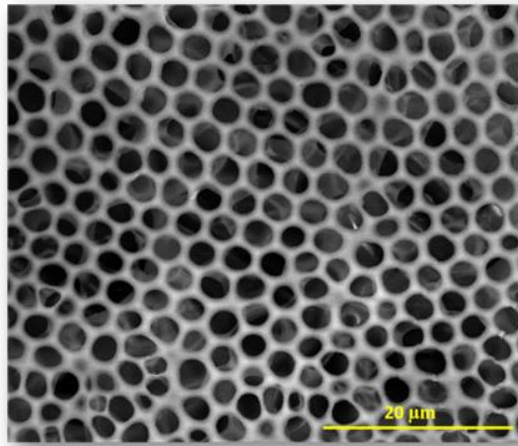


Figure 4.2. SEM pictures of a PES polymeric membrane with honeycomb geometrical structure (Mag 1600X).

4.2 From self-assembly to direct assisted self-assembly: a phenomenological study on bulk properties for preparation of honeycomb Polysulfone membranes

Extensive structural order is highly desired for the implementation of membrane processes for sea water desalination, including membrane distillation. In this case, narrow pore distribution together with defined pore size, structural order at long range, stability of the interfacial area, are necessary for an efficient process with a long operational time [3]. Several manufacturing methodologies have been proposed for the fabrication of highly defined textures, but often overly expensive materials/production processes, the use of pollutant materials, as well as the loss of controlled texture at long range, have resulted in being too restrictive for related scale-up.. Among the most breakthrough strategies, there is one inspired by the natural condensation of water droplets from humid air on cold surfaces, which is well known as we said breath figure self-assembly. Despite the literature referring to several models of honeycomb structures [4-6], the formation of highly ordered multiscale polymeric textures still remains a hard struggle. On the other hand, thermodynamics, kinetics, and entropy factors, which regulate the materials assembly, are generally somewhat complex and unclear [7-11].

Currently, there is a still considerable lack of knowledge about the forces dominating the degree of structural order on the scale, while the scale-up of defined structures realistically needs to use practical and efficient means for achieving desired features at longer range.

Also, there is the necessity to demonstrate this technique as a practical route for the preparation of honeycomb membranes with open regular pores from a large number of

polymers, including those with traditionally poor affinity to water and scarce ability to stabilize floating droplets at longer range.

Herein, a common PES with low affinity to water has been chosen as a polymer type due to its excellent thermal stability, outstanding toughness and suitability to come in contact with food and water. The objective has been to generate different chemical microenvironments and study the behavior of water droplets dynamics during self-assembly when the hydrophilic/ hydrophobic balance was changed in solution. Despite the fact that the technique seems to be easy to handle, the mechanisms leading to the formation of high-definition polymeric architectures appear to be rather complicated. Various controlling factors and mechanisms have been taken into account to explain the behavior of the droplet lattices during the tailoring procedure. In particular kinetics factor as solution viscosity and density of solvent used represented a starting point in order to have success in the mechanism. Speranza et al. [10] demonstrated that condensed droplets can freely move through media at lower viscosity, thus forming highly ordered lattices in a shorter time and also that 3D air bubbles networks can be formed when solvent lighter than water are used. At the same time thermodynamic effects stabilize the formation of well ordered nanopores array where involving Shimomura mechanism, which explains that the initial water droplets do not levitate and aren't ordered on the surface, and Marangoni forces that cause the submerging of water droplets into the organic solution. In this work, a commercial nonionic surfactant (Tween 20) [12], in a concentration ranging from 10^{-5} to 10^{-3} M, was chosen as a model surfactant to improve the hydrophilic/hydrophobic balance. It was also thought to create more complex blends by adding alcohols at different length. The aim was to achieve a very high degree of order through honeycomb film textures with well-shaped and well-sized pores through fruitful interactions established at the water-casting solution interface, thus suppressing local disorder and structurally random regions. In this work, the combination of PES/surfactant/alcohols allow to move from traditional self-assembly to assisted self-assembly due to suitable hydrophilic/hydrophobic ratio in mixture (Figure 4.3). As a result, packing pores with modulated size have been achieved in extensively controlled PES honeycomb geometries, where local disorders are entirely suppressed. The approach used appears somewhat interesting to control kinematic and thermodynamic forces in order to give new inputs to the production of this kind of membrane on a larger scale, especially for polymers exhibiting low ability to stabilize water droplets during flotation through the solution.

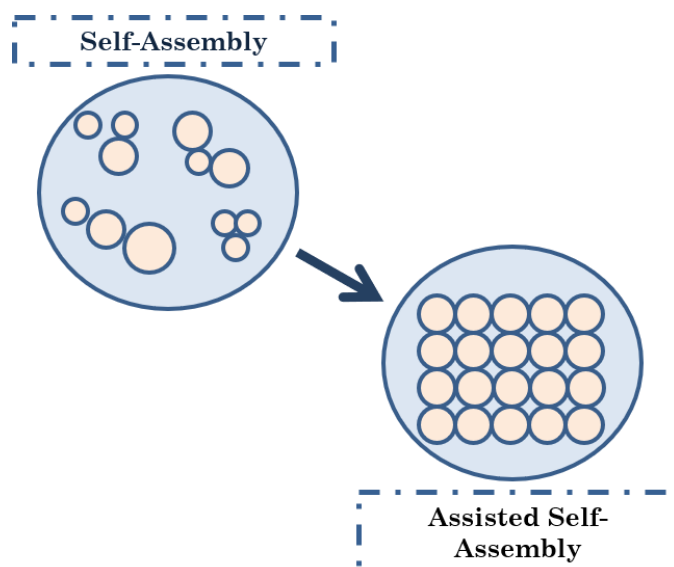


Figure 4.3. Schematic representation of water droplet fluctuation during Self-Assembly and Assisted Self-Assembly

4.2.1 Influence of the Surfactant on the Surface Structural Order

At first mixtures of PSU in DCM containing 2-propanol at 12 wt % and Tween20 at different content (10^{-5} – 10^{-3} M) were prepared. The behavior of the solutions with increasing content of surfactant has been examined when coming in contact with humid air, while kinetics and thermodynamic aspects have been analyzed as well. As the concentration of the surfactant increases, a local increase in gelation comes through the solution, thus resulting in an increased kinematic viscosity (Figure 4.4).

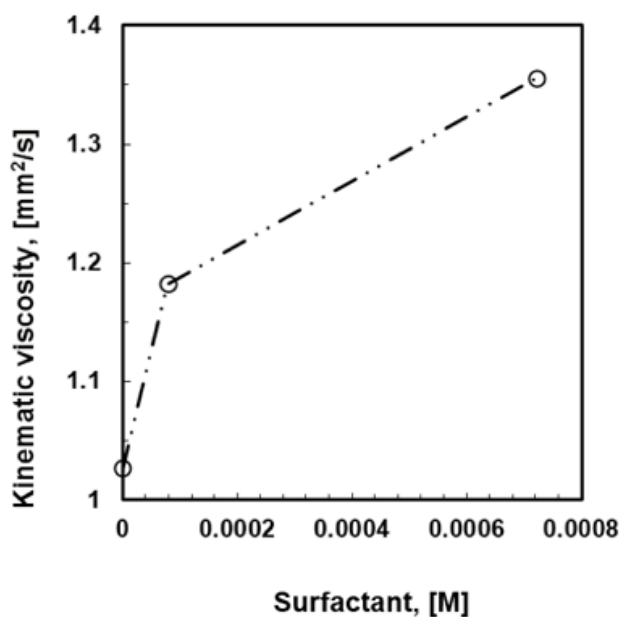


Figure 4.4. Effects of the surfactant loading on the kinematic viscosity of the PSU/DCM/2-propanol (12 wt %) solutions.

In the absence of surfactant, 2-propanol is unable to provide the assistance necessary to fully prevent local disorder for the polymer PES. Undesired broadness in the pore distribution takes place due to the coexistence of different porous domains, thus resulting in an average pore size of approximately 3.6 μm (Figure 4.5a).

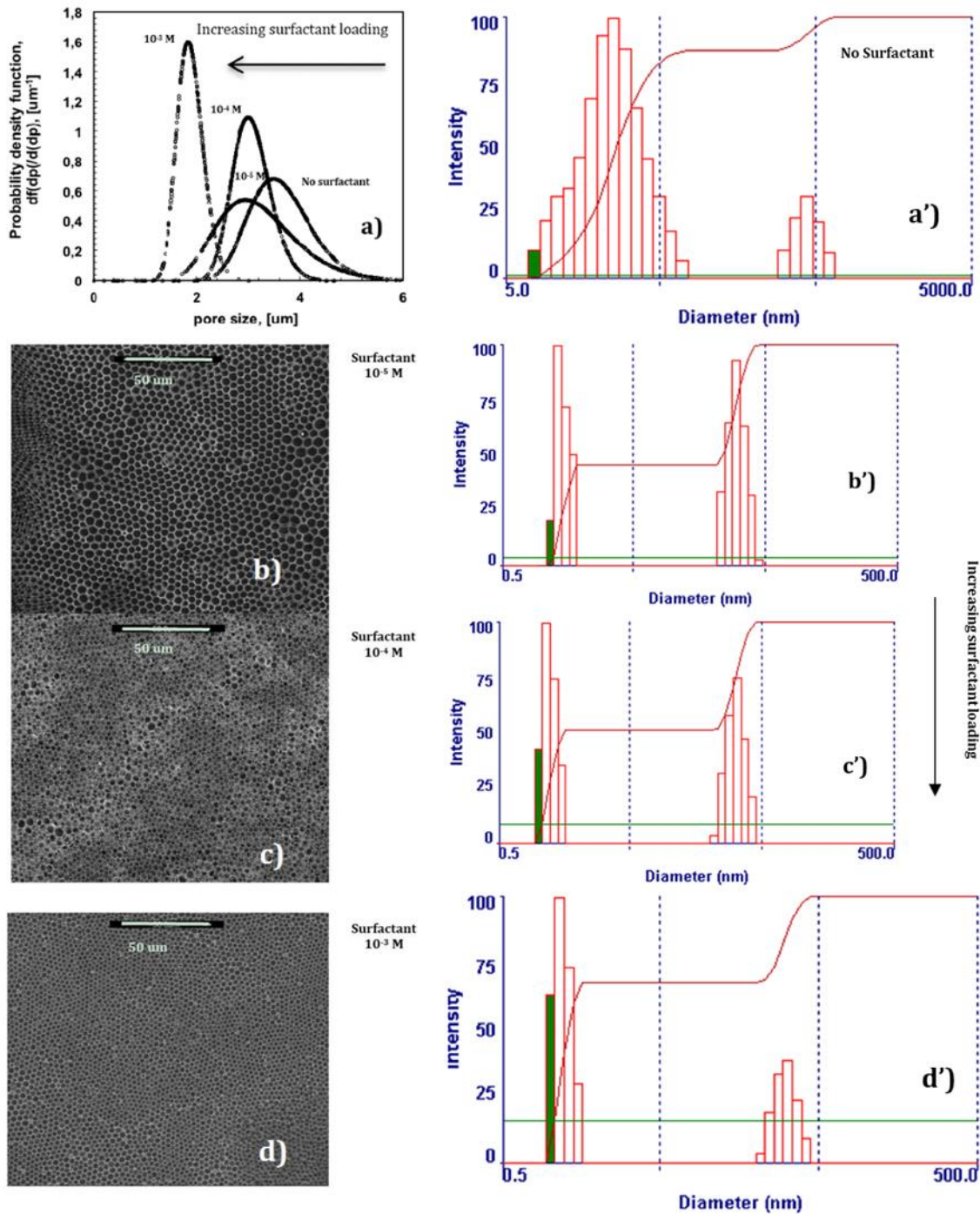


Figure 4.5. Changes in the pore size and distribution with rising content of surfactant (a); Effects of surfactant/alcohol complex on membrane morphology (SEM micrographics (b–d) and formation of aggregates in precursor polymeric solutions (Dynamic Light Scattering (a'–d'))).

Instead, a progressive addition of Tween20 to the solution leads to the gradual control of the dynamics of the water droplets, making the collisions softer. SEM micrographs show how larger and geometrically confused regions progressively make space for more defined lattices as the content of the surfactant increases in the mixture (Figure 4.5b–d). This suggests a slowing down of the droplets during motion, which avoids coalescence or uncontrolled growth rate at the margin of the single lattices. As a result, an enhanced degree of the order of the texture is obtained (Figure 4.5a). In this context, the surfactant assists the polymer in the stabilization of droplets during self-assembly, producing additional fluid viscosity at the droplet-solution-droplet interface. The reduced kinetics prevents the nearest soft particles from merging in bigger bubbles, limiting or, at best, suppressing local disorder at the boundary of the droplet islands. Dynamic Light Scattering (DLS) experiments yield further indications about a cooperative interaction between the surfactant and polymer (Figure 4.5 a'–d'). In the absence of surfactant, two distinct populations of aggregates can be appreciated in solution within a size range of 5–5000 nm, the first one covering a broader range of heterogeneous assemblies (Figure 4.5a'). The gradual addition of the surfactant in solution significantly reduces the broadness of two populations, decreasing the aggregates' size by one order of magnitude, and leads to a gradual diminution of the second population in favor of the smallest one (Figure 4.5b'–d'). Because of the complexity and heterogeneity of the mixtures, establishing the shape and type of the aggregates is not easy at this stage. However, it is undoubtedly due to the relationship between the increasing uniformity of aggregates in solution and the major order of the final texture, which can be regarded as the result of a cooperative action of the various components dispersed in the mixture. It is also relevant to observe how a mono-dispersive pore size distribution matches with a gradual reduction of the pore size as the surfactant rises in content (Figure 4.5).

Given that the radius of the droplets is time-dependent and proportional to $R < t^{1/3}$ in the beginning, and to $R < t$ in the end [9], very narrow pore size distributions with the formation of a smaller pore size can be regarded as the result of a massive nucleation and a reduced droplet growth rate. There seems to be quick droplet saturation over the liquid surface in contact with moisture, while the boundary of each single droplet island becomes indiscernible at nearly the highest loading of surfactant. What described leads to the regular and uniform structure shown in the figure (Figure 4.5d). In this regard, the imprinting action of the droplets is exhausted when the lattice is formed over the entire surface area of the solution touching the moisture. However, this can also be considered a reasonable consequence of a very fast and assisted moisture uptake. Indeed, an increase in the overall surface tension—a value of 28.30 mJ/m² against 26.50 mJ/m² estimated for the pure

solvent—has been measured for solutions at the highest amount of surfactant. This would suggest that a large number of polar head groups is directed outward from the surface and is prepared to interact with condensing droplets. In order to confirm the ability of the surfactant to interact favorably with the water droplets, interfacial tensions have been measured at the interface established between a single water droplet and the surrounding polymeric solution with increasing content of Tween20. The droplets have been automatically injected into the solution by using a syringe and the surface tension value has been measured according to the pendant drop method. Indeed, the decrease in the interfacial tension values with rising concentration of the surfactant confirms a tendency of the system to reach a minimum of energy (Figure 4.6).

This means that when the surfactant dissolved in the polymeric solution comes in contact with water droplets, the related polar heads establish attractive hydrophilic interactions at the interface while the hydrophobic tails are pointed towards the rest of the nonpolar solution, thus causing a decrease in the overall interfacial tension. These experimental findings are in full agreement with those found by Kojima et al. [13] about the ability of amphiphilic copolymers to establish hydrophilic interfacial forces with water droplets during the formation of honeycomb patterns. Herein, the ability of the surfactant to enhance the process of stabilization of the droplets becomes much stronger at higher concentrations, resulting in a higher uniformity of the structural order as well as in a gradual reduction of the pore size (Figure 4.5a–d). This means that the larger availability of the surfactant leads to quicker water uptake and stabilization over the entire surface area of the solution exposed to humid air.

On this basis, there is a clear indication about the necessity to adjust the hydrophilic/hydrophobic balance in solution in order to move water droplets from self-assembly to assisted self-assembly, especially when using polymers with poor ability to rearrange themselves and interact at the interface of local different microenvironments.

It is relevant to observe how the hydrophilic/hydrophobic balance becomes somewhat marked at higher concentrations of surfactant, which is greater than that indicated as necessary to reach the critical micelle concentration in a binary aqueous solution (CMC, 10^{-2} mM) [14]. In this respect, it must be stressed that the working chemical environment is rather different from the aqueous one, the mixture being nonpolar and containing four different components. This makes it difficult to unequivocally identify the aggregation state of the surfactant, especially in the presence of additional amphiphilic compounds such as alcohols, which allow intermolecular interactions to establish within hydrophilic and hydrophobic domains, causing important changes in CMC as well [15]. Nevertheless, it is unquestionable

that the increase in the concentration of surfactant causes a major number of monomers in proximity to the surface and in the bulk; these monomers could aggregate but also continue to migrate freely towards the surface, making polar heads promptly more available to interact with water and assist the dispersion of the aqueous phase in the continuous oil phase, as clearly confirmed by decreasing interfacial tension values (Figure 4.6).

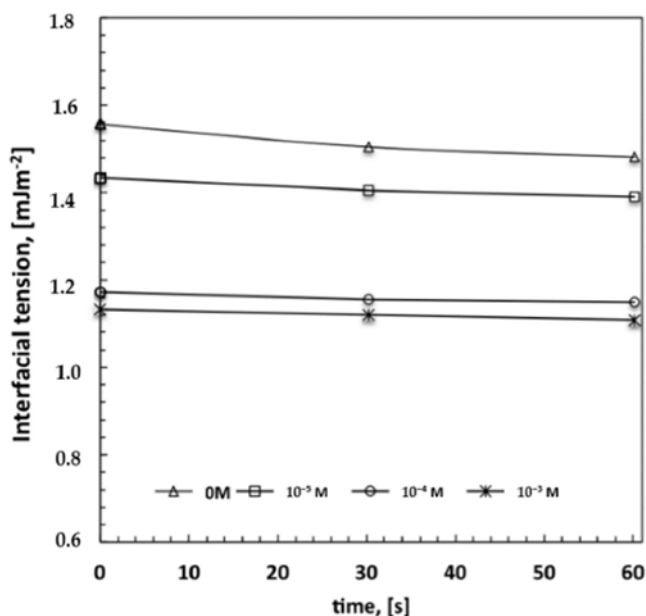


Figure 4.6. Estimation of interfacial tension values between a water droplet and polymeric solution containing increasing amount of surfactant.

The average interfacial tension values were calculated from five measurement results with a standard deviation that decreases from ± 0.23 to ± 0.13 with rising surfactant content into the mixture. The result is a quicker formation of lattices from a larger number of smaller, stabilized water droplets, which leave an open pore size uniformly distributed over the entire surface area of the film. This clearly implies a predominance of droplet nucleation over the related growth rate.

4.2.2 Influence of the Alcohol Chain Length on the Pore Size

The pore size can be regarded as the result of a different balance between droplet nucleation and the growth rate steps. A massive droplet nucleation is, in fact, expected to lead to a very fast coverage of the surface with a formation of smaller pores, whereas a lengthy rearrangement extends the growth rate, yielding bigger air bubbles. In this respect, the chemistry of the polymeric mixture has been further changed with the purpose to direct the time-scale of nucleation and the growth rate, respectively. Alcohols with different structure $(CH_2)_n = 2-4$ containing the OH end group have been added to the mixture, keeping the

concentration of the surfactant constant at 10^{-4} M, in order to examine the effects of changing hydrophobic/hydrophilic balance on the pore formation. As shown in Figure 4.7, the addition of alcohols to the polymeric mixture brings about a marked effect on the value of the overall surface free tension. The latter tends to increase with the length and bulky chain of the alcohol, while the pore size decreases from 4.0 to 0.8 μm through the overall film surface.

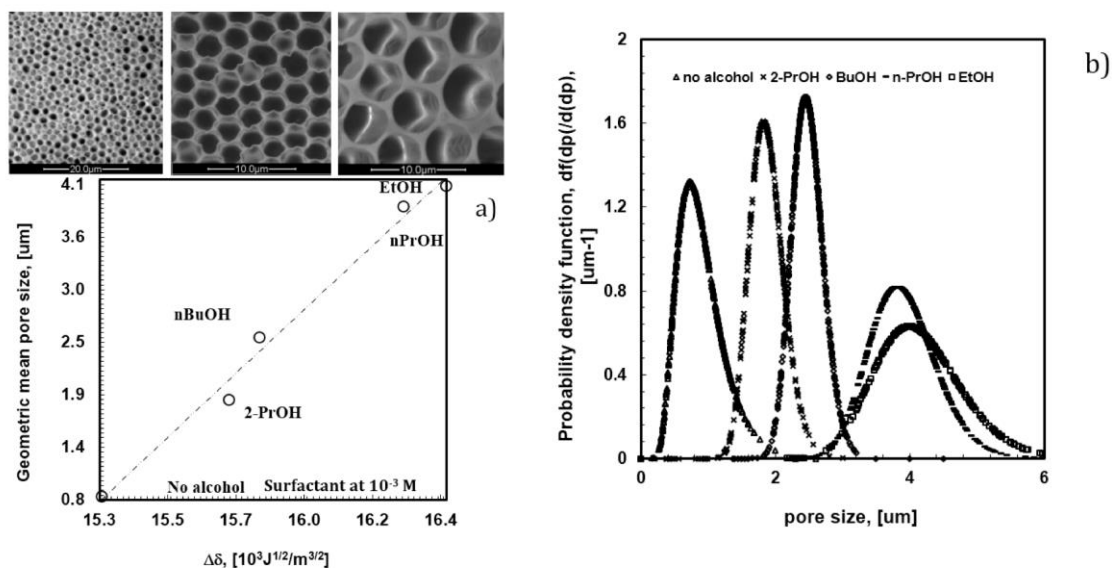


Figure 4.7. Variation of pore size (a) and pore distribution (b) as a function of the different length and bulky chain of alcohols contained in PSU/DMC solutions with surfactant at 10^{-4} M.

The increase in the surface free tension affects the scale of affinity, causing inevitably higher values of the solubility parameter (δ) of the solution. The latter is a thermodynamic indicator of the attractive or repulsive interactions established between two systems coming in contact [16]. The difference between the solubility parameters ($\Delta\delta$, $10^3 \text{J}^{1/2}/\text{m}^{3/2}$) of two media yields a clear indication about the level of affinity; thus, small differences indicate a great affinity, whereas large differences suggest a poor attraction. Concerning the systems investigated in this study, smaller differences have been estimated between the solubility parameters of water ($72.86 \text{ mJ}/\text{m}^2$ at 20°C) and the composite solutions when the lipophilic component of the alcohol overcomes the hydrophilic one. In this case, a smaller pore size is obtained (Figure 4.7a). Differently, a larger pore size is measured for films prepared from solutions containing alcohols with higher polar character (Figure 4.7a).

Undeniably, alcohols with shorter tails exhibit increased polarity and have a higher ability to interact with the polar heads of the surfactant, thus reducing their availability towards water droplets. On the contrary, alcohols with longer and bulky chains exhibit more amphiphilic character, taking their dissolution closer to the hydrophobic regions of the

surfactant, where dispersive cooperative intermolecular interactions are better established. This implies a larger availability of the polar heads to face water droplets. As a result, a quicker nucleation of droplets with formation of smaller pore size is obtained when polar heads of the surfactant are more available. This can be envisaged as a direct consequence of a higher hydrophobic molecular interaction established into the bulk of the polymeric solution.

In this regard, it is also relevant to observe that such an availability of the head polar groups at the solution surface-air interface becomes much higher in the absence of alcohols. This suggests a decisive role of the alcohol in the rearrangement of the surfactant at the water-solution interface. Indeed, the difference between the solubility parameters of water and the casting solution is somewhat low in absence of alcohol (Figure 4.7a). In this case, intermolecular interactions between alcohols and surfactant fail necessarily and a larger number of free monomers in solution orient the polar part outward, yielding major availability to interact with floating droplets. Under these conditions, a larger number of small droplets are formed and stabilized over the entire surface area in contact with humidity. The consequence is a massive nucleation, which leads to highly ordered textures with pores of $0.8 \mu\text{m}$ (Figure 4.7b).

Again, it is also relevant to examine the incidence of the alcohol length chain on the kinematic viscosity. Figure 4.8 shows how the rising molecular weight together with the bulky structure of the alcohol causes an effective increase in the solution viscosity (Figure 4.8).

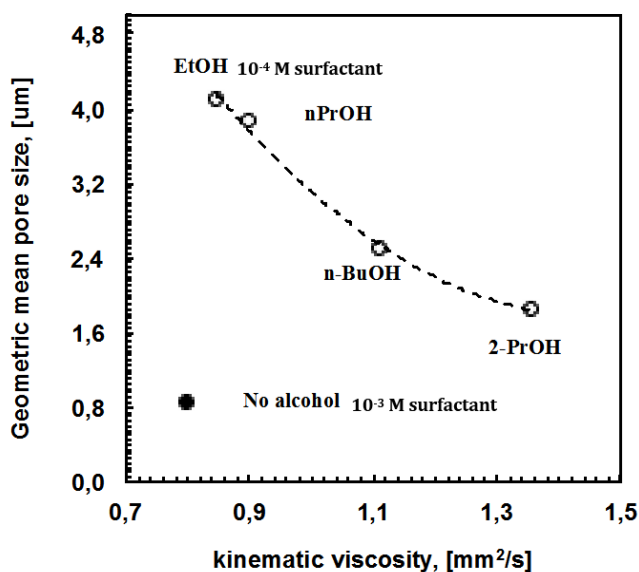


Figure 4.8. Geometric pore size vs. kinematic viscosity for solutions (o) containing surfactant at 10^{-4} M and alcohols with different length and bulky chains.

This is expected to further enhance the capability of encapsulation of the polymeric solution, thereby reducing the risk of coalescence and harsh collisions.

The viscosity factor becomes, however, non-influential in the absence of alcohols; the rate of moisture uptake and coverage for the entire surface area rather than speedy droplet flotation seems to decide the smaller pore arrangement in ordered textures. Comparing a solution of PSU/DMC containing surfactant at 10^{-4} M with ethanol at 12 wt % and a solution of PSU/DMC containing surfactant at 10^{-3} M without alcohol, similar values of kinematic viscosity can be appreciated (Figure 4.8); however, a significant reduction of around 80% is observed for the pore size as the polymeric solution contains surfactant alone. This suggests that different mechanisms can take place during droplet self-assembly. The surfactant favors moisture uptake and a quicker nucleation rate, whereas the alcohol competes with water in the establishment of intermolecular interactions with the surfactant, reducing the related degree of freedom with the effect of extending the growth rate of the floating droplets depending on the intrinsic polar character of the mixture.

On this basis, the surfactant seems to have a decisive and predominant role in the uptake and stabilization of floating water droplets, whereas the alcohol affects the time scale, resulting in a modular pore size.

It's clear that changes in the hydrophilic-hydrophobic balance cause a competition between droplet nucleation and growth rate steps. Using other classes of amphiphilic compounds, changes in this balance are expected to further modify the time scale with consequences on the final texture of the polymeric porous film [2].

The intent of this work was to demonstrate the necessity to move from traditional self-assembly to assisted self-assembly approaches, thus preserving structural order and yielding uniformly modulated pore size at longer range. Of course, the precondition for a successful scale-up has to pass through the adjustment of thermodynamic and kinetic parameters and, consequently, the manipulation of bulk properties of the solutions used, enabling one to contrast undesired effects due to low ability of the polymer to stabilize the droplets but also to the frequent sensitivity of the droplet assembly to little changes in the external environment.

4.3 Organization of ordered honeycomb PES membranes via hydrophobic ionic liquid crystals surfactant

In the perspectives to achieve more ordered geometries, toward direction of Assisted-Self Assembly, a new class of materials has been explored as surfactants: Ionic Liquid Crystals (ILCs) with a cationic head and chains of different length. Ionic liquid crystals [17] can be considered as materials that combine the properties of liquid crystals and ionic liquids, as mentioned in Chapter 3. In particular herein was explored the potential of a subclass of pyridinium salts, viologen salt, as surfactant in order to move hydrophilic/hydrophobic balance in favor of new fruitful interaction. They are an example of electrochromic materials and they include all those compounds generated by the quaternization of the 4,4'-core bispyridyl, i.e. the 4,4'-bispyridine salts 1,1'-disubstituted. This kind of material in this research work, was used to assist self-assembly in order to improve the structural order, in favor of a greater surface roughness, higher hydrophobicity and porosity, and therefore better structural-properties relationship.

In fact, comparing Tween 20 and 1,1'-ditetradecyl-4,4'-dipyridinium [bis(trifluoromethanesulfonyl)amide (14Bp14(Tf₂N)₂)] used both as surfactants, there is an increasing in wetting resistance in time (Figure 4.9) when the viologen is used, thanks to the presence of the two long symmetric saturated alkyl chains and of the hydrophobic anion, mentioned before, with respect to polar head of Tween 20. Hydrophobicity is one of the most important parameters for having good performances in water desalination (Membrane Distillation MD). Measurements were carried out with water as liquid probe achieving results showed in the following graphs with a standard deviation of ± 0.5 .

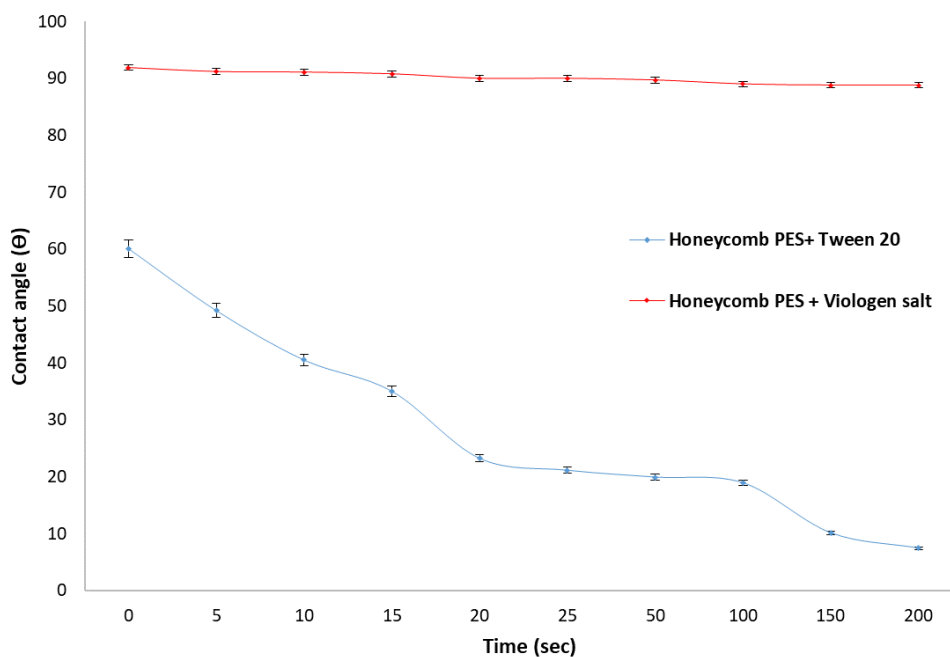


Figure 4.9. Differences in resistance to wetting measured by Contact Angle (θ) for PES honeycomb membranes with Tween 20 and PES honeycomb membrane with viologen salt (both at concentration percentage of 15 wt %).

In previous work [12], Tween20 was successfully used to obtain extensive structural order in PES honeycomb surfaces under humid atmosphere. However, this surfactant caused a hydrophilic character for the surface making it unsuitable for MD purposes.

On the other hand, the attempt to use commercial ionic surfactants such as imidazolium derivatives was fairly modest due to the inconsistency of the membranes. Therefore, the necessity to get a suitable hydrophile/lipophile balance (HLB) with marked hydrophobic character for membrane surfaces let us identify the family of viologen salts as a good source of compounds having desired features. Considering that 14bp14(Tf₂N)₂ has two long symmetric saturated alkyl chains and a hydrophobic anion, with relatively low charge density – the salt is, in fact, highly soluble in low polar solvents as DCM and poorly soluble in water –, a low HLB was expected with consequent increasing in the interfacial tension value. This enabled the viologen to prevent spreading of the water and stabilize the droplets, which maintain a globular shape leaving well designed and uniformly distributed pores, while undesired coalescence events were successfully suppressed. This experimental evidence is in a full accordance with what reported by Fukuhira et al. [18] about the role of HLB in the establishment of suitable interfacial tension for the stabilization of water droplets during self-assembly through polymeric solutions.

Fig. 4.10a shows the full spectra of the viologen in dichloromethane obtained by dissolving 80 mg of salt in 0.75 mL of deuterated solvent (0.072 M). Successively, a volume of 10 μ L

of water was added to the tube – this is in excess of the solubility of water in DCM of ca. 2.4 μL /0.75 mL of DCM – and a second spectrum was recorded; finally, an amount of 90 mg of polysulfone was further added to the NMR tube and the last spectrum of the mixture was recorded. All spectra were calibrated by setting the residual solvent resonance of all of them to 5.32 ppm. Fig. 4.10b shows clearly the aromatic region of the spectra, while the presence of water does not produce any significant effects on the viologen spectrum. It can be observed a very minor broadening of the resonances only due to no perfect homogeneity of the magnetic field. In contrast, there is a clear shift of the aromatic resonances of the viologen after the addition of excess PES and both aromatic signals of the viologen are deshielded. The shift is of about 0.1 ppm and suggests a strong interaction of the aromatic core of the viologen with polysulfone. The polysulfone aromatic resonances also appear to be affected by the presence of viologen, though the presence of water makes the lines broader.

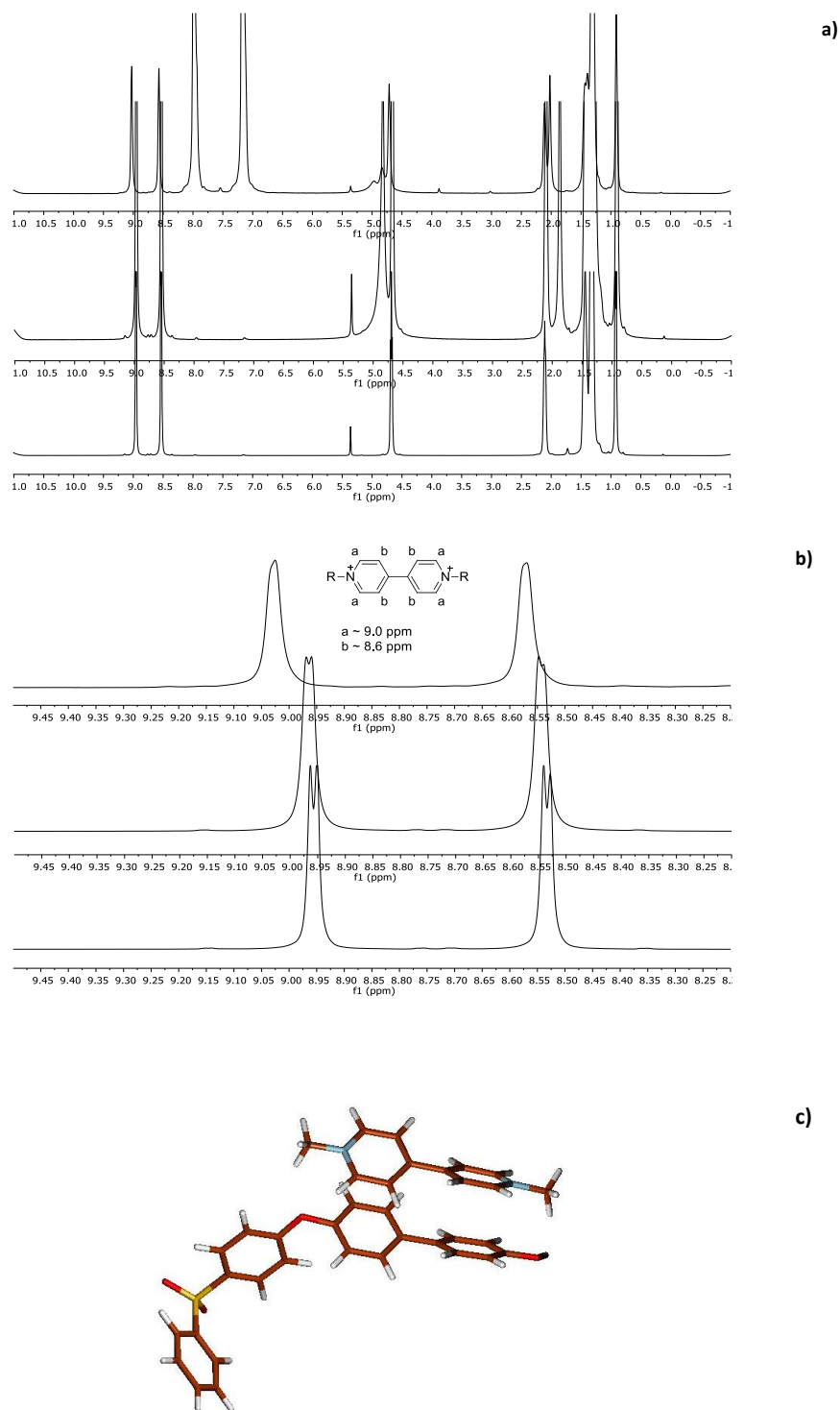


Figure 4.10. ^1H NMR full spectra (a) and aromatic region (b) (500 MHz, 300 K, CD_2Cl_2): 14bp14(Tf_2N) $_2$ (bottom); after addition of water (middle); after addition of PES (top). DFT optimized structure of the Viologen-PES model complex in DCM (c).

To further support these findings, it was also run a density functional theory (DFT) investigation of the interaction energy of simple model structures [13], [19-20]. Because charged species are involved, it has been important to include long-range solvent effects to estimate interaction energies, thus the PCM model has been employed for dichloromethane.

The optimized structure of the model complex is shown in Fig. 4.10c. The interaction energy, ΔE , is obtained as $\Delta E = E_{\text{cmplx}} - E_{\text{Viol}} - E_{\text{PES}}$, where E_{cmplx} is the electronic energy of the complex, and E_{Viol} and E_{PES} are the electronic energies of the optimized structure of isolated model viologen and model PES structures, still in dichloromethane. The result is $\Delta E = -18$ kcal/mol. The many approximations involved in the calculations does not allow a quantitative analysis of the results, nevertheless the calculated value is not negligible and it points to a significant interaction of the two moieties through π - π stacking.

These experimental and theoretical findings yield clear indication about a concrete cooperation between polymer and viologen salt with a remarkable effect on the structural definition of the membrane morphology, as largely confirmed by SEM micrographs collected onto PES honeycomb membranes prepared from solutions without (Fig. 4.11a) and with (Figure 4.11b) salt viologen. Indeed, locally disordered patterns observed onto the honeycomb PES membrane without 14bp14(Tf₂N)₂ leave the place to well-stitched honeycomb domains up when the viologen is added to the PES solution.

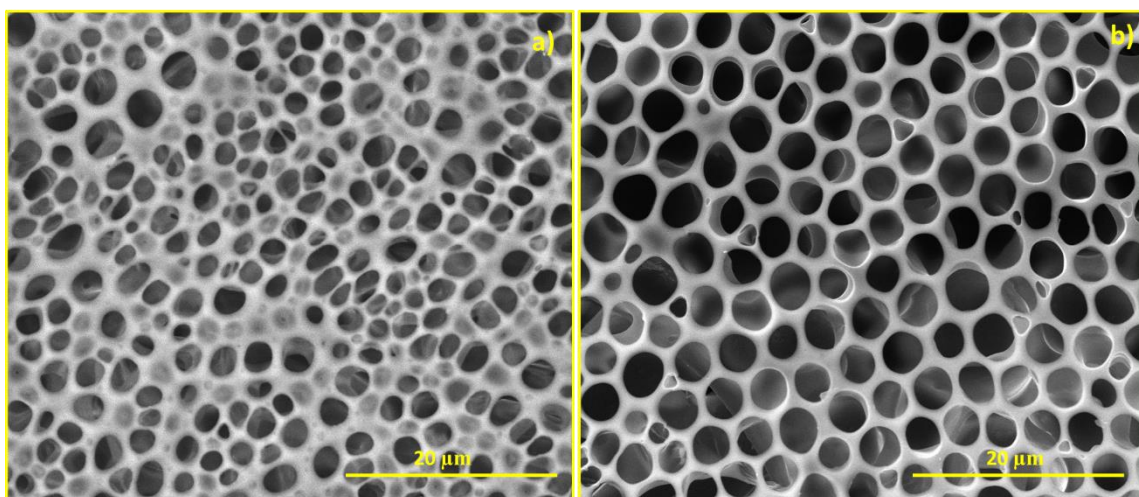


Figure 4.11. Different structures of Honeycomb membranes: a) PES honeycomb membrane without a) and with, b) viologen salt as surfactant. Magnification 5000 X.

This kind of membranes have the structure, very close to that considered ideal in membrane technology: perfect and ordered pores that can produce the same events in several points of membranes surface. The close correlation between honeycomb morphologies, overall porosity and resistance to wetting have made it ideal for this kind of technology, reaching higher values with respect to traditional commercial membranes. This happened both in terms of fluxes and mass transport across membrane pores. Despite of, we have encountered critical issues in Membrane Distillation performances. It's important to consider that PES honeycomb membrane was dipped in a solution of HYFLON AD/HFE (0.5 w/w), in order

to impart a hydrophobic character to the surface without troubles for the honeycomb texture. The typical zigzag profile of this kind of geometry produced indeed an important microscale roughness ($R_a = 473 \pm 90 \mu\text{m}$), which is undoubtedly responsible for the enhanced hydrophobic character of the membrane. Unfortunately, the membrane pore size has been too much large to prevent wetting events with long time, even if coated with hydrophobic moieties. In fact a preliminary test carried out with a NaCl solution of 5mM, lead to a not competitive rejection value for MD process (Figure 4.12). In this direction new strategies have been implemented, combining per-fluorinated materials, mechanical supports and tailor-made honeycomb membranes. The multi-layered honeycomb membranes allowed to achieve greater fluxes, with competitive rejection factors. This methodology will be discussed in detail the next paragraph.

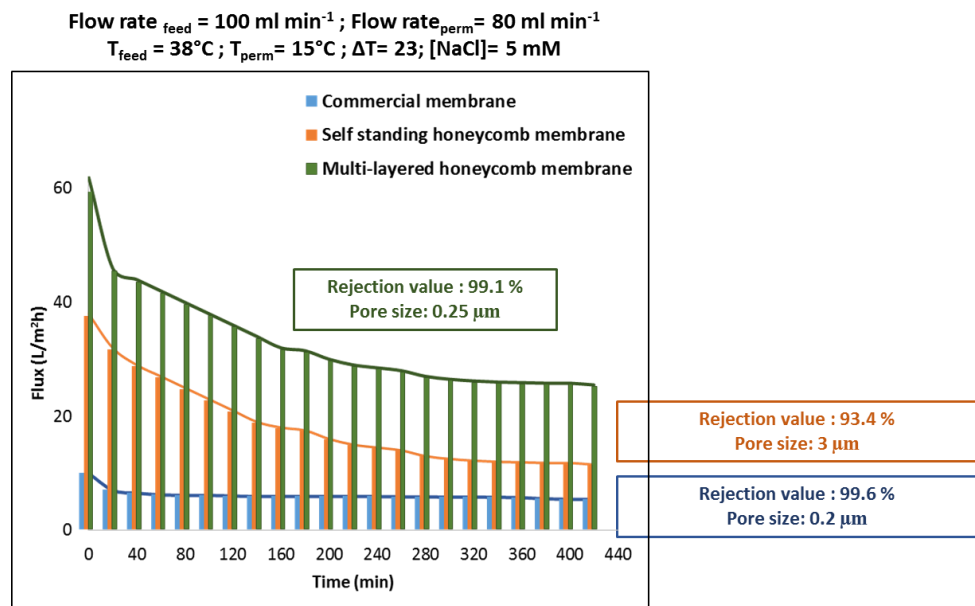


Figure 4.12. Flux and rejection achieved with: PVDF commercial membrane; Self-standing PES honeycomb membrane (hydrophobized with a dip coating in HYFLON 0.5 wt % solution); Multi-layered honeycomb membrane enriched of HYFLON AD nanocoating and of a mechanical support.

4.4 Layered honeycomb membranes: HYFLON AD porous nanofilm suspended onto PES honeycomb top surface

As we said in introduction chapters, today, there is a great demand of advanced materials-based processes designed to supply clean water from natural sources. Membrane Distillation has a great potential in water desalination. Despite of Osmosis Reverse is the leader technology in desalination, high energy consumption and brine disposal are problem which can bring limited recovery of water. The integration of other membrane thermal process such

as a Membrane Distillation, can give a good response due to lower operating temperatures and pressures, higher rejection factor, and lower susceptibility to concentration polarization phenomena.

One of the problems, is certainly the possibility to find membrane materials with suitable structural and chemical features that represents the suitable combination to use them in MD for an efficient production of desalted water. Onto membrane surface a large number of well-shaped pores uniformly spread through a nanostructured skin layer would distinguish the placed interface, to achieve more interesting results. From the productivity point of view, this aspect was observed and validated in the work, but the further investigation for a choice of materials at low thermal conductivity would be a practical route for solving the bottleneck in the energy consumption. For the first time, a nanostructured porous film has been textured from HYFLON AD solutions and suspended onto a honeycomb sub-layer by using a BF method. It has been generated an ultrathin fully-fluorinated porous membrane ($\delta 80 \pm 5$ nm) from a low thermal conductivity material (HYFLON AD) (around $0.1 \text{ Wm}^{-1}\text{K}^{-1}$), suspended then on a thicker orderly honeycomb pattern ($\delta 40 \pm 2$ m). In this way it was possible to find a suitable compromise between structural and chemical qualities for a sustainable desalination. Furthermore, HYFLON AD as a semi-crystalline nature of the hydrophobic polymer, which makes self-standing films somewhat brittle and difficult to manage, but on the other hand, a textured sub-layer was necessary to provide everywhere a rigid structural order for the formation of uniformly extensive ultrathin layer with targeted morphological features.

Honeycomb PES membranes, widely studied in the first part of the work, have been considered with the suitable features as the ideal support for ultra-thin HYFLON AD nanocoatings, prepared using the same BF technology. In particular, PES membranes containing viologen salt, after studies carried out on the basis of pore size distribution and interfacial tension, have been chosen as the ideal combination of materials for our purpose. PES honeycomb membranes prepared from mixture of polymer and $14\text{bp}14(\text{Tf}_2\text{N})_2$ showed uniformly distributed pores around $3 \mu\text{m}$, which are perfectly packed in a long-range honeycomb geometry against membranes prepared without the viologen salt and exhibiting a broader pore distribution with a mean pore size of $3.5 \mu\text{m}$. It was observed also how measurements of interfacial tension at solution-water droplet interface showed a slight increasing in the value when the PES solution was added with $14\text{bp}14(\text{Tf}_2\text{N})_2$. A value of $1.1 \pm 0.2 \text{ mJ/m}^2$ was estimated for solutions containing PES without viologen salt while a value of $1.5 \pm 0.2 \text{ mJ/m}^2$ was measured for the solution containing both the PES and viologen salt. Thus, this ordered open honeycomb structure could be regarded as an ideal

lattice on which a thinner porous layer can be further suspended. Nevertheless, the suspension of a uniform tiny film on somewhat large air voids required the establishment of suitable controlling interfacial forces [21]. Anyway, as we said before, the prevention of wetting in desalination, due to a not suitable pore size, brought our studies the finding of new material: the HYFLON AD. The hydrophobic character with low thermal conductivity, make its manipulation ideal for better performances in MD process with a selectivity-productivity trade off which go in a single direction. From a generical point of view from our studies was possible to detect:

- Local disorder suppressed when in PES solution was added $14\text{bp}14(\text{Tf}_2\text{N})_2$ as surfactant (Figure 4.13b and c) with uniformly pore size distribution with respect to PES honeycomb membrane without the viologen salt (Figure 4.13a).
- Reduced pore size in HYFLON AD nanocoating with respect to traditional PES honeycomb membranes (Figure 4.13d and e). Detail about pore size distribution of different systems are reported in Figure 4.14.

Procedure used and structure properties relationships will be discussed in the next paragraphs.

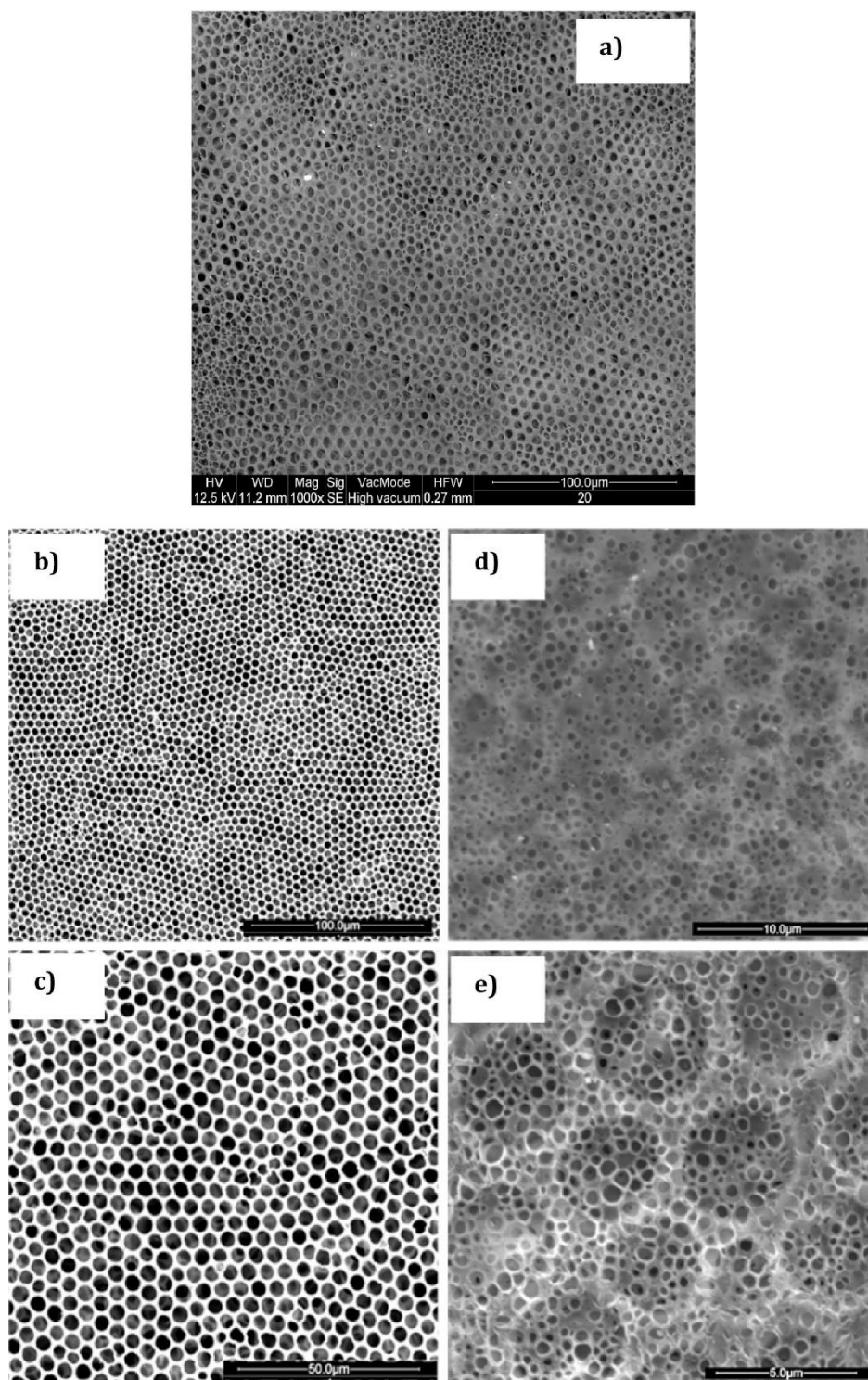


Figure 4.13. SEM micrographs: (a) Image collected onto PES honeycomb membranes without viologen salt, (b) and (c) images collected onto PES honeycomb membranes containing the viologen salt (enlargements at 10,000 and 16,000 \times), (d) and (e) images collected on the ultrathin suspended HYFLON AD layer (enlargements at 1000 and 2000 \times).

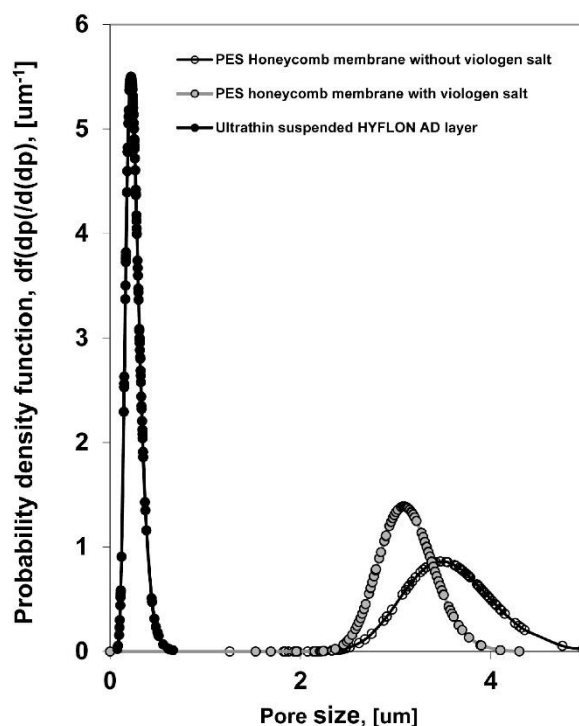


Figure 4.14. Pore size distribution for PES honeycomb membranes with and without viologen salt and with ultrathin suspended HYFLON AD layer.

4.4.1 HYFLON AD nanocoating preparation

In order to make the nanostructured membrane more handle and resistant to mechanical solicitations, a polyamide-based support ($\delta = 100 \mu\text{m}$) has been used during the formation of PES honeycomb membranes. Then PES honeycomb sub-layer has been dipped initially in ethanol (22.10 mJ/m^2) in order to impart a temporary hydrophilic character to the membrane and let water (72.80 mJ/m^2) spread and enter temporarily inside the big pores. In this way, a uniform shield can be formed for the successive hydrophobic HYFLON AD solution ($4.8 \pm 0.2 \text{ mJ/m}^2$). Then, the fluorinated nanofilm has been formed at the interface of two liquids, while water droplets from surrounding humid air have shaped further smaller pores through the entire polymeric layer according to BFs (Fig. 4.14d and e). The relatively low amount of fluorinate solution adsorbed onto the honeycomb sub-layer together with the very quick evaporation of the solvent leads shortly to the full perforation of the nanofilm. At the same time circularly shaped pores with a very narrow distribution and a size less than of one order of magnitude can be appreciated with respect to PES honeycomb sub-layer. Indeed, the solvent evaporation elapses rapidly so that a large water uptake is induced, while the hydrophobic character of the solution prevents droplet spreading. As a result, the area of each single big pore (around $5 \mu\text{m}^2$) estimated for PES honeycomb membranes is split in

many smaller pores, each one covering an area of $0.05 \mu\text{m}^2$ for a total surface porosity of 9.45%.

4.4.2 Structure–properties relationships

Membranes produced were characterized from several points of view, in order to evaluate those morphological parameters that make them suitable for desalination via Membrane Distillation technology.

From mechanical tests, it was confirmed a slight increase of 8% in the Young module for membranes with support, while the tensile strength reached a value of $25 \pm 2 \text{ Nmm}^{-2}$, which is around 9 times higher than that estimated for self-standing PES honeycomb membranes (Figure 4.15a and b).

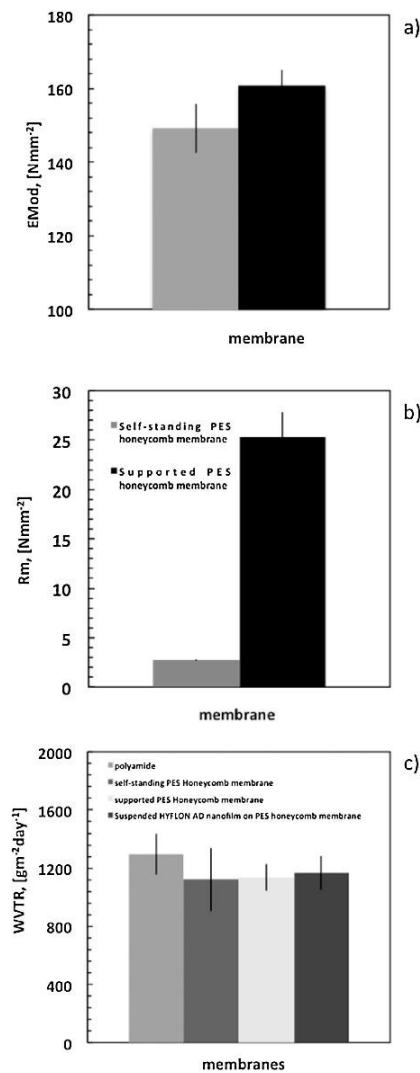


Figure 4.15. Effect of mechanical support on mechanical resistance (a and b) and water vapor transmission rate (WVTR) (c) at 25 °C.

Permeability tests have been carried out according to the right cup method procedure, in order to assess possible added resistance to the water vapor transfer. Figure 4.15c shows a comparison of the values of the water vapor transmission rate (WVTR) measured at 25 °C for the membranes at different fabrication steps. The experimental evidence showed that the mechanical support does not affect the WVTR properties of membranes. This is due to the fact that the selective layer is represented from HYFLON AD nanocoating, characterized from a reduced pore size and increased overall porosity. Furthermore, this coating is very thin, leading to much higher breathability and higher fluxes.

The role of chemical and morphological changes in the surface has been also examined in relation to wetting properties. Contact angle measurements have been performed in order to assess the resistance to water and salt solutions spreading. PES honeycomb membrane showed a good resistance to water (around $\theta = 115^\circ$) due to the singular honeycomb topography that contrasts the liquid spreading according to the Cassie–Baxter's rule [22], where the drop of liquid does not wet the whole the surface below, but only lies on the peaks of the surface roughness, leaving air trapped between them. So the surface roughness of membranes produced has the responsibility in the good hydrophobic character. However, when the surface comes in contact with NaCl solution (5 mM) at a lower surface free tension, a quicker spreading has been observed resulting in contact angle values of around 80° (Fig. 4.16a).

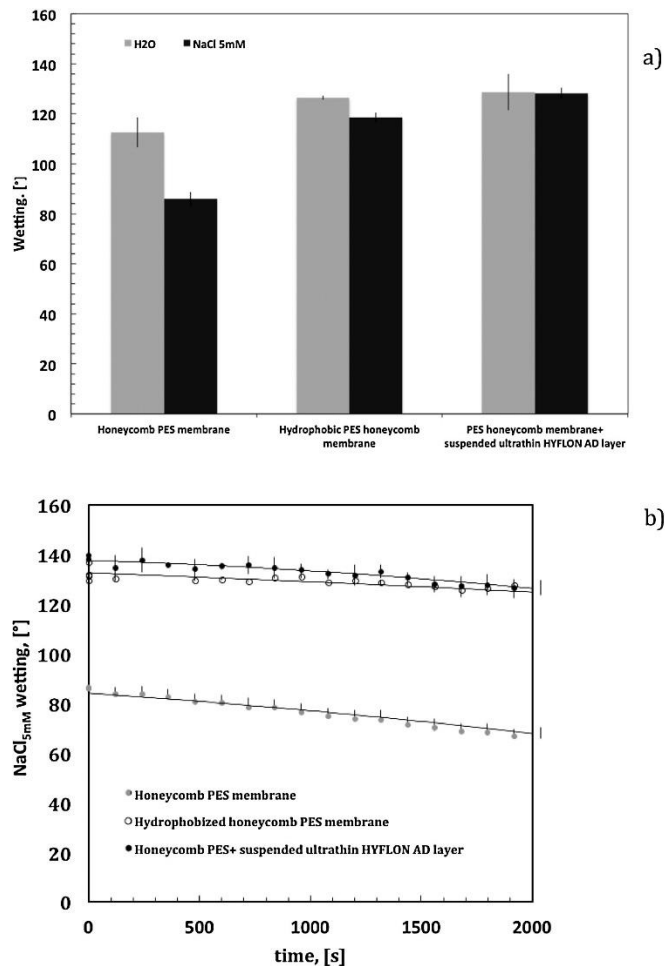


Figure 4.16. Wetting properties estimated for honeycomb PES membranes with and without suspended porous HYFLON AD nanofilm: Contact angle values at time zero (a) and kinetics (b) for pure water and NaCl solution 5 mM.

A better and durable result was instead achieved when a porous nanofilm of HYFLON AD is suspended onto the PES honeycomb texture. In this case, the ultrathin nanoporous film reduced significantly the surface roughness factor ($Ra = 22 \pm 3 \mu\text{m}$) making it not particularly effective; rather, the large perfluorinated component of HYFLON AD has given a major waterproof character to the membrane surface. Chemical composition together with formation of very small pore size contrasts the liquid intrusion with time. As a result, comparable and longer resistance to wetting has been observed for both the water and salt solutions (Fig. 4.16b), as largely confirmed by water desalination experiments.

4.4.3 Membrane productivity-efficiency trade-off

Thermally driven membrane distillation experiments have been implemented in Direct Contact mode in order to assess the performance of the tailor-made membrane during salty solution treatment. Preliminary experiments with pure water have been carried out and an

increase of 104% in water flux has been observed moving from commercial PVDF to self-standing PES honeycomb texture. A further increase of 75% in flux has been measured through the ultrathin HYFLON AD membrane when it was suspended onto self-standing PES honeycomb textures (Figure 4.17a). The average flux seems to be dependent on the thickness of the active skin layer mainly, confirming that shorter pathways enhance the membrane productivity (Figure 4.17b). Indeed, microscopy micrographs endorse the formation of a large number of small pores like well-defined holes through a very tiny layer (Figure 4.18). AFM topography has shown the formation of a uniform polymeric layer bringing numerous circular small pores. SEM images discern further between the HYFLON AD porous nanofilm and largely porous sub-layer, providing clear indication about the suspension of the fluorinated nanofilm onto bigger free-resistance air bubbles embedded in PES textures. Likewise, ATR spectra collected onto the membrane surface confirmed the ultra-thinness of the fluorinated layer, considered that a slight contribution of infrared modes associated with PES backbone's sulfone groups continues to be detectable in spite of the radical change in the surface chemistry. From a morphological point of view, this has implied less resistance to the diffusion of water vapor due to very short free pathways through the active skin layer. Also, the reduction of one order of magnitude for the pore size prevented local wetting events, which can be, in itself, responsible for additional liquid resistance and/or back diffusion. It is undeniable that the lowest average flux estimated for PES honeycomb textures can be ascribed to additional resistance produced by local wetting events [23, 24] Liquid water stagnant inside the big pores may be responsible for transitions from Cassie–Baxter to Wenzel state. Experiments, carried out with salty solution (NaCl 5 mM) over seven continuous working hours, yielded clear indication about the partial wetting of self-standing PES honeycomb textures. Constant fluxes have been indeed measured, but with a rejection factor of around 92%. This suggested salt passage through preferential channels associated with possible water back diffusion. Instead, the deposition of a fully fluorinated layer with pores less than one order of magnitude – 0.25 against 3.0 μm – allowed the membrane to block local liquid intrusion while water vapor molecules passed freely through the ultrathin layer. As a result, enhanced water vapor flux could be appreciated (Figure 4.17). A further enrichment of the average water flux could be obtained when PES honeycomb texture was mechanically supported (Fig. 4.17a). Straightly, the mechanical support did not affect the transport across the membrane, since its resistance to mass transfer was negligible (Figure 4.15c). Rather, it imparted higher robustness to the assembled layers, thereby preventing local structural distortions or small clefts through which local wetting or

retro-flux events could take place with inevitably flux decline. The use of a mechanical support allowed a further increase of 3.4 times in the average water flux.

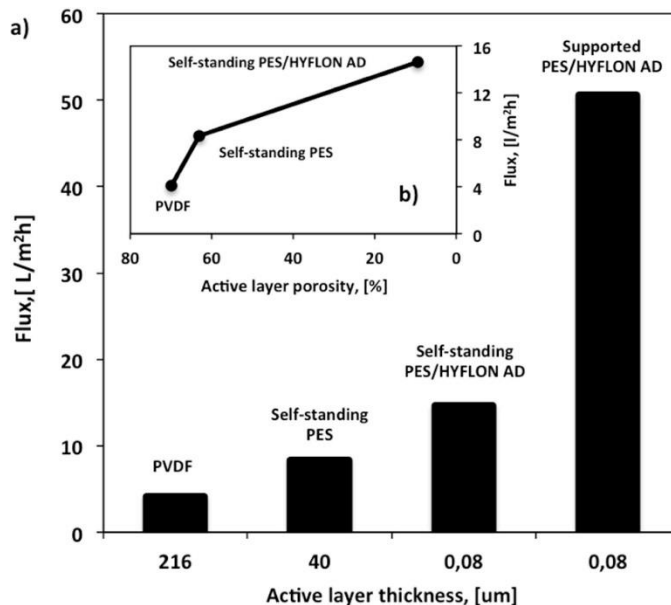


Figure 4.17. Water flux measured through different kinds of membranes (Feed: bi-distilled water; T_{feed} : 38 °C; ΔT = 23 °C; Feed flow rate: 100 mL min⁻¹): thickness (a) and porosity (b) effects on water vapor flux.

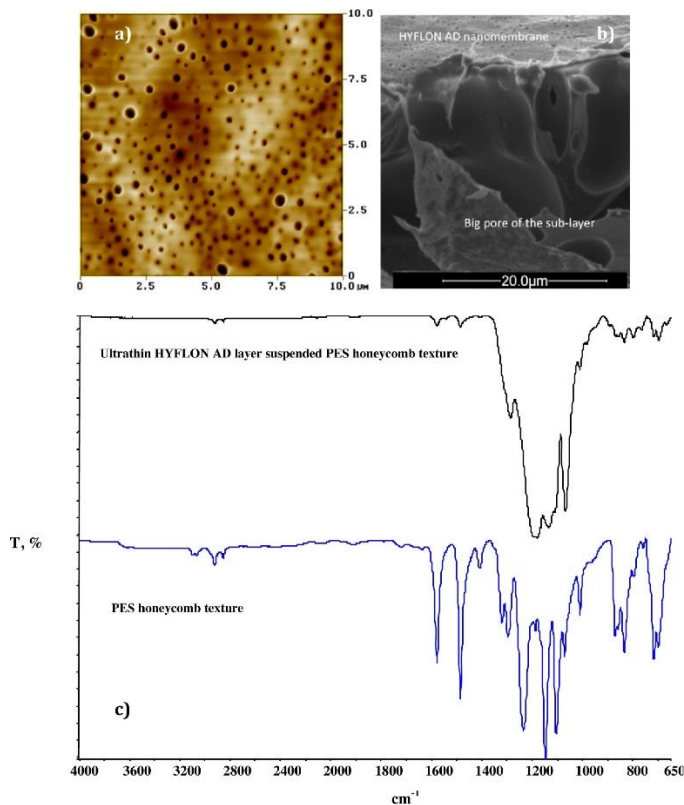


Figure 4.18. Detection of the ultrathin porous HFLON AD layer (a) AFM topography (b) SEM micrograph and (c) ATR spectra.

According to these evidences, the ultrathin porous HYFLON AD membrane has been suspended onto supported PES honeycomb textures and has been tested in a DCMD plant using NaCl solution. Rejection factors of 99.1% have been obtained against values of 99.6% estimated for commercial PVDF flat membranes processed in the same plant and under comparable experimental conditions (Fig. 4.19).

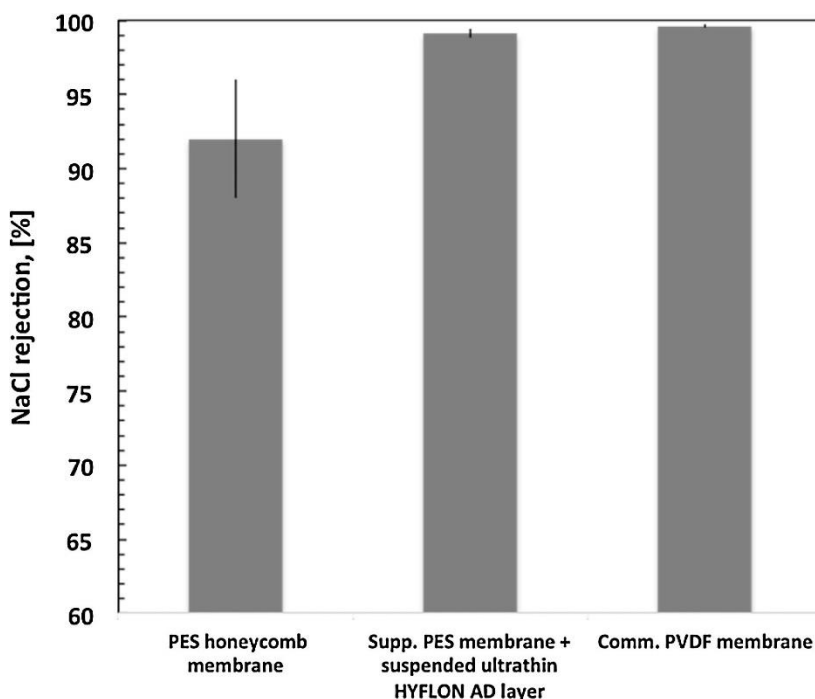


Figure 4.19. Salt rejection estimated for home-made and commercial membranes under comparable working conditions (NaCl 5 mM, $T_{\text{feed}} = 38$ °C; Feed flow rate = 100 mL min⁻¹).

Conversely, a by far superior performance has been estimated under the productivity-energetics profile. Figure 4.20 shows a comparison of water flux and thermal efficiency estimated for the tailor-made membrane (Supported flat PES/HYFLON AD) and some commercial membranes (Supported flat PVDF and PP hollow fiber) tested under similar working conditions ($T_{\text{feed}} = 38$ °C; $T_{\text{perm}} = 15$ °C) as well as home-made (Flat PVDF) and commercial membranes (Flat PES and PP) tested under decisively different processing temperature ($T_{\text{feed}} = 55.5$ °C; $T_{\text{perm}} = 49.5$ °C). As clearly depicted, the ultrathin suspended HYFLON AD membrane was over the productivity-thermal efficiency trade-off established for traditional membrane systems having flat and hollow fiber configurations and processed under comparable conditions, respectively. An average water flux of 51 Lm⁻² h⁻¹ versus a thermal efficiency of 70.2% was appreciated for the new tailor-made membrane, whereas fluxes less than 5 Lm⁻² h⁻¹ and thermal efficiency not superior to 35% has been estimated for commercial membranes traditionally used in DCMD operations. Other membranes

processed at much higher feed temperature showed a thermal efficiency ranging from 55 to 80% approximately, but an average flux much lower (less than $13 \text{ Lm}^{-2} \text{ h}^{-1}$) [25]. Provided that the thermal conductivity of the materials remains a discriminating factor for controlled heat loss, membrane thickness together with other structural parameters played its part in the optimization of the flux-thermal efficiency trade-off.

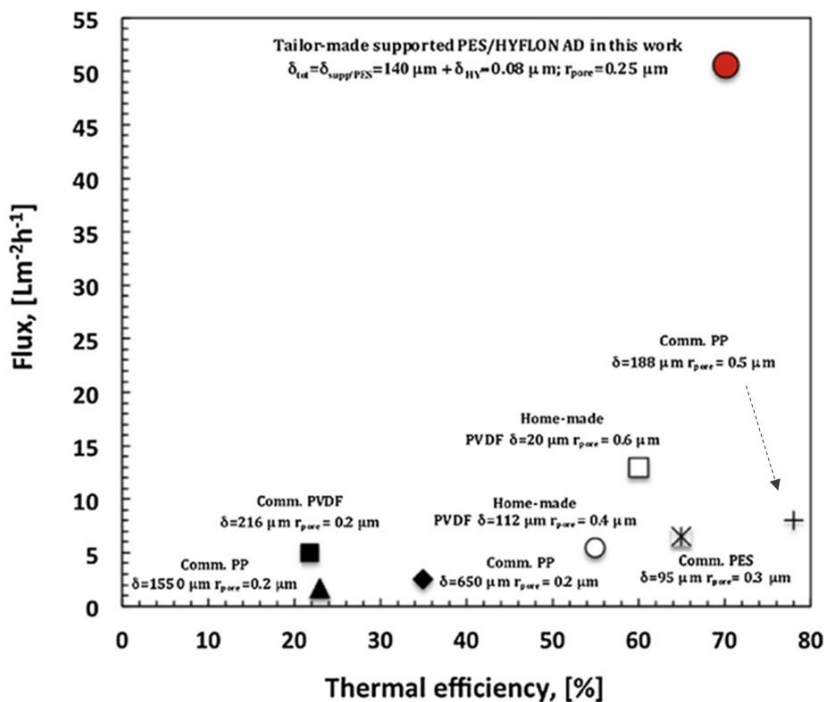


Figure 4.20. Compared flux and thermal efficiency trade-off for home-made PES/HYFLON AD, PVDF and PP commercial membranes (filled markers) ($T_{feed} 38 \text{ }^\circ\text{C}$ and $\Delta T = 23 \text{ }^\circ\text{C}$) and home-made PVDF and commercial PES and PP membranes (empty markers) ($T_{feed} 55.5 \text{ }^\circ\text{C}$ and $\Delta T = 6 \text{ }^\circ\text{C}$).

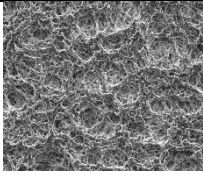
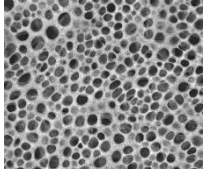
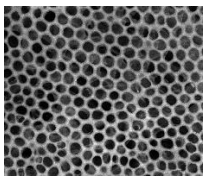
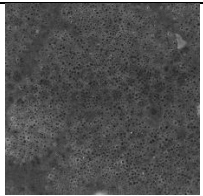
Therefore, higher fluxes and higher thermal efficiency were observed for the tailor-made membrane, as the result of well-addressed assembly of materials over different length scale. This better result is a first encouraging step toward the accomplishment of a needed goal such as the production of desalted water at lower energetic consumption when softer processing conditions are applied.

The experimental findings discussed in this work confirm the concrete possibility to use thinner suspended porous layers at low thermal conductivity as fruitful interfaces for advanced membrane distillation processes wherein a large productivity can be associated with a limited heat loss. Indeed, HYFLON AD exhibits a thermal conductivity of $\sim 0.1 \text{ Wm}^{-1} \text{ K}^{-1}$ that combined with an ultrathin porous low-resistant pathway provides the ideal solution for achieving a suitable compromise between reduced thermal consumption and enhanced mass transfer.

4.4.4 A synthetic summary of properties-performances relationship for honeycomb membranes produced

We can summarize that as it was widely described above, several approaches were applied before to find the most suitable honeycomb home tailored membrane. In table 4.1 are reported most important morphological parameters of all produced honeycomb membranes with their performances in MD process, in order to compare results achieved with different types of honeycomb studied.

Table 4.1. Major morphological properties and performances of the different types of honeycomb membranes produced and studied in this thesis work.

| Membranes | SEM top surface (5.0 X Mag) | Pore size (μm) | Contact angle ^a ($^{\circ}$) | Active layer thickness (μm) | Average flux ^b ($\text{L}/\text{m}^2\text{h}$) | Rejection ^c (%) |
|--|---|--------------------------------|---|---|---|-------------------------------|
| Commercial PVDF |  | 0.2 | 132 | 216 | 6 | 99.6 |
| Honeycomb PES |  | 3.5 | 90 | - | - | - |
| Hydrophobic honeycomb PES-viologen salt ^d |  | 3.0 | 126 | 40 | 14 | 93.4 |
| Honeycomb PES- Viologen salt with the HYFLON nanocoating ^e |  | 0.25 | 135 | 0.08 | 51 | 99.1 |

^aHerein contact angle is referred to time= 0 sec and estimated with water as liquid probe. ^bAverage flux is referred to the medium value achieved during the entire MD experiments.

^c Rejection was estimated with $[\text{NaCl}] = 5\text{mM}$ as described in the text. ^dHydrophobic self-standing PES was only dipped onto an Hyflon solution at 0.5 wt % and then air-dried under the hood.

°PES honeycomb membrane with the HYFLON nanocoating was mechanically supported as described in the text.

All the elements fit perfectly together when the HYFLON nanocoating is suspended on the top surface of the honeycomb PES membranes, using a mechanical support, for improving resistance to breakage. These achievements can be regarded as the result of a directed nano-assembly of materials in a well-defined volumetric space, where suitable structure-chemistry interplay is obtained. Reduced pathways together with use of fluorinated materials at lower thermal conductivity make the designed membrane extremely promising for future competitively productive and energetically favored water desalination. These interesting and high performing nanostructured membranes, are very promising in desalination of saline waters at low concentration deriving from permeate of other membrane operations. So, they can be used with success in membrane technology, for water treatment in the view of integrated membrane processes.

4.5 Conclusions

For the first time, an ultrathin porous membrane based on HYFLON AD has been successfully suspended onto a supported PES honeycomb texture [26] in order to fabricate fruitful interfaces for new-concept membrane distillation operations, which can be distinguished for the unusual productivity-thermal efficiency trade-off. The challenge to manipulate and shape a highly hydrophobic polymer such as HYFLON AD in a very tiny porous layer can be regarded as the result of a fine manipulation of structure–transport properties relationships.

Compared with other home-made and commercial membranes, this novel nanostructured membrane exhibited better performances. Higher capability to transfer large amounts of water with appreciable salt rejection were obtained when softer processing temperatures were selected, resulting in an exciting thermally high-efficiency membrane distillation process.

References

- 1 H. Yabu, Fabrication of honeycomb films by the breath figure technique and their applications, *Sci. Tech. Adv. Mat.*, 19 (2018) 802–822, <https://doi.org/10.1080/14686996.2018.1528478>.
- 2 A. Zhang, H. Bai, L. Li, Breath Figure: A Nature-Inspired Preparation Method for Ordered Porous Films, *Chem. Rev.*, 115 (2015) 9801–9868, <https://doi.org/10.1021/acs.chemrev.5b00069>.
- 3 A. Gugliuzza, M.C. Aceto, F. Macedonio, E. Drioli, Water droplets as template for next generation self-assembled poly-(etheretherketone) with Cardo membranes. *J. Phys. Chem. B*, 112 (2008) 10483–10496, <https://doi.org/10.1021/jp802130u>.
- 4 B. Yu, H. Cong, Z. Li, H. Yuan, Q. Peng, M. Chi, S. Yang, R. Yang, R.S. Wickramasinghe, J. Tang, Fabrication of highly ordered porous membranes of cellulose triacetate on ice substrates using breath figure method, *J. Polym. Sci. Part B Polym. Phys.*, 53 (2015) 552–558, <https://doi.org/10.1002/polb.23667>.
- 5 J. Bonsik, L. Donghyun, L. Si-Hyung, Y. Sungho, A facile method to fabricate a 3-D porous structure with ag nanowires as a sensor platform, *Sci. Adv. Mater.*, 7 (2015) 784–788, <https://doi.org/10.1166/sam.2015.1955>.
- 6 R. Kurita, K. Hayashi, X. Fan, K. Yamamoto, T. Kato, O. Niwa, Microfluidic device integrated with pre-reactor and dual enzyme-modified microelectrodes for monitoring in vivo glucose and lactate, *Sens. Actuators B*, 87 (2002) 296–303, [https://doi.org/10.1016/S0925-4005\(02\)00249-6](https://doi.org/10.1016/S0925-4005(02)00249-6).
- 7 A. Gugliuzza, V. Pingitore, D. Miriello, E. Drioli, Functional carbon nanotubes for high-quality charge transfer and moisture regulation through membranes: Structural and functional insights, *Phys. Chem. Chem. Phys.*, 17 (2015) 12919–12926, <https://doi.org/10.1039/C5CP00750J>.
- 8 M. Srinivasarao, D. Collings, A. Philips, S. Patel, Three-Dimensionally Ordered Array of Air Bubbles in a Polymer Film, *Science*, 292 (2001) 79-83, <https://doi.org/10.1126/science.1057887>.
- 9 N. Maruyama, T. Koito, J. Nishida, T. Sawadaishi, X. Cieren, K. Kjiro, O. Karthaus, M. Shimomura, Mesoscopic patterns of molecular aggregates on solid substrates, *Thin Solid Films*, 327 (1998) 854–856, [https://doi.org/10.1016/S0040-6090\(98\)00777-9](https://doi.org/10.1016/S0040-6090(98)00777-9).
- 10 V. Speranza, F. Trotta, E. Drioli, A. Gugliuzza, High-Definition Polymeric Membranes: Construction of 3D Lithographed Channel Arrays through Control of Natural Building

- Blocks Dynamics, *ACS Appl. Mater. Interface*, 2 (2010) 459-466, <https://doi.org/10.1021/am900701r>.
- 11 F.A. Escobedo, Engineering entropy in soft matter: The bad, the ugly and the good, *Soft Matter*, 10 (2014) 8388–8400, <https://doi.org/10.1039/C4SM01646G>.
 - 12 A. Gugliuzza, M.L. Perrotta, E. Drioli, Controlled Bulk Properties of Composite Polymeric Solutions for Extensive Structural Order of Honeycomb Polysulfone Membranes, *Membranes*, 6 (2016) 27, <https://doi.org/10.3390/membranes6020027>.
 - 13 M. Kojima, Y. Hirai, Y. Hiroshi, M. Shimomura, The effects of interfacial tensions of amphiphilic copolymers on honeycomb-patterned films, *Polym. J.*, 41 (2009) 667–671, <https://doi.org/10.1295/polymj.PJ2009027>.
 - 14 M. Johnson, Détergents: Triton X-100, Tween-20, et autres. *Mater. Methods*, 3 (2013) 163–175, <https://doi.org/10.13070/mm.en.3.163>.
 - 15 T. Sidim, G. Acar, Alcohols effect on critic micelle concentration of polysorbate 20 and cetyl trimethyl ammonium bromine mixed solutions, *J. Surfact. Deterg.*, 16 (2013) 601–607, <https://doi.org/10.1007/s11743-012-1429-x>.
 - 16 R.J. Good, C.J. van Oss, Modern Approaches to Wettability, in: M.E. Schroder, G.L. Loeb, (Eds.), Springer: New York, NY, USA, 1992.
 - 17 K. Binnemans, Ionic Liquid Crystals, *Chem. Rev.*, 105 (2005) 4148–4204, <https://doi.org/10.1021/cr0400919>.
 - 18 Y. Fukuhira, H. Yabu, K. Ijiro, M. Shimomura, Interfacial tension governs the formation of self-organized honeycomb-patterned polymer films, *Soft Matter*, 5 (2009) 2037-2041, <https://doi.org/10.1039/B821183C>.
 - 19 E. Marotta, F. Rastrelli, G. Saielli, Aggregation Behavior of Octyl Viologen Di[bis(trifluoromethanesulfonyl)amide] in Nonpolar Solvents, *J. Phys. Chem. B*, 112 (2008) 16566-16574, <https://doi.org/10.1021/jp808306r>.
 - 20 A.Li, H.S. Muddana, M.K. Gilson, Quantum Mechanical Calculation of Noncovalent Interactions: A Large-Scale Evaluation of PMx, DFT, and SAPT Approaches, *J. Chem. Theory Comput.*, 10 (2014) 1563-1575, <https://doi.org/10.1021/ct401111c>.
 - 21 L. De Bartolo, A. Gugliuzza, S. Morelli, B. Cirillo, A. Gordano, E. Drioli, Novel PEEK-WC membranes with low protein affinity related to surface free energy parameters, *J. Mater. Sci: Mater. Med.*, 15 (2004) 877-883, <https://doi.org/10.1023/BJMSM.0000036275.60508.50>.
 - 22 A. Gugliuzza, Membrane wettability in: E. Drioli, L. Giorno (Eds.), *Encyclopedia of Membranes*, Springer-Verlag, Berlin, 2016, pp. 1254-1256.

- 23 L.D. Tijing, Y.C. Woo, J.-S. Choi, S. Lee, S.H. Kim, H.K. Shon, Fouling and its control in membrane distillation—A review, *J. Membr. Sci.*, 475 (2015) 215-244, <https://doi.org/10.1016/j.memsci.2014.09.042>.
- 24 A. Murakami, H. Jinnai, A. Takahara, Wetting Transition from the Cassie–Baxter State to the Wenzel State on Textured Polymer Surfaces, *Langmuir*, 30 (2014) 2061-2067, <https://doi.org/10.1021/la4049067>.
- 25 L. Eykens, I. Hitsov, K. De Sitter, C. Dotremont, L. Pinoy, I. Nopens, B. Van der Bruggen, Influence of membrane thickness and process conditions on direct contact membrane distillation at different salinities, *J. Membr. Sci.*, 498 (2016), 353-364, <https://doi.org/10.1016/j.memsci.2015.07.037>.
- 26 M.L. Perrotta, G. Saielli, G. Casella, F. Macedonio, L. Giorno, E. Drioli, A. Gugliuzza, An ultrathin suspended hydrophobic porous membrane for high-efficiency water desalination, *App. Mat. Today*, 9 (2017) 1-9, <https://doi.org/10.1016/j.apmt.2017.04.009>.

Chapter 5

2D materials assisted Membrane Crystallization Technology:

A new combined experimental-computational approach

5.1 Introduction

In the field of membrane technology, Membrane Crystallization (MCr) is a promising membrane process on which research is focusing growing attention. It has allowed over time to bring a lot of advantages in terms of kinetics when compared to the traditional crystallization process, for the recovery of minerals from saline and brackish waters and also for different compound like pharmaceuticals, protein and so on [1]. This technology takes advantages such as higher purity level, separation of polymorphic forms, narrow crystal shape and crystal size distribution, and faster nucleation times, as detailed in Chapter 2. A major concern is the difficulty to shorten nucleation time directing uniformly size and shape of the crystals according to specific purposes. Commercial membranes enable one to recover crystals from sea or brackish water [2, 3], but there is a realistic difficulty to manage the process for making them fruitful and selective on scale.

This study explored in particular the potential of graphene and bismuth selenide (Bi_2Se_3), confined in hydrophobic PVDF membranes, in MCr technology through an integrated computational-experimental approach. This work demonstrated how the confinement of graphene flakes influenced and assisted crystals nucleation and growth rate, reducing induction time when a supersaturated NaCl solution is used. Computational results found agreement with experimental data, making real the possibility to explore the nanomaterials behavior in membrane, at microscopic level as well.

Nowadays, in membrane technology it has become increasingly important the ability to carry out parallel scientific studies from both experimental and theoretical point of view, in order to have not only a prediction on materials or processes performance, but also to understand at microscopic level the reason of occurring single events. Recent studies carried out by Tsai et al [4] have analyzed from a computational point of view how the presence of a polymeric membrane can influence nucleation phenomena reducing induction times and crystal growth in number and size distribution [5-7]. The aim of the present study was, instead, to assess the potential of graphene and other 2D materials for the optimizing and the improving of

crystallization kinetics when working in heterogeneous systems such as membranes in contact with salt solutions.

Chackraborty and Patey [8] detected the mechanism of crystal nucleation in a supersaturated solution of NaCl in water, observing how crystals nucleated in the part of the solution, where there is an excess of local salts. MCr allowed the achieving of a higher control on nucleation and crystal growth kinetics, because working in heterogeneous phase with a better control of supersaturation [9], which purity level, polymorphic form, narrow crystal shape and crystal size distribution depend from. However, there is an urgency to explore kinetics and thermodynamics events from experimental and computational point of views in order to get major knowledge about controlling forces and/or dynamics and, hence, to direct the events according to desired targets [10].

Briefly, graphene (G) was used as nanofiller in PVDF polymeric membranes at three different concentration for MCr testing: PVDF- G 0.5 wt %, PVDF-G 5 wt % and PVDF-G10 wt %. Higher concentration (G5 wt % and G10 wt %) with respect to pristine PVDF were used for fully atomistic investigations. Then, Bi₂Se₃ was used at the same concentration percentage of the graphene-PVDF system with which we achieved best results (5 wt %). Major details about the membrane preparation and the building up of MD boxes have been provided in the materials and methods sections (Chapter 3).

5.2 Graphene-PVDF based membranes characteristics

Because of its interesting morphological properties, graphene is very commonly used like filler in polymer composites [11]. Properties and performances of graphene-polymer composites depend on the quality of graphene filler and polymer matrix, but also on the dispersion of the filler in matrix [12, 13]. Blending was chosen for preparing polymer composites, since it is straightforward and promising for large-scale production. In particular, graphene hydrophobic powder was added to solvent under magnetic stirring and then sonicated at 80 °C. When the powder was completely dispersed into the solvent, the solution was equilibrated at 30 °C and PVDF polymer was added under mechanical stirring. SEM pictures show graphene flakes homogeneously distributed in polymer membranes matrix, especially along the sections (Figure 5.1). Nevertheless, graphene flakes tend to localize also in some portions of membranes surface, (Figure 5.2), in particular when used at higher concentration.

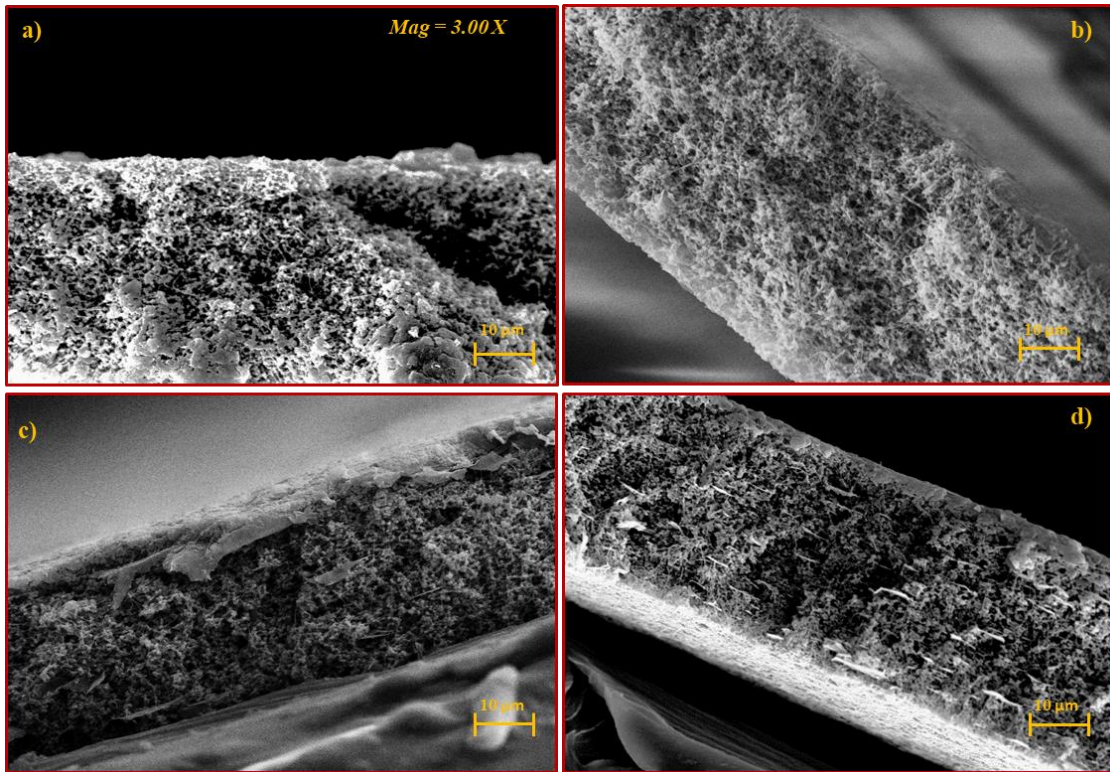


Figure 5.1. SEM pictures of graphene-based membranes cross sections: a) pristine PVDF, b) PVDF-G 0.5 wt %, c) PVDF-G 5 wt %, d) PVDF-G 10 wt %. Magnification 3.00X.

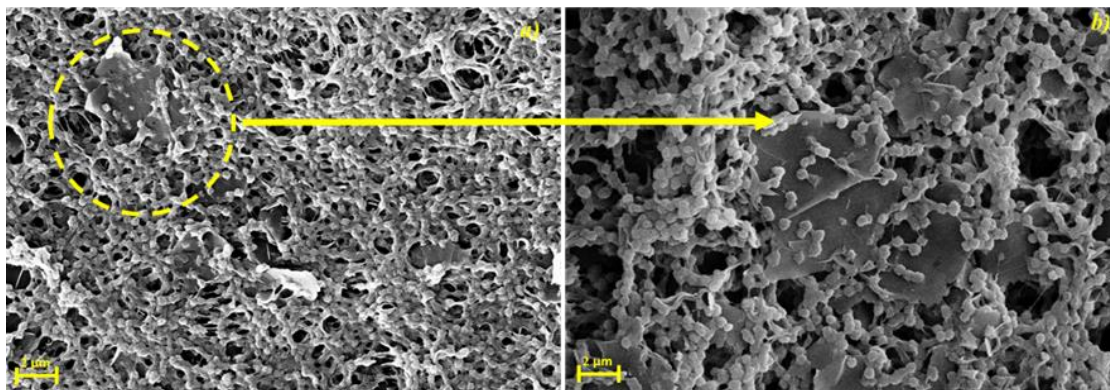


Figure 5.2. SEM pictures of graphene 5 wt %-based membrane top surfaces. Magnification 10.00X.

All membranes designed using graphene like nanofiller, were produced according the same procedure and before their usage in MCr plants, they were characterized in order to evaluate structure-properties relationships. Morphological parameters of membranes produced, are reported in table 5.1.

Table 5.1. Morphological parameters of membranes produced.

| System | Contact angle with water* (Θ) | Contact angle with NaCl* (Θ) | Mean pore diameter (μm) |
|----------------------------|--|---|--|
| PVDF | 139 \pm 3 | 117 \pm 6 | 0.53 \pm 0.02 |
| PVDF G 0.5 wt % | 139 \pm 3 | 135 \pm 2 | 0.27 \pm 0.01 |
| PVDF G 5 wt % | 146 \pm 5 | 144 \pm 5 | 0.65 \pm 0.07 |
| PVDF G 10 wt % | 156 \pm 5 | 145 \pm 2 | 0.78 \pm 0.05 |

**Contact angle measurements carried out with ultrapure water and [NaCl] 5.3 mol/L, detected at time= 0 sec.*

With graphene at higher concentration percentage (5 and 10 wt %), despite of graphene flakes were homogenously distributed in the matrix, some aggregation of the materials tended to form. These made pore size of G5 and G10 wt% bigger with respect to the others, in particular to G 0.5 wt %. With the last one we had a pore size in the range of $\approx 0.3 \mu\text{m}$ with a very narrow pore size distribution. High concentration of graphene flakes tends to create gap inside the matrix giving rise to little holes that are the bigger pores. In parallel, boxes representing graphene-PVDF based membranes were realized also trough MD simulations, choosing systems with the higher concentration of graphene. At first, as fully described in materials and methods session, Material Studio software was used to design starting models (Figure 5.3a, 5.3b and 5.3c), then Gromacs version 5.1.4 was used to allow the interaction between polymer surface and salts in order to define final box sizes (Figure 5.3d).

Theoretical parameters of models achieved are reported in table 5.2.

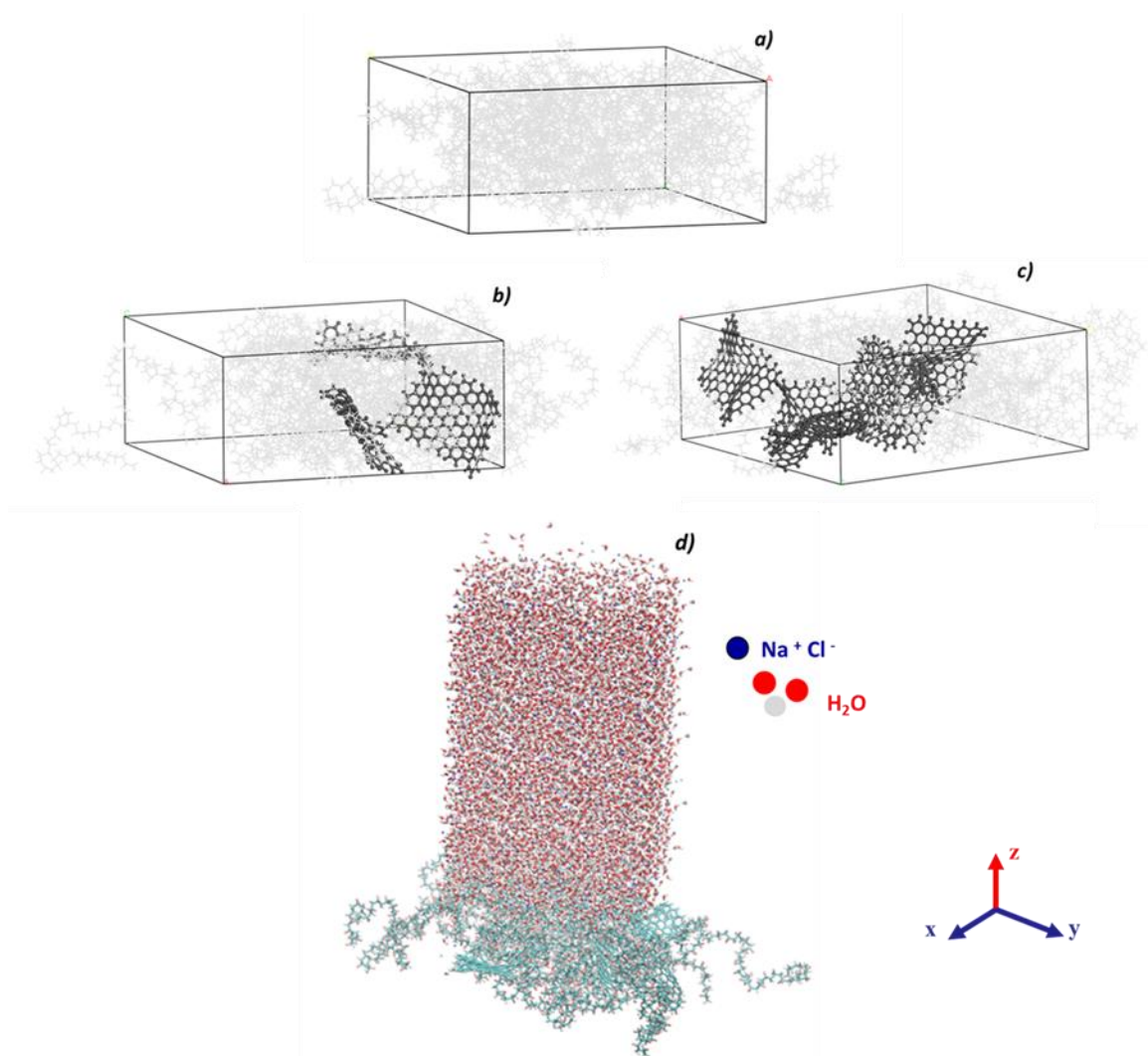


Figure 5.3. Models built through Material Studio Software. a) PVDF pristine b) PVDF-G 5 wt % c) PVDF-G 10 wt %. Grey lines represent PVDF chains, while black ball and sticks, graphene sheets. Final box of d) PVDF- G 5 wt % extended with Gromacs software.

Table 5.2. Theoretical parameters of membrane systems produced.

| System | V box (nm ³) | N° of NaCl molecules | N° of H ₂ O molecules | NaCl initial concentration (mol/L) |
|-----------------------|--------------------------|----------------------|----------------------------------|------------------------------------|
| PVDF | 350.23 ± 4.23 % | 793.5 ± 4.4 % | 7405.5 ± 4.4 % | 6.016 ± 0.100 % |
| PVDF G 5 % wt | 337.08 ± 0.56 % | 765.5 ± 1.2 % | 7052.5 ± 1.3 % | 6.012 ± 0.017 % |
| PVDF G 10 % wt | 357.16 ± 0.57 % | 772.0 ± 0.0 % | 7197.5 ± 0.1 % | 6.013 ± 0.216 % |

Experimentally, a larger amount of graphene widens the pore size distribution (Figure 5.4), even if improved hydrophobicity of the membrane surface can be appreciated, with a higher resistance to wetting when high saline concentrations were used (Figure 5.5).

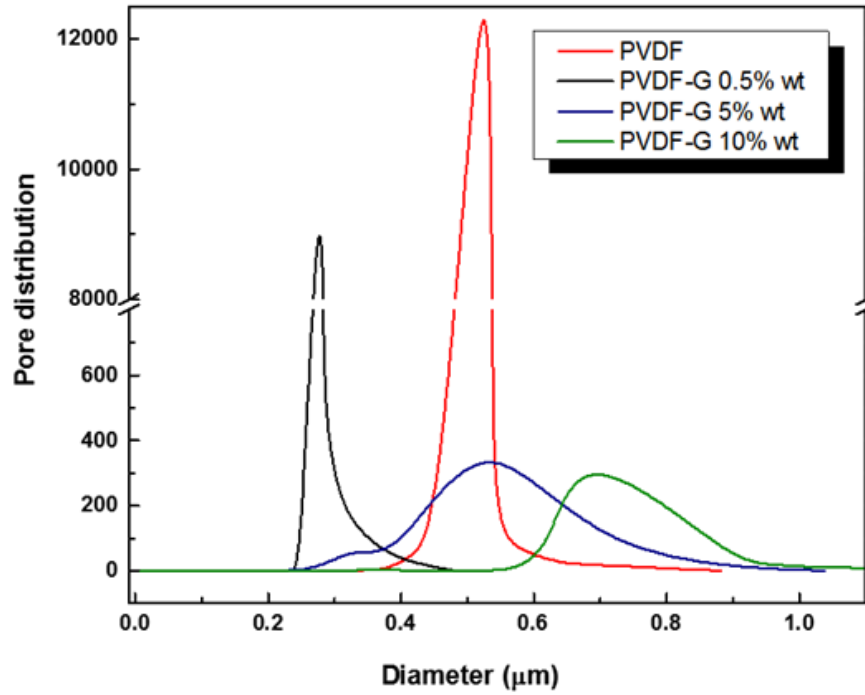


Figure 5.4. Pore size distribution of graphene-based membranes.

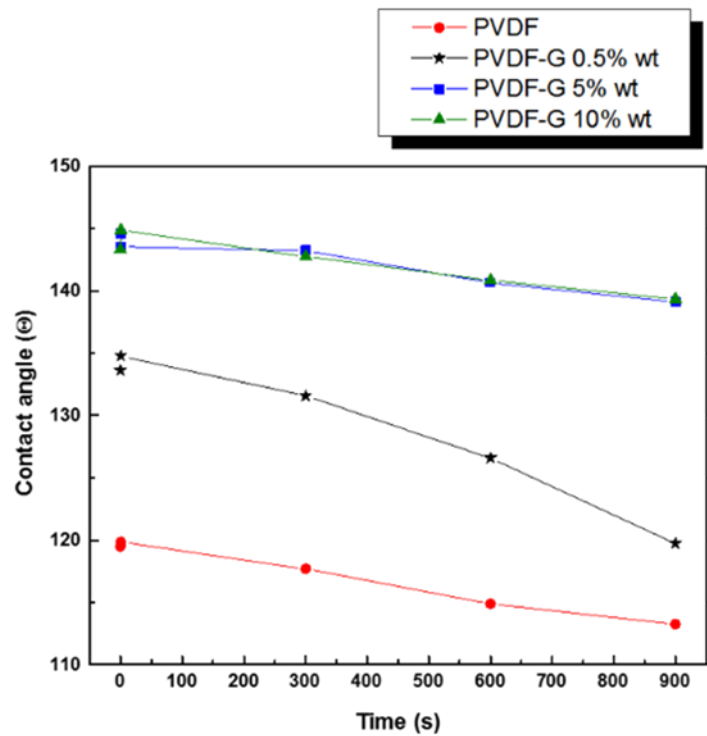


Figure 5.5. Contact Angle measurements with NaCl 5.3 mol/L as a liquid probe.

Resistance to wetting from salt solution at 5.3 mol/L was investigated by measuring the contact angle value with time according to sessile drop method. In particular, with long time (kinetics) analysis, each measurement was done covering the droplet by using of quartz cuvette in order to reduce effects due to the solvent evaporation.

Membrane Crystallization process was carried out via Membrane Distillation plant using these operative conditions: $T_{feed} = 308$ K; F_{ow} rate $_{feed}$ 250 ml/min; Flow rate $_{perm} = 100$ ml/min; $[NaCl] = 5.3M$; $\Delta T = 25$.

With the different systems, we achieved fluxes not very different among them, just a little bit higher for PVDF and Graphene at 10 wt %, and for PVDF and Graphene at 5 wt %. A little bit reduced flux was obtained with pristine PVDF, while with the system at Graphene concentration of 0.5 wt % were achieved the lowest flux. Despite of long operational time carried out with MCr processes, and high concentration of NaCl solution employed, Graphene based membranes worked very well, maintaining high resistance to wettability as a function of time, thus preventing liquid intrusion and allowing high values of salt rejection. Fluxes and rejections are reported in Table 5.3

Table 5.3. Fluxes (L/m^2h) and Rejection factor (%) to NaCl salt (5.3 mol/L) achieved at the end of MCr process with membrane systems produced.

| System | Fluxes (L/m^2h)* | Rejection (%) |
|------------------|----------------------|--------------------|
| PVDF | 5.66 \pm 0.09 | 99.975 \pm 0.007 |
| PVDF- G 0.5 wt % | 3.82 \pm 0.008 | 99.990 \pm 0.000 |
| PVDF-G 5 wt % | 6.38 \pm 0.30 | 99.985 \pm 0.007 |
| PVDF- G 10 wt % | 6.15 \pm 0.69 | 99.965 \pm 0.007 |

* Fluxes were normalized at thickness and overall porosity.

5.3 MCr process: experimental and computational data

Interestingly, in presence of graphene the induction times were reduced, when compared to pristine PVDF. In particular, the system with the lowest concentration wt % of graphene was that where occurred inferior nucleation times, thus following the trend that when the amount of G increased, NaCl crystals induction times was greater (Figure 5.6a). After a few hours of MCr process, an initial detection of feed salts solution was done evaluating presence or not of NaCl nuclei. When they appeared, a clear salt solution of sodium chloride left space to small aggregates that represented the forming nuclei. From the first visible crystals, three

times were evaluated, in order to building up kinetics parameter of crystals achieved. For each time, three samples were considered, in order to have a total amount of more or less of one hundred crystals.

For what concerns NaCl crystals induction time, the trend obtained with experimental studies is in full agreement with theoretical induction time (Figure 5.6b), where with G nanostructures (5 and 10 wt %) nuclei appeared in faster times. From a heterogenous salt solution where disorderd ions were visible, it was possible to discern ordered sequences of Na^+ Cl^- atoms that matched to ions aggregates. If we compare experimental and computational data of membrane systems produced, with respect with only NaCl bulk solution, the trend is confirmed. In fact from an experimental point of view [14] the nucleation time for the only NaCl salt solution is of 385 min, while from theoretical data reported in litterature [4] it is of 16 ns.

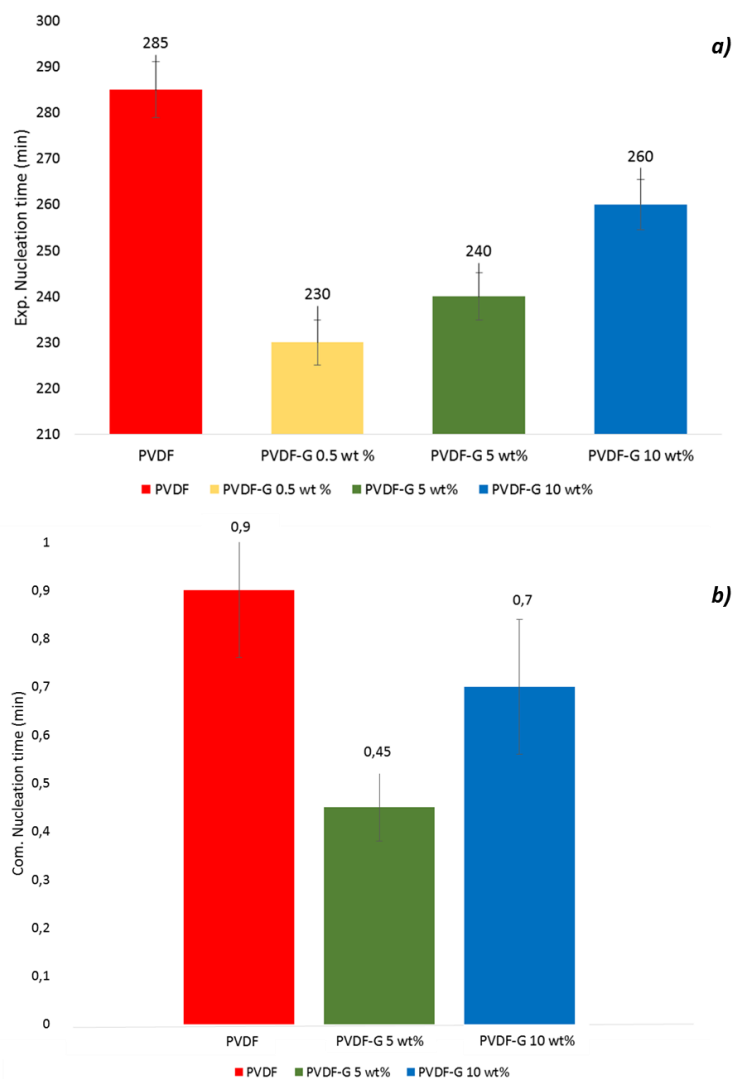


Figure 5.6. a) Experimental 1st observation of NaCl crystals. b) Nucleation time detected through MD simulation.

With the increasing of graphene concentration percentage in polymeric membranes, a gradual increase in induction times was however observed from experimental and theoretical point of views. The calculation of the nucleation rate (B^0) (Table 5.4), allowed us to deduce the velocity with which the crystals formed, and the related crystals amount. From the first time where first nuclei are observed until the 3rd sample (final products), it's possible to see how the formation of NaCl crystals was faster with those systems which have an amount in graphene of 0.5 and 5 wt %.

It is important to remember that when the formation of nuclei occurs, the construction of accurate kinetic parameters takes place by analyzing three samples in three consecutive times, with a distance of 30 minutes from each other.

The PVDF- G 5 wt % membrane presented the highest value of B^0 ($1.239.871 \times 10^3$ no/L*min) at the beginning of the nucleation step, while similar results were achieved for pristine PVDF and PVDF-G 10 wt%. An intermediate position was instead evaluated for system with graphene at 0.5 wt %. The B^0 can be connected with the calculation of electron donor parameter γ^- (mJm^{-2}) (Table 5.5). The correlation can be done in particular at the first time of crystals detection where γ^- and B^0 (1st sample) are in full agreement, with highest value for PVDF-G 5 wt % system. This is possible because for this system there's a more massive nucleation. This is due to the capability of this membrane to promoter water sequestration from ion-water resulting resulting also in a less-time consuming ion-ion aggregation and, hence, in a shortened nuclei formation. It is shown as almost all nanocomposite PVDF membranes showed higher results with respect to pristine PVDF, except PVDF-G 10 wt%.

Table 5.4. Nucleation rate (B^0) for G-PVDF membranes.

| NaCl parameter | Time | PVDF | PVDF G 0.5 wt % | PVDF G 5 wt % | PVDF G 10 wt % |
|---|-----------------|----------------|-----------------|-----------------|----------------|
| Nucleation B^0 (* 10^3) (no/L*min) | 1 st | <u>490.593</u> | <u>822.718</u> | <u>1239.871</u> | <u>375.303</u> |
| | 2 nd | 257.598 | 244.381 | 141.651 | 114.322 |
| | 3 rd | 149.088 | 80.879 | 71.088 | 106.420 |

Table 5.5. Electron donor parameter (γ^-).

| System | Electron donor parameter γ^- (mJm^{-2}) |
|-----------------|---|
| PVDF | <u>0.05</u> |
| PVDF-G 0.5 wt % | <u>0.69</u> |

| | |
|----------------|--------------------|
| PVDF-G 5 wt % | <u>1.69</u> |
| PVDF-G 10 wt % | <u>0.03</u> |

From theoretical point of view, the water-ion and ion-ion Coordination Number (CN) and crystal cluster appearance were investigated with time. The coordination numbers was computed by using standard radial distribution functions (rdf) and then counting the average number of ions or water within the first hydration shell of the counterions (or integrating the rdf up to the location of the first minimum).

These measures allowed estimating the time scale of induction times, which resulted faster according to the following order: PVDF-G 5 wt % > PVDF-G 10 wt %, > PVDF, after few nanoseconds of simulations. These results are in agreement with nucleation B_0 estimated at the first time of crystals detection, where happened the observation of 1st crystals formed. Furthermore, after ≈ 30 ns a plateau was reached, with some statistical error due to a partial further dissolution of the ions. The relationship between experimental and computational data is connected with the nucleation rate, relating to more Na^+ Cl^- interactions that occur among ions involved in crystals formation. Trend estimated with MCr experiments, carried out with Graphene systems, find agreement with theoretical data because the much more massive nucleation happened for PVDF-G 5 wt % leads to a highest CN at the first times of simulation, while for pristine PVDF and PVDF- G 10 wt % there's almost a curve overlap (B^0 not so different at first time of crystals detection).

The Na^+ Cl^- coordination number increased with time indicating a fast crystallization, up to a value of about $n^+ = 5.0$, not that of $n^+ = 6$, which is the value for a perfect cubic crystal, due to the remaining ions that stay in solution.

Conversely, the Na^+ O (H_2O) coordination number drops from the value of $n^+=5.4$ (lower than $n^+=5.9$ at infinite dilution solution) as the cation-anion coordination number surges (figure 5.7a).

In Figure 5.7b) is indicated the comparison of the coordination numbers at the beginning of the simulations and at the same concentrations both in the bulk and when the solution is in contact with the polymeric interface. The coordination number was lower in the bulk and ions seemed more homogeneously distributed. Moreover, those values remained almost constant longer than those for PVDF and PVDF-G systems due to the retarded nucleation time (of about 20 ns) instead of few nanoseconds of the PVDF systems.

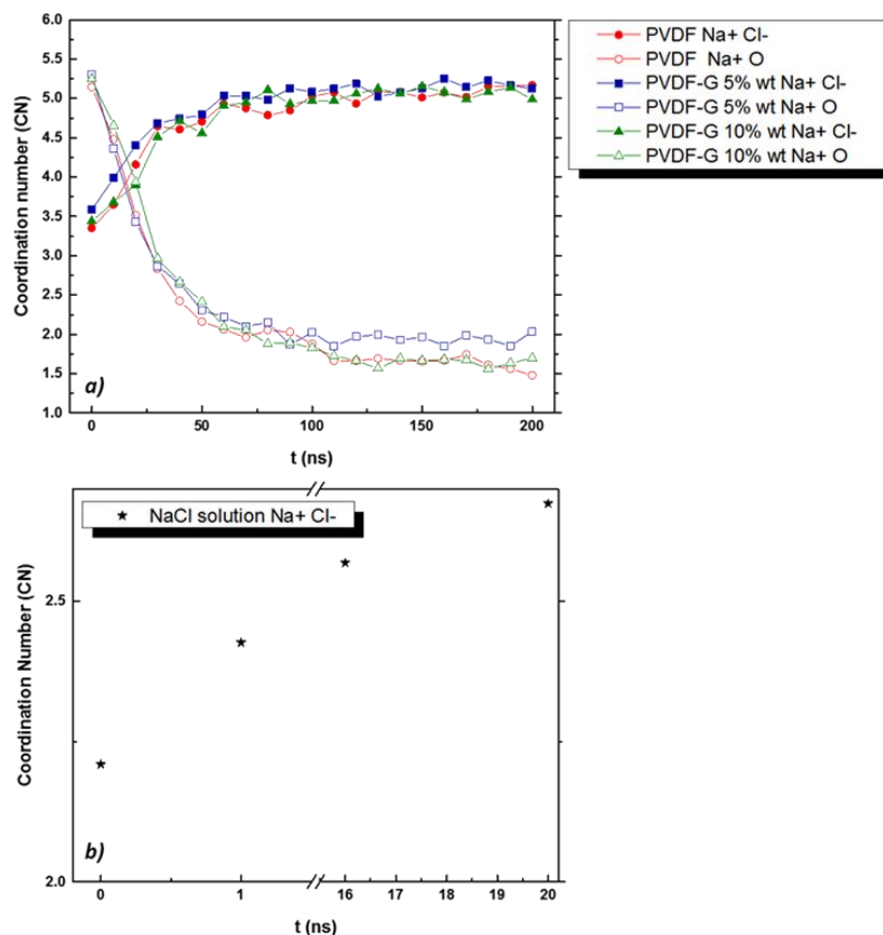


Figure 5.7. a) Coordination numbers of Na⁺ Cl⁻ pairs plotted vs simulation time. Here O denotes the oxygen atom of the water molecule. b) Coordination numbers for Na⁺ Cl⁻ in bulk solution. Data have been taken from Tsai et al. [4].

In graphene system at 5 wt %, nucleation and also kinetics growth happened faster, leading to a more significant growth of crystals formed. This respond so to a highest crystal growth in terms of number and also size (Figure 5.8).

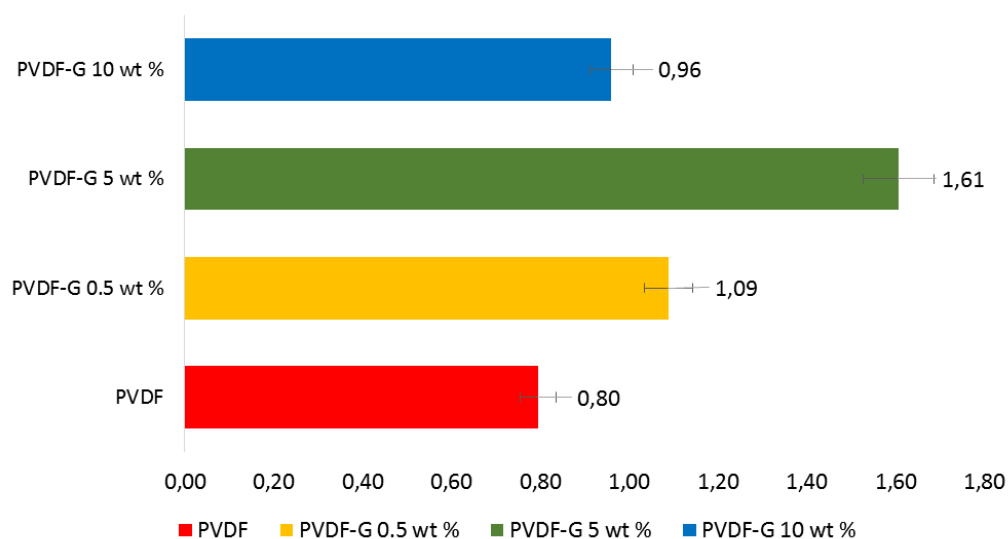


Figure 5.8. Average crystal growth achieved with Graphene-PVDF membranes produced.

When different systems are compared in terms of dimension (Table 5.6), bigger crystals are estimated at the end of the process for PVDF-G 5 wt % with respect to the others.

Table 5.6. Mean diameter (μm) for G-PVDF membranes.

| NaCl parameter | Time | PVDF | PVDF G 0.5 wt % | PVDF G 5 wt % | PVDF G 10 wt % |
|---|-----------------|-------------|------------------------|----------------------|-----------------------|
| Mean diameter (μm) | 1 st | 20.6 | 17.32 | 13.47 | 16.9 |
| | 2 nd | 42.5 | 34.38 | 47.87 | 61.5 |
| | 3 rd | 65.1 | 52.20 | 83.89 | 67.6 |

In figure 5.9 is represented how crystals evolved in time, in particular at the beginning and at the end of their crystal growth, demonstrating all details analyzed and described above: higher values of B^0 and best value of CV [%] for PVDF-G 5 wt % (Table 5.7) followed by G 0.5 wt %, with higher dimensions of crystals (Table 5.6).

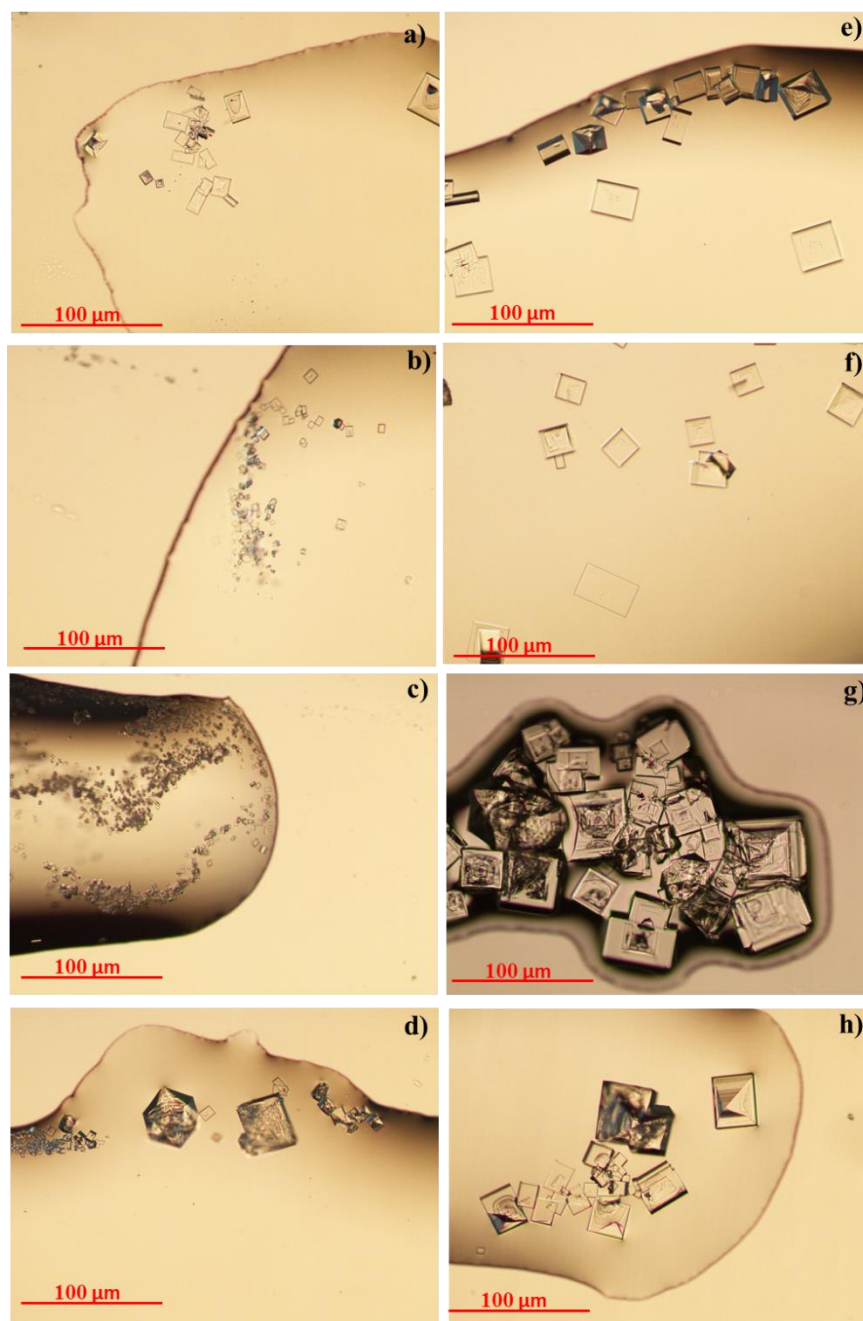


Figure 5.9. Crystals observations with optical microscope (10X magnification) at the beginning and at the end of the process for a) and e) PVDF; b) and f) PVDF-G 0.5 wt %; c) and g) PVDF-G 5 wt %; d) and h) PVDF-G 10 wt %.

In terms of coefficient of variation CV, expression of homogeneity of the crystal size and shape distribution, the best result 26.67% was achieved with PVDF-G 5 wt %, suggesting clearly a narrow crystal size distribution (CSD) curve (Table 5.6). This is an interesting target from industrially point of view, considering that values of CV no less than 50% are usually obtained for all systems produced. Summarizing, PVDF-G 5 wt% is the system that works better, because a much more massive nucleation is induced along with a bigger and

somewhat uniform crystals growth. However, in all case major uniformity in crystal distribution was achieved when graphene was confined in polymeric frameworks.

Table 5.7. Coefficient of Variation CV [%] achieved at the end of MCr process with membranes produced, at the 3rd time of crystals analysis.

| NaCl parameter | PVDF | PVDF G 0.5 wt % | PVDF G 5 wt % | PVDF G 10 wt % |
|----------------|------|-----------------|---------------|----------------|
| CV [%] | 48.1 | 32.2 | 26.67 | 35.8 |

Through MD studies, crystal growth was observed within 200 ns from supersaturated solutions. The NaCl molar concentrations at nucleation time were 6.087 (mol/L), 6.085 (mol/L), 6.089 (mol/L), respectively, for pristine PVDF, PVDF-G 5 wt % and PVDF-G 10 wt %. In computational studies the salt concentration was set at a relatively high value because it facilitates nucleation of salt crystals at faster times.

It was observed that NaCl crystallized into a face-centered cubic (FCC) lattice (Figure 5.10), a cubic with space group Fm3m and Z =4 (four formula units per cell), where the lattice parameter is $a = 5.6601 \text{ \AA}$ at room temperature (Figure 5.10). This value is slightly larger than that determined by X-ray diffraction measurements of 5.6401 \AA of Walker et al. [15] on synthetic NaCl powders.

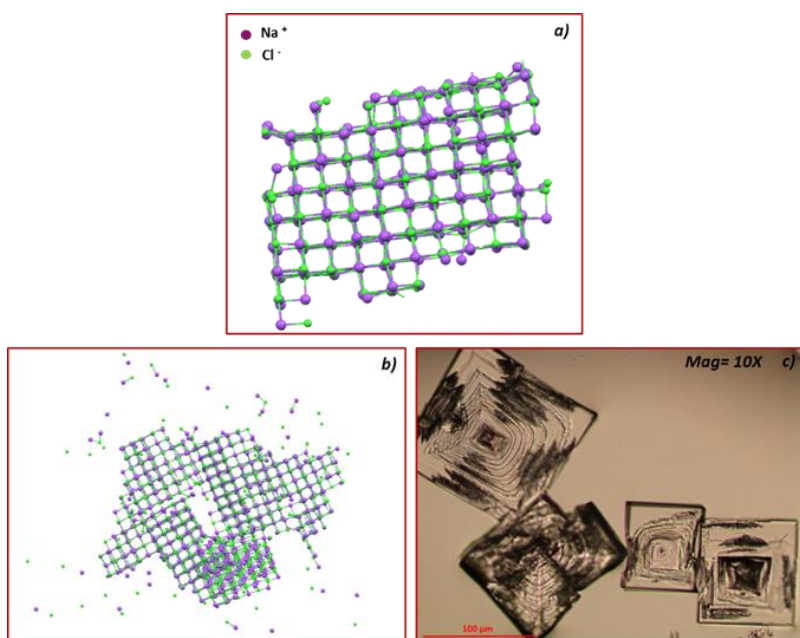


Figure 5.10. NaCl crystals formed at the end of MCr process with PVDF-G 5% wt system. a) Fcc lattice: Na⁺ ions in purple and Cl⁻ ions in green, b) Computational and c) Experimental (Magnification 10 X) observations.

Theoretically, the crystal growth was checked by using the magnification $r^2h(r)$ of the radial distribution function $g(r)$ [16].

Here $g^{+-}(r)^{-1}$ is the Na^+ - Na^+ radial distribution function, and multiplication by r^2 serves to magnify the structural details. The function $h^{+-}(r)$ was averaged over all ions in the system. However, ions in the crystal growing contributed to the long-range structure. At the first ns of MD simulation, $r^2h^{+-}(r)$ was very short ranged and referred to the metastable solution with one discernible peak indicating a few ordered ions. At 200 ns of simulation, the structural peaks, related to the ion-ion correlation, were more distinct indicating the growth of NaCl crystals (Figure 5.11). The particular evidence is that ion-ion interactions become very marked after a few nanoseconds of simulation, indicating a fast crystallization, confirmed by the formation of cluster of critical size that does not dissociate after an equilibration time of $t = 180$ ns.

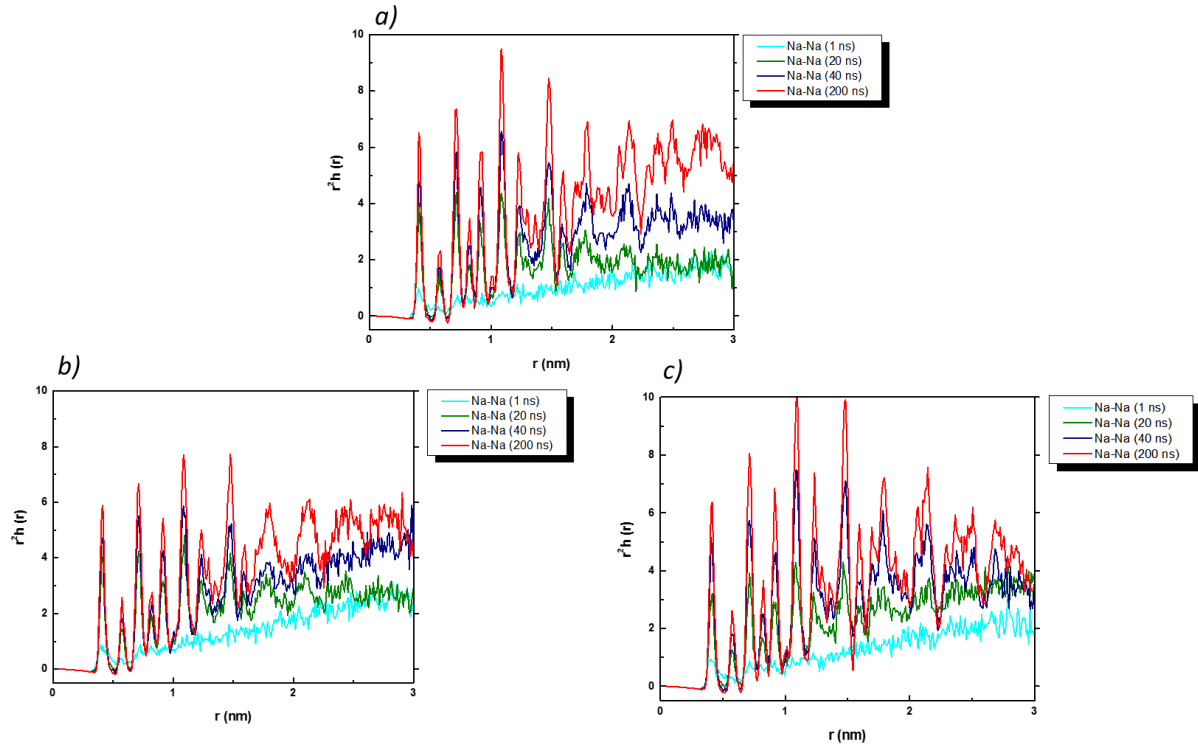


Figure 5.11. r^2 square magnification for a) pristine PVDF, b) PVDF-G 5 wt %, c) PVDF-G 10 wt %.

Through theoretical studies, it was difficult to measure effective number and size of NaCl crystals formed, in order to obtain computational kinetics parameter, but it was possible to analyze maximum distance of aggregates (cluster of NaCl crystals) formed along X, Y and Z axes directions (\AA). The highest value was achieved for crystals in NaCl bulk solution, then with PVDF pristine and G 10 wt %, while for G 5 wt % smaller size of the dimension of the three axes was detected. A reduced size of maximum clusters of crystals can be

envisaged as the result of an aggregation of a lot number of crystals resulting from a massive nucleation. This would justify and support the experimental datum related to the very quick growth rate observed when PVDF-G5 wt % membranes were worked. Furthermore from a theoretical point of view, by measuring X, Y and Z axes sizes, it was possible to identify a more compact and less extensive system (due to a greater preponderance of aggregates) for PVDF and graphene at 5 wt% (Figure 5.12).

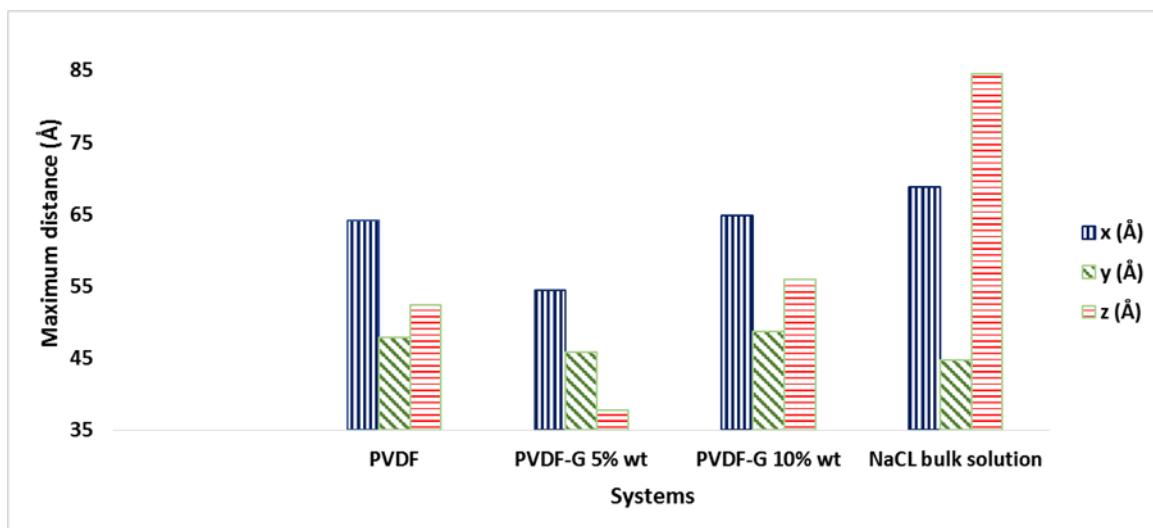


Figure 5.12. X, Y, Z axes dimensions for NaCl crystals achieved at the end of MD crystallization process for PVDF, PVDF-G 5 wt %, PVDF-G 10 wt % and only NaCl bulk solution*[4].

From Figure 5.13a', 5.13b' and 5.13c' it is possible to see how the system with more compacted aggregates was the PVDF-G 5 wt %, at the end of simulations performed (200 ns), in agreement with the experimental datum. In all three figures, at the beginning of the simulations clouds of disordered ions appeared, evolving in ordered structures with time.

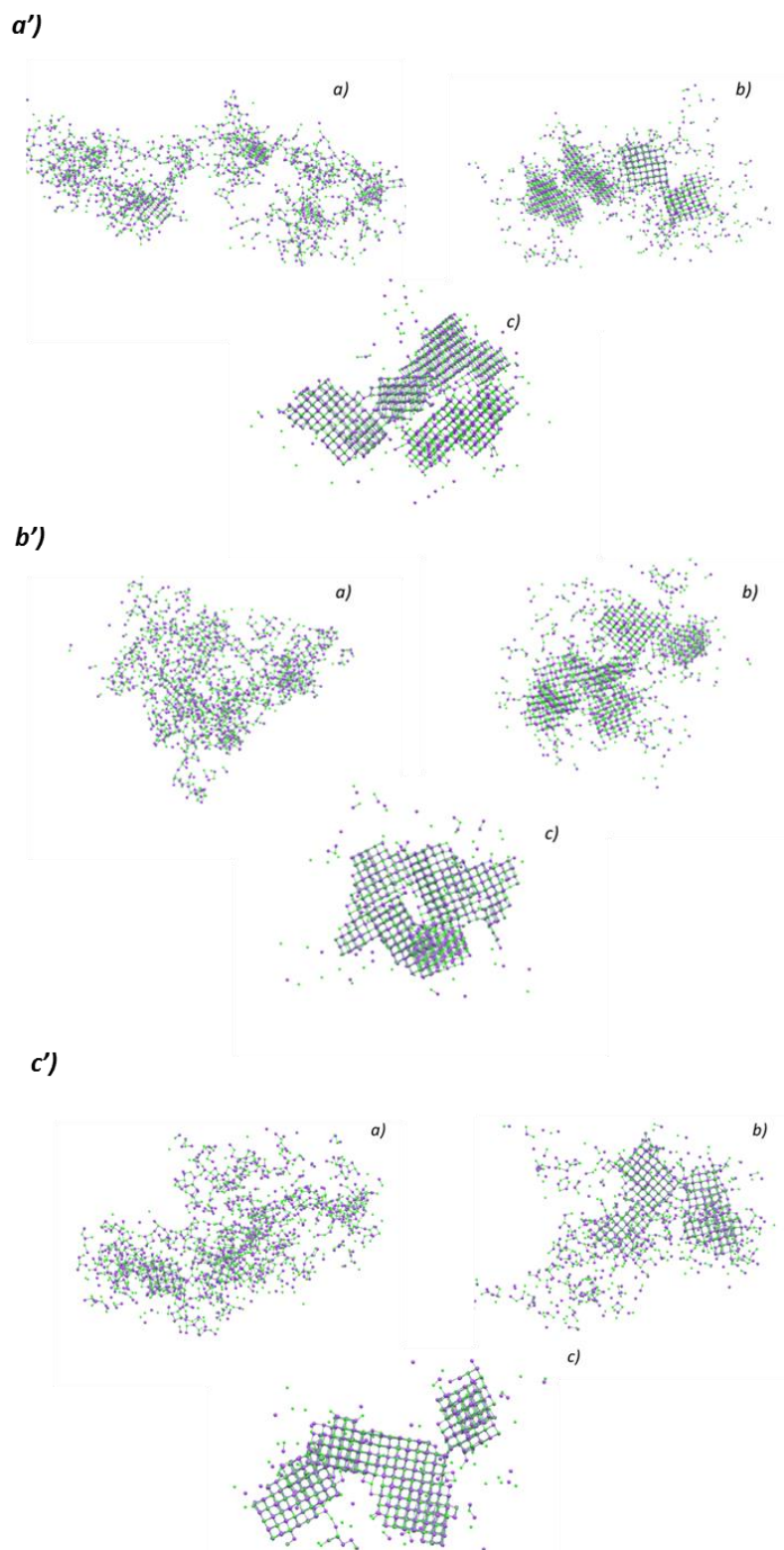


Figure 5.13. Crystal growth at a) 1 ns, b) 20 ns, c) 200 ns for pristine PVDF a'); PVDF-G 5 wt % b'); PVDF-G 10 wt % c').

Graphene, as nanofiller inside polymer matrix at different concentration, has allowed to modulate nucleation time and NaCl crystal growth.

Through computational studies, water uptake (%) was estimated at 1 ns of simulation because PVDF blended with graphene membrane systems showed nucleation and crystals formation before this time.

At 1 ns we detected values of $1.39 \% \pm 0.12$ and $1.40 \% \pm 0.03$ of water uptake, respectively for PVDF-G 5 wt % and PVDF-G 10 wt %, and of $1.19 \% \pm 0.01$ for the pristine PVDF (Figure 5.14). This indicates that the presence of graphene in PVDF membranes has the ability to improve water sorption from ion-water cluster, leading to the induction of supersaturation in faster times.

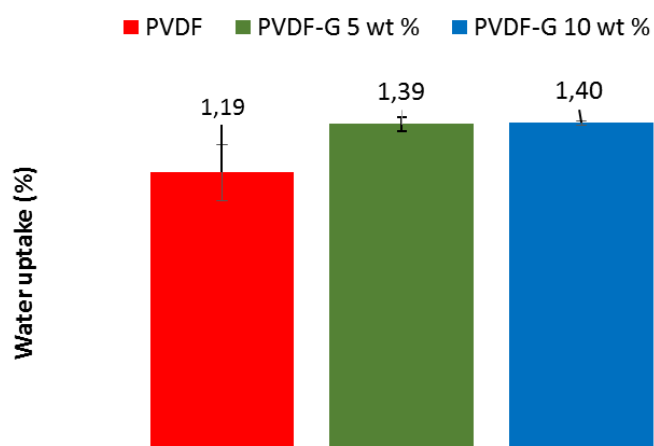


Figure 5.14. Water uptake (%) at 1 ns of simulation for PVDF, PVDF-G 5 wt % and PVDF-G 10 wt %.

Gontarek et al [17] studied penetration and diffusion of water molecules through free gaps between graphene platelets and polymers. They seem to take place via intermolecular interactions at defect sites of the filler, including edges and vacancies.

The radial distribution function, $g(r)$, related to specific interactions between the O of H₂O molecules and the PVDF and graphene into the membrane, calculated from molecular dynamics runs, supported the experimental observations of the water diffusion with larger interactions with a graphene layer in comparison to the polymer (Figure 5.15).

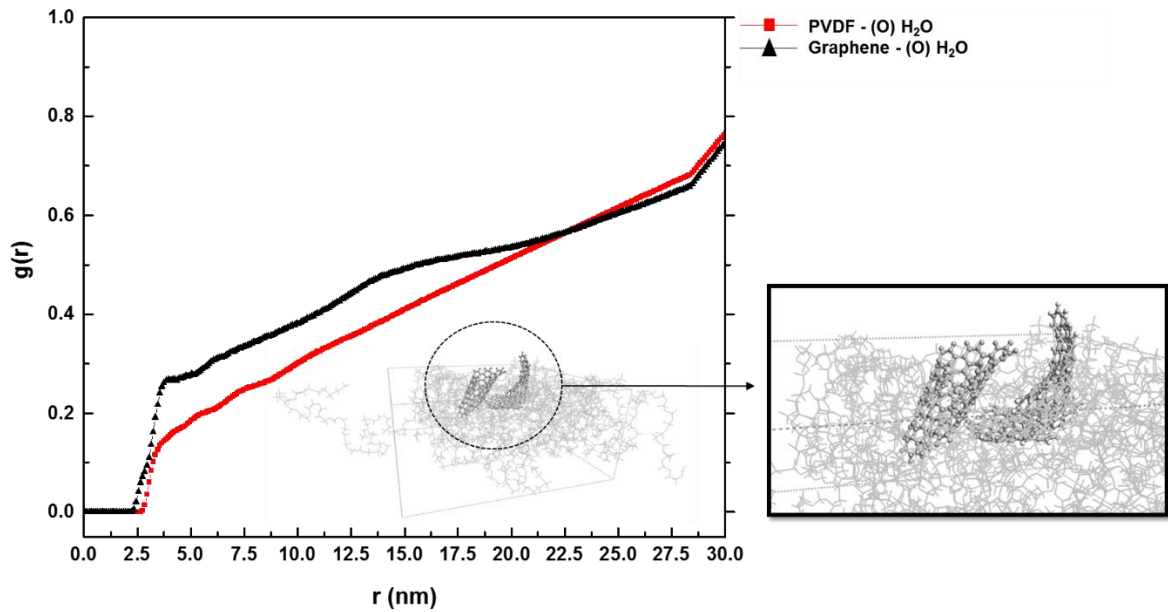


Figure 5.15. Radial Distribution Function (RDF) related to interaction between graphene and water (element O), black line, and PVDF chains and water (element O), red line.

In figure, a peak appears at about 3.8 Å from the graphene layer, indicating a positive interaction (although small) between one graphene platelet and the O of the water molecules. This could be due to the spatial distribution of graphene edges from the polymeric model that interface directly with water molecules diffusing through the membrane. On the other hand, the much smoother curve for the PVDF/H₂O radial distribution indicates a much weaker interaction.

5.4 Beyond graphene: bismuth selenide

One of the most innovative and also appealing 2D materials, is bismuth selenide (Bi₂Se₃), which falls in the class of materials named “topological insulators”. Despite interest and approach to use it in many fields is growing over time, their technological and real applications have been limited to thermoelectric applications [18-20], Terahertz photodetectors [21] and lasers [22, 23]. Recently, Macedonio et al. [24] explored the potential of bismuth chalcogenides in MCr processes detecting assisted crystals nucleation and growth due to very fast induction times. The mechanism proposed was a ‘water exclusion from ion-water clusters’ as a responsible of a quicker ion-ion aggregation. The vacancies in Bi₂Se₃ confined in PVDF matrix were envisaged to promote chemisorption, thus resulting in assisted salt crystallization.

To see real differences between graphene and other 2D materials, in this work the potential of this inorganic salt was explored at a concentration percentage lower with respect that discussed in literature, but comparable with that of the best performing system G 5 wt %. BSE images showed a discrete dispersion of nanocrystals through the matrix (Figure 5.16). In terms of morphological parameters (Table 5.8), bismuth selenide (BS)/PVDF membranes, compared to G%/PVDF, showed bigger pore size and a pore size distribution slightly narrow, (Figure 5.17). In terms of resistance to wetting, PVDF-BS 5 wt % membrane resisted to wettability when used for a long time with high concentration salt solution, without losing its powerful in time, as shown in Figure 5.18. However, the contact angle value was lower than G5/PVDF

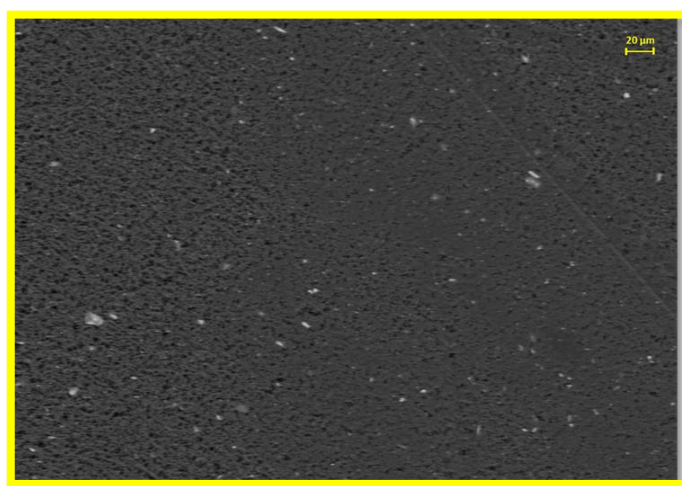


Figure 5.16. Bi_2Se_3 -PVDF membrane top surface. 500X Magnification with signal NTS-BSD.

Table 5.8. Morphological parameters of Bi_2Se_3 -PVDF membranes.

| System | Contact angle with water* (Θ) | Contact angle with NaCl* (Θ) | Mean pore diameter (μm) |
|-------------------|---|--|---|
| PVDF BS 5 wt % | 146 \pm 5 | 143 \pm 3 | 0.84 \pm 0.04 |

*Contact angle measurements carried out with water and $[\text{NaCl}]$ 5.3 mol/L, detected at time = 0 sec.

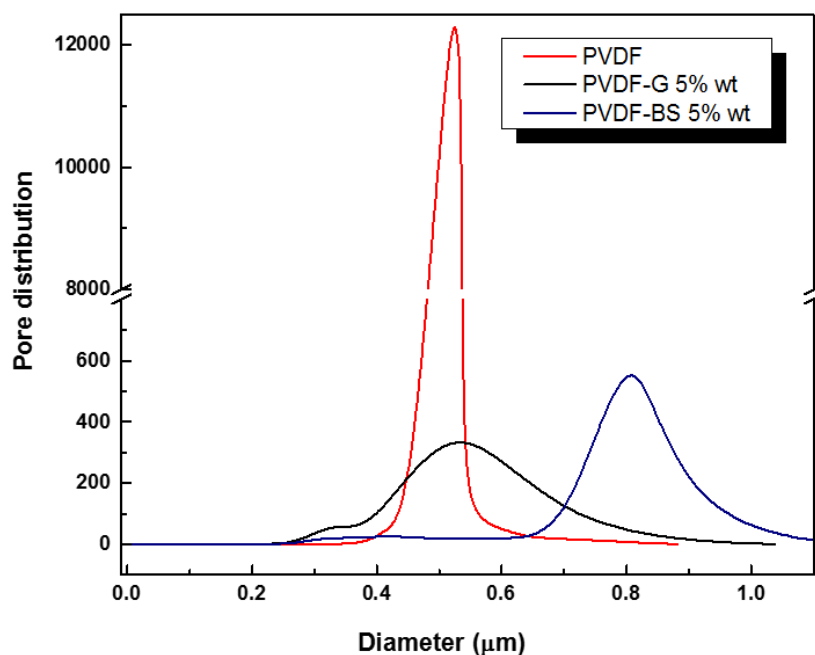


Figure 5.17. Pore size distribution for pristine PVDF, PVDF-G 5 wt % and PVDF-BS 5 wt %.

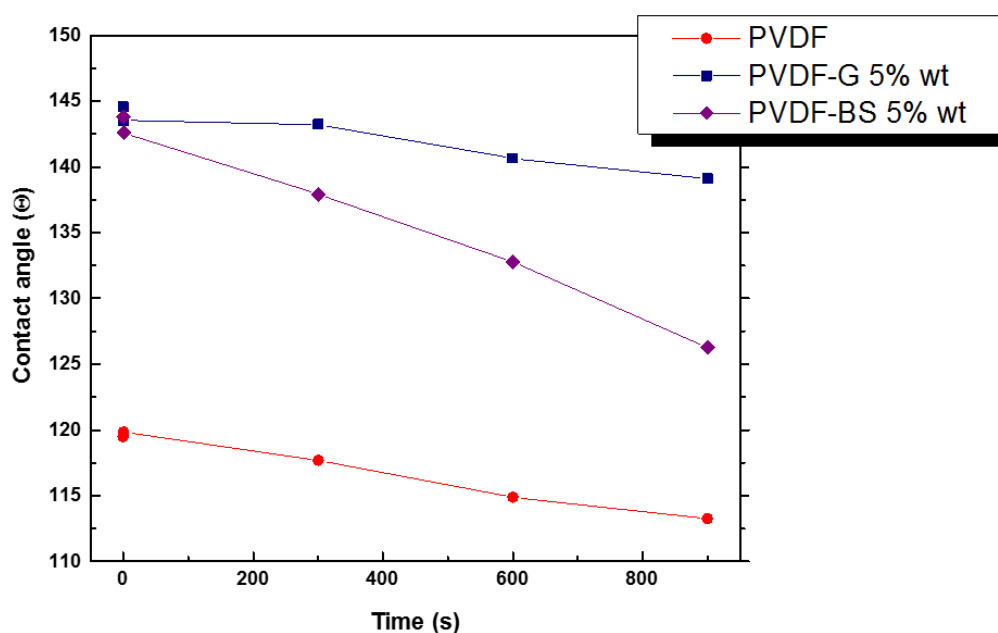


Figure 5.18. Long time contact angle measurements with $[NaCl]$ 5.3 mol/L for pristine PVDF, PVDF-G 5 wt %, PVDF-BS 5 wt %.

Membrane Crystallization tests were carried out with the same experimental condition used for PVDF/G5 (T_{feed} = 308 K; Flow rate_{feed} = 250 ml/min; Flow rate_{perm} = 100 ml/min; $[NaCl]$ = 5.3 mol/L; ΔT = 25). The confinement of bismuth selenide brought to very reduced nucleation times (Table 5.9) with bigger dimension, (Figure 5.19) when compared with PVDF-G 5 wt %. With BS based membranes, similar fluxes to other system were obtained

(at about 4.32 L/m²h), but leading up-taking water and so supersaturation in a very lower time, with a rejection to NaCl of 99.99% (Table 5.10).

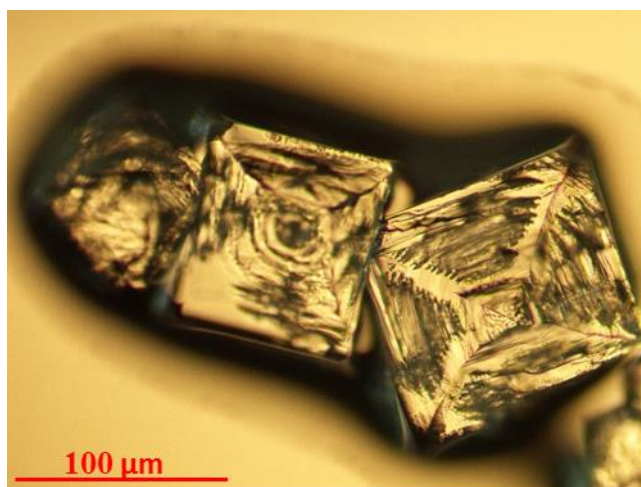


Figure 5.19. Figure 5 NaCl crystals achieved at the end of MCr process with BS 5% wt PVDF membrane. Magnification 10X

Table 5.9. Experimental 1st sample of NaCl crystals (min).

| System | (min) |
|----------------|-------|
| PVDF | 285 |
| PVDF-G 5 wt % | 240 |
| PVDF-BS 5 wt % | 225 |

Table 5.10. Rejection factor (%) to NaCl salt (5.3 mol/L) achieved at the end of MCr process.

| System | Rejection (%) |
|-----------------|---------------|
| PVDF | 99.975 |
| PVDF-G 5 wt % | 99.985 |
| PVDF- BS 5 wt % | 99.990 |

In the case of BS 5 wt %- PVDF membrane, the density of nuclei population B^0 was lower than pristine PVDF and PVDF-G5 wt % (Table 5.11). This was justified by the correlation with electron donor parameter γ - (mJm⁻²) (Table 5.12) which showed as the greater number of vacancies inside membrane matrix is the key point for an enhanced water sequestration.

So a faster nucleation occurred, due to faster supersaturation, leaving to NaCl crystals to grow more. In fact average crystal growth achieved was the highest with respect to all the systems studied (Figure 5.20).

Table 5.11. Nucleation rate (B^0) for BS-PVDF membranes.

| NaCl parameters | Time | PVDF | PVDF G 5 wt % | PVDF BS 5 wt % |
|---------------------------------------|-----------------|----------------|------------------|----------------|
| Nucleation $B^0(*10^3)$ (no/L*min) | 1 st | 490.593 | 1.239.871 | 113.306 |
| | 2 nd | 257.598 | 141.651 | 114.820 |
| | 3 rd | 149.088 | 71.088 | 33.704 |

Table 5.12. Electron donor parameter (γ -).

| Systems | Electron donor parameter γ - (mJm^{-2}) |
|-----------------|--|
| PVDF | 0.05 |
| PVDF-G 5 wt % | 1.69 |
| PVDF- BS 5 wt % | 0.76 |

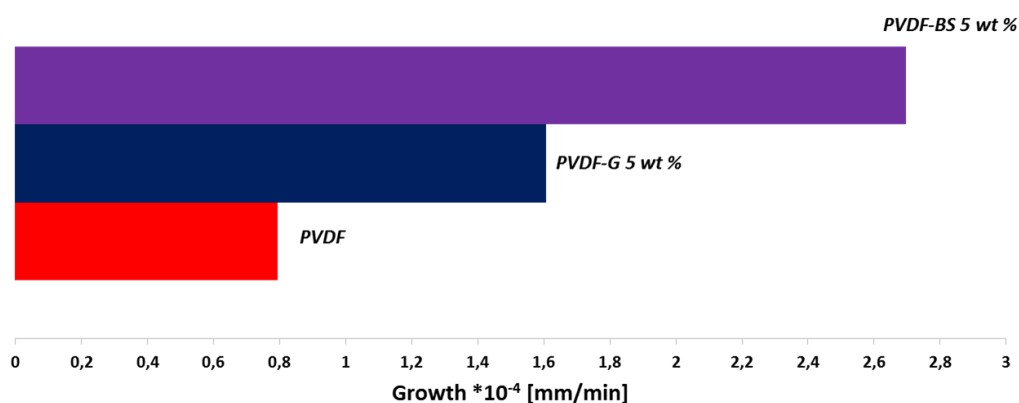


Figure 5.20. Crystal growth achieved with PVDF-BS 5 wt % compared with PVDF pristine and PVDF-G 5 wt % membranes.

The CV was comparable to that obtained with pristine PVDF, even if inferior than 50% indicating homogenous crystals shape and size distribution. Despite of reduced nucleation time of BS/PVDF, the best results in terms of CV were detected with graphene at 5% wt, how is shown in Table 5.13. The significant difference was observed in terms of mean size of final products: crystals achieved at the end of the process were bigger in BS 5 wt % inside polymer matrix as nanofiller, able to assist membrane crystallization technology.

Table 5.13. NaCl parameters (at the 3rd time) for MCr experiments.

| NaCl parameters | Time | PVDF | PVDF G 5 wt % | PVDF BS 5 wt % |
|--|-----------------|-------------|----------------------|-----------------------|
| Mean diameter (µm) | 3 rd | 65.1 | 83.89 | 125.22 |
| Coefficient of variation CV [%] | 3 rd | 48.1 | 26.67 | 46.40 |

Presence of bismuth selenide crystals in PVDF hydrophobic polymeric membranes brought an interesting reduction time in crystals formation leading to bigger crystal size and uniform size and shape distribution. Defects at the surface can be suggested to allow sorption of water, causing quicker supersaturation and then ion aggregation. Therefore, fluxes comparable with pristine PVDF were achieved, but a higher and better rejection to salts was targeted. This is the evidence that modulating interaction from these kinds of materials confined in polymeric membranes it is possible to have interesting performance to assist membrane crystallization process from several point of view.

As a result, the inclusion of fillers inside the membrane had an extraordinary capacity to enhance water sequestration from ion–water clusters. The final result was the occurrence of ion-ion aggregation with remarked effects on the nucleation step, but also on the evolution of the crystals growth and size distribution.

This capability has been confirmed by XPS measurements carried out on surfaces of graphene, epitaxially grown on Ni(111) and Bi₂Se₃ single crystal (exfoliated in situ by micromechanical cleavage) exposed to water at room temperature (Figure 5.21) [25].

Both epitaxial graphene and Bi₂Se₃ topological insulators were able to stabilize water at room temperature with partial dissociation for the case of graphene. Based on experimental evidence, chemisorption mechanisms are hence suggested to promote water sequestration from salt solutions, thereby resulting in a more controlled formation and growth of crystals.

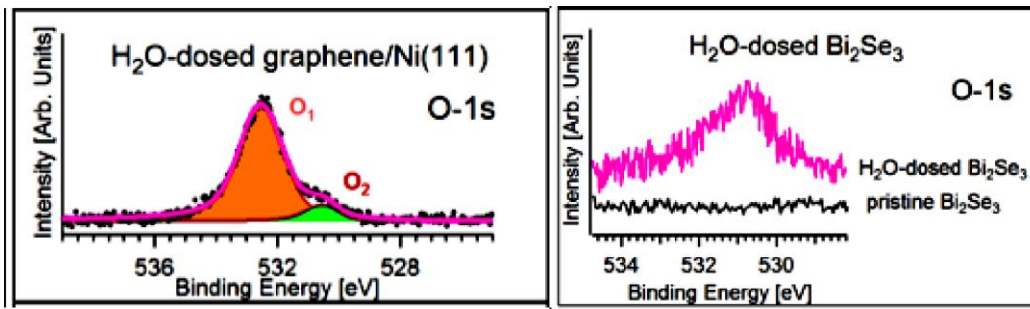


Figure 5.21. a) panel) O-1s core level for water-dosed graphene/Ni(111). Photon energy is 650 eV. The two components in the spectrum are associated to intact water molecules (denoted as “O1”) and hydroxyl group coming from water decomposition (denoted as “O2”). Photon energy is 650 eV. Data have been taken from [26] (b) panel) O-1s core level in pristine and H₂O-dosed (1000 L) Bi₂Se₃. Photon energy is 654 eV. Experiments and water dosage were carried out at room temperature. A Shirley background was subtracted from raw data. Data have been taken from [24].

In terms of final crystals growth (3rd sample) and observation of 1st crystals appeared (Figure 5.22), if we compare commercial PVDF flat sheet membranes, [2] we achieved reduced induction times and highest value of growth rate for all the systems produced, with best value for PVDF-G 5 wt % and PVDF-BS 5 wt %, herein indicating how was significant sorption of water that led to supersaturation faster and that gave rise to a quicker crystals growth.

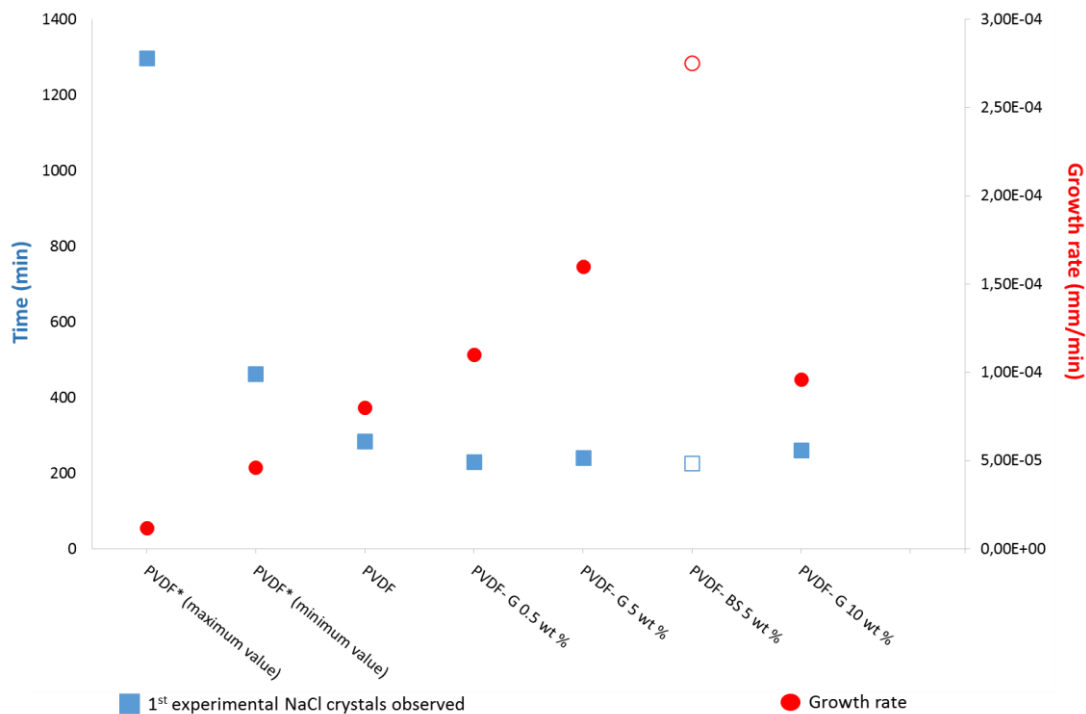


Figure 5.22. Observation of 1st crystals formed (blue squares) and growth rate at the 3rd sample (red circles) for all membrane systems designed, in comparison with PVDF*commercial membranes reported from literature [2].

5.5 Conclusions

Graphene-based PVDF membranes at different concentration percentage of nanofiller (0.5, 5, 10 wt %) and bismuth selenide-PVDF membranes (5 wt %) allowed to evaluate fruitful interaction between modified membranes in crystal nucleation and growth of NaCl salts, when applied in MCr. When graphene platelets and Bi₂Se₃ are blended in traditional polymer matrix of PVDF, the results achieved show a reduced induction time in crystals formation and a higher crystal growth under specific stoichiometric conditions. Better values of CV [%] were also reached with graphene and bismuth selenide based membranes with respect to pristine PVDF. The events can be connected with the interesting feature of the vacancies which characterize the materials. This enabled ability to promote water sequestration in faster times, removing water from ion-water clusters and reaching supersaturation in less time.

Furthermore, the integrated experimental–computational approach showed that graphene polymeric surfaces speeded up crystal nucleation in comparison with the pristine PVDF, confirming the experimental results and thus resulting in a reciprocal validation and in useful correlations between MD and the experimental analysis. The use of 2D materials as nanofiller in MCr can be considered one of the promising approaches to obtain high performing membranes for water desalination purpose.

References

- 1 G. Di Profio, E. Curcio, A. Cassetta, D. Lamba, E. Drioli, Membrane crystallization of lysozyme: Kinetic aspects, *J. Cryst. Growth*, 257 (2003) 359–369, [https://doi.org/10.1016/S0022-0248\(03\)01462-3](https://doi.org/10.1016/S0022-0248(03)01462-3).
- 2 Z. Cui, X. Lia, Y. Zhanga, Z. Wanga, A. Gugliuzza, F. Militano, E. Drioli, F. Macedonio, Testing of three different PVDF membranes in membrane assisted crystallization process: Influence of membrane structural-properties on process performance, *Desalination*, 440 (2018) 68-77, <https://doi.org/10.1016/j.desal.2017.12.038>.
- 3 C.C. Koa, A. Ali, E. Drioli, K.L. Tunga, C.H. Chena, Y.R. Chena, F. Macedonio, Performance of ceramic membrane in vacuum membrane distillation and in vacuum membrane crystallization, *Desalination*, 44 (2018) 48-58, <https://doi.org/10.1016/j.desal.2018.03.011>.
- 4 J.H. Tsai, M.L. Perrotta, A. Gugliuzza, F. Macedonio, L. Giorno, E. Drioli, K. Tung, E. Tocci, Membrane-Assisted Crystallization: A Molecular View of NaCl Nucleation and Growth, *App. Sci.*, 8 (2018) 2145, <https://doi.org/10.3390/app8112145>.
- 5 J.J. De Yoreo, P.G. Vekilov, Principles of Crystal Nucleation and Growth, *Rev. Miner. Geochem.*, 54 (2003) 57– 93, <https://doi.org/10.2113/0540057>.
- 6 M. Kowacz, M. Prieto, A. Putnis, Kinetics of crystal nucleation in ionic solutions: Electrostatics and hydration forces, *Geochim. Cosmochim. Acta*, 74 (2010) 469–481, <https://doi.org/10.1016/j.gca.2009.10.028>.
- 7 J. Anwar, D. Zahn, Uncovering Molecular Processes in Crystal Nucleation and Growth by Using Molecular Simulation, *Angew. Chem., Int. Ed.*, 50 (2011) 1996–2013, <https://doi.org/10.1002/anie.201000463>.
- 8 D. Chackraborty, G.N. Patey, How Crystals Nucleate and Grow in Aqueous NaCl Solution, *J. Phys. Chem. Letters*, 4 (2013) 573-578, <https://doi.org/10.1021/jz302065w>.
- 9 E. Drioli, G. Di Profio, E. Curcio, Progress in membrane crystallization, *Curr. Op. Chem. Eng.*, 1 (2012) 178-182, <https://doi.org/10.1016/j.coche.2012.03.005>.
- 10 F. Anisi, K.M. Thomas, H.J.M. Kramer, Membrane-assisted crystallization: Membrane characterization, modelling and experiments, *Chem. Eng. Sci.*, 158 (2017) 277-286, <https://doi.org/10.1016/j.ces.2016.10.036>.
- 11 P.S. Goh, A.F. Ismail, Graphene-based nanomaterial: The state-of-the-art material for cutting edge desalination technology, *Desalination*, 356 (2015) 115-128, <https://doi.org/10.1016/j.desal.2014.10.001>.

- 12 A. Ananda, B. Unnikrishnana, J.Y. Maoa, H.J. Lina, C.C. Huanga, Graphene-based nanofiltration membranes for improving salt rejection, water flux and antifouling—A review, *Desalination*, 429 (2018) 119-133, <https://doi.org/10.1016/j.desal.2017.12.012>.
- 13 X. Huang, Z. Yin, S. Wu, X. Qi, Q. He, Q. Zhang, Q. Yan, F. Boey, H. Zhang, Graphene-Based Materials: Synthesis, Characterization, Properties, and Applications, *Small*, 7 (2011) 1876-1902, <https://doi.org/10.1002/sml.201002009>.
- 14 J. Zhao, M. Hong, L. Duan, Q. Kang, L. He, The mass transfer process and the growth rate of NaCl crystal growth by evaporation based on temporal phase evaluation, *Opt. Las. Eng.*, 50 (2012) 540-546, <https://doi.org/10.1016/j.optlaseng.2011.07.013>.
- 15 D. Walker, P.K. Verma, L.M.D. Cranswick, R.L. Jones, S.M. Clark, S. Buhre, Halite-sylvite thermoelasticity, *Am. Mineral.*, 89 (2004) 204–210, <https://doi.org/10.2138/am-2004-0124>.
- 16 G. Lanaro, G. N. Patey, Molecular Dynamics Simulation of NaCl Dissolution, *J. Phys. Chem. B*, 119 (2015), 119 4275–4283, <https://doi.org/10.1021/jp512358s>.
- 17 E. Gontarek, F. Macedonio, F. Militano, L. Giorno, , M. Lieder, A. Politano, E. Drioli, A. Gugliuzza, Adsorption-assisted transport of water vapour in super-hydrophobic membranes filled with multilayer graphene platelets, *Nanoscale*, 00 (2019) 1-9, <https://doi.org/10.1039/C9NR02581B>.
- 18 Y. Xu, Z. Gan, S.C. Zhang, Enhanced Thermoelectric Performance and Anomalous Seebeck Effects in Topological Insulators, *Phys. Rev. Lett.*, 112 (2014) 226801, <https://doi.org/10.1103/PhysRevLett.112.226801>.
- 19 M. Hong, Z.G. Chen, L. Yang, G. Han, J. Zou, Enhanced Thermoelectric Performance of Ultrathin Bi₂Se₃ Nanosheets through Thickness Control, *Adv. Electron. Mater.*, 1 (2015) 1500025, <https://doi.org/10.1002/aelm.201500025>.
- 20 M. Stordeur, The Thermoelectric Figure of Merit in the Mixed Crystal System p-(Bi_{1-x}Sbx)₂ Te₃, *Phys. Status Solidi B*, 161 (1990) 831–835, <https://doi.org/10.1002/pssb.2221610237>.
- 21 L. Viti, D. Coquillat, A. Politano, K.A. Kokh, Z.S. Aliev, M.B. Babanly, O.E. Tereshchenko, W. Knap, E.V. Chulkov, S.M. Vitiello, Plasma-Wave Terahertz Detection Mediated by Topological Insulators Surface States, *Nano Lett.*, 16 (2016) 80–87, <https://doi.org/10.1021/acs.nanolett.5b02901>.
- 22 K. Li, Y. Song, Z. Yu, R. Xu, Z. Dou, J. Tian, L-band femtosecond fibre laser based on Bi₂Se₃ topological insulator, *Laser Phys. Lett.*, 12 (2015) 105103, <https://doi.org/10.1088/1612-2011/12/10/105103>.

- 23 C. Zhao, Y. Zou, Y. Chen, Z. Wang, S. Lu, H. Zhang, S. Wen, D. Tang, Wavelength-tunable picosecond soliton fiber laser with Topological Insulator: Bi₂Se₃ as a mode locker, *Opt. Express*, 20 (2012) 27888–27895, <https://doi.org/10.1364/OE.20.027888>.
- 24 F. Macedonio, A. Politano, E. Drioli, A. Gugliuzza, Bi₂Se₃-assisted membrane crystallization, *Mater. Horiz.*, 5 (2018) 912- 919, <https://doi.org/10.1039/C8MH00612A>.
- 25 A. Gugliuzza, F. Macedonio, A. Politano, E. Drioli, Prospects of 2D materials-based membranes in water desalination, *Chem. Eng. Trans.*, 74 (2019), in press.
- 26 A. Politano, M. Cattelan, D. W. Boukhvalov, D. Campi, A. Cupolillo, S. Agnoli, N. G. Apostol, P. Lacovig, S. Lizzit, D. Farias, G. Chiarello, G. Granozzi, R. Larciprete, Unveiling the Mechanisms Leading to H₂ Production Promoted by Water Decomposition on Epitaxial Graphene at Room Temperature, *ACS Nano*, 10 (2016) 4543-4549, <https://doi.org/10.1021/acsnano.6b00554>.

Conclusions

This PhD work advanced knowledge on the design of new nanostructured membranes for application in water desalination, through the exploration of different methodologies, different materials, for two distinct processes. The work focused on the design, development and application of two kind of nanostructured functional membranes fabricated according two different strategies:

- Layered Honeycomb PES/Hyflon AD nanostructured membranes wherein the manipulation of the structure according to ‘bottom-up’ approaches led to an effective increase in productivity and energetic efficiency. In fact, this is an aspect in high demand for Membrane Distillation (MD) technology, via direct contact configuration (DCMD).
- 2D nanomaterials-based PVDF membranes realized by using well established phase inversion techniques, which made Membrane Crystallization (MCr) shorter in time and towards better quality of NaCl crystals.

In detail, the manufacturing approach used to prepare the membranes were breath figures (BF) bioinspired approach and traditional dry/wet phase inversion via solid-liquid demixing, respectively.

Fluxes, rejections, energy efficiency together with nucleation time and growth rate of the crystals were studied through identification of structure-chemistry relationships based on experimental evidence and in some cases, computational investigations.

Major outcomes per type of membranes are summarized hereafter:

1. In the field of self-assembly, which means the capability of some materials to assemble spontaneously in complex nanostructures, this work provided the possibility to move from self- to assisted-assembly mechanisms by using surfactants. The approach was to change the hydrophilic-hydrophobic balance of the polymer solution using polyoxyethylene (20) sorbitan monolaurate (Tween 20) as a traditional surfactant, combined with alcohols with increasing length and bulky chains in order to obtain pore size within a broad range of microns. Depending on the local microenvironment generated, droplet nucleation and growth rate steps have been competitively promoted due to controllable forces established at the water-solution interface. Changes in the interfacial tension have been concerned with the ability of amphiphilic components of the solution to stabilize water droplets through the hydrophobic fluid. It was demonstrated that the manipulation of the polymeric

solution makes a better control of the water droplet dynamics at longer range possible, leading to open pores uniformly packed in ordered, extensive honeycomb textures.

2. Ionic Liquid Crystals (ILCs) were explored as surfactants for improving structural order in honeycomb membranes. They possess a cationic head and chains of different length. Their using made it possible to improve the hydrophilic / hydrophobic balance and to create significantly more ordered geometries. At first Tween20 was successfully used to obtain extensive structural order in PES honeycomb surfaces under humid atmosphere, but this surfactant causes a hydrophilic character for the surface making it unsuitable for MD purposes. Then, the necessity to get a suitable hydrophilic/lipophilic balance (HLB) with marked hydrophobic character for membrane surfaces, led us to identify the family of viologen salts as a good source of compounds having desired features. Specifically, the viologen 14bp14(Tf₂N)₂ had the chemical structure that represented the target for the high hydrophobicity required thanks two peculiarities: the two aliphatic segment chains (C14) and the hydrophobic anion bis(trifluoromethanesulfonyl)amide (Tf₂N⁻).
3. Hyflon AD was used to generate a nanoporous layer onto Honeycomb PES top surface exploiting breath figure techniques. This implementation allowed to fabricate new interesting interfaces for membrane distillation technology via direct contact configuration. In fact, it was possible to obtain much improved productivity-thermal efficiency trade off. An average water flux > 50 L/m²h and a thermal efficiency > 70.2 % was appreciated for the new honeycomb tailor-made membranes, whereas fluxes less than 5 L/m²h and thermal efficiency not superior to 35% has been estimated for commercial membranes traditionally used in DCMD operations. Other membranes processed at much higher feed temperature show a thermal efficiency ranging from 55 to 80% approximately, but an average flux much lower (less than 13 L/m²h). The breakthrough was the possibility to manipulate a polymer (highly hydrophobic) traditionally used in dense structure, Hyflon AD, in a very tiny porous layer. So, the combination of a new highly porous nanostructure, done by a perfluorinated material with lower thermal conductivity, make the designed membrane extremely promising for future competitively productive and energetically favored water desalination.
4. Graphene-PVDF based membranes at different concentration percentage of nanofiller (0.5, 5, 10 wt %), were investigated in MCr technology via DCMD

configuration, with respect to tailor made pristine PVDF membrane. The objective was to evaluate possible fruitful interaction for crystal nucleation and growth of NaCl salts, combining the experimental studies with a computational work. From the experimental point of view results achieved showed reduced induction time in crystals formation when the nanofiller is dispersed into polymer matrix. In particular, times of crystals formation are in a range from 230 to 260 min with respect to 286 min for pristine PVDF. The trend consisted in the increasing of induction time when the graphene concentration (wt %) increased (from 0.5 to 10 wt %). Furthermore, better values of CV [%] were reached with graphene-PVDF based membranes with respect to pristine PVDF, leading to a more homogenous crystals shape and size distribution. The range for CV was from 26.67 % to 35.8 % for graphene-PVDF membranes with respect to pristine PVDF, where CV was 48.1 %. The best value of CV (26.67 %) was reached for PVDF-Graphene 5 wt %, which showed also the highest crystal growth (1.6×10^{-4} mm/min) with respect to pristine PVDF and other graphene-PVDF based membranes produced. In addition to graphene, a new 2D material was explored: the bismuth selenide (Bi_2Se_3), for its use as nanofiller in polymer PVDF matrix, at the same amount of graphene system with which we had the best results (5 wt %). It was possible to obtain even more reduced induction time (225 min), with a difference really evident: bigger crystals (mean diameter 125.22 μm) in less time, due to particular feature of this particular material to promote water uptake faster, thus reaching supersaturation in less time. Furthermore, with respect to other 2D nanomaterials-PVDF membranes studied, was reached the highest crystal growth with a value of 2.75×10^{-4} mm/min. Bismuth selenide is considered one of the promising 2D material to use in desalination technology.

5. Graphene (G)-PVDF membranes were also studied from a computational point of view. The presence of nanostructures inside polymer PVDF matrix, was evaluated with molecular dynamics, using a highlighted software particularly used in biosciences but not in membrane technology. In this case we studied systems with the high amount of graphene (5 and 10 wt %). The sense was not to identify a concentration effect as in the experimental session but in particular to observe molecular implication of graphene nanostructures in membrane crystallization phenomena with respect to pristine PVDF. The integrated experimental–computational approach showed that graphene polymeric surfaces speeded up crystal nucleation in comparison with the pristine PVDF, confirming the experimental results and thus resulting in a reciprocal validation and in useful correlations between

MD and the experimental analysis. In particular, reduced induction time were reached with G systems: 0.45 and 0.70 ns respectively for PVDF-G 5 and PVDF-G 10 wt %, with respect to 1 ns for pristine PVDF. Furthermore, the ability of graphene to induce supersaturation in less time is in full agreement with theoretical studies where the water uptake was validated by the detection of radial distribution function (rdf) between graphene layer and water. It shows how the interactions among them are much higher with respect to PVDF chains. These preliminary simulations provided the stimuli to investigate other mono and bivalent crystals and other related mixtures in view to predict crystallization with different complex polymeric matrices.

6. At this stage, an economical analysis was not carried out. From a performance point of view, as major achievements we had: with multi-layered honeycomb membranes, higher fluxes and higher thermally efficiency with respect to commercial membranes. It was used the DC configuration of Membrane Distillation process, overcoming the limitation of the low water productivity, typical for this kind of configuration. With 2D materials confined in PVDF networks, we achieved shorter time in nuclei and crystals formation in association with major uniformity in number, shape and size distribution. For the up scaling is necessary to consider further improvements in order to guarantee energy- and time-saving point of views, but also for what concerns the recovery of added-value products, as was did on lab scale From the point view of environmental and human health, the polymers used are inert and biocompatible [1, 2], whereas 2D materials chosen are considered green [3]. Graphene is a carbonaceous material, while bismuth selenide is an abundant metal considered scarcely toxic. Raman investigations on filtrated from feed and permeate streams have been carried out after MD experiments. No traces of nanomaterials were revealed, yielding indication of a good stability of the composite systems for the observed period.

To conclude, we can confirm that honeycomb multi-layered membranes allowed to overcome productivity-selectivity trade-off obtained with commercial membranes in DCMD. In fact, it was possible to achieve higher productivity and at the same time higher energy efficiency preserving consistent salt rejection, let us thinking the possibility to implement competitive DCMD technology to treat saline streams.

In parallel, for the first time a silico-experimental approach was used in MCr technology using 2D materials as nanofillers in PVDF membranes, leading to better-quality crystals due

to the possibility to control induction times and growth rate. Experimental results are in full agreement with theoretical data.

This work provides new insights in the design of advanced nanostructured functional membranes for the improving of MD and MCr performance. Despite of different preparation methods are used, the new membranes have a common objective: to shift the productivity-efficiency trade-off through increase in mass and reduction of heat transfer, but also through regulation of kinetics and thermodynamics controlling for the nucleation-growth steps of salt crystals. This work offers a clear example about how the quality of interface can change the final performance of a purification process. Novel interactive interfaces were realized by the choice of different materials and different assembly procedures, tuning structure-properties relationship for the desired application: Membrane Distillation and Membrane Crystallization. One of the major limitations is, however, the lacking of membranes with suitable features for equipping MD and MCr devices. Commercial membranes meet partially some fundamental requirements from these two technologies, but they have not the capacity to give major propulsion and competitiveness on the market. In this thesis advanced functional membranes were prepared with new chemical-physical features suggesting different strategies to combine different materials in a unique system. In perspective, further optimization and identification of materials as well as assembly procedures will be necessary to move from proof-of-concept to scalable prototypes of membranes and MD/MCr operations.

References

1. G. Laroche, Y. Marois, R. Guidoin, M.W. King, L. Martin, T. How, Y. Douville, Polyvinylidene fluoride (PVDF) as a biomaterial: from polymeric raw material to monofilament vascular suture, *J Biomed Mater Res.* 29 (1995), 1525-1536. <https://doi.org/10.1002/jbm.820291209>.
2. Y. Yu, H. Sun, H. Orbay, F. Chen, C. G. England, W. Cai and X. Wang, Biocompatibility and In Vivo Operation of Implantable Mesoporous PVDF-Based Nanogenerators, *Nano Energy*, <http://dx.doi.org/10.1016/j.nanoen.2016.07.015>.
3. T.P.D Shareena, D. McShan, A. K. Dasmahapatra, P. B. Tchounwou, A Review on Graphene-Based Nanomaterials in Biomedical Applications and Risks in Environment and Health, *Nano-Micro Lett.* 10 (2018), 1-34. <https://doi.org/10.1007/s40820-018-0206-4>.